UNIVERSITY OF CALIFORNIA
RIVERSIDE

Decoding the Molecular Mechanisms Underlying Electronic Cigarette Toxicity in Lung, Cancer and Stem Cells

A Dissertation submitted in partial satisfaction
of the requirements for the degree of

Doctor of Philosophy

in

Bioengineering

by

Atena Zahedi

December 2018

Dissertation Committee:
Dr. Prue Talbot, Chairperson
Dr. Bir Bhanu
Dr. Jiao Liao

The Dissertation of Atena Zahedi is approved:

_____

_____

_____

Committee Chairperson

University of California, Riverside

Acknowledgements

The text and figures in Chapter 2, in part or in full, are a reprint of the material as it appears in Plos ONE 2016. The text and figures in Chapter 3, in part or in full, are a reprint of the material as it appears in Scientific Reports 2018. The text and figures in Chapter 5, in part or in full, are a reprint of the material as it appears in iScience 2018. The text and figures in Chapter 6, in part or in full, are a reprint of the material as it appears in Lung Cancer 2018. This dissertation consists of the research carried out over the past five years in Dr. Prue Talbot's lab.

Dedication

This dissertation is dedicated to all the people in my lives who inspire me to grow every single day. To my brother, whose strong compassionate heart is the shining star that guides me north. And to my mom, who has taught me courage and given me the power of love and faith. And to my loving husband, who was my brilliant tutor, and showed me the beauty of sustained perseverance; who stood by my side throughout this rough road. And to my dad, who encouraged me to embrace my aptitudes. And to my grandmother who showed boundless kindness and love to her little girl. Her memories will never cease to warm my heart and soul. And to my advisor Dr. Prue Talbot, who is a loving mentor who has been my greatest supporter, and inspires me to follow in her footsteps. And a special thanks to my brilliant and supportive PhD labmate, Rattapol Phandthong. And to my esteemed colleague and friend, Dr. Vincent On, whom I have had the pleasure of publishing several research articles with. And to his advisor, Dr. Bir Bhanu, who has guided me as an NSF fellow IGERT fellow, and been a valuable committee member. And to Dr. Jiayu Liao and Dr. Victor Rodgers and other esteemed faculty who has guided me on my path.

ABSTRACT OF THE DISSERTATION

Decoding the Molecular Mechanisms Underlying Electronic Cigarette Toxicity in Lung, Cancer and Stem Cells

by

Atena Zahedi

Doctor of Philosophy, Graduate Program in Bioengineering
University of California, Riverside, December 2018
Dr. Prue Talbot, Chairperson

Electronic cigarettes (ECs), popular nicotine-delivery devices, have emerged as potential health hazards. ECs contain nicotine, flavor chemicals, and solvents used to generate aerosols. The purpose of my dissertation was to develop bioassays and video bioinformatics tools to characterize effects of disposable-style ECs on cultured lung cells, stem cells, and cancer cells. A screening method was developed to identify toxic EC products and evaluate their modes of action (MOAs). StemCellQC software can assess the health of pluripotent embryonic stem cell (ESC) colonies and extract data on dynamic processes such as cell proliferation, spreading, migration, and cell death. MitoMo software was developed to assess mitochondrial (important and sensitive organelles) health parameters such as mitophagy, morphology, dynamics, membrane potential, oxidative stress, calcium levels, and mtDNA nucleoids.

A two-tiered screen was performed to identify harmful EC products. Based on tier 1 assays, two brands were identified for further investigation. In tier 2 assays, Greensmoke exposure led to a decrease in growth rate, cytoskeletal depolymerization, adhesion defects, oxidation of mitochondrial proteins, and eventual apoptosis. Vuse exposure produced an epithelial-to-

mesenchymal transition (EMT) and increased α-smooth muscle actin, a fibrosis biomarker. It also caused loss of cell-to-cell junctions, migratory behavior, internalization of junctional stabilizers E-cadherin and P120-catenin, and nuclear translocation of β-catenin (dual role as a transcription factor for EMT). EMT is the initial step enabling metastasis of cancer cells, which is a concern for former smokers with a pre-existing lung tumor. Fibrosis, epithelial cell disruption, and oxidative damage can lead to chronic lung diseases.

The effects of ECs were studied on neural stem cells (NSCs) as an in vitro model for early development, since ECs are often targeted to youth and pregnant mothers, raising developmental risks. The high nicotine content in Vuse caused oxidative stress, autophagy defects, and a stress-induced mitochondrial hyperfusion (SIMH). Exposure to Vuse aerosols also led to upregulation and desensitization of nicotinic acetylcholine receptors (nAChRs). These findings are critical considering that nicotine is now widely available in EC products. Mitochondrial damage, oxidative stress and autophagy dysfunction can cause faulty stem cell populations, which may accelerate aging and lead to cancer, diabetes, neurodegenerative disorders.

Table of Contents

List of Figures

List of Tables

List of Videos

Chapter 1

Introduction

INTRODUCTION TO TOBACCO SMOKE

Cigarette smoking is the number one preventable cause of death in the United States [1]. The chemicals that are inhaled during smoking are deposited in the lungs where they can be absorbed by the bronchioles and alveoli. Absorption can also occur through the oral mucosa, olfactory bulbs and the skin. Components of tobacco smoke, including nicotine, are then transferred via circulation throughout the body [1]. Nicotine triggers chemical reactions in the brain/neurons, leading to the release of dopamine and endorphins associated with pleasure. Cigarette smoke contains more than 7,000 chemicals including known carcinogens such as polycyclic aromatic hydrocarbons (PAHs), tobacco-specific nitrosamines (TSNAs), benzene, formaldehyde, carbon monoxide and cyanide, acrolein, and polonium [2]. Some of these toxicants are shown in Figure 1.1 and Table 1.1.

Manufactured cigarettes are the dominant tobacco product, and approximately 20% of the world's adult population smokes cigarettes [1]. In some countries, more than 30% of boys and girls between ages 13-15 have smoked [1]. This is critical because 9 out of 10 adult smokers first try cigarettes during adolescence [3]. Smokers as well as non-smokers can be exposed to cigarette smoke. The smoke that is actively inhaled by the user is called mainstream smoke and includes nicotine, particulate matter or "tar", and gas components [1]. The smoke that is exhaled by a smoker and released from the burning tip of a cigarette is called secondhand smoke (SHS), which can be passively inhaled by non-smokers. The smoke that gets deposited on indoor surfaces is referred to as third hand smoke (THS) [4–6]. Infants and children are particularly at risk for THS by oral and skin exposure to carpets, dust, and furniture.

Figure 1.1. Some of the Toxicants Present in Tobacco Smoke. Some of the extremely harmful chemicals such as Arsenic, Formaldehyde, Cadmium and Benzene are present in Tobacco smoke from both regular and e-cigarettes. The image Courtesy of LifeBridge Health

Tobacco smoke is a recognized health hazard that has been directly linked to many disorders ranging from lung diseases, such as emphysema, chronic obstructive pulmonary disease (COPD), pulmonary fibrosis and cancer, to cardiovascular diseases, myocardial infraction, and stroke [4]. Cigarette smoke can also worsen and/or contribute to other ailments, such as bone deterioration, diabetes, vision degeneration, and reproductive/birth defects. Tobacco smoking can cause developmental defects in higher-risk users, such as adolescents and pregnant women [7]. It can induce reproductive defects, such as miscarriages, still births, sudden infant death syndrome

(SIDS), low birth weights, ectopic implantation, and neuro-developmental defects [8–10]. Figure 1.2 depicts some of the health effects associated with tobacco smoke.

EFFECTS OF TOBACCO ON LUNG DISEASE

Tobacco smoke damages the cells of the lung, resulting in scarring, loss of elasticity, diminished ability to exchange gases, and increased mucus production [11]. This can cause serious respiratory conditions and diseases such as asthma, chronic obstructive pulmonary disease (COPD), and idiopathic pulmonary fibrosis (IPF) [4,12]. Cigarette smoke can trigger/worsen asthma attacks due to activation of CD4 lymphocytes and eosinophils, as well as elevated immunoglobulin E (antibodies produced by the immune system) that increase sensitivity to allergens [13]. Smoking can also increase production of pro-inflammatory cytokines IL-4, IL-8, TNF-α, and NF-κβ, all of which impair responses to anti-inflammatory aids (corticosteroids) [13].

Table 1.1. Abbreviated List of Harmful and Potentially Harmful Constituents (HPHC) in Tobacco. Source: Table courtesy of US Department of Health and Human Services.

HPHCs in Cigarette Smoke	HPHCs in Smokeless Tobacco	HPHCs in Roll-your-own Tobacco and Cigarette Filler[6]
Acetaldehyde	Acetaldehyde	Ammonia
Acrolein	Arsenic	Arsenic
Acrylonitrile	Benzo[a]pyrene	Cadmium
4-Aminobiphenyl	Cadmium	Nicotine (total)
1-Aminonaphthalene	Crotonaldehyde	NNK*
2-Aminonaphthalene	Formaldehyde	NNN**
Ammonia	Nicotine (total and free)	
Benzene	NNK*	
Benzo[a]pyrene	NNN**	
1,3-Butadiene		
Carbon monoxide		
Crotonaldehyde		
Formaldehyde		
Isoprene		
Nicotine (total)		
NNK*		
NNN**		
Toluene		

* 4-(methylnitrosamino)-1-(3-pyridyl)-1-butanone

** N-nitrosonornicotine

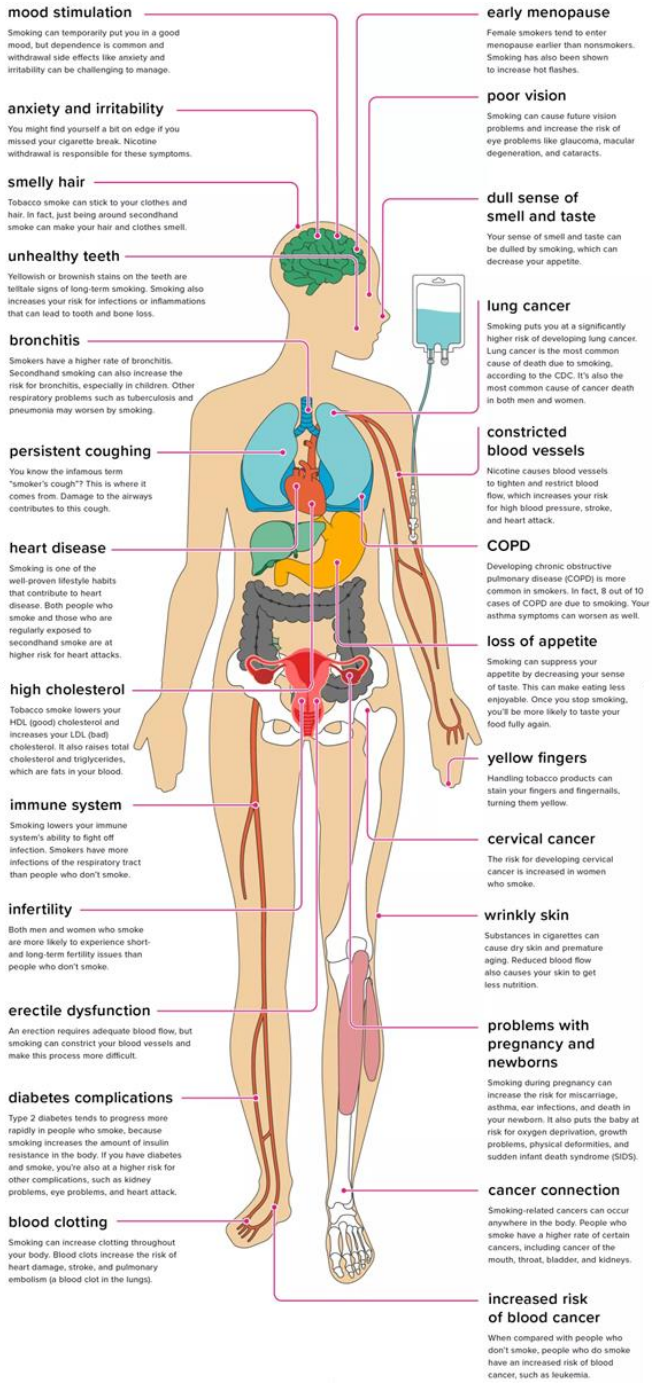

Figure 1.2. Some of the Health Effects Associated with Smoking. Diagram below, depicts the various biological effects that Tobacco smoke can induce through its systemic distribution throughout the body. For example, it can stimulate moods, anxiety and irritability in the brain, whereas, it can cause bronchitis, COPD and cancer in the lung. It can also cause reproductive damage such as infertility, erectile dysfunction or even cervical cancer. Courtesy of www.healthline.com/health/smoking/effects-on-body#1

COPD is an irreversible, progressive, inflammatory disease that develops in response to inhaled irritants and kills more than 3 million people worldwide every year [14,15]. In COPD, there is diminished air exchange in the lung due to loss of elasticity, damage/thickening of the airway walls, and/or increased mucus production that clogs the airways [15]. Cigarette smoke recruits inflammatory cells (neutrophils, macrophages, and Tc1/CD8 lymphocytes) into the lung [16]. Superoxide and nitric oxide in cigarette smoke also cause neutrophils to produce peroxynitrite, which can inactive histone deacetylase 2 (HDAC2) and upregulate inflammatory genes [17]. The inflammatory response is also mediated by chemotactic factors, oxidative damage due to free radicals in tobacco smoke, and breakdown of the lung connective tissue by proteases [15].

Smoking is also a risk factor for lung fibrosis, another progressive disease that causes lung scarring. The underlying mechanism is largely unknown, although oxidative stress has been suggested as a promoting factor [18,19]. Reactive oxygen species (ROS) in cigarette smoke can cause oxidation of proteins, lipids, and DNA [20]. The most common type of fibrosis is idiopathic pulmonary fibrosis (IPF), which is driven by the proliferation and differentiation of fibroblasts (initiated by cell/tissue damage), leading to increased deposition of extracellular matrix (ECM) and an increased number of myofibroblasts [21]. Myofibroblasts are spindle-shaped with increased numbers increased of actin stress fibers, which contribute to the contractile phenotype that is responsible for the structural remodeling of the lung (fibrotic phenotype) [22].

EFFECTS OF TOBACCO ON CANCER AND ITS PROGRESSION

In United States, cancer is the second leading cause of death, after heart disease [23]. Lung cancer is the most common cause of death due to cancer [24], and smoking is the number one preventable risk factor [4]. Cigarette smoking is also linked to cancer in other organs/tissues where smoke is directly deposited (e.g., the oropharynx and mouth), as well as distal sites such as the

pancreas and urinary bladder, as assessed by IARC and the United States Surgeon General [1,4]. Genome-wide association studies (GWAS) have identified other factors that predispose people to cancer, such as susceptibility genes (e.g., tumor suppressors TP53, BRCA, and TERT), and genetic loci that contain nicotinic acetylcholine receptors, major histocompatibility complex (MHC), DNA repair, and cell-cycle regulation genes [25].

Since tobacco smoke is a complex mixture containing over 7000 compounds, it is difficult to pinpoint a single mechanism that links it to lung cancer. However, it is well established that 73 carcinogens, including PAHs and TSNAs, in tobacco smoke can contribute to lung cancer [26]. Once in the body, most carcinogens are metabolized by CYP enzymes (cytochrome P450) and glutathione S-transferase, which create reactive intermediates during their detoxification to water soluble forms [26]. These electrophilic compounds (such as carbo-cations or epoxides) then react with DNA, causing adducts that can lead to mutations in important oncogenes (genes that when mutated lead to cancer) [26]. Tobacco smoke also contains co-carcinogens such as catechol and hydroquinone [27] that influence protein kinase C (PKC) signaling, which promotes lung cancer invasion and metastasis [28].

Tobacco smoke also causes inflammation, oxidative stress, and epigenetic changes, all of which can lead to cancer [1,26]. Tobacco smoke activates NF-κβ signaling, which causes production of IL-6, TNF-α, and other pro-inflammatory cytokines/chemokines that stimulate tumor proliferation and angiogenesis [29]. Furthermore, free radicals are present in tobacco smoke and/or can be generated indirectly by inflammation, which can contribute to carcinogenesis [1,30]. Lastly, chronic smoke exposure can cause abnormal DNA methylation that upregulates epithelial-to-mesenchymal transition (EMT), anchorage-independent growth, and RAS/MAPK pathways, which sensitize cells to transformations by oncogenic events such as KRAS mutation [31].

Tobacco smoke also induces cancer metastasis to secondary sites, making treatment difficult and often leading to the death of the patient [32–34]. Metastasis is a coordinated series of events that starts with an EMT, allowing cancer cells to detach from their site of origin and migrate to other tissues [35]. Cigarette smoke causes down-regulation and internalization of epithelial cadherin (E-cadherin), a key stabilizer of cell-to-cell junctions, which prevents migratory behavior [36]. Additional tobacco studies report internalization of other junctional proteins β-catenin and p120-catenin [37–41]. β-catenin is also a transcription factor that can activate Wnt signaling, leading to upregulation of genes involved in proliferation (e.g. MYC and cyclin D1) and stemness (e.g. CD44) [1,41]. P120-catenin can also initiate transcription of downstream Rho GTPases, which contributes to increased invasiveness [42,43]. Other biomarkers for EMT are vimentin, N-cadherin, and transcription factors Snail, Twist, and Slug [44].

EFFECTS OF TOBACCO ON DEVELOPMENT AND ADOLESCENT

Since the brain continues to develop throughout adolescence, the effects of tobacco smoke are greater and more persistent during this sensitive period of increased plasticity and rapid growth of brain circuitry [7,45]. Yuan et al. (2015) summarized that nicotine exposure during adolescence impacts brain development, changes neuronal signaling and cognition function, and causes epigenetic changes [45]. Nicotine binds nicotinic acetylcholine receptor (nAChRs) in the brain and activates neuronal firing resulting in dopamine release [46]. Nicotine exposure causes changes in firing activity that lead to functional/structural changes in the dopaminergic pathways (involved in reward processing and addiction) [47]. Moreover, nicotine exposure during adolescence affects the serotonin pathway [45]. Chronic nicotine exposure can also cause cognitive deficits such as reduced attention span, increased impulsivity, and enhanced predisposition to attention deficit hyperactivity

disorder (ADHD), anxiety and depression [45]. Teenaged smokers are more likely to participate in risky sexual behavior and have increased risk for substance abuse [45].

Nicotine can also cross the placenta and affect a developing fetus [48], and smoking has been associated with a number of reproductive [49] and development defects [50]. Prenatal tobacco exposure increases the incidences of: ectopic pregnancy (implantation outside of the uterus), infertility (due to decreases in sperm and egg health), premature delivery, spontaneous abortion, perinatal mortality, low weight babies, placental abruption, infant irritability and hypertonicity (stiff baby syndrome), and sudden infant death syndrome (SIDS) [8–10]. As discussed in the above paragraph, nAChRs are important in organization of the brain circuitry during development. At the cellular level, they have key roles in cell survival and apoptosis (regulating cell number), forming neural/sensory circuits, and development of the catecholamine system [9]. Prenatal nicotine exposure can increase activity, inattention, impulsivity, and delinquent/aggressive behaviors (leading to ADHD, conduct disorder (CD), and cognitive deficits) [8]. Even passive in utero exposure to secondhand smoke can cause these psychopathologies in the offspring [50].

Our lab has utilized in vitro organotypic models to show that exposure to tobacco smoke can affect reproduction [10], for instance by decreasing ciliary beat frequency in hamster oviducts [51] or by inhibiting oocyte cumulus complex pick-up by oviduct [49]. Either of these outcomes could cause ectopic pregnancy. We also utilized human embryonic stem cells (hESCs) and mature stem cells as ideal in vitro models for studying the effects of tobacco products on the early stages of development and differentiation [10,52–54]. Exposure of stem cells to tobacco products reduces their proliferation, migration, and ability to differentiate [55–57]. Research from our lab has also shown that exposure to THS extracts caused a mitochondrial stress response in mouse neural stem cells (mNSCs) and decreased transcription of apoptosis-related genes (including Aifm2, Bbc3, and Bid) [58]. Although stress-induced mitochondrial hyperfusion (SIMH) is a pro-survival

mechanism, prolonged exposure to THS extracts can cause collapse of mitochondrial membrane potential, eventually leading to NSC death.

INTRODUCTION TO ELECTRONIC CIGARETTES:

With the decline of cigarette smoking [59], there has been an increase in the use of alternative electronic nicotine delivery systems (ENDS), such as electronic cigarettes (ECs), especially among adolescents [7]. ECs typically deliver nicotine, flavor chemicals, and solvents, such as propylene glycol and glycerin, in an aerosol that users inhale. ECs come in numerous brands, shapes, and designs that include cig-a-like models, disposable cartomizer models, and customizable tanks (Figure 1.3). Tank style ECs allow consumers to vary e-liquid flavors, nicotine content, and power. In contrast, disposable-style ECs typically come in fewer flavor profiles (mostly tobacco and menthol) and pre-set nicotine concentrations. Furthermore, they generally have small batteries that generate modest puffs and do not allow power variation. For the purpose of this dissertation, I will be focusing on cartomizer-style ECs from big-tobacco companies. These include: (1) GreenSmoke Menthol (GSM) and Red Label Tobacco (GSRLT) from Altria; (2) BluCig Menthol and Tobacco from Lorillard (now Imperial Tobacco Group), (3) V2 Tobacco from Swedish Match, (4) Vuse Menthol (VM) and Tobacco (VT) from RJ Reynolds, and (5) Mark10 Menthol and Classic Tobacco from Nu Mark (formerly Altria).

NEED FOR EC TOXICOLOGICAL INVESTIGATIONS:

The impact of ECs on human health is not well understood, and the mid-to-long term consequences of EC exposure are still unknown. Because they deliver aerosolized nicotine without combustion, many experts claim that they are “harm-reduction” alternatives [60–62]. However, studies now show that some EC aerosols expose consumers to toxicants that cause health effects

[59]. Flavor chemicals are particularly worrisome because there is little inhalation safety information on them for humans. Our lab and others have found that ECs sometimes contain high concentrations of flavor chemicals, and these can be cytotoxic when tested in vitro [63–67]. Fruity, sweet, and menthol flavored ECs dominate the market and have cytotoxic effects on respiratory cells [68]. Aerosolization of flavor chemicals and solvents (PG and glycerol) can generate toxic volatile organic chemicals (VOCs) [69], such as diacetyl [66,67,70,71]. One study measured over 115 VOCs in EC aerosols, which were undetected in unheated liquids [72]. Moreover, upon heating the dominant solvents, PG and glycerol, can be converted to reaction products such as propylene oxide, propanal, 2-propenol, methyl glyoxal, glycidol, and other known carcinogens such as acrolein, acetaldehyde, formaldehyde, and benzene [2,69,73–76].

Figure 1.3. Diversity of e-cigarette products. The variety in the form and style of the e-cigarettes are far beyond the traditional scope of regular cigarettes, which in turn has expanded their usage and popularity in consumers of all ages. Photo Courtesy of Mandie Mills, CDC.

Although ECs have lower concentrations of TSNA than conventional cigarettes [74,77], recent studies demonstrate their ability to cause DNA damage [78,79], which could contribute to cancer development. Furthermore, ECs are sometimes advertised as "smoking cessation" devices, since nicotine concentration can be progressively decreased, allowing users to wean themselves off. However, according to the recent Surgeon General's report and other studies, EC user topographies can lead to nicotine delivery that exceeds that of combustible cigarettes [7,80]. Moreover, the diverse flavors and customizable features of ECs have enormous appeal to adolescents, and the widespread use of ECs among middle and high school students is producing a generation of nicotine addicts at an "epidemic" rate [7]. The Surgeon General's report reinforced the need to conduct extensive research on EC to better understand the health consequences of their use and to be better able to inform the public, especially adolescents, of their dangers [7].

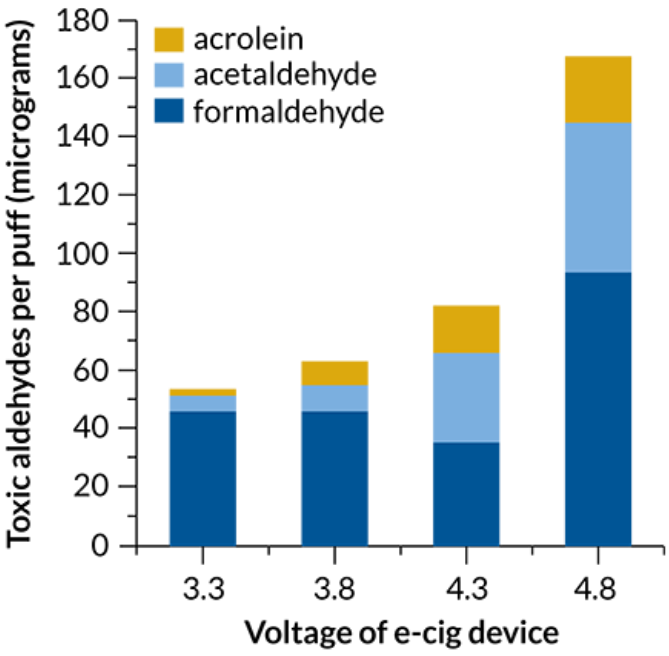

Figure 1.4. Effects of EC voltage on emission of aldehydes. There is a direct correlation between the EC voltage and the amount of emitted carcinogens such as acrolein, acetaldehyde and formaldehyde. Image: Courtesy of Sleiman *et al.* 2016 report [2]

The concentration of toxic byproducts can be greatly increased when using higher voltages and temperatures [2,66,73]. Figure 1.4 shows increased emission of toxic aldehydes with increased voltage of EC devices [2]. Goniewicz et al. (2014) first compared the compounds (such as formaldehyde, acetaldehyde, acrolein, toluene, NNN, and NNK) in ECs versus "cigarette equivalents" (amount emitted in one combustible tobacco cigarette versus 15 "typical" puffs of an EC). They showed that the levels of formaldehyde and carbonyl were lower in ECs [74]. However, Jensen et al. (2015) subsequently showed that EC aerosols can contain formaldehyde at levels far surpassing that of cigarettes [73]. Gillman et al. (2016) did a similar comparative study at four different "power" settings and showed that two EC devices generated higher levels of formaldehyde and acrolein than conventional cigarettes and that aldehyde levels increased with higher power settings [81].

Several labs have detected other potentially hazardous (and unapproved) compounds in ECs [7]. For instance, one FDA study detected amino-tadalafil and rimonabant, the active ingredient for Cialis and an obesity drug respectively, in some EC products [82]. Furthermore, thermal degradation of sugars (found in popular sweet EC flavors) leads to emission of toxic furans including 5-hydroxymethylfurfural and furfural in EC aerosols [83]. Also, it is now established that EC aerosols contain high levels of fine particles, generated when the solvents are aerosolized [84]. Offermann et al. (2015) showed that in direct (first-hand) EC exposure, the hazard quotients were exceeded for 7 of 9 toxic chemicals, while for passive (second-hand) exposure, the hazard quotient was exceeded for propylene glycol and nicotine based on California EPA's exposure level standards for non-carcinogenic health effects [85].

EC liquid and aerosols also contain metals and non-metal elements (including nanoparticles) at potentially unsafe levels [86–90]. Some of the elements reported in EC aerosols are found on the Food and Drug Administration's (FDA) harmful and potentially harmful

constituents (HPHC) list [91]. These elements may originate from coils, wires, solder joints, and fiberglass wicks in ECs [87,90]. Our lab first reported that EC aerosols contained tin, silver, iron, nickel, aluminum, chromium, and silicate nanoparticles with 9/11 elements present in EC aerosol at concentrations than higher or equal to those found in conventional cigarettes [87]. In cytotoxicity testing, the e-liquids containing high levels of tin particles were cytotoxic and inhibited attachment and survival of human pulmonary fibroblasts [87]. Lerner et al. (2016) exposed human lung fibroblasts to EC aerosols containing copper nanoparticles, resulting in increased mitochondrial ROS and subsequent upregulation of an antioxidant response element (ARE) protein, NAD(P)H quinone dehydrogenase 1 (Nqo1) [88]. They also detected reduced stability of the mitochondrial electron transport chain (ETC) complex IV, as well as DNA fragmentation in the nucleus [88]. Our recent paper explored the effects of selenium (another element found in elevated levels in some EC brands) on A549 lung epithelial cells and showed that it caused mitochondrial swelling and rupture, leading to loss of membrane potential, mitophagy, and eventual cell death [92]. A study by Olmedo et al. (2018) concluded that EC users are exposed to lower concentrations of Cd than conventional cigarettes users, but not other hazardous metals [90]. Therefore, the potential health consequences of inhaling metals and other elements present in EC aerosols is high and requires further investigation [93].

Nicotine, a highly addictive psychoactive chemical now readily available for purchase, presents another major health concern [7,59]. Case reports have been made on intentional or accidental nicotine poisoning [59]. Our lab has shown that so-called “nicotine-free” as well as counterfeit EC and do-it-yourself products labeled 0 mg/ml of nicotine did in fact contain nicotine [94–96]. Therefore, users can become unintentionally exposed to nicotine. Also, the FDA warns that some popular EC products used by adolescents (e.g., JUUL) contain extremely high concentrations of nicotine (60 mg/mL), which increases the risk of neuro-developmental effects

and nicotine addiction. Moreover, marketing of ECs as safer alternatives has led to their increased use during pregnancy [97]; however, the nicotine consumed by EC users is similar to that of conventional cigarettes [80]. Since nicotine itself is a teratogen, this raises the question of whether EC use during pregnancy has the potential to induce the same developmental effects summarized earlier [45]. Nicotine can also contribute to tissue remodeling by inducing secretion of key factors (dermal matrix proteins collagen type Iα1, elastin, and matrix metalloproteinase 1) by fibroblasts [98,99]. Even secondhand EC aerosols contain nicotine, particles, flavorings such as diacetyl, VOCs, and heavy metals [7,100], posing health concerns for EC users as well as non-users subjected to passive vaping.

ASSESSING CYTOTOXICITY OF ECS AND THEIR CONSTITUENTS

Many labs have begun examining the cytotoxicity of ECs and their constituents, including the solvents (PG/VG) and flavor chemicals [7], on cell health using in vitro cultures [57,65,66,68,101–109], animal models [110–115], and humans [116,117]. Although flavor chemicals in EC may be approved for ingestion, the inhalation safety of many are still unknown [66,67,70,71].

Our lab and others have shown that EC toxicity is correlated with type and amount of flavor chemicals [106,110]. We first screened various e-liquids on embryonic stem cells and lung cells and showed a correlation between cytotoxicity and increased number/height of flavor chemical peaks on HPLC analysis [106]. Next, we discovered two highly toxic cinnamon-flavored chemicals cinnamaldehyde (CAD) and 2-methoxycinnamaldehyde in e-liquids [64,65]. Farsalinos et al. (2015) analyzed 159 EC products from 36 manufacturers, and detected diacetyl and acetyl propionyl in a majority (74.2 %) of the products [118]. Another study showed that 39 out of 51 products contained diacetyl and its substitute 2,3-pentanedione, even in tobacco and menthol-

flavored ECS [67]. Exposure to 2,3-pentanedione causes airway epithelial damage [119]. Currently, there are no health-based standards for the general public on diacetyl inhalation.

Inhalation of solvents (PG and glycerin) are also under investigation. Some claim that they are harmless [84], whereas other showed that they can affect cell viability [66,101,120]. Volunteers experienced slight airway obstruction and increased dyspnea when exposed to PG mist for 1 min; whereas long-term exposure of children lead to or exacerbated the onset of allergic symptoms [121]. Lim et al. (2014) reviewed case reports of PG toxicity in children, which can cause adverse effects, such as hyperosmolarity, lactic acidosis, hemolysis, central nervous system (CNS) toxicity, and cardiac arrhythmia [122]. Also, ethylene glycol was found in some EC brands as a substitute for PG/glycerin [123], even though its ingestion has been linked to serious neurological, metabolic, and renal health effects [124]. Lastly, an important consideration is the potential for PG to produce toxicity due to changes in osmolarity [103].

TOXICOLOGICAL EFFECTS OF ECS ON LUNG CELLS

EC exposure causes oxidative damage, inflammation, and death in lung cells in vitro [108,125,126]. Lerner et al. (2015) reported that flavored ECs contained reactive oxygen species (ROS) that caused oxidative stress and inflammatory responses (IL-8 and IL-6 secretion) in human lung fibroblast and epithelial cells (H292 and BEAS-2B) exposed at an air-liquid interface (ALI) [110]. They showed that oxidative stress correlated with the concentration of the flavor chemicals with sweet and fruity flavors being the most potent. In particular, lung fibroblasts secreted high levels of IL-8 in response to cinnamon flavored e-liquids. One review summarized that EC aerosols and e-liquids caused the following responses in primary airway epithelial cells and cell lines: (1) reduced viability, (2) increased production of inflammatory factors, (3) oxidative stress, (4) reduction of antimicrobial defenses, and (5) pro-carcinogenic events [127]. Lei et al. (2017) showed

that nicotine in ECs dysregulate lung fibroblast repair responses (stimulated with TGF-β1, a driver of pro-fibrotic or obstructive inflammatory diseases) by inhibiting myofibroblast differentiation, gel contraction, and wound healing [104]. Scott et al. (2018) investigated the effects of EC on human alveolar macrophages, and showed loss of viability, release of cytokine/chemokine/proteases, and inhibition of phagocytosis [128]. Loss of protective cells and their phagocytotic abilities have significant implications for impaired bacterial clearance in the lung.

Animal models have also been used to study the effects of ECs on health. In a mouse model of asthma (mimicked by systemic ovalbumin exposure), ECs enhanced the development of allergic airway inflammation, increased eosinophil levels of Th1-cytokines, and worsened hyper-responsiveness [113]. Wu et al. (2014) also showed that nicotine-free e-liquid increased respiratory infection to human rhinovirus (HRV) in a mouse model and that addition of nicotine amplified the effects [108]. Lerner et al. (2015) found that exposure of mice to EC aerosols increased pro-inflammatory cytokines and reduced lung glutathione levels [110]. In another paper, mice exposed to EC aerosols developed COPD-like tissue damage that correlated with nicotine concentration [114]. Inhalation of nicotine-containing EC aerosols increased airway hyperactivity, distal airspace enlargement, mucin production, cytokine and protease expression, whereas exposure to nicotine-free EC aerosols did not have these effects. They also mimicked this response in normal human bronchial epithelial cells (NHBE) exposed at an ALI, showing that exposure to nicotine-containing EC aerosols impaired ciliary beat frequency, airway surface liquid volume, cystic fibrosis transmembrane regulator and ATP-stimulated K+ ion conduction, and decreased FOXJ1 and KCNMA1. EC exposure in animal models can also lead to reduced weight and postnatal lung growth in neonatal mice, oxidative stress, neurobiological changes, such as an increase in nAChR

in different brain regions and behavioral changes, including spontaneous withdrawal, episodic memory, and addiction-related emotional response [126].

Studies of ECs on human health effects are limited with virtually none on long-term effects. One study showed that 5 min of EC use led to an increase in lung flow resistance, which is related to a decrease in exhaled nitric oxide (FeNO) and increased lung inflammation [129]. A second study showed increased production of the pro-inflammatory cytokine IL-6 and host defense molecules (e.g. SPLUNC1) in EC treated airway epithelial cells from a non-smoker [108]. Serum cotinine levels of EC users are shown to be similar to conventional cigarette smokers [130]. Although only mild effects such as upper respiratory irritation have been reported following PG exposure [131], one study reported that factors such as the VG/PG ratio, type of flavor, and levels of nicotine correlate to the degree of "throat hit" in consumers [117]. Carnevale et al. (2016) showed an increase in markers of oxidative stress (soluble NOX2-derived peptide, 8-isoPGF2α, vitamin E, and NO bioavailability) and endothelial dysfunction (reduced flow-mediated dilation FMD) in blood samples after EC use [132]. In a study on 42 healthy habitual EC users versus non-users, there was increased cardiac sympathetic activity, low/high frequency ratio (a measure of heart rate variability), and low-density lipoprotein oxidizability (a measure of oxidative stress), all of which suggest potential cardiovascular risk [133].

Several labs are gathering information about potential EC health effects using case reports and Internet reports from consumers. Hua et al. (2016) reviewed 27 case reports published between 2012 and 2016. The reports documented nicotine poisoning, mechanical injury due to EC battery explosions, and other health effects such as infantile necrotizing colitis, reversible cerebral vasoconstriction syndrome (RCSV), ulcerative colitis, atrial fibrillation, and acute myocardial infarction [116]. A review of existing literature (in PubMed, EMBASE and CINAHL) identified 76 studies leading the conclusion that: (1) in 34% of the articles the authors had a conflict of

interest, (2) PG is a compound of concern, and (3) reports on short-term adverse events were often flawed by selection bias [121]. Users and the general public should be aware of potential "Conflicts of Interest" when studying research articles for information on EC. The 2018 National Academies of Sciences, Engineering, and Medicine (NASEM) report comprehensively summarized the "Public Health Consequences of E-Cigarettes" using human studies and case reports associated with EC use. They found that some people have reported allergic reactions to PG, asthma worsening, and lipoid pneumonia [59].

EFFECTS OF EC ON CANCER AND ITS PROGRESSION

As mentioned above, EC aerosols contain carcinogens such as formaldehyde, acetaldehyde, diacetyl, acrolein, and glyoxal, as well as oxidizing agents, which can contribute to cancer development [2,63,65,67,72,75]. One study on Salmonella typhimurium showed that ECs and their particulates (captured on Cambridge filter pads) had limited mutagenic activity [109]. Tommasi et al. (2017) also reported limited mutagenicity in mouse and human cells exposed to EC aerosols; however, their exposure times were relatively short [134]. In contrast, another study reported that EC aerosols increased production of free radicals and DNA oxidation in a rat lung model [78]. They showed that EC aerosols damage DNA at the chromosomal level in peripheral blood (DNA strand breaks in leucocytes and micronuclei in reticulocytes), as well as at the gene level as evidenced by an increase in point mutations in cells isolated from urine. Ganapathy et al. (2017) used the primer anchored DNA damage detection (q-PADDA) and 8-oxo-dG (measure of oxidative DNA damage) assays to show DNA damage in normal human bronchial epithelium (Nuli1), premalignant dysplastic oral mucosal keratinocytes (POE9n), and oral squamous cell carcinoma cells (UM-SCC-1) [79]. They also showed that EC aerosols induced significant ROS and decreased antioxidant activity, both of which can contribute to carcinogenesis. Another

important animal study revealed that EC aerosols damaged DNA in mouse lung, bladder, and heart, and impaired DNA repair activity in the lung [111].

PAHs and TSNAs in ECs are also a concern, as they are both classified as carcinogens [135,136]. One study found that vaping increased indoor air PAH levels by 20%, raising concerns for secondhand exposure [135]. TSNAs, including N-nitrosonornicotine (NNN) and nicotine-derived nitrosamine ketone (NNK), are classified as group 1 carcinogens, although there are conflicting studies on their reported levels [121,137]. Some studies found TSNA levels higher (as high as 86.92 ug/L) in EC aerosols [138], while others found lower levels relative to cigarette smoke [139]. Canister et al. (2017) explored whether ECs can induce cytochrome P450 (CYP) changes, whose activation is associated with metabolism of carcinogens in the body to reactive intermediates. They observed an increase in CYP2A1/2 (activating for PAHs), CYP2B1/2 (activating for olefins and halogenated hydrocarbons), CYP2C11 (activating for TSNAs and mycotoxins), and CYP3A (activating for hexamethyl phosphoramide and TSNAs) [78]. CYP activation is correlated with increased P53 mutations in tobacco smokers [140], which can directly contribute to cancer.

Nicotine has been linked to cancer development [98] and metastasis [39,141,141–144]. Although nicotine itself is not a carcinogen, it can bind to receptors that initiate Akt, PKA, and other pathways contributing to carcinogenesis [26]. Nicotine also promotes proliferation, inhibits apoptosis, and enhances angiogenesis in cancer [26,145,146]. Nicotine can increase survival of cancer cells by upregulating the expression of p53 [98]. Moreover, nicotine causes metastasis of cancer cells due to its ability to induce an EMT [144] or by α7 nAChR-mediated activation of cell migration via the RAF-MEK-ERK or PI3K-ROCK pathways [98]. Activation of nAChRs can also regulate expression of transcription factors, RNA-binding proteins, protein processing factors, and plasma membrane associated proteins [98]. The α7 nAChRS also increase expression of

proliferative and survival genes [98,147,148]. Functional nAChRs are also present in mitochondria, and their activation prevents cytochrome c release, thereby inhibiting apoptosis [98,149].

Smoking has also been associated with progression of cancer in other ways, such as by increasing cancer stem cells (CSC) and causing drug resistance. β-catenin activation has been associated with stem cell renewal. CSCs are a subpopulation of stem-like cells within tumors which have the capacity to self-renew, differentiate, and seed tumors when transplanted in vivo [150]. CSCs are generally thought to be resistant to cancer drug/therapies, hence play an important role in cancer relapse and metastasis [150]. To date, no study has investigated the effects of ECs on cancer progression. It is also not yet clear whether EC exposure can induce any of the molecular and behavioral phenotypes associated with cancer metastasis, increased stemness, or drug resistance. This thesis focuses on addressing these questions.

EFFECTS OF ECS ON DEVELOPMENT AND YOUTH

Today, more adolescents are using EC than conventional tobacco products in the US [151], and the number of youth who have taken up vaping tripled between 2011 to 2013 [152]. There is serious concern about the widespread use of high-nicotine content EC, such as the top-selling brand JUUL, by youth [153]. The CDC reports that incidents of children getting nicotine poisoning through swallowing, breathing, or absorbing e-liquids is on the rise [154]. To make matters worse, the 2018 National Academy of Medicine report showed evidence that EC use leads to increases in the frequency and amount of smoking in the future [59]. Specifically, teens who try ECs are seven times more likely to take up conventional cigarettes. Figure 1.5 highlights some of the health threats that ECs pose to adolescents.

Nicotine exposure through EC presents the same health effects previously summarized for tobacco smoke. The amount of nicotine intake varies between EC products with most “cig-a-like”

products (except products such as JUUL and Vuse) often delivering less than tank styles [118], as well as in between EC users due to differences in topography [155]. The nicotine concentrations present in various e-liquids affect the plasma nicotine levels in EC users, which can reach levels close to or even exceeding that of cigarette users [7,80,156]. Nicotine dependence (addiction) among adults and adolescents is also well established [4]. As discussed above, prenatal exposure to nicotine correlates with upregulation of nAChRs, which can disrupt normal cell replication, differentiation, and brain development. Given the potentially high nicotine exposure due to compensatory vaping, EC users are at significance risk for nicotine dependence and the associated

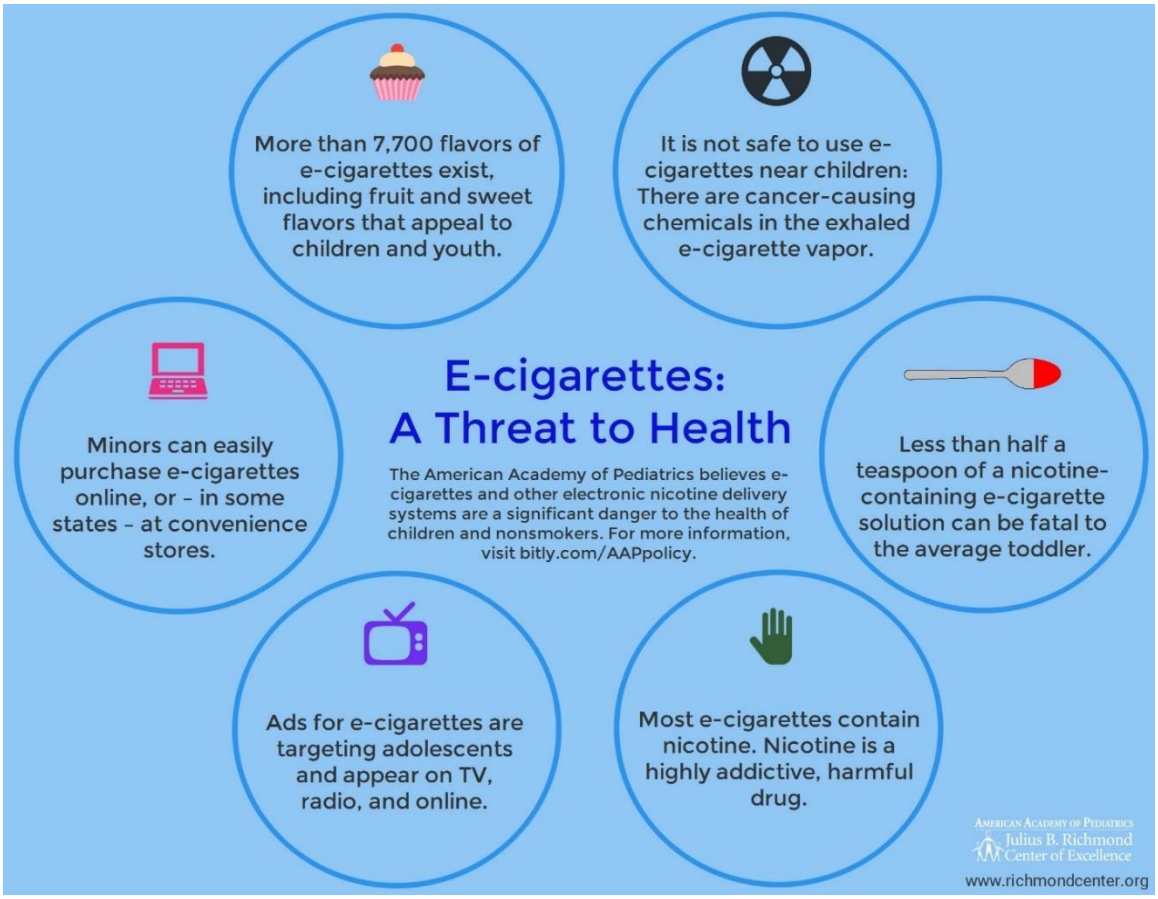

Figure 1.5. E-cigarettes: A Threat to Health. The lack of regulations, attractive design and abundance of different flavors often appealing to the children and youth (whose body are far more vulnerable to the toxins than adults) has turned ECs to an engraving public health threat according to the American Academy of Pediatrics. Image Courtesy of American Academy of Pediatrics

effects of withdrawal, nicotine tolerance, and cognitive disturbances [157]. Preliminary studies report lower dependence scores for adult EC users; however, nicotine dependence score measurements have not yet been standardized, especially for the youth [7].

EC use during pregnancy is also on the rise, and there is a misconception that it is a safe alternative. The effects of maternal EC use on the developing human fetus or offspring are largely unknown [97]. Current concerns about EC use during pregnancy are based on known effects of maternal nicotine exposure. Healthcare providers often misinform pregnant women or are not fully informed themselves. One study investigated EC use during pregnancy, revealing that the prevalence ranges between 0.6% to 15%, and the amount of consumed nicotine was similar to that of cigarette smokers [97]. The CDC warns that there is currently not enough evidence to conclude that ECs can help smokers quit or are less harmful, especially to pregnant mothers [158].

In animal studies, the dangers of ECs to the developing fetus can occur through many routes, such as the immune system, neural development, lung function, and cardiac function. One in vivo study used frog embryos and mammalian neural crest cells to model EC exposure to a developing fetus [159]. Damage to neural crest cells can cause craniofacial defects (e.g. cleft palate), since these cells form the bones, cartilage, skin, teeth, and glands lineages [160] In the frog embryos, all the e-liquids caused cleft palate with the more complex mixed flavor e-liquids causing the most dramatic facial effect. In the e-liquid treated neural crest cells, there was a diminished ability to differentiate and produce the derivative tissues. Hiemstra and Bals (2016) summarized in vivo assessments and pointed out that neonatal mice exposed to EC had reduced lung growth, impaired alveolar cell proliferation, and decreased total body weight [127].

Another critical concern is the effect of EC on human stem cells throughout development, as well as adulthood. One study showed that exposure of hESCs to PAHs reduced their differentiation into human primordial germ cells (PGCs), which form the oocytes and sperm [161].

Stem cells are also important for repair and cell homeostasis throughout the entire human lifespan, and damage due to toxicants or gradual aging can inhibit their proper functioning [162–164]. Our lab and others have shown that stem cells are highly sensitive to environmental and other toxicants [52,53,64,65,101,106,161,165–167]. Therefore, stem cells serve as excellent models for evaluating safety limits of toxicants [168–171]. During development, stem cells in the brain are particularly vulnerable [172]. Ultimately, damage to stem cells due to ECs could negatively impact a developing embryo or infant, or even an adult.

A NEED FOR BETTER METHODS FOR TOXICOLOGICAL EVALUATION

There is a need for rapid toxicological evaluations to allow research to keep up with the explosion of EC products and over 7,000 EC flavors [59,83]. Iskandar et al. (2016) proposed an in vitro systems toxicology framework consisting of three layers of assessment: (1) cell viability; (2) cell cycle, cell death, mitochondrial health, oxidative stress, and transcription factors, and (3) impact on 3D epithelial tissues [103]. However, most labs do not have the necessary resources and equipment for this strategy, this approach is not easily scalable, and it does not cover cancer-specific endpoints. Rowell et al. (2017) used multiple screening assays (cell number count using DAPI, viability using calcein and MitoTracker Red, and cytotoxicity using LDH assay) [173]. They also proposed using confluent cultures to evaluate cytotoxicity versus sub-confluent cultures for inhibition of proliferation, yet their study did not go in depth into MOAs. Sassano et al. (2018) developed an open-source high-throughput (HTP) screening assay for evaluation of e-liquid toxicity using a 384-well plate setup [120]. However, they only used human embryonic kidney (HEK) cells, which are a transformed cell line and are not a direct target of EC exposure. Our lab [65,66,94] and others [103,120] have combined gas chromatography/mass spectrometry (GC-MS)

analysis to correlate EC toxicity and flavor chemicals, showing that vanillin and cinnamaldehyde are particularly harmful.

In developing better multi-disciplinary toxicological approaches, choosing the right cell type, experimental models, and target assays are critical. For potential teratogens, it is important to consider early (pre- or post-natal) stages of development, which are most sensitive and susceptible to harm. For cytotoxicity screening, immortalized or cancer cell types (e.g. CL-1548 and A549) may not provide adequate sensitivity [174]. Human embryonic and adult stem cells, organoids and ALI systems serve as excellent in vitro alternatives, given that animal models are costly and have limited throughput. NSC have well-defined mitochondria and are ideal for bioinformatics analysis and toxicological evaluation [92,175–177] and are potential targets of EC aerosols via inhalation through the olfactory tracks [178]. Future studies can also incorporate patient-derived induced pluripotent stem cells (iPSCs) from healthy and diseased patients, to take into consideration factors such as genetic susceptibility and environmental factors.

Studying the effects of ECs on cancer progression is challenging, given the plasticity of cancer [179]. Biological stressors such as cell damage/death, inflammation, metabolic reprogramming, or cell cycle defects/senescence all play roles in cancer development [180]. Potential carcinogens in EC products may contribute to multiple stages of cancer progression (e.g. proliferation, angiogenesis, metastasis, and resistance). In contrast to the need for sensitivity in the screening phase, cancer epithelial cells such as A549 are good in vitro models for studying modes of action (MOAs) such as EMT [181]. Machine learning can help classify and track tumor cell heterogeneity (using morphological and functional phenotyping) as well as other dynamic, cancer-specific endpoints, such as cell differentiation, migratory patterns, metabolic state, and cell cycle perturbations [182–184].

Mitochondrial defects cause by ECs are broad and encompass factors such as oxidative damage, dynamics, bioenergetics, and calcium homeostasis. Lerner et al. (2016) showed that exposure of lung fibroblasts to EC aerosols (and their copper nanoparticles constituents) at the ALI caused mitochondrial ROS, electron transport chain (ETC) complex IV instability, and genotoxicity [88]. Lei et al. (2017) demonstrated that dysregulated wound healing in nicotine/EC treated cells was mediated via mitochondrial oxidative stress and inhibition of OXPHOS complex III [104]. Mitochondrial dysfunction can ultimately lead to premature aging and a variety of diseases, such as cancer, diabetes, mitochondrial myopathies, and neurodegenerative diseases [185–190]. There is also some evidence that mitochondria are involved in cancer aggressiveness [183,191]. Further investigations are required to determine what EC products and constituents drive mitochondrial toxicity.

Video bioinformatics provides a powerful solution for EC toxicological evaluations by allowing extraction of functional readouts from dynamic biological processes [192]. Machine-learning approaches can be used to identify and classify cellular-, organelle-, and molecular-level phenomena. This dissertation introduces two video bioinformatics software tools, StemCellQC and MitoMo, with immense potential to impact toxicology and pharmacology, medicine, and biological fields. StemCellQC can identify affected biological processes and predict health at the stem cell colony level, while MitoMo provides a diverse array of protocols for studying mitochondrial behaviors and functions (such as morphology, dynamics, oxidation, organization, calcium levels, etc.). Lastly, a two-tiered toxicological protocol was developed for rapid and comprehensive screening of EC products and constituents and determining disease-specific MOAs.

POTENTIAL CONTRIBUTIONS TO THE FIELD

Research into ECs can provide valuable information to public health officials and regulatory agencies. The 2009 Family Smoking Prevention and Tobacco Control Act outlaws the use of flavorings, except for tobacco and menthol, in regular cigarettes but not in EC products. Furthermore, none of the safety assessments, such as the GRAS ("generally recognized as safe") provision under Section 201(s) of Federal Food, Drug, and Cosmetic Act (FFDCA), cover effects of flavor chemicals via inhalation [193]. To date, the FDA has not published a fully comprehensive HPHC list for ECs, similar to the list for tobacco smoke as abbreviated in Table 1.1 [3]. Nor has the FDA established quality control guidelines for manufacturing and labeling of EC products. In 2016, the FDA's Center for Tobacco Products finally issued "deeming" regulations to extend its authority to ECs, however, these regulations will not go into effect until 2023.

Meanwhile, there is still considerable debate on whether ECs are in fact harm-reduction devices [61,62]. Even with over 800 peer-reviewed studies to date, their long-term health effects are relatively unexplored given their short time on the market [59]. While some evidence suggests that ECs contain lower levels of toxicants in comparison to conventional cigarettes, they are not without harm. There are reported cases of poisonings, explosions, and respiratory symptoms, such as coughing, wheezing, and asthma exacerbations, particularly in infant and adolescent demographics. However, whether they will lead to respiratory diseases, neurodevelopmental defects, and cancer is still unknown. There is still insufficient research on how ECs affect pregnancy outcomes or fetal health in humans [59]. Although there is some evidence that complete substitution can reduce exposure to toxicants/carcinogens, many EC consumers are dual users, and for those that use only EC, the risk for switching to conventional cigarettes is high, especially in young users [7]. ECs have gone from cessation tools to a trendy recreational use. Yet, nicotine intake via ENDS can be comparable to that from tobacco [7,80], depending on the type of device,

nicotine content in the e-liquids, and user topography [59]. Hence, the impact to public health, particularly adolescents and former smokers, is potentially high and not fully understood. Additional research investigations are needed to inform the general public and EC consumers about health effects.

The effects of ECs on mitochondria are particularly important, since mitochondrial dysfunction can negatively impact many biological processes such as energy production, stem cell maintenance and differentiation, and cell death [194–197]. Nicotinic responses are also of interest, given that functional nAChRs have been discovered in mitochondria. Moreover, mitochondria are potential targets of metal exposure, and elements of concern in ECs include chromium, nickel, lead, manganese, copper, zinc, selenium and arsenic [59,86,87,89,90]. However, so far only one study has compared metal concentrations in EC aerosols to biomarkers of metal exposure in humans. Mitochondrial analysis software has immense toxicological applications and may serve as predictive biomarkers of harm in human liquid-biopsies such as urine, saliva, and exhaled breath condensate (EBC) of EC users.

There is still no evidence that EC use is associated with intermediate cancer endpoints in humans (examples of intermediate endpoints are polyp lesions). However, limited evidence from "prospective" biomarkers of cancer in animal studies suggests that EC use increases risk for cancer. These studies have reported an increase in oxidative stress, DNA damage, and impaired DNA repair in response in short-term exposures. It is not clear whether mitochondria dysregulation can also contribute to the cancer-promoting effects of ECs.

This thesis explores the potential of acute and sub-chronic EC exposure to harm in vitro cultured cells. Cells from the lungs and brain are studied, and adult lung, lung cancer and brain stem cell are compared. The specific purposes of this dissertation are to: (1) introduce two bioinformatics software tools, StemCellQC and MitoMo, and to apply these to problems involving

EC toxicity, (2) screen fluids and aerosols from popular brands of cartomizer style ECs for toxicity using a two-tiered approach that characterizes MOA effects, (3) evaluate the effects of EC fluids and aerosols on mitochondria in NSC, and (5) examine the effects of EC fluids and aerosols on induction of an EMT in lung cancer cells.

REFERENCES

[1] B.W. Stewart, C.P. Wild, World Cancer Report 2014, 2014.

[2] M. Sleiman, J.M. Logue, V.N. Montesinos, M.L. Russell, M.I. Litter, L.A. Gundel, H. Destaillats, Emissions from electronic cigarettes: Key parameters affecting the release of harmful chemicals, Environ. Sci. Technol. 50 (2016) 9644–9651.

[3] U.S. Department of Health and Human Services, Guidance for Industry: Reporting harmful and potentially harmful constituents in tobacco products and tobacco smoke under Section 904(a)(3) of the Federal Food, Drug and Cosmetic Act, 904 (2012) 10. http://www.fda.gov/downloads/TobaccoProducts/GuidanceComplianceRegulatoryInformation/UCM297828.pdf.

[4] United States Department of Health and Human Services, The Health Consequences of Smoking—50 Years of Progress A Report of the Surgeon General, 2014.

[5] V. Bahl, P. Jacob, C. Havel, S.F. Schick, P. Talbot, Thirdhand cigarette smoke: Factors affecting exposure and remediation, PLoS One. 9 (2014) 1–9.

[6] P. Jacob, N.L. Benowitz, H. Destaillats, L. Gundel, B. Hang, M. Martins-Green, G.E. Matt, P.J. Quintana, J.M. Samet, S.F. Schick, P. Talbot, N.J. Aquilina, M.F. Hovell, J.-H. Mao, T.P. Whitehead, Thirdhand Smoke: New Evidence, Challenges, and Future Directions, Chem. Res. Toxicol. 30 (2017) 270–294.

[7] United States Department of Health and Human Services, E-Cigarette use among youth and young adults: a report of the surgeon general, 2016.

[8] M.D. Cornelius, N.L. Day, Developmental consequences of prenatal tobacco exposure, Curr. Opin. Neurol. 22 (2009) 121–125.

[9] J.B. Dwyer, S.C. McQuown, F.M. Leslie, The dynamic effects of nicotine on the developing brain, Pharmacol. Ther. 122 (2009) 125–139.

[10] P. Talbot, In vitro assessment of reproductive toxicity of tobacco smoke and its constituents, Birth Defects Res. Part C - Embryo Today Rev. 84 (2008) 61–72.

[11] Centers for Disease Control and Prevention, Smoking and Respiratory Diseases, (n.d.). https://www.cdc.gov/tobacco/data_statistics/sgr/50th-anniversary/pdfs/fs_smoking_respiratory_508.pdf (accessed January 12, 2018).

[12] 10 of the Worst Diseases Smoking Causes, Am. Lung Assoc. (2018). https://www.lung.org/our-initiatives/tobacco/reports-resources/sotc/by-the-numbers/10-worst-diseases-smoking-causes.html.

[13] A. Tamimi, D. Serdarevic, N.A. Hanania, The effects of cigarette smoke on airway inflammation in asthma and COPD: Therapeutic implications, Respir. Med. 106 (2012) 319–328.

[14] K.F. Rabe, H. Watz, Chronic obstructive pulmonary disease, Lancet. 389 (2017) 1931–1940.

[15] J. Vestbo, S.S. Hurd, A.G. Agustı, P.W. Jones, C. Vogelmeier, A. Anzueto, P.J. Barnes, L.M. Fabbri, F.J. Martinez, M.M. Nishimura, R.A. Stockley, D.D. Sin, R. Rodriguez-Roison, Global strategy for the diagnosis , management , and prevention of chronic obstructive pulmonary disease GOLD executive summary, Am. J. Respir. Crit. Care Med. 187 (2013) 347–365.

[16] J. Lee, V. Taneja, R. Vassallo, Cigarette smoking and inflammation: Cellular and molecular mechanisms, J. Dent. Res. 91 (2012) 142–149.

[17] P.J. Barnes, Reduced histone deacetylase in COPD: Clinical implications, Chest. 129 (2006) 151–155.

[18] American Lung Association, Types, Causes and Risk Factors of Pulmonary Fibrosis, 2018. www.lung.org/lung-health-and-diseases/lung-disease-lookup/pulmonary-fibrosis/introduction/types-causes-and-risk-factors.html.

[19] R.C. Stone, I. Pastar, N. Ojeh, V. Chen, S. Liu, K.I. Garzon, M. Tomic-canic, Epithelial-Mesenchymal Transition in Tissue Repair and Fibrosis, Cell Tissue Res. 365 (2016) 495–506.

[20] E. Barreiro, V.I. Peinado, J.B. Galdiz, E. Ferrer, J. Marin-Corral, F. Sánchez, J. Gea, J.A. Barberà, Cigarette smoke-induced oxidative stress: A role in chronic obstructive pulmonary disease skeletal muscle dysfunction, Am. J. Respir. Crit. Care Med. 182 (2010) 477–488.

[21] C.K. Oh, L.A. Murray, N.A. Molfino, Smoking and idiopathic pulmonary fibrosis, Pulm Med. 2012 (2012) 808260.

[22] B.C. Willis, R.M. DuBois, Z. Borok, Epithelial Origin of Myofibroblasts during Fibrosis in the Lung, Proc. Am. Thorac. Soc. 3 (2006) 377–382.

[23] American Cancer Society, Cancer Facts and Figures 2017, American Cancer Society, Atlanta, 2017.

[24] American Lung Association, Lung Cancer Fact Sheet, (2018). https://www.lung.org/lung-health-and-diseases/lung-disease-lookup/lung-cancer/resource-library/lung-cancer-fact-sheet.html (accessed January 12, 2018).

[25] P. Brennan, P. Hainaut, P. Boffetta, Genetics of lung-cancer susceptibility, Lancet Oncol. 12 (2011) 399–408.

[26] S.S. Hecht, Lung carcinogenesis by tobacco smoke, Int. J. Cancer. 131 (2012) 2724–2732.

[27] S.S. Hecht, S. Carmella, H. Mori, D. Hoffmann, A Study of Tobacco Carcinogenesis. XX. Role of Catechol as a Major Cocarcinogen in the Weakly Acidic Fraction of Smoke Condensate, J. Natl. Cancer Inst. 66 (1981) 163–169.

[28] R. Gopalakrishna, Z.H. Chen, U. Gundimeda, Tobacco smoke tumor promoters, catechol and hydroquinone, induce oxidative regulation of protein kinase C and influence invasion and metastasis of lung carcinoma cells., Proc. Natl. Acad. Sci. 91 (1994) 12233–12237.

[29] H. Takahashi, H. Ogata, R. Nishigaki, D.H. Broide, M. Karin, Tobacco Smoke Promotes Lung Tumorigenesis by Triggering IKKβ- and JNK1-Dependent Inflammation, Cancer Cell. 17 (2010) 89–97.

[30] P. Lonkar, P.C. Dedon, Reactive species and DNA damage in chronic inflammation: Reconciling chemical mechanisms and biological fates, Int. J. Cancer. 128 (2011) 1999–2009.

[31] M. Vaz, S.Y. Hwang, I. Kagiampakis, J. Phallen, A. Patil, H.M. O'Hagan, L. Murphy, C.A. Zahnow, E. Gabrielson, V.E. Velculescu, H.P. Easwaran, S.B. Baylin, Chronic Cigarette Smoke-Induced Epigenomic Changes Precede Sensitization of Bronchial Epithelial Cells to Single-Step Transformation by KRAS Mutations, Cancer Cell. 32 (2017) 360–376.e6.

[32] CDC, What Are the Risk Factors for Lung Cancer?, Www.Cdc.Gov. (2017).

[33] E. Veljkovic, J. Jiricny, M. Menigatti, H. Rehrauer, W. Han, Chronic exposure to cigarette smoke condensate in vitro induces epithelial to mesenchymal transition-like changes in human bronchial epithelial cells, BEAS-2B, Toxicol. Vitr. 25 (2011) 446–453.

[34] L. Zhang, M. Gallup, L. Zlock, C. Basbaum, W.E. Finkbeiner, N.A. McNamara, Cigarette smoke disrupts the integrity of airway adherens junctions through the aberrant interaction of p120-catenin with the cytoplasmic tail of MUC1, J. Pathol. 229 (2013) 74–86.

[35] J.E. Talmadge, I.J. Fidler, AACR centennial series: The biology of cancer metastasis: Historical perspective, Cancer Res. 70 (2010) 5649–5669.

[36] A.W. Lambert, D.R. Pattabiraman, R.A. Weinberg, Emerging Biological Principles of Metastasis, Cell. 168 (2017) 670–691.

[37] I. Mellman, Y. Yarden, Endocytosis and Cancer, Endocytosis. (2014) 1–24. doi:10.1101/cshperspect.a016949.

[38] H.H. Popper, Progression and metastasis of lung cancer, Cancer Metastasis Rev. 35 (2016) 75–91.

[39] W. Zou, Y. Zou, Z. Zhao, B. Li, P. Ran, Nicotine-induced epithelial-mesenchymal transition via Wnt/β-catenin signaling in human airway epithelial cells, Am. J. Physiol. Cell. Mol. Physiol. 304 (2013) L199–L209.

[40] K. Kim, Z. Lu, E.D. Hay, Direct evidence for a role of β-catenin/LEF-1 signaling pathway in induction of EMT, Cell Biol. Int. 26 (2002) 463–476.

[41] P.D. McCrea, C.J. Gottardi, Beyond β-catenin: prospects for a larger catenin network in the nucleus, Nat. Rev. Mol. Cell Biol. 17 (2015) 55–64.

[42] M. Yanagisawa, D. Huveldt, P. Kreinest, C.M. Lohse, J.C. Cheville, A.S. Parker, J.A. Copland, P.Z. Anastasiadis, A p120 catenin isoform switch affects rho activity, induces tumor cell invasion, and predicts metastatic disease, J. Biol. Chem. 283 (2008) 18344–18354.

[43] A.B. Reynolds, p120-catenin: Past and present, Biochim. Biophys. Acta - Mol. Cell Res. 1773 (2007) 2–7.

[44] J.M. Lee, S. Dedhar, R. Kalluri, E.W. Thompson, The epithelial-mesenchymal transition: New insights in signaling, development, and disease, J. Cell Biol. 172 (2006) 973–981.

[45] M. Yuan, S.J. Cross, S.E. Loughlin, F.M. Leslie, Nicotine and the adolescent brain, J. Physiol. 593 (2015) 3397–3412.

[46] P.D. Livingstone, J. Srinivasan, J.N.C. Kew, L.A. Dawson, C. Gotti, M. Moretti, M. Shoaib, S. Wonnacott, A7 and Non-A7 Nicotinic Acetylcholine Receptors Modulate Dopamine Release in Vitro and in Vivo in the Rat Prefrontal Cortex, Eur. J. Neurosci. 29 (2009) 539–550.

[47] S. Mastwal, Y. Ye, M. Ren, D. V. Jimenez, K. Martinowich, C.R. Gerfen, K.H. Wang, Phasic Dopamine Neuron Activity Elicits Unique Mesofrontal Plasticity in Adolescence, J. Neurosci. 34 (2014) 9484–9496.

[48] R. Wickstrom, Effects of Nicotine During Pregnancy: Human and Experimental Evidence, Curr. Neuropharmacol. 5 (2007) 213–222.

[49] M. Knoll, P. Talbot, Cigarette smoke inhibits oocyte cumulus complex pick-up by oviduct in vitro independent ciliary beat frequency, Reprod. Toxicol. 12 (1998) 57–68.

[50] L.M. Gatzke-Kopp, T.P. Beauchaine, Direct and passive prenatal nicotine exposure and the development of externalizing psychopathology, Child Psychiatry Hum. Dev. 38 (2007) 255–269.

[51] M. Knoll, R. Shaoulian, T. Magers, P. Talbot, Ciliary beat frequency of hamster oviducts is decreased in vitro by exposure to solutions of mainstream and sidestream cigarette smoke., Biol. Reprod. 53 (1995) 29–37. http://www.ncbi.nlm.nih.gov/pubmed/7669854.

[52] S. Lin, V. Tran, P. Talbot, Comparison of toxicity of smoke from traditional and harm-reduction cigarettes using mouse embryonic stem cells as a novel model for preimplantation development., Hum. Reprod. 24 (2009) 386–97.

[53] S. Lin, S. Fonteno, J.-H. Weng, P. Talbot, Comparison of the toxicity of smoke from conventional and harm reduction cigarettes using human embryonic stem cells., Toxicol. Sci. 118 (2010) 202–12.

[54] P. Talbot, S. Lin, Mouse and human embryonic stem cells: can they improve human health by preventing disease?, Curr. Top. Med. Chem. 11 (2011) 1638–1652.

[55] T.K. Ng, L. Huang, D. Cao, Y.W.-Y. Yip, W.M. Tsang, G.H.-F. Yam, C.P. Pang, H.S. Cheung, Cigarette smoking hinders human periodontal ligament-derived stem cell proliferation, migration and differentiation potentials, Sci. Rep. 5 (2015) 7828.

[56] J.M. Greenberg, C.M. Carballosa, H.S. Cheung, Concise Review: The Deleterious Effects of Cigarette Smoking and Nicotine Usage and Mesenchymal Stem Cell Function and Implications for Cell-Based Therapies, Stem Cells Transl. Med. 6 (2017) 1815–1821.

[57] A. Shaito, J. Saliba, A. Husari, M. El-Harakeh, H. Chhouri, Y. Hashem, A. Shihadeh, M. El-Sabban, Electronic Cigarette Smoke Impairs Normal Mesenchymal Stem Cell Differentiation, Sci. Rep. 7 (2017) 1–11.

[58] V. Bahl, K. Johnson, R. Phandthong, A. Zahedi, S.F. Schick, P. Talbot, Thirdhand cigarette smoke causes stress-induced mitochondrial hyperfusion and alters the transcriptional profile of stem cells, Toxicol. Sci. 153 (2016) 55–69.

[59] and M. National Academies of Sciences, Engineering, Public Health Consequences of E-Cigarettes, The National Academies Press, Washington, DC, 2018.

[60] A. Mcneill, L.S. Brose, R. Calder, S.C. Hitchman, P. Hajek, M. H, E-cigarettes : an evidence update A report commissioned by Public Health England, 2015. www.gov.uk/government/uploads/system/uploads/attachment_data/file/454516/Ecigarettes_an_evidence_update_A_report_commissioned_by_Public_Health_England.pdf.

[61] Z. Cahn, M. Siegel, Electronic cigarettes as a harm reduction strategy for tobacco control: A step forward or a repeat of past mistakes?, J. Public Health Policy. 32 (2011) 16–31.

[62] R. Polosa, B. Rodu, P. Caponnetto, M. Maglia, C. Raciti, A fresh look at tobacco harm reduction: The case for the electronic cigarette, Harm Reduct. J. 10 (2013) 1–11.

[63] M.A. Ogunwale, M. Li, M. V. Ramakrishnam Raju, Y. Chen, M.H. Nantz, D.J. Conklin, X.A. Fu, Aldehyde Detection in Electronic Cigarette Aerosols, ACS Omega. 2 (2017) 1207–1214.

[64] R.Z. Behar, B. Davis, Y. Wang, V. Bahl, S. Lin, P. Talbot, Identification of toxicants in cinnamon-flavored electronic cigarette refill fluids, Toxicol. Vitr. 28 (2014) 198–208.

[65] R.Z. Behar, W. Luo, S.C. Lin, Y. Wang, J. Valle, J.F. Pankow, P. Talbot, Distribution, quantification and toxicity of cinnamaldehyde in electronic cigarette refill fluids and aerosols, Tob. Control. 25 (2016) ii94-ii102.

[66] R.Z. Behar, W. Luo, K.J. Mcwhirter, J.F. Pankow, P. Talbot, Analytical and toxicological evaluation of flavor chemicals in electronic cigarette refill fluids, Sci. Rep. 8 (2018) 1–11.

[67] J.G. Allen, S.S. Flanigan, M. LeBlanc, J. Vallarino, P. MacNaughton, J.H. Stewart, D.C. Christiani, Flavoring Chemicals in E-Cigarettes: Diacetyl, 2,3-Pentanedione, and Acetoin in a Sample of 51 Products, Including Fruit-, Candy-, and Cocktail-Flavored E-Cigarettes, Environ. Health Perspect. 124 (2016) 733–739.

[68] N.J. Leigh, R.I. Lawton, P.A. Hershberger, M.L. Goniewicz, Flavourings significantly affect inhalation toxicity of aerosol generated from electronic nicotine delivery systems (ENDS), Tob. Control. 25 (2016) ii81-ii87.

[69] P.G. Shields, M. Berman, T.M. Brasky, J.L. Freudenheim, E. Mathe, J.P. McElroy, M.-A. Song, M.D. Wewers, A Review of Pulmonary Toxicity of Electronic Cigarettes In The Context of Smoking: A Focus On Inflammation, Cancer Epidemiol. Biomarkers Prev. 36 (2016) 1011–1014.

[70] J.L. Barrington-Trimis, J.M. Samet, R. McConnell, Flavorings in Electronic Cigarettes An Unrecognized Respiratory Health Hazard?, JAMA. 312 (2014) 2493–2494.

[71] C.L. Sherwood, S. Boitano, Airway epithelial cell exposure to distinct e-cigarette liquid flavorings reveals toxicity thresholds and activation of CFTR by the chocolate flavoring 2,5-dimethypyrazine, Respir. Res. 17 (2016) 1–11.

[72] J.S. Herrington, C. Myers, Electronic cigarette solutions and resultant aerosol profiles, J. Chromatogr. A. 1418 (2015) 192–199.

[73] P.R. Jensen, W. Luo, J.F. Pankow, R.M. Strongin, D.H. Peyton, Hidden Formaldehyde in E-Cigarette Aerosols, N. Engl. J. Med. 372 (2015) 392–394.

[74] M.L. Goniewicz, J. Knysak, M. Gawron, L. Kosmider, A. Sobczak, J. Kurek, A. Prokopowicz, M. Jablonska-Czapla, C. Rosik-Dulewska, C. Havel, P. Jacob, N. Benowitz, Levels of selected carcinogens and toxicants in vapour from electronic cigarettes, Tob. Control. 23 (2014) 133–139.

[75] K. Bekki, S. Uchiyama, K. Ohta, Y. Inaba, H. Nakagome, N. Kunugita, Carbonyl compounds generated from electronic cigarettes, Int. J. Environ. Res. Public Health. 11 (2014) 11192–11200.

[76] L. Kosmider, A. Sobczak, M. Fik, J. Knysak, M. Zaciera, J. Kurek, M.L. Goniewicz, Carbonyl compounds in electronic cigarette vapors: Effects of nicotine solvent and battery output voltage, Nicotine Tob. Res. 16 (2014) 1319–1326.

[77] J.W. Flora, N. Meruva, C.B. Huang, C.T. Wilkinson, R. Ballentine, D.C. Smith, M.S. Werley, W.J. McKinney, Characterization of potential impurities and degradation products in electronic cigarette formulations and aerosols, Regul. Toxicol. Pharmacol. 74 (2016) 1–11.

[78] D. Canistro, F. Vivarelli, S. Cirillo, C. Babot Marquillas, A. Buschini, M. Lazzaretti, L. Marchi, V. Cardenia, M.T. Rodriguez-Estrada, M. Lodovici, C. Cipriani, A. Lorenzini, E. Croco, S. Marchionni, P. Franchi, M. Lucarini, V. Longo, C.M. Della Croce, A. Vornoli, A. Colacci, M. Vaccari, A. Sapone, M. Paolini, E-cigarettes induce toxicological effects that can raise the cancer risk, Sci. Rep. 7 (2017) 2028.

[79] V. Ganapathy, J. Manyanga, L. Brame, D. McGuire, B. Sadhasivam, E. Floyd, D.A. Rubenstein, I. Ramachandran, T. Wagener, L. Queimado, Electronic cigarette aerosols suppress cellular antioxidant defenses and induce significant oxidative DNA damage, PLoS One. 12 (2017) 1–20.

[80] C.P. Ramôa, M.M. Hiler, T.R. Spindle, A.A. Lopez, N. Karaoghlanian, T. Lipato, A.B. Breland, A. Shihadeh, T. Eissenberg, Electronic cigarette nicotine delivery can exceed that of combustible cigarettes: A preliminary report, Tob. Control. 25 (2016) e6–e9.

[81] I.G. Gillman, K.A. Kistler, E.W. Stewart, A.R. Paolantonio, Effect of variable power levels on the yield of total aerosol mass and formation of aldehydes in e-cigarette aerosols, Regul. Toxicol. Pharmacol. 75 (2016) 58–65.

[82] M.E. Hadwiger, M.L. Trehy, W. Ye, T. Moore, J. Allgire, B. Westenberger, Identification of amino-tadalafil and rimonabant in electronic cigarette products using high pressure liquid chromatography with diode array and tandem mass spectrometric detection, J. Chromatogr. A. 1217 (2010) 7547–7555.

[83] S. Soussy, A. El-Hellani, R. Baalbaki, R. Salman, A. Shihadeh, N.A. Saliba, Detection of 5-hydroxymethylfurfural and furfural in the aerosol of electronic cigarettes, Tob. Control. 25 (2016) ii88-ii93.

[84] K.I. Cotta, A Review on the Safety of Inhalation of Propylene Glycol in E-cigarettes, Glob. J. Pharm. Pharm. Sci. 2 (2017) 1–9.

[85] F. Offermann, Chemical emissions from e-cigarettes: Direct and indirect (passive) exposures, Build. Environ. 93. 93 (2015) 101–105.

[86] M. Williams, K. Bozhilov, S. Ghai, P. Talbot, Elements including metals in the atomizer and aerosol of disposable electronic cigarettes and electronic hookahs, PLoS One. 12 (2017) 1–24.

[87] M. Williams, A. Villarreal, K. Bozhilov, S. Lin, P. Talbot, Metal and silicate particles including nanoparticles are present in electronic cigarette cartomizer fluid and aerosol, PLoS One. 8 (2013) e57987.

[88] C.A. Lerner, P. Rutagarama, T. Ahmad, I.K. Sundar, A. Elder, I. Rahman, Electronic cigarette aerosols and copper nanoparticles induce mitochondrial stress and promote DNA fragmentation in lung fibroblasts, Biochem. Biophys. Res. Commun. 477 (2016) 620–625.

[89] V.B. Mikheev, M.C. Brinkman, C.A. Granville, S.M. Gordon, P.I. Clark, Real-time measurement of electronic cigarette aerosol size distribution and metals content analysis, Nicotine Tob. Res. 18 (2016) 1895–1902.

[90] P. Olmedo, W. Goessler, S. Tanda, M. Grau-Perez, S. Jarmul, A. Aherrera, R. Chen, M. Hilpert, J.E. Cohen, A. Navas-Acien, A.M. Rule, Metal Concentrations in e-Cigarette Liquid and Aerosol Samples: The Contribution of Metallic Coils, Environ. Health Perspect. 126 (2018).

[91] Harmful and Potentially Harmful Constituents in Tobacco Products and Tobacco Smoke; Established List, 2012.

[92] A. Zahedi, V. On, R. Phandthong, A. Chaili, G. Remark, B. Bhanu, P. Talbot, Deep Analysis of Mitochondria and Cell Health Using Machine Learning, Sci. Rep. (2018) 1–15.

[93] C.J. Brown, J.M. Cheng, Electronic cigarettes: Product characterization and design considerations, Tob. Control. 23 (2014).

[94] E.E. Omaiye, I. Cordova, B. Davis, P. Talbot, Counterfeit Electronic Cigarette Products with Mislabeled Nicotine Concentrations, Tob. Regul. Sci. 3 (2017) 347–357.

[95] B. Davis, M. Dang, J. Kim, P. Talbot, Nicotine concentrations in electronic cigarette refill and do-it-yourself fluids, Nicotine Tob. Res. 17 (2015) 134–141.

[96] B. Davis, A. Razo, E. Nothnagel, M. Chen, P. Talbot, Unexpected nicotine in Do-it-Yourself electronic cigarette flavourings, Tob. Control. 25 (2016) e67–e68.

[97] J.R. Whittington, P.M. Simmons, A.M. Phillips, S.K. Gammill, R. Cen, E.F. Magann, V.M. Cardenas, The Use of Electronic Cigarettes in Pregnancy: A Review of the Literature, Obstet. Gynecol. Surv. 73 (2018) 544–549.

[98] S.A. Grando, Connections of nicotine to cancer, Nat. Rev. Cancer. 14 (2014) 419–429.

[99] J. Arredondo, L.L. Hall, A. Ndoye, V.T. Nguyen, A.I. Chernyavsky, D. Bercovich, A. Orr-Urtreger, A.L. Beaudet, S.A. Grando, Central role of fibroblast α3 nicotinic acetylcholine receptor in mediating cutaneous effects of nicotine, Lab. Investig. 83 (2003) 207–225.

[100] C. Khachatoorian, P. Jacob, N.L. Benowitz, P. Talbot, Electronic cigarette chemicals transfer from a vape shop to a nearby business in a multiple-tenant retail building, Tob. Control. (2018) 1–7.

[101] R.Z. Behar, Y. Wang, P. Talbot, Comparing the cytotoxicity of electronic cigarette fluids, aerosols and solvents, Tob. Control. (2017) 1–9.

[102] P.C. Shivalingappa, R. Hole, C. Van Westphal, N. Vij, Airway exposure to e-cigarette vapors impairs autophagy and induces aggresome formation, Antioxid. Redox Signal. 24 (2015) 186–204.

[103] A.R. Iskandar, I. Gonzalez-Suarez, S. Majeed, D. Marescotti, A. Sewer, Y. Xiang, P. Leroy, E. Guedj, C. Mathis, J.P. Schaller, P. Vanscheeuwijck, S. Frentzel, F. Martin, N. V. Ivanov, M.C. Peitsch, J. Hoeng, A framework for in vitro systems toxicology assessment of e-liquids, Toxicol. Mech. Methods. 26 (2016) 389–413.

[104] W. Lei, C. Lerner, I.K. Sundar, I. Rahman, Myofibroblast differentiation and its functional properties are inhibited by nicotine and e-cigarette via mitochondrial OXPHOS complex III, Sci. Rep. 7 (2017) 1–13.

[105] C. Anderson, A. Majeste, J. Hanus, S. Wang, E-Cigarette Aerosol Exposure Induces Reactive Oxygen Species, DNA Damage, and Cell Death in Vascular Endothelial Cells., Toxicol. Sci. 154 (2016) 1–9.

[106] V. Bahl, S. Lin, N. Xu, B. Davis, Y.H. Wang, P. Talbot, Comparison of electronic cigarette refill fluid cytotoxicity using embryonic and adult models, Reprod. Toxicol. 34 (2012) 529–537.

[107] A. Scott, S.T. Lugg, K. Aldridge, K.E. Lewis, A. Bowden, R.Y. Mahida, F.S. Grudzinska, D. Dosanjh, D. Parekh, R. Foronjy, E. Sapey, B. Naidu, D.R. Thickett, Pro-inflammatory effects of e-cigarette vapour condensate on human alveolar macrophages, Thorax. 73 (2018) 1161–1169.

[108] Q. Wu, D. Jiang, M. Minor, H.W. Chu, Electronic cigarette liquid increases inflammation and virus infection in primary human airway epithelial cells, PLoS One. 9 (2014).

[109] D. Thorne, I. Crooks, M. Hollings, A. Seymour, C. Meredith, M. Gaca, The mutagenic assessment of an electronic-cigarette and reference cigarette smoke using the Ames assay in strains TA98 and TA100, Mutat. Res. Toxicol. Environ. Mutagen. 812 (2016) 29–38.

[110] C.A. Lerner, I.K. Sundar, H. Yao, J. Gerloff, D.J. Ossip, S. McIntosh, R. Robinson, I. Rahman, Vapors produced by electronic cigarettes and E-juices with flavorings induce toxicity, oxidative stress, and inflammatory response in lung epithelial cells and in mouse lung, PLoS One. 10 (2015) 1–26.

[111] H.-W. Lee, S.-H. Park, M. Weng, H.-T. Wang, W.C. Huang, H. Lepor, X.-R. Wu, L.-C. Chen, M. Tang, E-cigarette smoke damages DNA and reduces repair activity in mouse lung, heart, and bladder as well as in human lung and bladder cells, Proc. Natl. Acad. Sci. 115 (2018) E1560–E1569.

[112] S.A. McGrath-Morrow, M. Hayashi, A. Aherrera, A. Lopez, A. Malinina, J.M. Collaco, E. Neptune, J.D. Klein, J.P. Winickoff, P. Breysse, P. Lazarus, G. Chen, The effects of electronic cigarette emissions on systemic cotinine levels, weight and postnatal lung growth in neonatal mice, PLoS One. 10 (2015) 2–11.

[113] H. Bin Lim, S.H. Kim, Inhallation of e-cigarette cartridge solution aggravates allergen-induced airway inflammation and hyper-responsiveness in mice, Toxicol. Res. 30 (2014) 13–18.

[114] I. Garcia-Arcos, P. Geraghty, N. Baumlin, M. Campos, A.J. Dabo, B. Jundi, N. Cummins, E. Eden, A. Grosche, M. Salathe, R. Foronjy, Chronic electronic cigarette exposure in mice induces features of COPD in a nicotine-dependent manner, Thorax. 71 (2016) 1119–1129.

[115] T.E. Sussan, S. Gajghate, R.K. Thimmulappa, J. Ma, J.H. Kim, K. Sudini, N. Consolini, S.A. Cormier, S. Lomnicki, F. Hasan, A. Pekosz, S. Biswal, Exposure to electronic cigarettes impairs pulmonary anti-bacterial and anti-viral defenses in a mouse model, PLoS One. 10 (2015) 1–15.

[116] M. Hua, P. Talbot, Potential health effects of electronic cigarettes: A systematic review of case reports, Prev. Med. Reports. 4 (2016) 169–178.

[117] Q. Li, Y. Zhan, L. Wang, S.J. Leischow, D.D. Zeng, Analysis of symptoms and their potential associations with e-liquids' components: A social media study, BMC Public Health. 16 (2016) 1–12.

[118] K.E. Farsalinos, K.A. Kistler, G. Gillman, V. Voudris, Evaluation of electronic cigarette liquids and aerosol for the presence of selected inhalation toxins, Nicotine Tob. Res. 17 (2015) 168–174.

[119] A.F. Hubbs, A.M. Cumpston, W.T. Goldsmith, L.A. Battelli, M.L. Kashon, M.C. Jackson, D.G. Frazer, J.S. Fedan, M.P. Goravanahally, V. Castranova, K. Kreiss, P.A. Willard, S. Friend, D. Schwegler-Berry, K.L. Fluharty, K. Sriram, Respiratory and olfactory cytotoxicity of inhaled 2,3-pentanedione in sprague-dawley rats, Am. J. Pathol. 181 (2012) 829–844.

[120] M.F. Sassano, E.S. Davis, J.E. Keating, B.T. Zorn, T.K. Kochar, M.C. Wolfgang, G.L. Glish, R. Tarran, Evaluation of e-liquid toxicity using an open-source high-throughput screening assay, PLoS Biol. 16 (2018) 1–24.

[121] C. Pisinger, M. Døssing, A systematic review of health effects of electronic cigarettes, Prev. Med. (Baltim). 69 (2014) 248–260.

[122] T.Y. Lim, R.L. Poole, N.M. Pageler, Propylene glycol toxicity in children, J. Pediactric Pharmacol. Ther. 19 (2014) 277–282.

[123] C. Hutzler, M. Paschke, S. Kruschinski, F. Henkler, J. Hahn, A. Luch, Chemical hazards present in liquids and vapors of electronic cigarettes, Arch. Toxicol. 88 (2014) 1295–1308.

[124] R. Hess, M.J. Bartels, L.H. Pottenger, Ethylene glycol: An estimate of tolerable levels of exposure based on a review of animal and human data, Arch. Toxicol. 78 (2004) 671–680.

[125] S. Hom, L. Chen, T. Wang, B. Ghebrehiwet, W. Yin, A. David, Platelet activation , adhesion , inflammation , and aggregation potential are altered in the presence of electronic cigarette extracts of variable nicotine concentrations, Platelets. 27 (2016) 694–702.

[126] A.M. Glasser, L. Katz, J.L. Pearson, R.S. Niaura, D.B. Abrams, C. Andrea, Overview of Electronic Nicotine Delivery Systems: A Systematic Review, Am. J. Prev. Med. 52 (2017) 1–65.

[127] P.S. Hiemstra, R. Bals, Basic science of electronic cigarettes: Assessment in cell culture and in vivo models, Respir. Res. 17 (2016) 1–5.

[128] A. Scott, S.T. Lugg, K. Aldridge, K.E. Lewis, A. Bowden, R.Y. Mahida, F.S. Grudzinska, D. Dosanjh, D. Parekh, R. Foronjy, E. Sapey, B. Naidu, D.R. Thickett, Pro-inflammatory effects of e-cigarette vapour condensate on human alveolar macrophages, Thorax. (2018) 1–9.

[129] C.I. Vardavas, N. Anagnostopoulos, M. Kougias, V. Evangelopoulou, G.N. Connolly, P.K. Behrakis, Short-term pulmonary effects of using an electronic cigarette: Impact on respiratory flow resistance, impedance, and exhaled nitric oxide, Chest. 141 (2012) 1400–1406.

[130] P. Callahan-Lyon, Electronic cigarettes: Human health effects, Tob. Control. 23 (2014).

[131] T.R. Rowell, R. Tarran, Will chronic e-cigarette use cause lung disease?, Am. J. Physiol. - Lung Cell. Mol. Physiol. 309 (2015) L1398–L1409.

[132] R. Carnevale, S. Sciarretta, F. Violi, C. Nocella, L. Loffredo, L. Perri, M. Peruzzi, A.G.M. Marullo, E. De Falco, I. Chimenti, V. Valenti, G. Biondi-Zoccai, G. Frati, Acute Impact of Tobacco vs Electronic Cigarette Smoking on Oxidative Stress and Vascular Function, Chest. 150 (2016) 606–612.

[133] R.S. Moheimani, M. Bhetraratana, F. Yin, K.M. Peters, J. Gornbein, J.A. Araujo, H.R. Middlekauff, Increased cardiac sympathetic activity and oxidative stress in habitual electronic cigarette users: Implications for cardiovascular risk, JAMA Cardiol. 2 (2017) 278–285.

[134] S. Tommasi, S.E. Bates, R.Z. Behar, P. Talbot, A. Besaratinia, Limited mutagenicity of electronic cigarettes in mouse or human cells in vitro, Lung Cancer. 112 (2017) 41–46.

[135] B. Moorthy, C. Chu, D.J. Carlin, Polycyclic aromatic hydrocarbons: From metabolism to lung cancer, Toxicol. Sci. 145 (2015) 5–15. doi:10.1093/toxsci/kfv040.

[136] C.E. Boström, P. Gerde, A. Hanberg, B. Jernström, C. Johansson, T. Kyrklund, A. Rannug, M. Törnqvist, K. Victorin, R. Westerholm, Cancer risk assessment, indicators, and guidelines for polycyclic aromatic hydrocarbons in the ambient air, Environ. Health Perspect. 110 (2002) 451–488.

[137] T. Cheng, Chemical evaluation of electronic cigarettes, Tob. Control. 23 (2014).

[138] H.J. Kim, H.S. Shin, Determination of tobacco-specific nitrosamines in replacement liquids of electronic cigarettes by liquid chromatography-tandem mass spectrometry, J. Chromatogr. A. 1291 (2013) 48–55.

[139] T.R. McAuley, P.K. Hopke, J. Zhao, S. Babaian, Comparison of the effects of e-cigarette vapor and cigarette smoke on indoor air quality, Inhal. Toxicol. 24 (2012) 850–857.

[140] L. P., S. S.N., R. Q., S. S.P., S. J.C., R.J. J.P., P. J.Y., p53, but not p16 mutations in oral squamous cell carcinomas are associated with specific CYP1A1 and GSTM1 polymorphic genotypes and patient tobacco use, Carcinogenesis. 19 (1998) 509–514.

[141] M.A. Yu, A. Kiang, J. Wang-Rodriguez, E. Rahimy, M. Haas, V. Yu, L.G. Ellies, J. Chen, J.B. Fan, K.T. Brumund, R.A. Weisman, W.M. Ongkeko, Nicotine Promotes Acquisition of Stem Cell and Epithelial-to-Mesenchymal Properties in Head and Neck Squamous Cell Carcinoma, PLoS One. 7 (2012) 1–14.

[142] P. Dasgupta, W. Rizwani, S. Pillai, R. Kinkade, M. Kovacs, S. Banerjee, M. Carless, E. Kim, D. Coppola, Nicotine induces cell proliferation, invasion and epithelial- mesenchymal transition in a variety of human cancer cell lines, Int. J. Cancer. 124 (2009) 36–45.

[143] E. Martínez-García, M. Irigoyen, Ó. González-Moreno, L. Corrales, Á. Teijeira, E. Salvo, A. Rouzaut, Repetitive nicotine exposure leads to a more malignant and metastasis-prone phenotype of SCLC: A molecular insight into the importance of quitting smoking during treatment, Toxicol. Sci. 116 (2010) 467–476.

[144] S. Singh, S. Pillai, S. Chellappan, Nicotinic Acetylcholine Receptor Signaling in Tumor Growth and Metastasis, J. Oncol. 2011 (2011) 1–11.

[145] C. Heeschen, J.J. Jang, M. Weis, A. Pathak, S. Kaji, R.S. Hu, P.S. Tsao, F.L. Johnson, J.P. Cooke, Nicotine stimulates angiogenesis and promotes tumor growth and atherosclerosis, Nat. Med. 7 (2001) 833–839.

[146] S. Mousa, S.A. Mousa, Cellular and molecular mechanisms of nicotine's pro-angiogenesis activity and its potential impact on cancer, J. Cell. Biochem. 97 (2006) 1370–1378.

[147] C. Schaal, S.P. Chellappan, Nicotine-Mediated Cell Proliferation and Tumor Progression in Smoking-Related Cancers, Mol. Cancer Res. 12 (2014) 14–23.

[148] R.D. Egleton, K.C. Brown, P. Dasgupta, Nicotinic acetylcholine receptors in cancer: multiple roles in proliferation and inhibition of apoptosis, Trends Pharmacol. Sci. 29 (2008) 151–158.

[149] G. Gergalova, O. Lykhmus, O. Kalashnyk, L. Koval, V. Chernyshov, E. Kryukova, V. Tsetlin, S. Komisarenko, M. Skok, Mitochondria express α7 nicotinic acetylcholine receptors to regulate Ca2+ accumulation and cytochrome c release: study on isolated mitochondria, PLoS One. 7 (2012) 1–8.

[150] Z. Yu, T.G. Pestell, M.P. Lisanti, R.G. Pestell, Cancer stem cells, Int. J. Biochem. Cell Biol. 44 (2012) 2144–2151.

[151] T.A. Wills, R. Knight, R.J. Williams, I. Pagano, J.D. Sargent, Risk Factors for Exclusive E-Cigarette Use and Dual E-Cigarette Use and Tobacco Use in Adolescents, Pediatrics. 135 (2015) e43–e51.

[152] R.E. Bunnell, I.T. Agaku, R.A. Arrazola, B.J. Apelberg, R.S. Caraballo, C.G. Corey, B.N. Coleman, S.R. Dube, B.A. King, Intentions to smoke cigarettes among never-smoking US middle and high school electronic cigarette users: National youth tobacco survey, 2011-2013, Nicotine Tob. Res. 17 (2015) 228–235.

[153] J.G. Willett, M. Bennett, E.C. Hair, H. Xiao, M.S. Greenberg, E. Harvey, J. Cantrell, D. Vallone, Recognition , use and perceptions of JUUL among youth and young adults, Tob. Control. (2018) 1–2.

[154] S. Asma, Y. Song, J. Cohen, M. Eriksen, T. Pechacek, N. Cohen, CDC Grand Rounds : Global Tobacco Control, Morb. Mortal. Wkly. Rep. 63 (2014) 277–297.

[155] R.Z. Behar, M. Hua, P. Talbot, Puffing topography and nicotine intake of electronic cigarette users, PLoS One. 10 (2015) 1–18.

[156] A.A. Lopez, M.M. Hiler, E.K. Soule, C.P. Ramôa, N. V. Karaoghlanian, T. Lipato, A.B. Breland, A.L. Shihadeh, T. Eissenberg, Effects of electronic cigarette liquid nicotine concentration on plasma nicotine and puff topography in tobacco cigarette smokers: A preliminary report, Nicotine Tob. Res. 18 (2016) 720–723.

[157] U.S. Department of Health and Human Services, How Tobacco Smoke Causes Disease: The Biology and Behavioral Basis for Smoking-Attributable Disease, 1st ed, Centers for Disease Control and Prevention, National Center for Chronic Disease Prevention and Health Promotion, Office on Smoking and Health, Atlanta, 2010.

[158] Centers for Disease Control and Prevention, E-Cigarettes and Pregnancy, (2016). https://www.cdc.gov/reproductivehealth/maternalinfanthealth/tobaccousepregnancy/e-cigarettes-pregnancy.htm (accessed June 12, 2018).

[159] A.E. Kennedy, S. Kandalam, R. Olivares-navarrete, J. Amanda, G. Dickinson, E-cigarette aerosol exposure can cause craniofacial defects in Xenopus laevis embryos and mammalian neural crest cells, (2017) 1–25.

[160] P.A. Trainor, Craniofacial Birth Defects: The Role of Neural Crest Cells in the Etiology and Pathogenesis of Treacher Collins Syndrome and the Potential for Prevention, Am. J. Med. Genet. Part A. 155 (2011) 270–279.

[161] K. Kee, M. Flores, M.I. Cedars, R.A.R. Pera, Human Primordial Germ Cell Formation Is Diminished by Exposure to Environmental Toxicants Acting through the AHR Signaling Pathway, Toxicol. Sci. 117 (2010) 218–224.

[162] M.B. Schultz, D.A. Sinclair, When stem cells grow old: phenotypes and mechanisms of stem cell aging, Development. 143 (2016) 3–14.

[163] S.K. Pazhanisamy, Stem cells, DNA damage, ageing and cancer, Hematol. Oncol. Stem Cell Ther. 2 (2009) 375–384.

[164] A. Behrens, Impact of genomic damage and ageing on stem cell function, Nat. Cell Biol. 16 (2014) 201–207.

[165] R.Z. Behar, V. Bahl, Y. Wang, S. Lin, N. Xu, B. Davis, P. Talbot, A method for rapid dose-response screening of environmental chemicals using human embryonic stem cells, J. Pharmacol. Toxicol. Methods. 66 (2012) 238–245.

[166] S.C. Lin, H. Yip, R. Phandthong, B. Davis, P. Talbot, Evaluation of Dynamic Cell Processes and Behavior Using Video Bioinformatics Tools, in: Video Bioinforma., Springer, 2015: pp. 167–186.

[167] S. Lin, P. Talbot, Methods for culturing mouse and human embryonic stem cells., Methods Mol. Biol. 690 (2011) 31–56.

[168] N. Yin, X. Yao, Z. Qin, Y.L. Wang, F. Faiola, Assessment of Bisphenol A (BPA) neurotoxicity in vitro with mouse embryonic stem cells, J. Environ. Sci. (China). 36 (2015) 181–187.

[169] K.S. Betts, Growing Knowledge: Using Stem Cells to Study Developmental Neurotoxicity, Environ. Health Perspect. 118 (2010) a432–a437.

[170] S. Liu, N. Yin, F. Faiola, Prospects and Frontiers of Stem Cell Toxicology, Stem Cells Dev. 26 (2017) scd.2017.0150.

[171] P. Talbot, N.I. Nieden, S. Lin, I. Martinez, B. Guan, B. Bhanu, Use of Video Bioinformatics Tools in Stem Cell Toxicology, in: Handb. Nanotoxicology, Nanomedicine Stem Cell Use Toxicol., 2014: pp. 379–402.

[172] P.M. Rodier, Developing brain as a target of toxicity, Environ. Health Perspect. 103 (1995) 73–76.

[173] T.R. Rowell, S.L. Reeber, S.L. Lee, R.A. Harris, R.C. Nethery, A.H. Herring, G.L. Glish, R. Tarran, Flavored e-cigarette liquids reduce proliferation and viability in the CALU3 airway epithelial cell line, Am. J. Physiol. - Lung Cell. Mol. Physiol. 313 (2017) L52–L66.

[174] S. Scheffler, H. Dieken, O. Krischenowski, M. Aufderheide, Cytotoxic evaluation of e-liquid aerosol using different lung-derived cell models, Int. J. Environ. Res. Public Health. 12 (2015) 12466–12474.

[175] J.N. Meyer, M.C.K. Leung, J.P. Rooney, A. Sendoel, M.O. Hengartner, G.E. Kisby, A.S. Bess, Mitochondria as a target of environmental toxicants, Toxicol. Sci. 134 (2013) 1–17.

[176] M.S. Attene-Ramos, R. Huang, S. Sakamuru, K.L. Witt, G.C. Beeson, L. Shou, R.G. Schnellmann, C.C. Beeson, R.R. Tice, C.P. Austin, M. Xia, Systematic Study of Mitochondrial Toxicity of Environmental Chemicals Using Quantitative High Throughput Screening, Chem. Res. Toxicol. 26 (2013) 1323–1332.

[177] E.A. Belyaeva, D. Dymkowska, M.R. Wieckowski, L. Wojtczak, Mitochondria as an important target in heavy metal toxicity in rat hepatoma AS-30D cells, Toxicol. Appl. Pharmacol. 231 (2008) 34–42.

[178] L. Kozlovskaya, M. Abou-Kaoud, D. Stepensky, Quantitative analysis of drug delivery to the brain via nasal route, J. Control. Release. 189 (2014) 133–140.

[179] C.E. Meacham, S.J. Morrison, Tumour heterogeneity and cancer cell plasticity, Nature. 501 (2013) 328–337.

[180] D. Hanahan, R.A. Weinberg, Hallmarks of Cancer: The Next Generation, Cell. 144 (2011) 646–674.

[181] A. Zahedi, R. Phandthong, A. Chaili, G. Lemark, P. Talbot, Epithelial-to-Mesenchymal Transition of A549 Lung Cancer Cells Exposed to Electronic Cigarettes, Lung Cancer. 122 (2018) 224–233.

[182] R.J. Giedt, P. Fumene Feruglio, D. Pathania, K.S. Yang, A. Kilcoyne, C. Vinegoni, T.J. Mitchison, R. Weissleder, Computational imaging reveals mitochondrial morphology as a biomarker of cancer phenotype and drug response, Sci. Rep. 6 (2016) 32985.

[183] F.E. Lennon, G.C. Cianci, R. Kanteti, J.J. Riehm, Q. Arif, V.A. Poroyko, E. Lupovitch, W. Vigneswaran, A. Husain, P. Chen, J.K. Liao, M. Sattler, H.L. Kindler, R. Salgia, Unique fractal evaluation and therapeutic implications of mitochondrial morphology in malignant mesothelioma, Sci. Rep. 6 (2016) 24578.

[184] F.E. Lennon, G.C. Cianci, N.A. Cipriani, T.A. Hensing, H.J. Zhang, C.-T. Chen, S.D. Murgu, E.E. Vokes, M.W. Vannier, R. Salgia, Lung cancer—a fractal viewpoint, Nat. Rev. Clin. Oncol. 12 (2015) 664–675.

[185] D.F. Bogenhagen, Does MtDNA nucleoid organization impact aging?, Exp. Gerontol. 45 (2010) 473–477.

[186] J. Gao, L. Wang, J. Liu, F. Xie, B. Su, X. Wang, Abnormalities of Mitochondrial Dynamics in Neurodegenerative Diseases, Antioxidants. 6 (2017) 25.

[187] J.G. McCarron, C. Wilson, M.E. Sandison, M.L. Olson, J.M. Girkin, C. Saunter, S. Chalmers, From structure to function: Mitochondrial morphology, motion and shaping in vascular smooth muscle, J. Vasc. Res. 50 (2013) 357–371.

[188] M.R. Duchen, Roles of Mitochondria in Health and Disease, Diabetes. 53 (2004).

[189] D.C. Chan, Mitochondria: Dynamic Organelles in Disease, Aging, and Development, Cell. 125 (2006) 1241–1252.

[190] J. Nunnari, A. Suomalainen, Mitochondria: In sickness and in health, Cell. 148 (2012) 1145–1159.

[191] F.E. Lennon, G.C. Cianci, R. Kanteti, J.J. Riehm, Q. Arif, V.A. Poroyko, E. Lupovitch, W. Vigneswaran, A. Husain, P. Chen, J.K. Liao, M. Sattler, H.L. Kindler, R. Salgia, Unique fractal evaluation and therapeutic implications of mitochondrial morphology in malignant mesothelioma., Sci. Rep. 6 (2016) e24578.

[192] B. Bhanu, P. Talbot, Video Bioinformatics, 2015.

[193] Flavor and Extract Manufacturers Association, Safety Assessment and Regulatory Authority to Use Flavors: Focus on Electronic Nicotine Delivery Systems and Flavored Tobacco Products, (2018). https://www.femaflavor.org/safety-assessment-and-regulatory-authority-use-flavors-focus-electronic-nicotine-delivery-systems (accessed June 12, 2018).

[194] E. Berger, E. Rath, D. Yuan, N. Waldschmitt, S. Khaloian, M. Allgauer, O. Staszewski, E.M. Lobner, T. Schottl, P. Giesbertz, O.I. Coleman, M. Prinz, A. Weber, M. Gerhard, M. Klingenspor, K.P. Janssen, M. Heikenwalder, D. Haller, Mitochondrial function controls intestinal epithelial stemness and proliferation, Nat. Commun. 7 (2016).

[195] J.L. Tilly, D.A. Sinclair, Germline energetics, aging, and female infertility, Cell Metab. 17 (2013) 838–850.

[196] H. Zhang, K.J. Menzies, J. Auwerx, The role of mitochondria in stem cell fate and aging, Development. 145 (2018) dev143420.

[197] J.M. Ross, J.B. Stewart, E. Hagström, S. Brené, A. Mourier, G. Coppotelli, C. Freyer, M. Lagouge, B.J. Hoffer, L. Olson, N.G. Larsson, Germline mitochondrial DNA mutations aggravate ageing and can impair brain development, Nature. 501 (2013) 412–415.

Section I: Developing Software to Study Cellular and Organelle Health

Chapter 2

Evaluating Cell Processes, Quality, and Biomarkers in Pluripotent Stem Cells Using Video Bioinformatics

ABSTRACT

There is a foundational need for quality control tools in stem cell laboratories engaged in basic research, regenerative therapies, and toxicological studies. These tools require auto- mated methods for evaluating cell processes and quality during *in vitro* passaging, expansion, maintenance, and differentiation. In this paper, an unbiased, automated high-content profiling toolkit, StemCellQC, is presented that non-invasively extracts information on cell quality and cellular processes from time-lapse phase-contrast videos. Twenty-four (24) morphological and dynamic features were analyzed in healthy, unhealthy, and dying human embryonic stem cell (hESC) colonies to identify those features that were affected in each group. Multiple features differed in the healthy versus unhealthy/dying groups, and these features were linked to growth, motility, and death. Biomarkers were discovered that predicted cell processes before they were detectable by manual observation. StemCellQC distinguished healthy and unhealthy/dying hESC colonies with 96% accuracy by non-invasively measuring and tracking dynamic and morphological features over 48 hours. Changes in cellular processes can be monitored by StemCellQC and predictions can be made about the quality of pluripotent stem cell colonies. This toolkit reduced the time and resources required to track multiple pluripotent stem cell colonies and eliminated handling errors and false classifications due to human bias. StemCellQC provided both user-specified and classifier-deter- mined analysis in cases where the affected features are not intuitive or anticipated. Video analysis algorithms allowed assessment of biological phenomena using automatic detection analysis, which can aid facilities where maintaining stem cell quality and/or monitoring changes in cellular

processes are essential. In the future StemCellQC can be expanded to include other features, cell types, treatments, and differentiating cells.

INTRODUCTION

Human pluripotent stem cells (hPSC) have enormous potential for enhancing our understanding of human prenatal development, modeling diseases-in-a-dish, treating patients with degenerative diseases, and evaluating the effects of drugs and environmental chemicals on cells that model human embryos and fetuses [1–3]. In each of these applications, there is a foundational unmet need for technology to non-invasively monitor the quality of hPSC during passaging, expansion, growth, experimentation, and differentiation [4, 5]. Ideally such tools should be rapid, non-invasive, resource saving, and non-biased. Video bioinformatics, which involves mining data from video images using algorithms that speed analysis and eliminate human bias, offers a solution to this problem and can be used to produce high quality software for stem cell applications [6–13].

Prior applications of video bioinformatics tools have successfully identified pluripotent stem cell colonies based on colony morphology [14], thereby speeding induced pluripotent stem cell (iPSC) derivation and reducing cost. Another study applied image processing soft- ware to fluorescent videos to identify iPSC after reprogramming [15], and a video bioinformatics method was developed to identify in vitro fertilized human embryos that will progress to blastocysts by 2 days after fertilization [16]. A recent report used phase-contrast video segmentation to generate lineage trees of neural stem cells using cell location, shape, movement, and size [17]. We previously developed in-house video segmentation tools to analyze single hESC and small colonies [8–11]. In a toxicological application of video bioinformatics using

CL-Quant software [18], cigarette smoke treatment altered hESC colony growth (area) and health [7]. While the above studies looked at single endpoints, multiple features related to cellular

processes and health can be extracted from video data thereby enhancing the depth of analysis and providing data on the kinetics of each endpoint. However, no software currently exists for automatic detection of pluripotent stem cell processes and quality in culture.

It is highly desirable to be able to multiplex multiple endpoints from a single experiment. The purpose of this study was to develop a high-content profiling software platform, StemCellQC, to automatically identify cell processes affected by culture/treatment and to classify the health of individual hESC colonies based on features extracted from phase contrast micro- scope video data. The method automatically segments the input colonies (non-labeled phase contrast images), extracts relevant novel features for each colony, utilizes the changes in features over time to identify cell processes that are affected by treatment, and statistically classifies healthy and unhealthy/dying colonies. StemCellQC's feature analysis and classification system provide an effective method to evaluate pluripotent stem cell colony processes and quality before use in experiments or clinical applications. Because hESC model the epiblast cells of embryos [19], which if harmed can lead to embryonic death or development of congenital defect(s), StemCellQC has the potential to be used as a novel technology to identify toxicants or drugs that could affect cellular processes in young embryos.

MATERIALS AND METHODS

Overall Design of the System

The overall design of the system will be discussed in Results (Fig S2.1). Each component is presented in the following Methods section.

Culture and Collection of hESC Videos

H9 hESC, purchased from WiCell Stem Cell Institute (Madison, Wisconsin), were maintained on Matrigel coated 6-well plates in mTeSR complete medium (Stem Cell Technologies, Vancouver, Canada) in a 37°C incubator with 90% humidity and 5% CO2 [7,20]. When cultures reached 80–85% confluency, they were detached using Accutase (eBiosciences, San Diego, CA) for 1 minute and used in experiments.

For live cell imaging in the BioStation CT (Nikon Instruments, Melville NY), hESC colonies were plated at 25–30% confluency and allowed to attach for 24 hours. To create groups of colonies that were healthy, unhealthy and dying, hESC were treated with Marlboro Red cigarette smoke solutions as described previously [7, 21]. Sidestream smoke (SS) was used at a dose of 1.1 puff equivalent (PE), where 1 PE is the amount of smoke that dissolves in 1 ml of medium in 60 sec. The 0.1PE concentration of SS smoke has an estimated concentration of nicotine of 1.2 μg/ml [22, 23], which is within the estimated tissue range of passive smokers [21].

All imaging was done using a 10x phase contrast objective in the BioStation CT using automatic Z-focus; cells were not stained, labeled, or genetically modified thereby permitting non-invasive analysis of cells. StemCellQC was tested on different magnifications (4x and 20x) and performs well. The dataset for feature analysis was made up of 34 videos of individual hESC colonies. 23 colonies were treated for 48 hours with sidestream cigarette smoke, while 11 control colonies were incubated in culture medium only.

Development and Use of StemCellQC Software

StemCellQC was written and developed with MATLAB 2015a programming environment. The MATLAB source code, a stand-alone executable version of this algorithm, and supplied test data are available online at http://vislab.ucr.edu/SOFTWARE/software.php. Scqc_multi.m is the

main program of the code and requires the following MATLAB toolboxes: Statistics and Machine Learning, Bioinformatics, System Identification, Image Processing, and Model-Based Calibration. The standalone alone executable requires the installation of the 64-bit version of MATLAB Runtime R2015a (8.5) available at http://www.mathworks.com/products/compiler/mcr/.

Categorization of hESC as Healthy, Unhealthy or Dying

Before the StemCellQC software is run, a training dataset was collected. Categorization of colonies as healthy, unhealthy, or dying by the end of 48 hours was provided by experts in culturing hESC and was based on biological observations listed in a decision tree (Fig S2.2). Categorization was used to validate the program's predictions of colony health.

Video Segmentation

An edge-based method and a region-based method were used to segment colonies in video images (frames). The edge-based method convolves the Sobel edge operator with the image to produce a gradient magnitude image and a gradient direction image. All gradient magnitudes below a calculated threshold were ignored and the rest were used as edges. This calculated threshold was automatically computed by the "edge" function in the Image Processing Toolbox from MATLAB. The edges in the image were dilated using two line structuring elements (vertical and horizontal) of three pixel lengths to merge connected regions of the colony. Connected components were then filled and smoothed with image erosion using a diamond structuring element of one-pixel radius to produce the segmentations. Segmented objects that are smaller than a user specified threshold, 3000 pixels in our case, were removed [24].

The Otsu's region-based method for segmentation [25, 26], which was used to compute the solidity feature, is the ratio of the colony area divided by the area of the convex hull. The con-

vex hull can be visualized as the shape enclosed by a rubber band stretched around a region-of-interest (ROI) [27]. Otsu's method produces a slightly larger segmented boundary which is smoother than the edge-based method. The main purpose of using solidity was to detect dead cells that were extruded from the stem cell colonies. Edge-based segmentation provides tight edge boundaries, which does not include the dead cells that are in the process of being expelled from the colony; whereas, Otsu's "larger" segmentation includes the dead cells. The concave regions of the segmentation that are produced by the dead cells affect the sensitivity of solidity. Therefore, solidity changes (primarily due to dead cells) are more pronounced when using Otsu's method. This larger boundary results in a larger convex hull which increases the sensitivity of the solidity feature. This allowed for better distinction between the peaks and valleys in the solidity plot.

For the region-based method, initially frames were smoothed to remove a small amount of noise using a 3x3 Gaussian filter. Next, Ostu's thresholding-based method was used to separate the pixels into the background and foreground by finding the optimal threshold for segmenting an image [25, 26]. Connected components were then found in the binary image. A morphological open operation (used to open gaps between loosely connected objects) was performed on the binary image to disconnect loosely connected pixels in the foreground. This is carried out by first eroding an object of interest (a connected component) and then dilating the output with a structuring element. To disconnect the objects, a circle with a radius of 12 pixels worked the best, and it was kept fixed for all the experiments. For both erosion and dilation, every pixel in the object was individually probed by the structuring element. The end result was a set of filtered connected components. Any holes in this region were filled, and the final ROIs were used to extract features.

Validation of Segmentation

The accuracy of segmentation was determined by manually segmenting hESC colonies using ImageJ and comparing the area and perimeter values to those obtained from the automatic seg- mentation (Fig S2.3).

Feature Extraction

Features based on appearance, morphology, and dynamics were extracted from segmented colonies. Dynamic features were obtained from morphological features by computing the rate of change of a feature over time. For example, to segment the protrusions extending from hESC, the main body of the colony (obtained using a morphological open algorithmic operation) was subtracted from the total colony segmentation. Also, the bright-to-total area ratio is the number of bright pixels divided by the area. Bright pixels were found by first computing a histogram of the intensities in the segmented colony to acquire the mean (μ) and standard deviation (σ). Then, a range of intensities (lower bound threshold = $\mu + 3\sigma$, upper bound threshold = $\mu + 6\sigma$) that best described dead cells in colonies were taken as the bright pixels. A complete list of features and their definitions is provided in Fig S2.9.

Identification of Key Features

Both biologically-based feature selection and statistical-based feature selection were used to identify those features that provided information on affected cellular processes and to distinguish healthy, unhealthy, and dying colonies. In addition, all the features were exhaustively applied to the classifier.

For biologically-based feature selection, plot observations over time can be interpreted by the user. A subset of features are shown as graphical plots in Figs 2.1–2.4. From the feature plots, the user

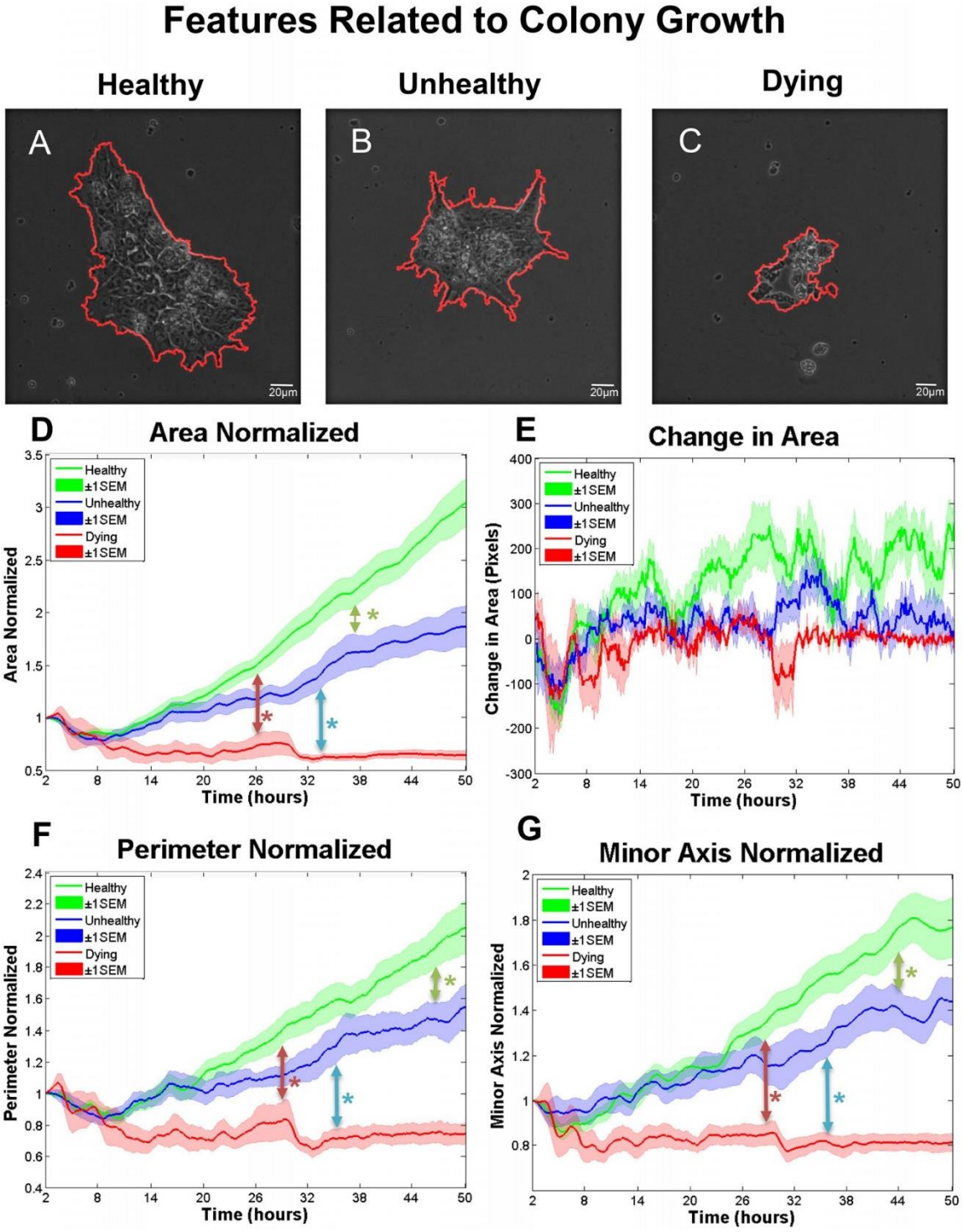
Features Related to Colony Growth
Healthy
Unhealthy
Dying
A
B
C
20μm
D
Area Normalized
Area Normalized
Time (hours)
E
Change in Area
Change in Area (Pixels)
Time (hours)
F
Perimeter Normalized
Perimeter Normalized
Time (hours)
G
Minor Axis Normalized
Minor Axis Normalized
Time (hours)
Healthy
±1SEM
Unhealthy
±1SEM
Dying
±1SEM

Figure 2.1. Features related to hESC colony growth. The outline of segmentation for a healthy (A), unhealthy (B), and a dying colony (C) at the last recorded frame. (D) Area normalized to the first time point for colonies that were healthy, unhealthy, and dying. Colonies first became significantly different by 2-way ANOVA at 37.6 hours for healthy vs unhealthy (green arrow), at 33.5 hours for unhealthy versus dying (blue arrow), and at 26.2 hours for healthy versus dying colonies (red arrow). (E) Change in area over time showing second contraction of dying colonies at 30–32 hours. (F) Perimeter over time normalized to the first time point for colonies that were healthy, unhealthy, and dying. Colonies first became significantly different by 2-way ANOVA at 46.6 hours for healthy versus unhealthy groups (green arrow), at 35.4 hours for unhealthy versus dying groups (blue arrow), and at 28.9 hours for healthy versus dying groups (red arrow). (G) Minor axis normalized to the first time point for colonies that were healthy, unhealthy, and dying. Colonies first became significantly different by 2-way ANOVA at 44.3 hour for healthy versus unhealthy groups (green arrow), at 36.5 hour for unhealthy versus dying groups (blue arrow), and at 28.9 hour for healthy versus dying group (red arrow). Number of colonies per group = 16 healthy, 12 unhealthy, 6 dying. Data are plotted as means ± SEM for each group. Arrows indicate first values that differed significantly from the control by 2-way ANOVA (* = $P < 0.05$).

can observe the non-overlapping standard error of the means (SEMs) to get a good indication of groups that are significantly different from each other. For a more rigorous statistical analysis, two-way ANOVAs with the Bonferroni post-test were performed to identify those features that were significantly different in the plotted data. For the solidity feature, a one-tailed independent samples t-test was used to determine if significant differences existed between means of healthy/unhealthy versus /dying colonies at 12 hours.

Statistical-based methods are useful in cases where the graphs for features may not reveal obvious effects, and they are good starting points to identify combinations or subsets of useful features. Filter methods which select variables regardless of the classification model are preferable for StemCellQC because of the use of multiple classifiers. 11 feature selection algorithms (10 methods from the Feature Selection @ Arizona State University toolbox [28]) and quadratic programming feature selection [29] were run on our dataset. These methods include Correlation-based Feature Selection (CFS) [30], Chi Square (Chi2) [31], Fast Correlation- based Filter (FCBF) [32], Fisher 9 [33], Gini Index 16 [34], InfoGain 6 [35], Sparse Multinomial Logistic Regression (SBMLR 3) [36], t-test [37], Kruskal Wallis [38], and Minimal-Redundancy-Maximal-Relevance [39]. The inputs for the feature selection algorithms are the average slope of each feature. The slope (incremental difference) is computed for each pair of adjacent frames for individual features. Next, the mean of these slopes is calculated for all 24 features. These features individually or in groups can be used to train the classifier.

Correlation of Key Features to Cellular Processes

Key features were interpreted to identify cellular processes such as growth, motility, and apoptosis, which differed in the healthy, unhealthy and dying groups. Also, two-feature plots were

constructed to detect correlations between features and identify temporal patterns over time (Fig 2.5, Videos S2.1 and S2.2).

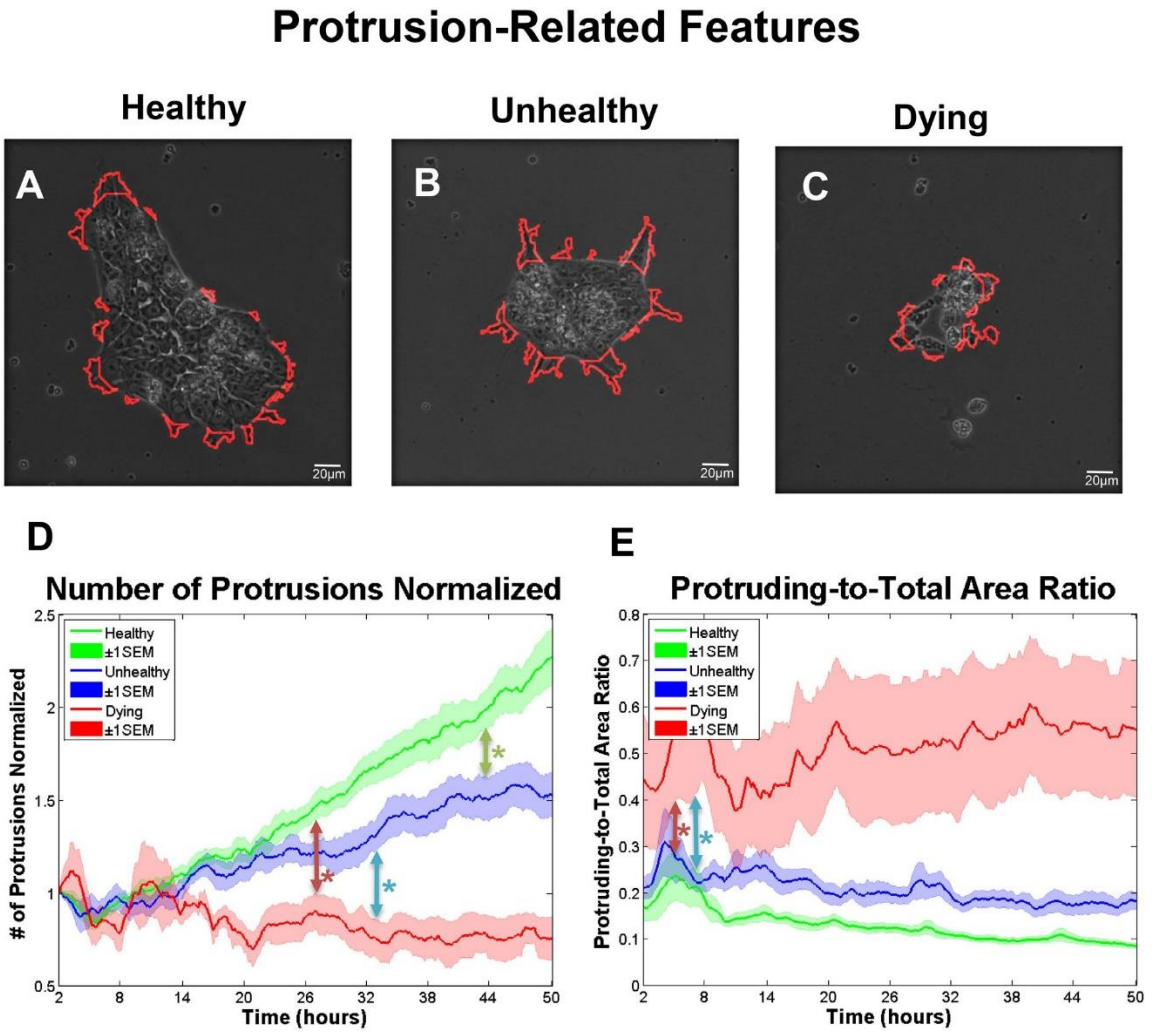

Figure 2.2. Surface protrusions on colonies can be used to study cell morphology and growth. (A) Segmentation of protrusions (red outline) for a healthy colony (A), unhealthy colony (B), and dying colony (C) at the last recorded time frame. (D) Number of protrusions over time normalized to the initial time point for healthy, unhealthy, and dying colonies. Colonies first became significantly different by 2-way ANOVA at 43 hours for healthy versus unhealthy groups (green arrow), at 33.3 hours for unhealthy versus dying groups (blue arrow), and at 27.1 hours for healthy versus dying group (red arrow). (E) Protruding-to- total area ratio for healthy, unhealthy, and dying colonies. Colonies first became significantly different by 2-way ANOVA at 6.8 hours for unhealthy versus dying groups (blue arrow), and at 4.8 hours for healthy versus dying groups (red arrow). Number of colonies per group = 16 healthy, 12 unhealthy, 6 dying. Data are plotted as means ± SEM for each group. Arrows indicate first values that differed significant from the control by 2-way ANOVA (* = $P < 0.05$).

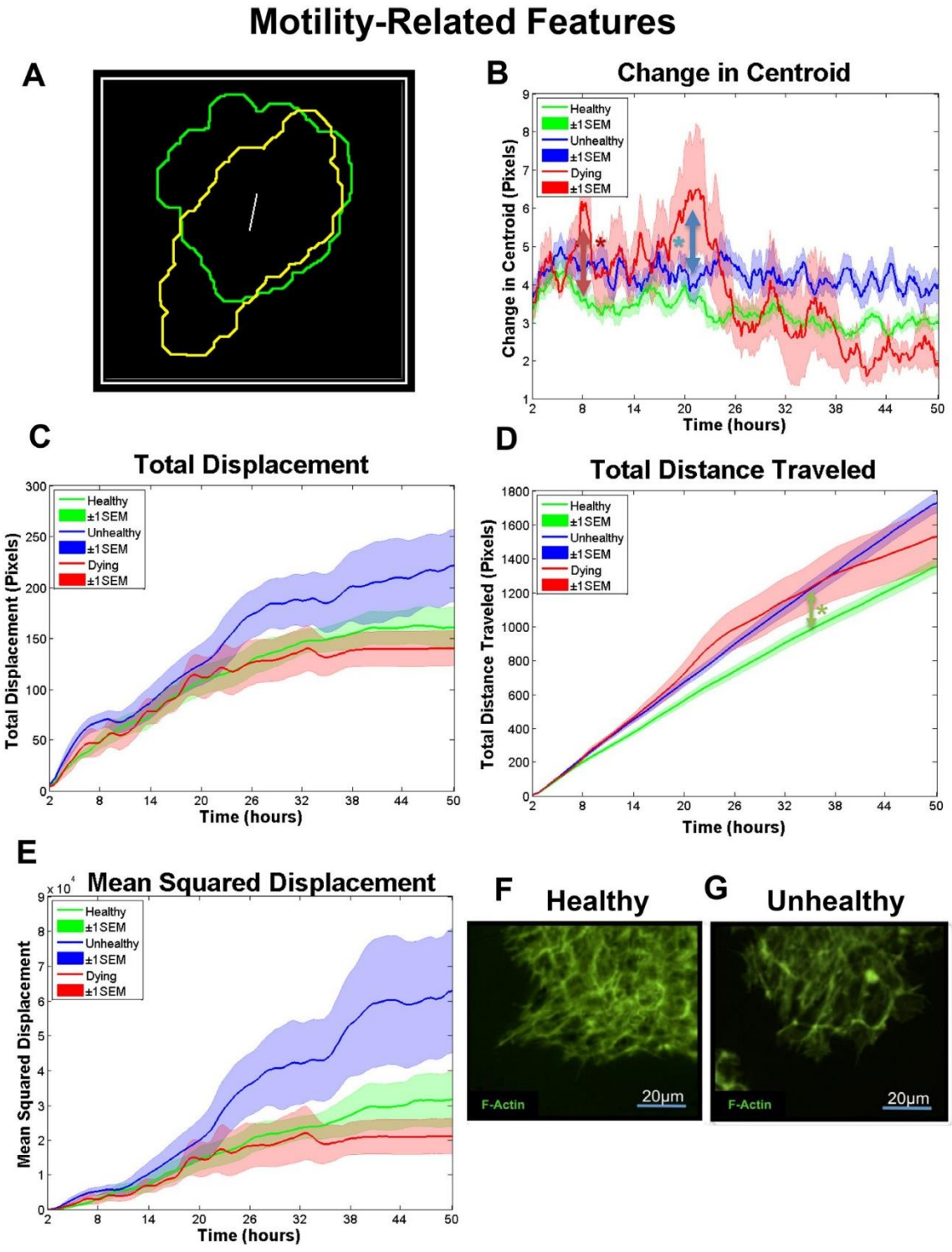
Motility-Related Features
A
B
Change in Centroid
Healthy
±1SEM
Unhealthy
±1SEM
Dying
±1SEM
Change in Centroid (Pixels)
Time (hours)
C
Total Displacement
Total Displacement (Pixels)
Time (hours)
D
Total Distance Traveled
Total Distance Traveled (Pixels)
Time (hours)
E
Mean Squared Displacement
x 10^4
Mean Squared Displacement
Time (hours)
F
Healthy
G
Unhealthy
F-Actin
20μm

Figure 2.3. Features related to hESC colony motility. Extracted contour of a healthy colony at 16 hours (yellow line) and 24 (green line) hrs. The distance between the centroids is indicated by the white line. (B) Change in centroid over time for healthy, unhealthy, and dying colonies. Colonies first became significantly different by 2-way ANOVA at 7.7 hours for healthy versus dying groups (red arrow), and at 20.6 hours for unhealthy versus dying groups (blue arrow). (C) The total displacement for healthy, unhealthy, and dying colonies. (D) The total distance traveled for healthy, unhealthy, and dying colonies. Colonies first became significantly different by 2-way ANOVA at 34.7 hours for healthy versus unhealthy groups (green arrow). (E) The mean squared displacement (MSD) for healthy, unhealthy, and dying colonies. (F-G) Localization of actin microfilaments in a healthy (F) and an unhealthy (G) colony which had fewer microfilaments than the untreated control. Number of colonies per group = 16 healthy, 12 unhealthy, 6 dying. Data are plotted as means ± SEM for each group. Arrows indicate first values that differed significant from the control by 2-way ANOVA (* = $P < 0.05$).

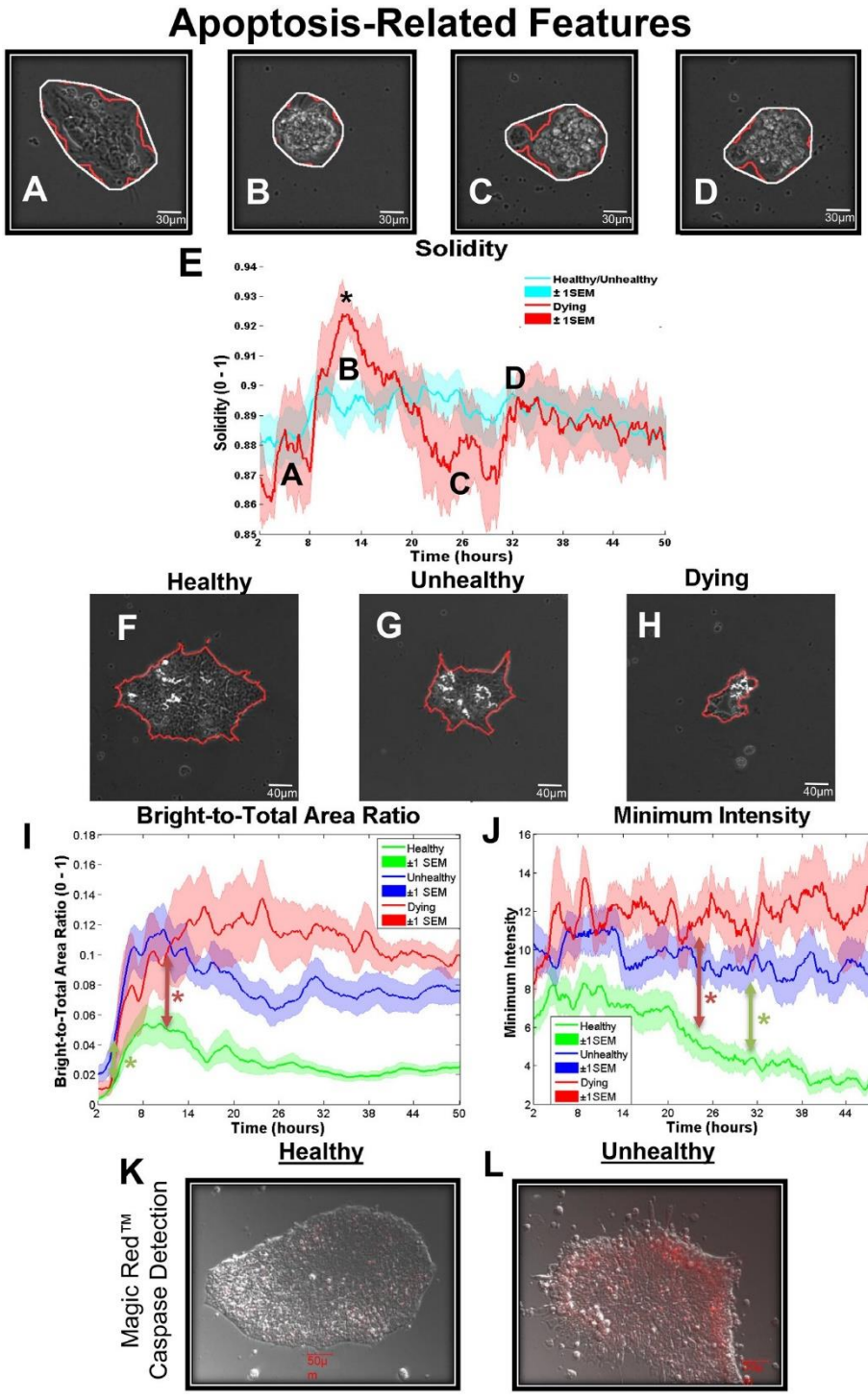
Apoptosis-Related Features
A
B
C
D
30µm
E
Solidity
Healthy/Unhealthy
± 1SEM
Dying
± 1SEM
Solidity (0 - 1)
Time (hours)
Healthy
Unhealthy
Dying
F
G
H
40µm
I
Bright-to-Total Area Ratio
Bright-to-Total Area Ratio (0 - 1)
Healthy
±1 SEM
Unhealthy
±1 SEM
Dying
±1 SEM
Time (hours)
J
Minimum Intensity
Minimum Intensity
Healthy
±1SEM
Unhealthy
±1SEM
Dying
±1SEM
Time (hours)
K
Healthy
L
Unhealthy
Magic Red™
Caspase Detection
50µm

Figure 2.4. Features related to cell death. (A-D) Frames representing the beginning of the video (A), the highest and lowest solidity values respectively (B and C), and the time of death of dying colonies (D). E) Solidity values over time for healthy/unhealthy (blue) versus dying colonies (red). Colonies that eventually died are distinguished by a large peak in solidity between 8–24 hours. A one-tailed independent sample t-test at 12 hours revealed that the two groups were significantly different ($P = 0.0285$). (F-H) White regions on top of hESC colonies (outlined in red) represent dead cells, shown at the end of recording for a healthy colony (F), unhealthy colony (G), and dying colony (H). (I) Bright-to-total area ratio over time for healthy, unhealthy, and dying colonies. Colonies first became significantly different by 2-way ANOVA at 4 hours for healthy versus unhealthy groups (green arrow), and at 11.5 hour for the healthy versus dying groups (red arrow). (J) Minimum intensity values for healthy, unhealthy, and dying colonies. Colonies first became significantly different by 2-way ANOVA at 31.5 hour healthy versus unhealthy groups (green arrow), and at 24 hours for healthy versus dying groups (red arrow). (K-L) A healthy (K) and an unhealthy (L) colony incubated with Magic Red to identify activated caspases 3&7. Number of colonies per group = 16 healthy, 12 unhealthy, 6 dying. Data are plotted as means ± SEM for each group. Arrows indicate first values that differed significant from the control by 2-way ANOVA (* =$P < 0.05$).

Classification as Healthy or Unhealthy/Dying

To automatically classify the dataset, all features measurements were first normalized with maximum-minimum normalization. 410 frames (collected over a 48 hour period) multiplied by 24 features results in a 9840 feature space. Therefore, in order to reduce the number of dimensions, the input value to the classifier was the mean slope of the data. Classes used by the classifier were healthy and unhealthy (the unhealthy group included dying colonies which were not classified separately since this group contained only 6 colonies).

To test the ability of the features to distinguish healthy versus unhealthy/dying colonies, several biologically selected features and additional features selected by 11 statistical methods were used to train three classifiers: (1) support vector machines (SVM), (2) K-nearest neighbor (KNN), and (3) naïve Bayes [33]. SVM uses the training data to create a boundary in multi- dimensional space, which can be used to classify future data samples. KNN takes a test sample and compares it to the K-nearest training samples in a multi-dimensional space. The KNN algorithm was used with $k = 3$ (the 3 closest neighbors to the sample). A majority vote is taken by these neighbors and used as a label for the test sample. Naïve Bayes is a probabilistic classifier based on Bayes' theorem that uses strong assumptions that features are independent from one another. An exhaustive test using all possible combinations of features was performed to determine the best classification results using combination of features.

A summary of the classification results using single features, combinations of features, and statistically determined features are shown in Tables 2.1–2.4 in the Results section.

Classification Validation

The classification experiments were run with 10-fold cross validation where the dataset was partitioned into 10 parts. The 34 videos gave six partitions containing three videos each and

four partitions containing four videos each. A 10-fold partition of the training data was used, which allowed for computation of a standard deviation of the results. One part was used as the test data once, while the other nine parts were used as training data. The partitions were randomized, and this process was repeated with 5 random permutations of the data. A percentage of correctly classified samples was calculated for each permutation by comparison to the manual labels. The classification results were then used to find the mean and standard deviation.

Molecular Validation

Apoptotic activity was detected using the Magic Red Caspases 3&7 Detection FLICA Kit (Immunochemistry Technologies, LLC, Bloomington, MN) as described previously [7]. Fluorescent staining of F-actin was performed using a phalloidin-Alexa Fluor 488 conjugate (Invitrogen, Carlsbad, CA) diluted 1:200 in 1% goat serum in phosphate buffered saline. hESC colonies in chamber slides were fixed using 4% paraformaldehyde for 10 minutes, incubated in blocking solution (3% goat serum in PBS) at room temperature for 1 hour, washed 5 times, and incubated in phalloidin-Alexa Fluor 488 for 1 hour at room temperature. Samples were mounted using Vectashield with DAPI (Vector Laboratories, Burlingame, CA) and imaged with a Nikon Eclipse Ti fluorescent microscope (Nikon, Melville, NY).

RESULTS

Feature Analysis

Features were analyzed graphically to identify those that differed in the healthy, unhealthy, and dying groups. Sets of affected features were then grouped according to the biological processes they represented (morphology, growth, motility, death) (Figs 2.1–2.4, Fig S2.4). The classifiers were run with 48, 36, 24, and 12 hours of video to show their effectiveness at different time points.

For all durations, all 24 features were run singularly through the classifiers and the ones with the highest accuracy are shown in Tables 2.1– 2.4 (Single Features). Additionally, exhaustive searches for combinations of up to 5 features were run to identify the most accurate results (Table 2.1 Combination of Features). Lastly, the best results from the 11 existing feature selection algorithms are also shown in Tables 2.1–2.4 (Feature Selection Methods).

Features Related to Colony Growth as Biomarkers of hESC Health

Extracted features related to colony growth (area, perimeter, minor axis, protrusions) were evaluated in healthy, unhealthy, and dying colonies. Area (the total number of pixels inside a segmented colony; Fig S2.5) differed in healthy, unhealthy and dying colonies (Fig 2.1A–2.1E). When area was normalized to the initial time point to account for variability in the starting size, all groups displayed an initial contraction which decreased area and lasted about 8 hours (Fig 2.1D). Contraction was likely caused by changes in temperature/CO2 during transfer to the BioStation. After contraction, healthy colonies displayed a steady increase in area until the end of recording, while unhealthy colonies grew at a slower and variable rate. Both groups followed a similar trend up to 16 hours, after which healthy and unhealthy growth rates deviated and become distinguishable by about 24 hours. Dying colonies could be distinguished from the healthy and unhealthy groups by about 10 hours when growth rates for the dying group clearly diverged. At 30 hours, dying colonies underwent a second contraction leading to a sharp decrease in area (Fig 2.1D and 2.1E). These colonies were interpreted to be dead based on this pronounced decrease in size and shedding of dead cells.

Perimeter, defined as the number of pixels constituting the colony periphery (red outline in Fig 2.1A–2.1C and 2.1F; Fig S2.5), provided additional information about colony growth. There was divergence in the perimeters of healthy and unhealthy colonies at approximately 25 hours (Fig

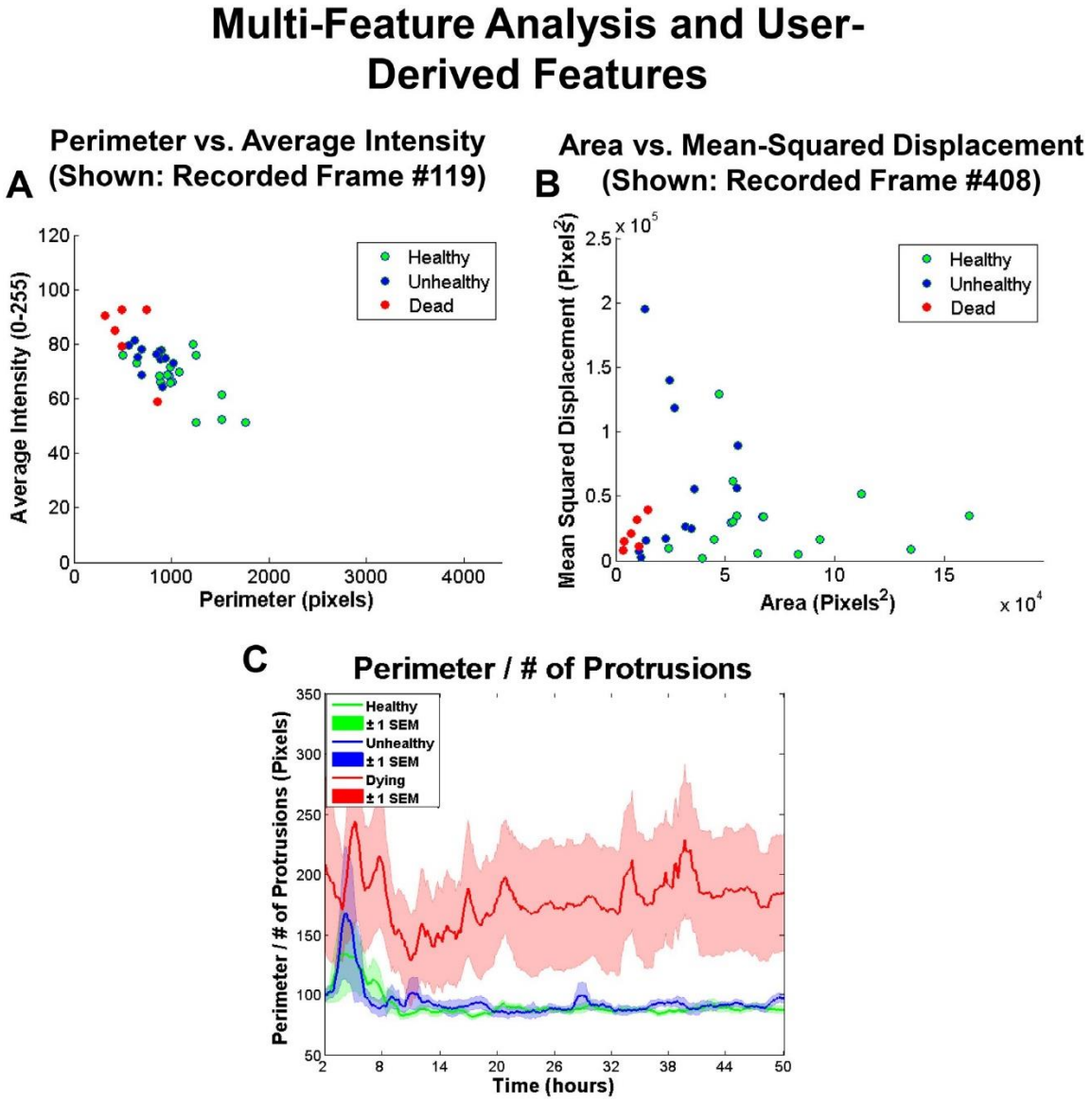

Figure 2.5. Two-Feature Plot Analysis. (A) Average intensity compared to perimeter running plot shown at approximately at 16 hours of incubation for all individual healthy (green), unhealthy (blue), and dying (red) hESC colonies. (B) Mean-squared displacement compared to area running plot shown at approximately 16 hours for all individual healthy (green), unhealthy (blue), and dying (red) hESC colonies. (C) User derived equation (perimeter divided by number of protrusions) plotted for healthy, unhealthy, and dying colonies.

Table 2.1. Classification Results Using 48 Hours of Video

48 Hours	***Classification Techniques**		
Single Features	**SVM**	**K-NN, k =3**	**Naïve Bayes**
1) Area	94.12 ± 0.00	94.12 ± 0.00	94.00 ± 0.91
2) Number of Protrusions	90.71 ± 1.35	96.06 ± 1.32	91.24 ± 0.65
3) Total Distance Travelled	84.24 ± 1.20	74.06 ± 1.48	84.88 ± 1.01
Combination of Features			
1) Area, Orientation, Num. of Protrusions	94.12 ± 0.00	94.71 ± 1.15	94.12 ± 0.00
2) Num. of Protrusions, Min. Intensity	**97.06 ± 0.00**	**97.06 ± 0.00**	**96.47 ± 1.15**
3) Major Axis, Minor Axis, Change in Centroid	93.53 ± 1.57	92.94 ± 1.62	90.00 ± 1.27
Feature Selection Methods			
**CFS	91.76 ± 1.32	96.47 ± 1.32	91.76 ± 1.32
***Chi Square	91.76 ± 0.00	91.76 ± 0.00	95.29 ± 1.61
****QPFS	91.76 ± 1.32	94.12 ± 3.60	91.76 ± 2.46

*Classification of colonies as healthy or unhealthy using three different classification techniques: SVM, KNN, and Naive Bayes.
**CFS selected the following features: Area, Number of Protrusions, and Change in Area.
***ChiSquare selected the following features: Area, Number of Protrusions, and Major Axis Length
****Quadratic Programming Feature Selection selected the following features: Total Distance Travelled, Major Axis Length, Minimum Radius.

Table 2.2. Classification Results Using 36 Hours of Video

36 Hours	***Classification Techniques**		
Single Features	**SVM**	**K-NN, k =3**	**Naïve Bayes**
1) Area	85.18 ± 1.25	88.00 ± 1.49	85.18 ± 1.49
2) Number of Protrusions	81.94 ± 1.10	73.65 ± 1.72	81.00 ± 1.34
3) Bright Area Ratio	81.76 ± 3.22	85.29 ± 0.00	76.47 ± 2.08
Combination of Features			
1) Area, Min. Radius, Num. of Protrusions, Change in Area, Change in Perimeter	96.47 ± 1.32	94.71 ± 1.32	94.71 ± 1.32
2) Area, Min. Radius, Change in Area, Change in Perimeter	95.88 ± 1.61	92.94 ± 1.61	95.88 ± 1.61
3) Area, Avg. Radius, Change in Area, Change in Perimeter	95.29 ± 1.61	92.94 ± 1.61	95.88 ± 2.63
Feature Selection Methods			
**CFS	91.18 ± 2.08	88.24 ± 2.08	90.00 ± 1.61
***SMBLR	85.88 ± 1.32	91.76 ± 1.32	90.59 ± 1.32
****FCBF	86.47 ± 1.61	87.65 ± 1.32	92.94 ± 1.61

*Classification of colonies as healthy or unhealthy using three different classification techniques: SVM, KNN, and Naive Bayes.
**CFS selected the following features: Area, Perimeter, Minor Axis Length, Minimum Intensity, Bright Area Ratio, Number of Protrusions, Change in Perimeter, Total Distance Travelled.
***SMBLR selected the following features: Number of Protrusions, Change in Perimeter, Minor Axis Length, Bright Area Ratio, Total Distance Travelled.
****FCBF selected the following features: Area, Perimeter, Minimum Intensity, Bright Area Ratio, Change in Perimeter, total Distance Travelled.

Table 2.3. Classification Results Using 24 Hours of Video

24 Hours	***Classification Techniques**		
Single Features	**SVM**	**K-NN, k =3**	**Naïve Bayes**
1) Area	83.35 ± 1.49	74.94 ± 2.00	82.47 ± 1.37
2) Number of Protrusions	75.29 ± 1.85	67.41 ± 1.95	71.35 ± 1.51
3) Perimeter	75.29 ± 4.36	73.53 ± 2.08	75.29 ± 1.61
Combination of Features			
1) Area, Orientation, Num. of Protrusions, Change in Perimeter, Change in Centroid	83.53 ± 1.61	91.17 ± 0.00	88.82 ± 1.31
2) Area, Avg. Radius, Change in Perimeter, Change in Centroid	88.24 ± 2.08	83.53 ± 1.61	90.59 ± 1.32
3) Orientation, Bright Area Ratio, Change in Perimeter, Change in Centroid	87.65 ± 1.32	88.24 ± 2.94	84.12 ± 1.61
Feature Selection Methods			
*CFS	84.71 ± 1.32	72.35 ± 4.46	78.24 ± 1.61
**SBMLR	78.24 ± 5.73	69.42 ± 3.35	83.53 ± 3.35
***FCBF	84.71 ± 1.32	72.35 ± 4.46	78.24 ± 1.61

*Classification of colonies as healthy or unhealthy using three different classification techniques: SVM, KNN, and Naive Bayes.
**CFS selected the following features: Area, Minor Axis Length, Bright Area Ratio, Change in Perimeter, Total Distance Travelled.
***SMBLR selected the following features: Area, Orientation, Number of Protrusions, Total Distance Travelled.
****FCBF selected the following features: Area, Minor Axis Length, Bright Area Ratio, Change in Perimeter, Total Distance Travelled.

Table 2.4. Classification Results Using 12 Hours of Video

12 Hours	***Classification Techniques**		
Single Features	**SVM**	**K-NN, k =3**	**Naïve Bayes**
1) Bright Area Ratio	67.06 ± 1.32	54.12 ± 1.61	64.70 ± 2.94
2) Total Distance Travelled	71.76 ± 2.63	65.29 ± 2.46	61.18 ± 3.83
3) Change in Centroid	64.71 ± 0.00	57.06 ± 3.35	67.06 ± 2.46
Combination of Features			
1) Max. Radius, Ratio of Protrusion Area, Change in Area, Change in Centroid	74.12 ± 2.46	75.88 ± 1.31	79.41 ± 3.60
2) Eccentricity, Min. Radius, Ratio of Protrusion Area, Change in Perimeter, Change in Centroid	71.18 ± 3.83	78.24 ± 3.35	78.24 ± 1.61
3) Min. Radius, Max Intensity, Change in Centroid	71.18 ± 2.46	80.59 ± 2.63	73.53 ± 0.00
Feature Selection Methods			
*CFS	71.76 ± 2.63	65.29 ± 2.46	61.18 ± 3.83
**SBMLR	67.65 ± 2.94	77.06 ± 2.46	64.12 ± 3.22
***FCBF	71.76 ± 2.63	65.29 ± 2.46	61.18 ± 3.83

*Classification of colonies as healthy/unhealthy using 3 different classification techniques: SVM, KNN, and Naive Bayes
**CFS selected the following features: Total Distance Travelled.
***SMBLR selected the following features: Change in Area, Total Distance Travelled.
****FCBF selected the following features: Total Distance Travelled.

2.1F), after which the rate of change in perimeter for unhealthy colonies slowed until about 33 hours when it underwent a growth spurt that lasted 3 hours. The dying colonies diverged from the other two groups at 8 hours and had an abrupt decrease in size at 30 hours, as was seen with area.

Minor axis (smaller axis of an ellipse fitted to a colony) (Fig S2.6) was affected in unhealthy/dying colonies (Fig 2.1G). After 23 hours, healthy colonies showed a steep increase in minor axis, suggesting that once healthy colonies reach a critical size, they have a less-elongated morphology.

Protrusions are dynamic cell processes that extend off colonies and take a variety of shapes (Fig 2.2A–2.2C; Fig S2.6). They allow colonies to attach, spread, and migrate, [40, 41]. The number of protrusions increased on healthy and unhealthy colonies and decreased on dying colonies during incubation (Fig 2.2D). The protruding-to-total area ratio, which is defined as the ratio of protrusion area divided by total colony area, had an inverse relationship with colony growth. Protrusion area decreased gradually in healthy and unhealthy groups, but increased slightly in the dying group (Fig 2.2E).

Colony Motility

The change in centroid feature allowed tracking of stem cell colony movement. This feature is determined by finding the centroid of each colony and calculating the distance between two successive frames (Fig S2.7). Outlines of a hESC colony at two times and the change in centroids are shown in Fig 2.3A. Change in centroid oscillations were smaller in the healthy and unhealthy groups than in the dying group (Fig 2.3B). The unhealthy and healthy groups were similar in the magnitude of their oscillations, but overall motility was less in the healthy colonies, probably because the larger sized healthy colonies required more energy and coordination for directed movement. After a certain area was reached, the center of the healthy colonies moved very

little as the colony continued to expand. It is also possible that smoke stimulated motility in unhealthy hESC to facilitate escape from exposure. The dying colonies displayed erratic motility and showed a significant decrease in movement after 20 hours as they were approaching death. Movements detected after death (30 hours) are due to slight segmentation differences between frames.

Total displacement detected how far a colony moved from its original starting point (Fig 2.3C; Fig S2.7), while total distance traveled is the sum of the entire trajectory of movement (Fig 2.3D; Fig S2.7). These features revealed information on the pattern of travel. Dying colonies traveled more up to 30 hours (when they died) than the other two groups, but their displacement was low indicating that they moved erratically near their original starting point. Unhealthy colonies moved further from their point of origin and travelled a longer total distance than healthy colonies. Both the healthy and unhealthy colonies displayed remarkably little variance in total distance travelled (Fig 2.3D).

The mean squared displacement (MSD) feature measures Brownian motion [42] and can be used to study cellular migration [43]. MSD is defined by the equation: $MSD(t) = ([(x(t + t0) - x(t0)]^2 + [y(t + t0) - y(t0)]^2)$, where MSD (t) can be approximated as ~ $t\beta(t)$. The logarithmic derivative exponent β can be used to determine the particular mode of motility, with $\beta > 1$ indicating super-diffusive movement, a form of diffusion where the colonies occasionally undergo very long steps. $\beta < 1$ indicates sub-diffusive movement, defined as a tendency for the colonies not to diffuse due to trapping (inability to move). For Brownian motion, or a random walk, β is approximately 1. The MSD feature is robust because it uses the squared value of displacement, making it less sensitive to small fluctuations. The MSD plot shows a similar trajectory for all three groups up until about 11 hours (Fig 2.3E), after which the healthy colonies display Brownian motion ($\beta = 1.04$). For dying colonies, sub-diffusive motility ($\beta = 0.21$) was

observed from 23–50 hours, consist with their death after 30 hours. The unhealthy group demonstrated sub- diffusive motility from 22–35 hours and 35–50 hours (β values = 0.76 and 0.52, respectively).

To investigate the molecular basis of the aforementioned effects on motility, F-actin was labeled with phalloidin-Alexa 488. Healthy colonies (Fig 2.3F) had a more robust actin cytoskeleton than unhealthy colonies (Fig 2.3G). Although F-actin was partially depolymerized by smoke treatment, there was sufficient functional F-actin in the treated colonies to allow colony movement. A decrease in F-actin may be linked to a decrease in the number of focal adhesions, which may facilitate motility in the unhealthy group [44,45]. Other studies have reported the inverse correlation between cell motility and polymerization state of the actin cytoskeleton [46].

Solidity as Predictor of Apoptosis

As colonies became rounder or more convex, their solidity increased and approached 1. Fig 2.4A–4D show hESC colonies at different times with outlines of their segmentations (red lines) and convex hulls (white lines). Solidity, which measured convexity (Fig 2.4E; Fig S2.8), identified colonies that were destined to die by 48 hours. Solidity for the healthy/unhealthy groups combined changed little during 48 hours (Fig 2.4E). These two groups were combined since solidity was a predictor of colony death, not health. In contrast, dying colonies had a significant spike in solidity at about 12 hours due to contraction and rounding of the colonies (B label in Fig 2.4E). This was followed by a drop that reached a minimum at 30 hours (C label in Fig 2.4E), when death occurred and extrusion of dead cells caused the convex hull to be less circular. Graphs of solidity can be used to identify at 12 hours, colonies that will die by 48 hours.

Colony Brightness Identifies Dying Cells

As cells within a colony die, they are extruded to the top of the colony where their brightness increases. The white areas in Fig 2.4F are dead cells on a healthy colony at the end of incubation. Significantly more dead cells were present on the unhealthy (Fig 2.4G) and dying colonies (Fig 2.4H). To quantify dead cells on top of colonies, a bright-to-total area ratio feature was used. This feature measured the number of bright pixels in the colony as a ratio to the total area and is an indicator of cell death. All groups exhibited an increase in bright-to-total area ratio during the first 6 hours when the colonies contracted (Fig 2.4I), after which the bright-to-total area ratios of healthy and unhealthy colonies decreased and the ratio for the dead colonies increased up to 16 hours and stayed elevated.

To compare the progression of colony brightness over time, a minimum intensity feature (lowest pixel intensity in the colony) was monitored (Fig 2.4J). Throughout incubation, healthy colonies displayed a lower minimum intensity than the unhealthy and dying colonies. These data support the idea that the unhealthy and dying colonies failed to spread as well on Matrigel as healthy colonies.

To confirm cell death, colonies were labeled with Magic Red which detects activated caspases 3&7, biomarkers for apoptosis. As shown by the red staining in Fig 2.4K and 2.4L, unhealthy colonies exhibited more caspase 3&7 activity than the healthy colonies.

3D Visualization of Features and Custom Features Enhance Data Mining

To mine additional biological information such as correlation of features, StemCellQC can plot features against each other and play the plot as a video over time (Videos S2.1 and S2.2). In Fig 2.5A, perimeter and average intensity, when plotted against each other, showed an inverse relation- ship (indicative of dead cells). In Fig 2.5B, area and the mean-squared displacement

features were plotted against each other to highlight individual colonies with elevated MSD values (mainly colonies from the unhealthy group). This type of analysis can also reveal outlier colonies within a group. In addition, StemCellQC is able to plot mathematical equations using the original 24 features. In Fig 2.5C, a user derived equation, ratio of perimeter to the number of protrusions, is plotted. This plot displays an estimate for the average length of a protrusion for each class and shows that the protrusions on dying colonies are about twice as long as those on healthy/unhealthy colonies (Fig 2.5C).

Classification Results

The input values used by the classifiers were the mean slopes of each feature. The nine individual features found by user-interpreted feature selection were tested separately giving each feature a classification rate (Table 2.1). Area was the best individual feature at predicting health with a 94% accuracy when using any classifier. By combining features that are not related to the same process, accuracy increased. When the number of protrusions and minimum intensity were combined, the system's ability to distinguish hESC colony health improved to 97% accuracy when using any classifier. Results for feature selection algorithms (CFS, ChiSquare and QPFS) were also shown. All three had at least 91% accuracy and CFS was 96.47% accurate with KNN.

The classifiers were also run with the first 36, 24, and 24 hours, which are shown in Tables 2.2–2.4. For 36 hours (Table 2.2), area was the best feature with 88% accuracy, and combination of features improved results to 96.47%. For 24 hours (Table 2.3), area was still the strongest feature with 83.35% accuracy and a combination improved results to 91.17% accuracy. For 12 hours (Table 2.4), however, total distance travelled is the strongest feature with 71.76% accuracy. It should be noted that for 12 hours most individual features performed at about 50–60% accuracy which is slightly better than chance, however when we combine features, we are able to improve

classification to 80.59% accuracy. Judging colony health by eye after a mere 12 hours of time is biased and difficult, making an 80.59% classification rate very useful. These tables show that while a certain combination of features work best using the full 48 hours of time, another combination may produce a more accurate classification if less time is used. With shorter video duration, there is an increase in accuracy using a combination of features; whereas, with longer durations, a single strong feature (such as area) can be sufficient to get accurate results.

DISCUSSION

StemCellQC is an innovative, cost effective, non-invasive software tool that utilizes bioinformatics to automatically monitor dynamic cell processes, cell morphology, and cell health during passaging, culture, expansion, maintenance, or experimental treatment of pluripotent stem cells. StemCellQC eliminates the need for labeling with dyes or fluorescent probes and eliminates tedious manual classification, which significantly decreases analysis time and classification errors due to observer bias.

Graphical plots of features provide quantifiable, real-time data on living hESC and are excel- lent analytical tools for comparing features across treatments and cell types. The plots can help users visualize trends or features that are not easily detectable by manual inspection. Cell process analysis is especially valuable in toxicological or drug studies as it provides insight into the mode of action of the treatment. For example, smoke treatment inhibited growth (area, perimeter, minor axis and protrusions), increased motility (change in centroid, total displacement, total distance traveled and MSD), and increased apoptosis (solidity and intensity features).

Chemical treatments other than cigarette smoke may affect other features, and in such cases, other cell processes could be revealed by feature analysis. Multiplexing cellular process

information (colony growth rate, motility, and apoptosis) increases the power of analysis, and in toxicological studies, this greatly increases the probability of detecting an effect if one exists.

StemCellQC can plot user-derived equations of features (for example: perimeter/number of protrusions) for customized types of analysis. The software can also create videos of various features plotted against each other. These plots enable correlation between features and help determine how biological processes are related over time. For example, an inverse relationship was found between colony size and colony brightness (dead cells on a colonies' surface).

Feature analysis, when combined with a classifier, enabled identification of healthy, unhealthy, and dying colonies. Area, which classified with 94% accuracy, was the strongest feature for predicting colony health. Changes in area are not always detected by human observation, especially when colonies do not die but experience stunted growth. In clinics or research laboratories, a decrease in growth rate may signal a problem with the culture or cell quality, and this would be rapidly detected in cultures monitored using StemCellQC. While smoke treatment slowed colony growth, factors that increase growth rate may be equally important and detectable by StemCellQC. For example, when chromosomal translocations occur in hESC, growth can be accelerated [47], and this would not be desirable in clinical or research labs. Combinations of features successfully increased the accuracy of classification of unhealthy/dying colonies to 97%. Depending on the rigor needed, change in area by itself will usually be sufficient to distinguish healthy from unhealthy/dying colonies.

By comparing changes in features over 48 hours, biomarkers that predict biological outcomes were found at early time points (Fig 2.6). For example, growth rate separated dying from healthy/unhealthy colonies by 16 hours and further separated healthy from unhealthy colonies by 26 hours (Fig 2.1D; Fig 2.6A and 2.6B). Similar distinctions can be made from graphs for other growth features (perimeter, minor axis, and number of protrusions) (Figs 2.1F and 2.1G and 2.2D

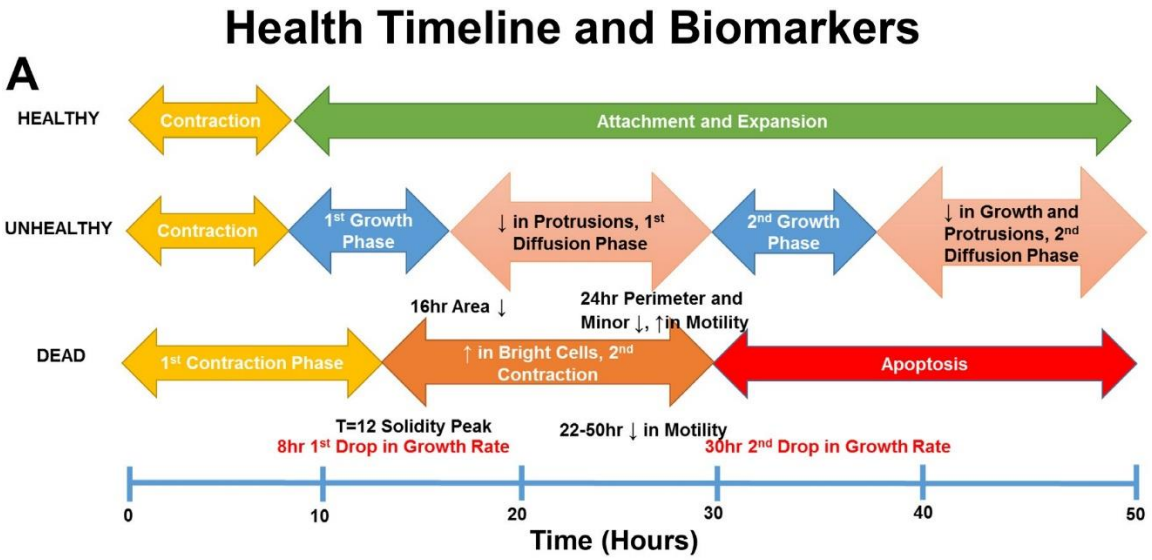

B

Extracted Biological Information	Time (hr)	Biomarker
Bright-to-total area ratio elevated as early as 6 hour	6-11	Apoptosis
Protruding-to-total area ratio elevated as early as 7 hour	7	Retraction/Apoptosis
Change in centroid significantly peaks as early as 8 hour	8	Motility/Apoptosis
Mean-squared displacement β values of >>1	11	Super-diffusive Motility
Peak in solidity at 12 hour	12	Apoptosis
Elevated total distance traveled as early as 14 hour	14	Motility/Apoptosis
Area separates from healthy group at 16 hour	16	Growth
Minimum intensity value declines as early as 20 hour	20	Health
Number of protrusions separates from healthy group at 22 hour	22	Growth/Morphology
Minor axis shows a sudden increase at 23 hour	23	Growth
Minimum intensity value elevated as early as 24 hour	24	Apoptosis
Change in centroid drops to consistent near-zero values	26	Motility/Apoptosis
Sudden drop in change in Area at 30 hour	30	Apoptosis
Mean-squared displacement β value of <<1	30	Sub-diffusive Motility

Figure 2.6. hESC Health Timeline and Biomarkers. (A) Changes in several feature values and biological events during 48 hours of incubation for healthy, unhealthy and control groups. This type of plot can be used to compare events in different groups. (B) Biomarkers that can be used to identify healthy, unhealthy, and dying colonies and their earliest detection times.

and 2.2E). Change in centroid was the strongest motility biomarker which cleanly separated healthy from dying colonies as early as 8 hours (Fig 2.3D). Solidity successfully separated dying colonies from healthy/unhealthy by 12 hours when used with Otsu's segmentation (Fig 2.4E), and bright-to-total area ratio separated all three groups from each other by 14 hours (Fig 2.4I). The biomarkers for dying colonies are powerful tools for monitoring apoptosis in living cultures without use of labels or probes, which themselves often produce unwanted effects.

CONCLUSIONS

StemCellQC is a versatile toolkit for analyzing cell processes, evaluating cell quality, and dis- covering biomarkers. It is designed for use with pluripotent stem cell colonies in culture, and is adaptable to other cell types. It can be used retrospectively or on-the-fly to solve numerous problems. There are at least four applications for StemCellQC. First, core facilities that culture pluripotent cells for distribution to research labs could monitor cell quality using non-invasive morphological tools to guarantee that distributed cells meet an acceptable uniform standard from day-to-day. This is especially important when the results of a research study may ultimately affect a patient's health. Second, StemCellQC can serve as a quality control tool in future clinics that deliver therapies based on pluripotent stem cells. Such clinics will need to maintain and differentiate cells that meet future FDA criteria for transplantation to patients. A record of cell quality produced by StemCellQC would be an important part of a patient's medical record, and could be mined after cell transfer to patients to better understand those features that work best for patient treatment. Third, hPSC can differentiate into specific cell types that can be used for studying genetic disorders, such as Huntington's disease [48]. StemCellQC can monitor the behavior of cells/colonies in disease-in-a-dish models to determine how cells respond to drug treatments [49]. Fourth, StemCellQC could be used in laboratories that perform drug testing or that monitor

chemical toxicity. Multiplexing data enhances the discovery of toxicants and bio- markers. hESC provide an excellent model for prenatal development, a process that cannot be studied experimentally in humans [20] and which is generally sensitive to environmental chemicals [50].

We are currently using StemCellQC with other pluripotent cell types and experimental conditions and found that it performed very well. We have found clear cut effects on processes such as growth, motility, death and morphology using StemCellQC with cells grown in optimal and suboptimal media, indicating StemCellQC will be useful for recognizing culture conditions that are not satisfactory. As more treatments are used, we anticipate that other processes or effects may be observed. In the future, StemCellQC software can be enhanced by adapting it to single cells and including features that correlate to cell processes such as stress, differentiation, and pluripotency. More classifiers can be added, and additional biomarkers will likely be discovered with new applications of the software.

SUPPORTING INFORMATION

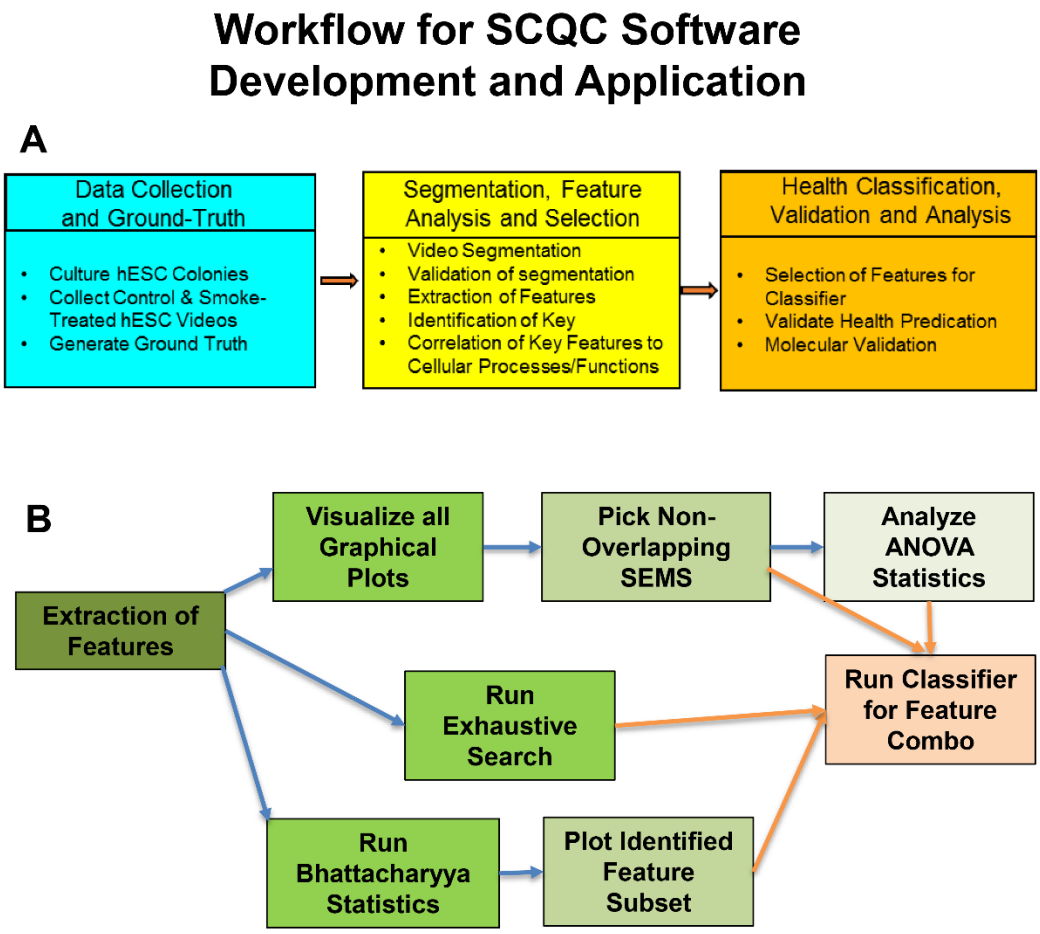

Figure S2.1. (A) Diagram showing workflow used to develop StemCellQC™. (B) Diagram showing feature selection methods for classification.

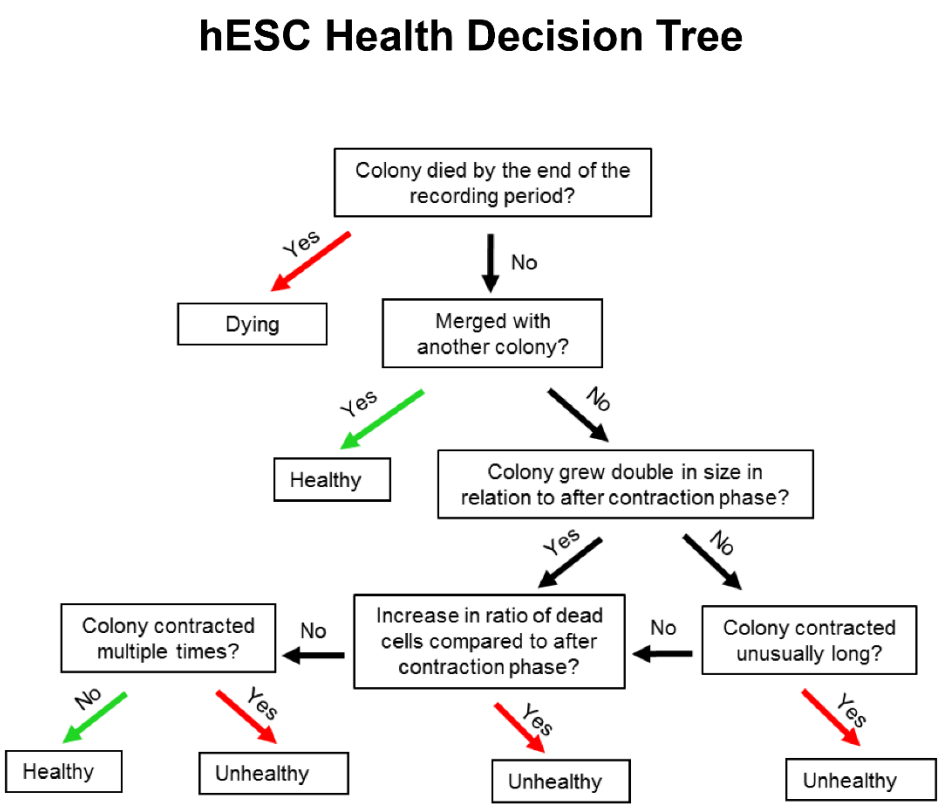

Figure S2.2. Decision tree showing method for classifying hESC colonies into healthy, unhealthy or dying groups. Red arrows show decisions resulting in classification of a colony as unhealthy or dying, green arrows show decisions resulting in classification as healthy, and black arrows indicate points where the classification process was continued.

Segmentation Ground Truth

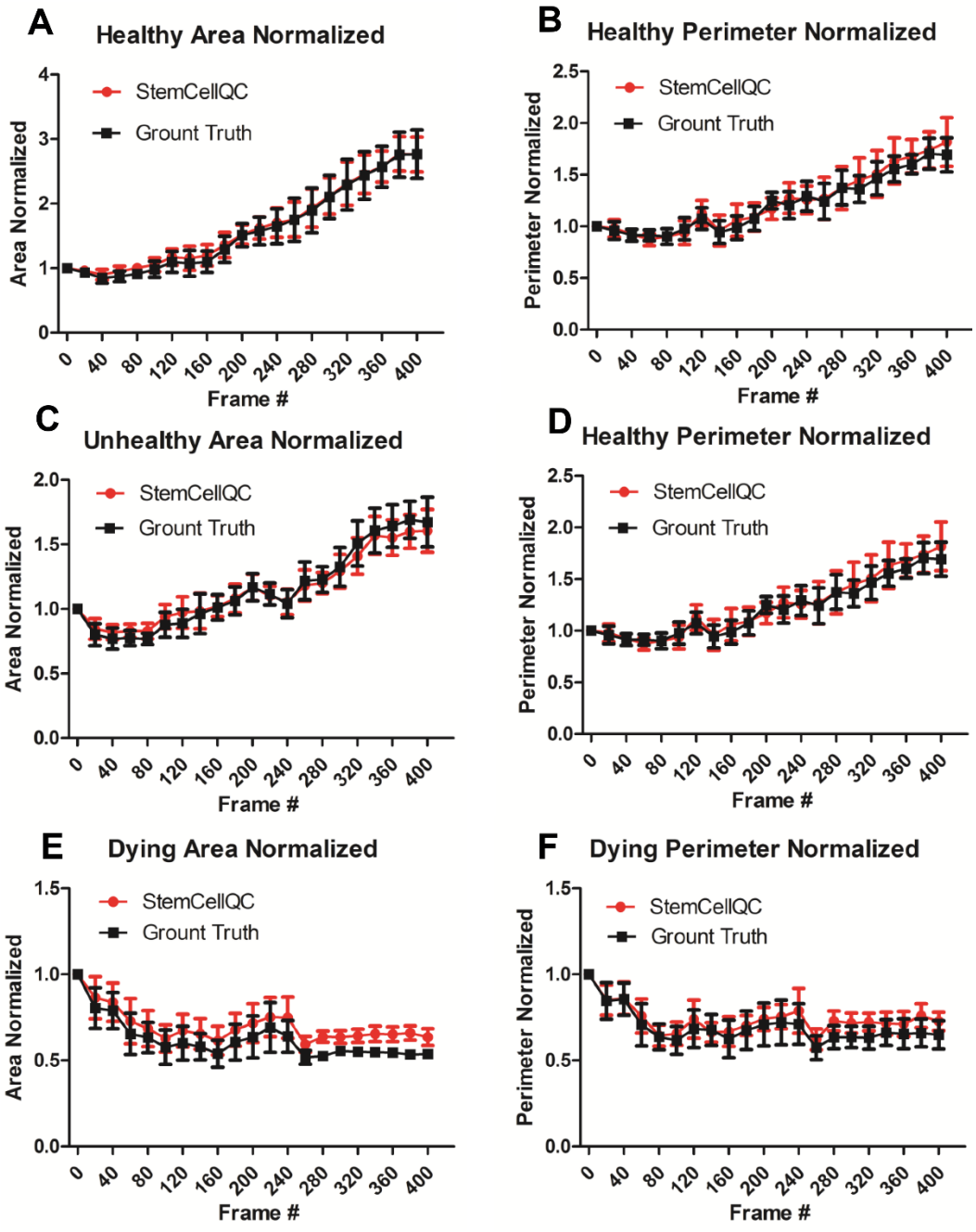

Figure S2.3. Ground truth verification of colony segmentation using ImageJ to manually segment 6 representative healthy, 6 unhealthy, and 6 dying colonies. (A, B) Normalized area and perimeter values for healthy colonies extracted by StemCellQC compared to ground truth using ImageJ. 2-way ANOVA revealed no significant differences. (C, D) Normalized area and perimeter values for unhealthy colonies extracted by StemCellQC compared to ground truth using ImageJ. 2-way ANOVA revealed no significant differences. (E, F) Normalized area and perimeter values for dying colonies extracted by StemCellQC compared to ground truth using ImageJ. 2-way ANOVA revealed no significant differences, except for a portion of the normalized area of dying colonies. This corresponds with slight over-segmentation of software due to detection of cellular debris ejected from dying colonies after their death at 30hours (* = $P < 0.05$).

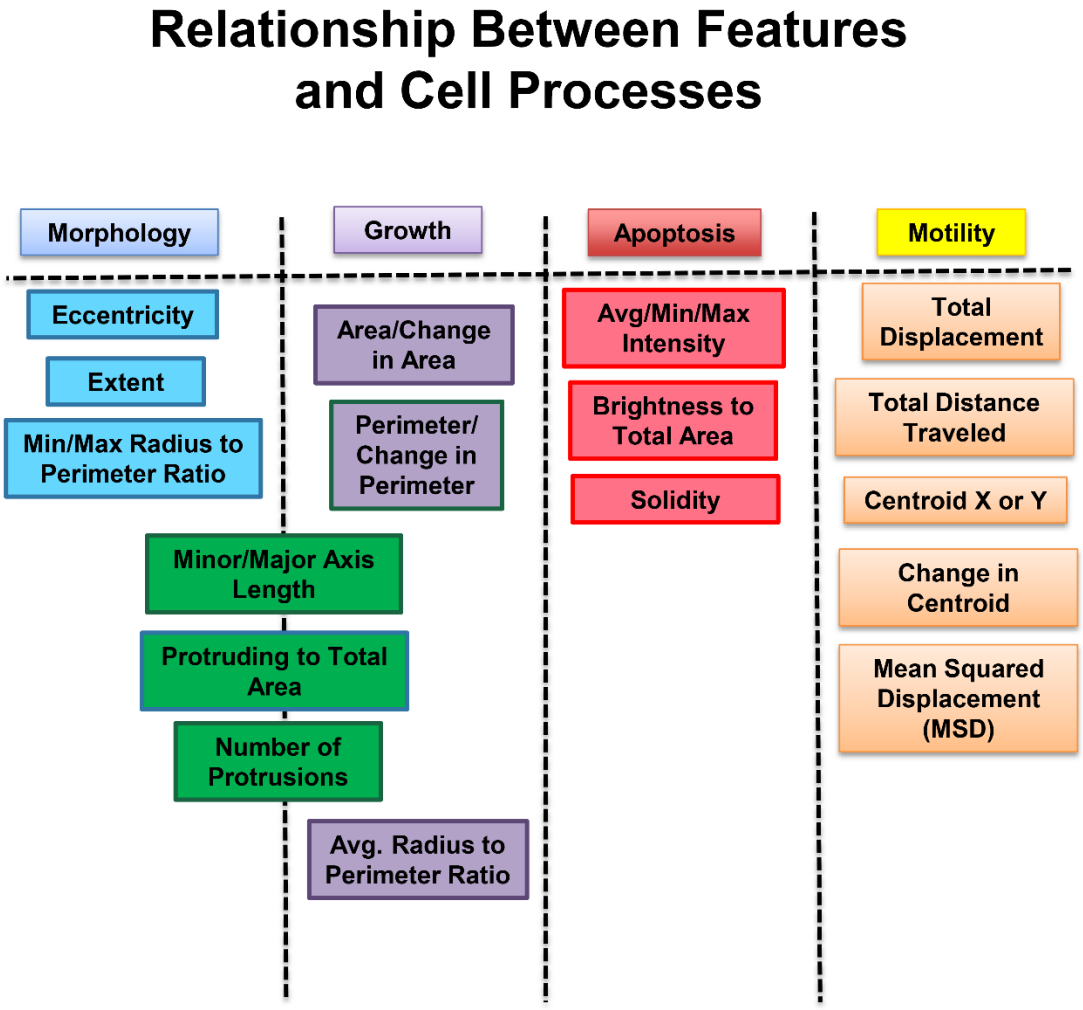

Figure S2.4. Relationship between features and cell processes.

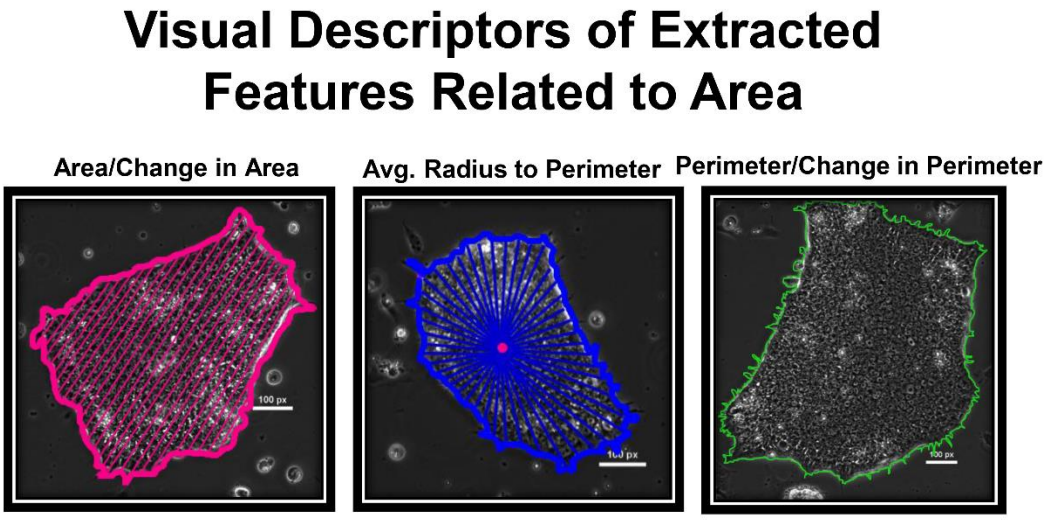

Figure S2.5. Visual descriptors of extracted features related to area.

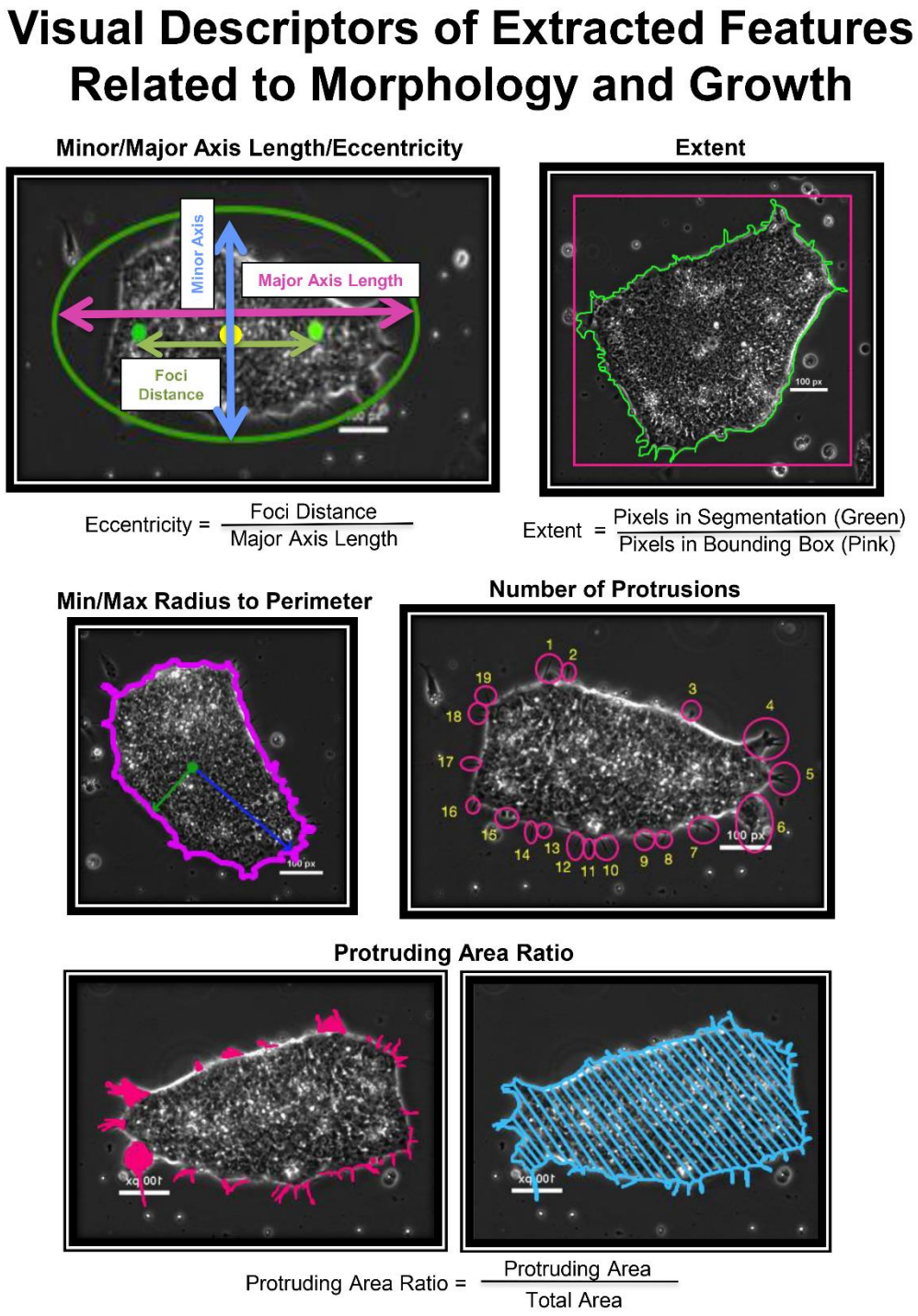

Figure S2.6. Visual descriptors of extracted features related to morphology and area.

Visual Descriptors of Extracted Features Related to Motility

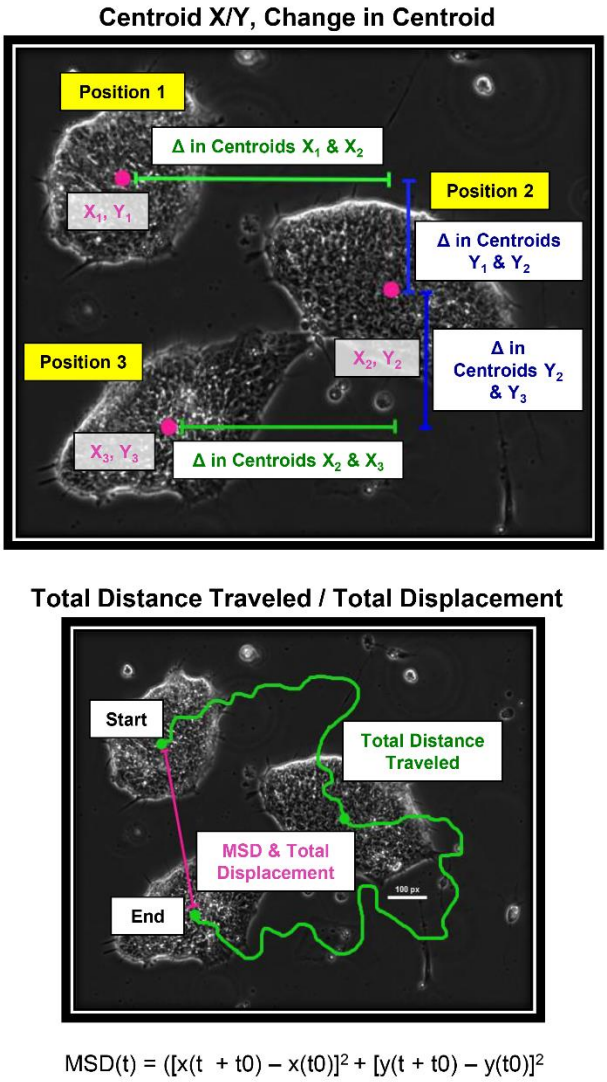

Figure S2.7. Visual descriptors of extracted features related to motility.

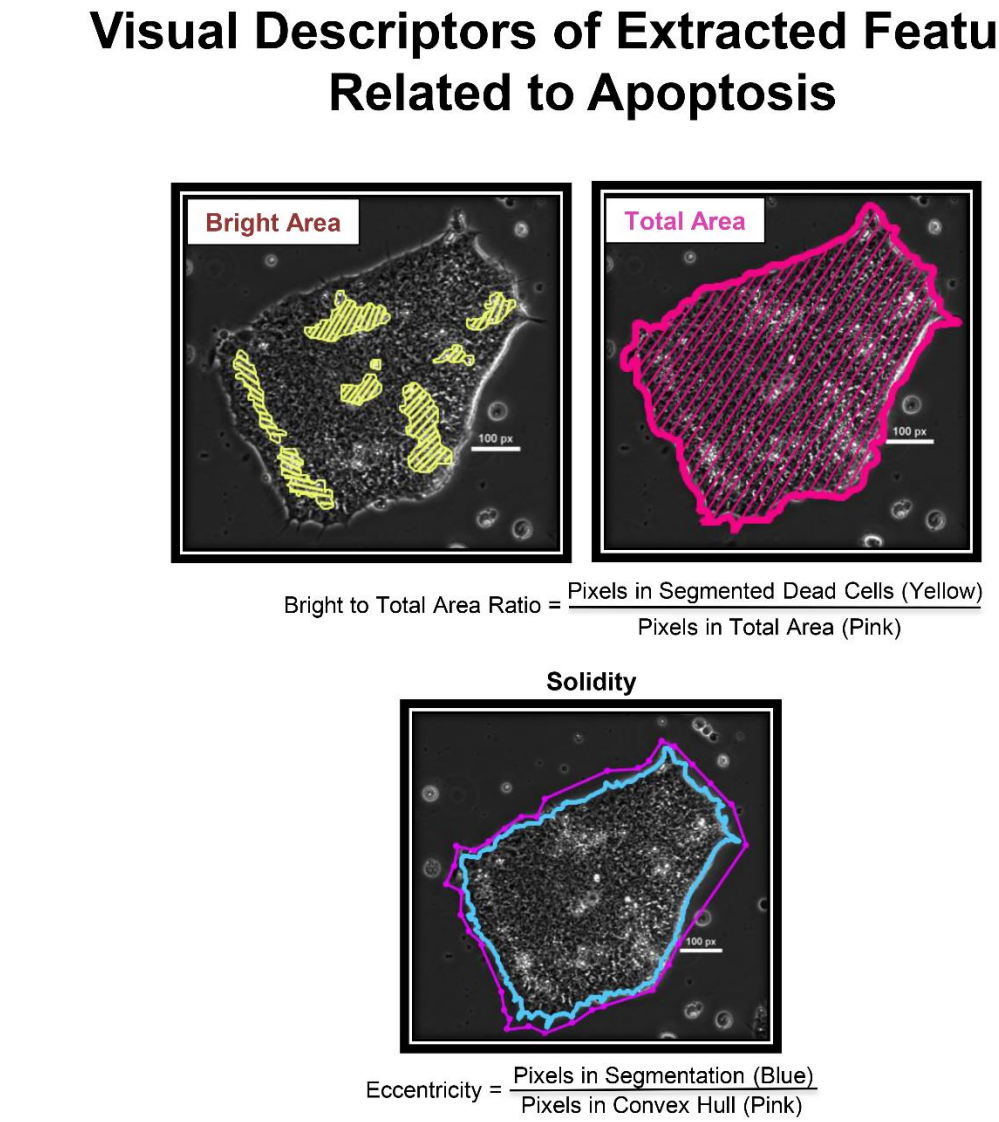

Figure S2.8. Visual descriptors of extracted features related to apoptosis.

List of Extracted Features and Definitions

Features	Description
Appearance Features	
Avg. Intensity	The mean of the intensity values of all pixels in the colony
Max Intensity	The pixel intensity of the brightest pixel in the colony
Min. Intensity	The pixel intensity of the least bright pixel in the colony
Morphological Features	
Area	The number of pixels in the colony.
Perimeter	The number of pixels constituting the boundary of the colony
Centroid	The location representing the geometric center of the colony
Extent	The ratio of the number of pixels in colony over the number of pixels in bounding box of colony
Solidity	The ratio of the number of pixels in colony over the number of pixels in convex hull of colony
Orientation	The angle between the x-axis and the major axis of the fitted ellipse which has the same second-moments as the colony
Major Axis	The length of the major axis of the fitted ellipse
Minor Axis	The length of the minor axis of the fitted ellipse
Eccentricity	The ratio of distance between the foci of the fitted ellipse and the length of it major axis (value between 0 and 1 with values closer to 0 being more circular
Min. Radius	The distance between the centroid and the closest perimeter pixel
Max. Radius	The distance between the centroid and the farthest perimeter pixel
Avg. Radius	The mean distance between the centroid and each perimeter pixel
Bright-to-Total Area Ratio	The ratio of the bright areas in the colony to the total area of the colony, it is found by further segmenting the colony with Otsu's method
Number of Protrusions	The number of regions in colony that protrude from the main body (specified by morphological operations) of the colony
Ratio of Protrusion Area	The ratio of the area consisting of the protrusions over the total area
Dynamic Features	
Change in Area	The difference in area between each successive frame
Change in Perimeter	The difference in perimeter between each successive frame
Change in Centroid	The pairwise difference in centroid between each successive frame
Mean Squared Displacement (MSD)	The squared displacement of the centroid from its initial position
Total Distance Traveled	The sum of all change in centroid values until current time point
Total Displacement	The pairwise difference between current centroid and initial centroid

Figure S2.9. List of Extracted Features and Definitions.

Video S2.1. Average intensity versus perimeter running plot shown for all individual healthy (green), unhealthy (blue), and dying (red) hESC colonies.
https://doi.org/10.1371/journal.pone.0148642.s010

Video S2.2. Mean-squared displacement versus area running plot shown for all individual healthy (green), unhealthy (blue), and dying (red) hESC colonies.
https://doi.org/10.1371/journal.pone.0148642.s011

Video S2.3. Phase contrast video of a representative healthy colony with the segmentation outlined in white.
https://doi.org/10.1371/journal.pone.0148642.s012

Video S2.4. Protrusions feature video of a representative healthy colony with the protrusions outlined in red.
https://doi.org/10.1371/journal.pone.0148642.s013

Video S2.5. Bright-to-total area ratio feature video with the bright dead cells of a representative unhealthy colony highlighted in white.
https://doi.org/10.1371/journal.pone.0148642.s014

Video S2.6. Solidity feature video of a representative dying colony with the convex hull shown in white and the colony segmentation outlined in red.
https://doi.org/10.1371/journal.pone.0148642.s015

REFERENCES

[1] V. Tabar, L. Studer, Pluripotent stem cells in regenerative medicine: challenges and recent progress., Nat. Rev. Genet. 15 (2014) 82–92.

[2] P. Talbot, S. Lin, Mouse and human embryonic stem cells: can they improve human health by preventing disease?, Curr. Top. Med. Chem. 11 (2011) 1638–1652.

[3] Z. Zhu, D. Huangfu, Human pluripotent stem cells: an emerging model in developmental biology., Development. 140 (2013) 705–17.

[4] K.G. Chen, B.S. Mallon, R.D.G. McKay, P.G. Robey, Human pluripotent stem cell culture: considerations for maintenance, expansion, and therapeutics., Cell Stem Cell. 14 (2014) 13–26.

[5] S.P. Sheehy, F. Pasqualini, A. Grosberg, S.J. Park, Y. Aratyn-Schaus, K.K. Parker, Quality metrics for stem cell-derived cardiac myocytes., Stem Cell Reports. 2 (2014) 282–94.

[6] S. Lin, S. Fonteno, S. Satish, B. Bhanu, P. Talbot, Video bioinformatics analysis of human embryonic stem cell colony growth., J. Vis. Exp. (2010) 11330.

[7] S. Lin, S. Fonteno, J.-H. Weng, P. Talbot, Comparison of the toxicity of smoke from conventional and harm reduction cigarettes using human embryonic stem cells., Toxicol. Sci. 118 (2010) 202–12.

[8] B.X. Guan, B. Bhanu, P. Talbot, S. Lin, Automated Human Embryonic Stem Cell Detection, 2012 IEEE Second Int. Conf. Healthc. Informatics, Imaging Syst. Biol. (2012) 75–82.

[9] B.X. Guan, B. Bhanu, N. Thakoor, P. Talbot, S. Lin, Human Embryonic Stem Cell Detection by Spatial Information and Mixture of Gaussians, 2011 IEEE First Int. Conf. Healthc. Informatics, Imaging Syst. Biol. (2011) 307–314.

[10] B. Guan, B. Bhanu, P. Talbot, S. Lin, AUTOMATIC CELL REGION DETECTION BY K-MEANS WITH WEIGHTED ENTROPY Benjamin X . Guan , Bir Bhanu , Ninad S . Thakoor Center for Research in Intelligent Systems University of California , Riverside University of California , Riverside, 2013 IEEE Int. Symp. Biomed. Imaging. (2013) 418–421.

[11] B. Guan, B. Bhanu, P. Talbot, S. Lin, Bio-Driven Cell Region Detection in Human Embryonic Stem Cell Assay, IEEE/ACM Trans. Comput. Biol. Bioinforma. (2014) 1–1.

[12] P. Talbot, N.I. Nieden, S. Lin, I. Martinez, B. Guan, B. Bhanu, Use of Video Bioinformatics Tools in Stem Cell Toxicology, in: Handb. Nanotoxicology, Nanomedicine Stem Cell Use Toxicol., 2014: pp. 379–402.

[13] The UC Riverside NSF Integrated Graduate Education Research and Training (IGERT) Program on Video Bioinformatics, (n.d.). http://www.cris.ucr.edu/IGERT/index.php (accessed March 16, 2015).

[14] K. Tokunaga, N. Saitoh, I.G. Goldberg, C. Sakamoto, Y. Yasuda, Y. Yoshida, S. Yamanaka, M. Nakao, Computational image analysis of colony and nuclear morphology to evaluate human induced pluripotent stem cells, Sci. Rep. 4 (2014) 6996.

[15] C.M. Megyola, Y. Gao, A.M. Teixeira, J. Cheng, K. Heydari, E.C. Cheng, T. Nottoli, D.S. Krause, J. Lu, S. Guo, Dynamic migration and cell-cell interactions of early reprogramming revealed by high-resolution time-lapse imaging, Stem Cells. 31 (2013) 895–905.

[16] C.C. Wong, K.E. Loewke, N.L. Bossert, B. Behr, C.J. De Jonge, T.M. Baer, R. a Reijo Pera, Non-invasive imaging of human embryos before embryonic genome activation predicts development to the blastocyst stage., Nat. Biotechnol. 28 (2010) 1115–1121.

[17] M. Winter, E. Wait, B. Roysam, S.K. Goderie, R.A.N. Ali, E. Kokovay, S. Temple, A.R. Cohen, Vertebrate neural stem cell segmentation, tracking and lineaging with validation and editing., Nat. Protoc. 6 (2011) 1942–52.

[18] S. V Alworth, H. Watanabe, J.S.J. Lee, Teachable, high-content analytics for live-cell, phase contrast movies., J. Biomol. Screen. 15 (2010) 968–77.

[19] J. Nichols, A. Smith, Pluripotency in the Embryo and in Culture, Cold Spring Harb. Perspect. Biol. 4 (2012) a008128–a008128.

[20] S. Lin, P. Talbot, Methods for culturing mouse and human embryonic stem cells., Methods Mol. Biol. 690 (2011) 31–56.

[21] S. Lin, V. Tran, P. Talbot, Comparison of toxicity of smoke from traditional and harm-reduction cigarettes using mouse embryonic stem cells as a novel model for preimplantation development., Hum. Reprod. 24 (2009) 386–97.

[22] M. Knoll, R. Shaoulian, T. Magers, P. Talbot, Ciliary beat frequency of hamster oviducts is decreased in vitro by exposure to solutions of mainstream and sidestream cigarette smoke., Biol. Reprod. 53 (1995) 29–37.

[23] M. Knoll, P. Talbot, Cigarette smoke inhibits oocyte cumulus complex pick-up by oviduct in vitro independent ciliary beat frequency, Reprod. Toxicol. 12 (1998) 57–68.

[24] Detecting a Cell Using Image Segmentation, (n.d.).

[25] N. Otsu, A Threshold Selection Method from Gray-Level Histograms, 20 (1979) 62–66.

[26] L. Shapiro, G. Stockman, Computer Vision, 2001.

[27] M. de Berg, M. van Krefeld, M. Overmars, O. Schwarzkopf, Computational Geometry: Algorithms and Applications, Springer, 2000.

[28] Z. Zhao, F. Morstatter, S. Sharma, S. Alelyani, A. Anand, H. Liu, Advancing Feature Selection Research, ASU Featur. Sel. Repos. Arizona State Univ. (2010) 1–28.

[29] N.X. Vinh, J. Chan, S. Romano, J. Bailey, Effective Global Approaches for Mutual Information Based Feature Selection, Proc. 20th ACM SIGKDD Int. Conf. Knowl. Discov. Data Min. (2014) 512–521.

[30] M. Hall, L. a Smith, Feature Selection for Machine Learning : Comparing a Correlation-based Filter Approach to the Wrapper CFS : Correlation-based Feature, Int. FLAIRS Conf. (1999) 5.

[31] H. Liu, R. Setiono, Chi2: Feature Selection and Discretizatino of Numeric Attributes, Proc. 7th IEEE Int. Conf. Tools with Artif. Intell. (1995).

[32] M.L. Bermingham, R. Pong-Wong, a Spiliopoulou, C. Hayward, I. Rudan, H. Campbell, a F. Wright, J.F. Wilson, F. Agakov, P. Navarro, C.S. Haley, Application of high-dimensional feature selection: evaluation for genomic prediction in man., Sci. Rep. 5 (2015) 10312.

[33] R.O. Duda, P.E. Hart, D.G. Stork, Pattern Classification, 2000.

[34] C. Gini, Variabilite e mutabilita, Rome Libr. Eredi Virgilio Veschi. (1912).

[35] T.M. Cover, J.A. Thomas, Elements of information theory, Wiley-Interscience, New York, NY, 1991.

[36] G. Cawley, N. Talbot, M. Girolami, Sparse multinomial logistic regression via bayesian l1 regularisation, Adv. Neural Inf. Process. Syst. 19 (2007) 209.

[37] D.C. Montgomery, G.C. Runger, N.F. Hubele, Engineering Statistics, John Wiley, New York, NY, 2001.

[38] L. Wei, Asymptotic Conservativeness and Efficiency of Kruskal-Wallis Test for K Dependent Samples, J. Am. Stat. Assoc. 76 (1981) 1006–1009.

[39] H.C. Peng, F.H. Long, C. Ding, Feature selection based on mutual information: Criteria of max-dependency, max-relevance, and min-redundancy, IEEE Trans. Pattern Anal. Mach. Intell. 27 (2005) 1226–1238.

[40] X. Wang, W. Song, N. Kawazoe, G. Chen, Influence of cell protrusion and spreading on adipogenic differentiation of mesenchymal stem cells on micropatterned surfaces, Soft Matter. 9 (2013) 4160.

[41] R. McBeath, D.M. Pirone, C.M. Nelson, K. Bhadriraju, C.S. Chen, Cell shape, cytoskeletal tension, and RhoA regulate stem cell lineage commitment, Dev. Cell. 6 (2004) 483–95.

[42] G.E. Uhlenbeck, L.S. Ornstein, On the theory of the Brownian motion, Phys. Rev. 36 (1930) 823–841.

[43] P. Dieterich, R. Klages, R. Preuss, A. Schwab, Anomalous dynamics of cell migration., Proc. Natl. Acad. Sci. U. S. A. 105 (2008) 459–63.

[44] C. Huang, Z. Rajfur, C. Borchers, M. Schaller, K. Jacobson, JNK phosphorylates paxillin and regulates cell migration, Nature. 6526 (2003) 219–223.

[45] B.S. Fogh, H. a B. Multhaupt, J.R. Couchman, Protein kinase C, focal adhesions and the regulation of cell migration., J. Histochem. Cytochem. 62 (2014) 172–84.

[46] H. Ke, J.Y. Zhang, S.K. Akiyama, J.E. French, BCL2 interaction with actin in vitro may inhibit cell motility by enhancing actin polymerization, Cell Adh. Migr. 5 (2011) 6–10.

[47] I. Barbaric, V. Biga, P.J. Gokhale, M. Jones, D. Stavish, A. Glen, D. Coca, P.W. Andrews, Time-Lapse Analysis of Human Embryonic Stem Cells Reveals Multiple Bottlenecks Restricting Colony Formation and Their Relief upon Culture Adaptation, Stem Cell Reports. 3 (2014) 1–14.

[48] C.K. Bradley, H.A. Scott, O. Chami, T.T. Peura, B. Dumevska, U. Schmidt, T. Stojanov, Derivation of Huntington's disease-affected human embryonic stem cell lines., Stem Cells Dev. 20 (2011) 495–502.

[49] J.D. Miller, Y.M. Ganat, S. Kishinevsky, R.L. Bowman, B. Liu, E.Y. Tu, P.K. Mandal, E. Vera, J.W. Shim, S. Kriks, T. Taldone, N. Fusaki, M.J. Tomishima, D. Krainc, T.A. Milner, D.J. Rossi, L. Studer, Human iPSC-based modeling of late-onset disease via progerin-induced aging, Cell Stem Cell. 13 (2013) 691–705.

[50] P. Grandjean, D. Bellinger, A. Bergman, S. Cordier, G. Davey-Smith, B. Eskenazi, D. Gee, K. Gray, M. Hanson, P. van den Hazel, J.J. Heindel, B. Heinzow, I. Hertz-Picciotto, H. Hu, T.T.-K. Huang, T.K. Jensen, P.J. Landrigan, I.C. McMillen, K. Murata, B. Ritz, G. Schoeters, N.E. Skakkebaek, S. Skerfving, P. Weihe, The faroes statement: human health effects of developmental exposure to chemicals in our environment, Basic Clin. Pharmacol. Toxicol. 102 (2008) 73–5.

Chapter 3

Deep Analysis of Mitochondria and Cell Health Using Machine Learning

ABSTRACT

There is a critical need for better analytical methods to study mitochondria in normal and diseased states. Mitochondrial image analysis is typically done on still images using slow manual methods or automated methods of limited types of features. MitoMo integrated software overcomes these bottlenecks by automating rapid unbiased quantitative analysis of mitochondrial morphology, texture, motion, and morphogenesis and advances machine-learning classification to predict cell health by combining features. Our pixel-based approach for motion analysis evaluates the magnitude and direction of motion of: (1) molecules within mitochondria, (2) individual mitochondria, and (3) distinct morphological classes of mitochondria. MitoMo allows analysis of mitochondrial morphogenesis in time-lapse videos to study early progression of cellular stress. Biological applications are presented including: (1) establishing normal phenotypes of mitochondria in different cell types; (2) quantifying stress-induced mitochondrial hyperfusion in cells treated with an environmental toxicant, (3) tracking morphogenesis in mitochondria undergoing swelling, and (4) evaluating early changes in cell health when morphological abnormalities are not apparent. MitoMo unlocks new information on mitochondrial phenotypes and dynamics by enabling deep analysis of mitochondrial features in any cell type and can be applied to a broad spectrum of research problems in cell biology, drug testing, toxicology, and medicine.

INTRODUCTION

Mitochondria are dynamic organelles capable of regulating cell fate, homeostasis, survival, and disease in eukaryotic cells [1-3]. Mitochondrial phenotypes (morphology, dynamics, and

organizational patterns) vary significantly in different cell types. During fusion and fission [4], mitochondria transition between morphological classes that include small puncta, tubes, networks, and "donuts" or rings [5, 6]. These morphologies are related to the metabolic state and bioenergetics of the cell and vary during processes such as cell division and differentiation [3,7]. Mitochondria have an intrinsic ability to sense their state of health, and when stressed, induce compensatory quality-control mechanisms, such as stress-induced mitochondrial hyperfusion (SIMH) or fission and degradation of damaged mitochondria (mitophagy), [6, 8-10] making them excellent organelles for evaluating cell health. Moreover, mitochondrial morphology and dynamics are altered in common neurodegenerative diseases, such as Alzheimer's disease (AD), Parkinson's disease (PD), amyotrophic lateral sclerosis (ALS), and Huntington's disease (HD) [11] and may vary within subclasses of diseases such as cancer, diabetes, myopathies and metabolic diseases [7, 11-14]. For example, changes in mitochondrial morphology, mainly fragmentation, and abnormal dynamics in axonal transport in neurons have been reported in HD patients [11]. In diseases such as cancer, mitochondria phenotypes have been shown to vary between tumors, and used to classify types of cancer [15, 16].

Because of their importance in homeostasis, stress, and human disease, there is need for technologies to analyze and quantify changes in mitochondrial morphology and dynamic behavior. Time-consuming manual protocols [17] are being replaced by software that provides automated analysis of mitochondrial features, making rapid high content analysis feasible. While mitochondrial analysis software is continually evolving, some existing programs have limitations with respect to accessibility. Some require that users know programming languages and have access to commercial image processing software not routinely available in all labs [18, 19]. In this paper, we introduce MitoMo, which is open-source, provides a user-friendly graphical user interface

(GUI) that does not require programming knowledge, can easily be adapted to any laboratory, and is flexible in allowing users to import pre-segmented images from any image processing software.

Because of limitations in existing software, there is an unmet need for software that can perform an integrated multi-feature analysis of morphology, motion, texture, and morphogenesis. While most software provide segmentation, feature extraction, and classification modules, they are limited in their image processing [20, 21] and types of feature analysis [15, 18, 20, 22-26]. Our software provides users with additional pre-processing (histogram matching, tophat) and post-segmentation (declumping, morphological operations) steps, which significantly improve the accuracy of segmentation. Most software use one type of classification algorithm (typically a decision tree type) [18, 21, 26] and are capable of only mitochondrial morphology analysis or cell classification. MitoMo provides users with multiple classification algorithms and performs both morphological and cell health classification. MitoMo can perform on multiple scales, enabling the study of individual mitochondria, patches of mitochondria, or mitochondrial populations in entire cells. It also divides feature data across the morphological classes of mitochondria to investigate the contribution of each class to an experimental stimulus or disease.

Mitochondrial morphology and dynamics are both coupled to mitochondrial function [12, 27], stress [8, 9, 28], and disease [11, 13, 14, 29]. Previous software have studied motion of individual mitochondria, such as their movement toward regions of energy demand [30]. Our novel intensity flow method [31] can study sub-organelle motion, which relates to the flow of molecules within the mitochondria, a type of motion has rarely been studied. Motion analysis was further expanded in MitoMo to include directionality with respect to any cellular structure. This reveals organizational changes of mitochondria inside the cell, which correlate to changes in energy demand or association with other cellular structures (e.g., endoplasmic reticulum, autophagosomes, etc). Lastly unlike other mitochondrial based software, MitoMo can be used to analyze video data,

thereby providing morphological information on mitochondrial morphogenesis during cell differentiation, toxicant treatment, or disease progression.

Our purpose is to introduce MitoMo an open-source, user-friendly software that integrates multiple feature types and goes beyond existing software to enhance mitochondrial analysis and cell health classification. Several applications of the MitoMo are presented to demonstrate its broad potential in cell and medical research, drug development, and toxicology.

RESULTS

MitoMo integrated pipeline:

MitoMo is an automated image/video processing and machine-learning software that is designed to work with fluorescent images. In the MitoMo pipeline (Fig. 3.1), still or time-lapse live- cell videos were collected from three different cell types that were transiently or stably transfected with MitoTimer, a mitochondria-targeted fluorescent reporter that enables quantification of mitochondrial protein oxidation. Any mitochondrial-targeted dye or reporter could be used with MitoMo to quantify functional readouts. Based on user preference, mitochondria can be segmented directly using global or adaptive thresholding and de-clumping procedures in MitoMo, or alternatively, images previously segmented with other software, such as CellProfiler [32], can be imported into the MitoMo graphical user interface (GUI). To train MitoMo for classification of mitochondrial morphology, features (listed in Methods) were extracted from individual punctate, networked, or swollen mitochondria. Segmented mitochondria were then automatically classified using machine-learning K-nearest neighbor (KNN) [33] and Naïve Bayes algorithms [34]. In the computational analysis of motion, the density of fluorescently-tagged mitochondrial proteins was assumed to be proportional to the pixel intensity. By computing the change in intensity between adjacent frames, the flow of fluorescently-tagged mitochondrial proteins can be estimated and

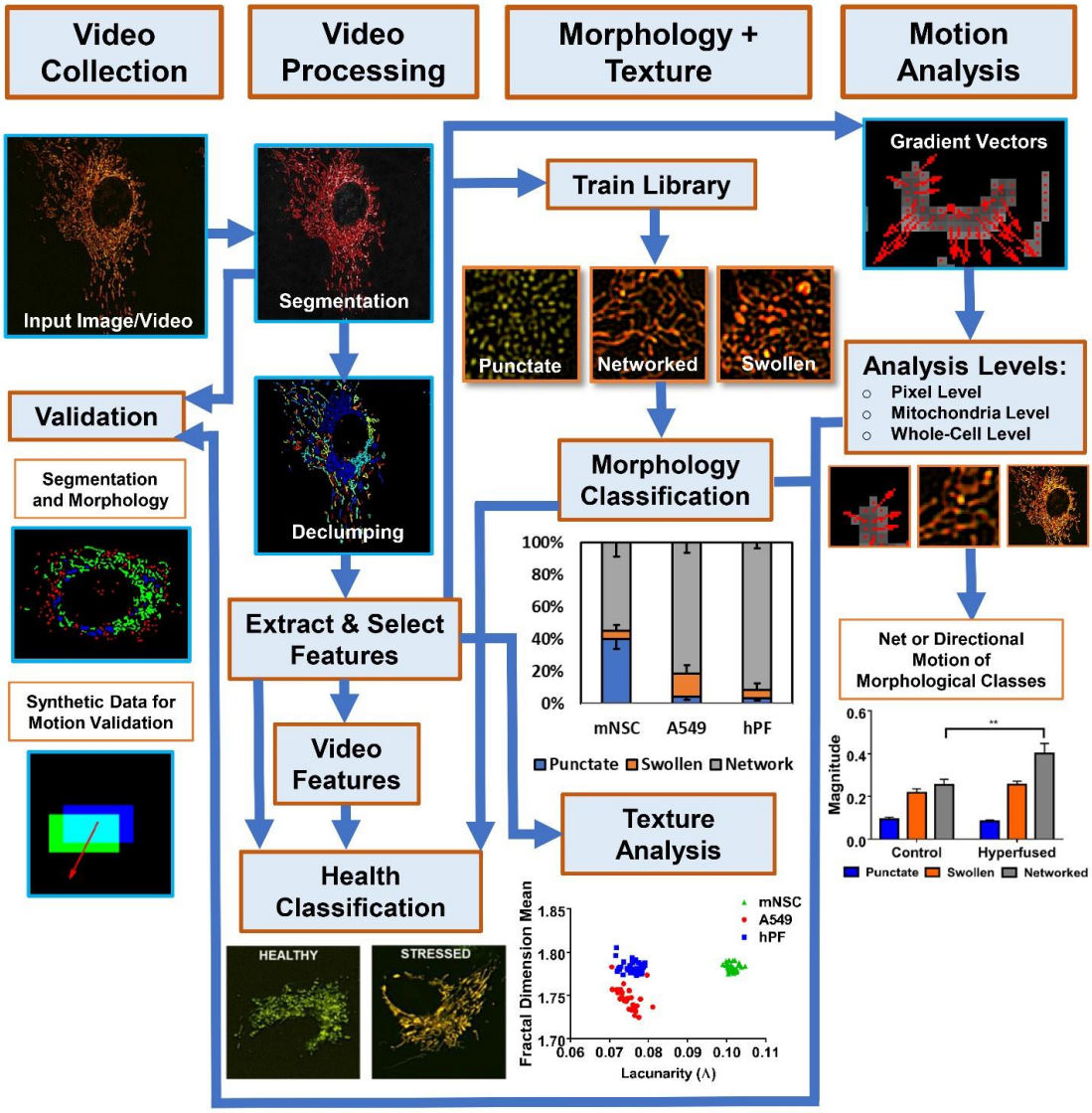

Figure 3.1. Overview of MitoMo software pipeline. Video frames of labeled mitochondria were captured and loaded into the MitoMo software. The videos were segmented and declumped, and 21 morphological, intensity, texture, and motion features were extracted for each frame. The selected features were then fed into a previously trained library of the three mitochondrial morphologies (punctate, networked, and swollen). The segmented mitochondria from the test videos (frames) were automatically morphologically classified using K-nearest neighbor (KNN) and Naïve Bayes. The resulting data were plotted into graphs, depicting the percentage of punctate, networked, and swollen mitochondria. The software can also perform motion analysis by computing the magnitude and orientation of the gradient vectors, and the net or directional motion can be plotted for the population of mitochondria in each cell. Motion analysis can be performed for the entire mitochondrial population within a cell, individual mitochondria, and/or morphological classes of mitochondria. Texture features, which are indicative of mitochondrial complexity and organization, can be extracted, Validation was performed to ensure accuracy of the segmentation, morphological classification, and motion analysis. Extracted features can be combined to perform health classification during low-level stress that is otherwise not detectable.

summed up at the individual pixel level, mitochondrial level, and whole-cell level. The extracted features are used to generate the motion gradient vectors at each individual pixel, and the net sum of the gradient vectors (magnitude) and their direction (orientation) can be plotted as outputs for the motion analysis. Texture features can also be used to investigate the organizational complexity (dense versus porous phenotype) and compactness of the mitochondria within cells. MitoMo multiplexes extracted features and machine learning methods to allow for high- throughput, unbiased, and time/resource-saving characterization and classification of mitochondrial health in any cell type.

Validation of MitoMo:

Segmentation and morphological classification, as performed by MitoMo, were rigorously validated. To assess accuracy, segmentation was manually drawn using ImageJ (Fig. 3.2A) and compared to segmentation performed by MitoMo (Fig. 3.2B). The percent overlay of the ground-truth segmentation versus the segmentation derived with MitoMo and/or CellProfiler was not statistically different (Fig. 3.2C). Morphological classification ground-truth was compared to the software's automatic classification (2D-E). Classification using eight features (Area, Major Axis, Minor Axis, Solidity, Perimeter, Max Radius, Median Radius, Integrated Intensity) resulted in 88% accuracy with Naïve Bayes and 80% accuracy using KNN with five neighbors on the training set. Classification accuracies were 89% with Naïve Bayes and 91% with KNN on the testing set (Fig. 3.2F).

MitoMo's motion algorithm was validated and compared against optical flow [35], which is a representation of the apparent motion of objects, surfaces, edges, and pixels in an image. Optical flow is commonly used for motion estimation to describe the transformation of one frame to another. In the calculation of optical flow, a major assumption is a brightness constraint that

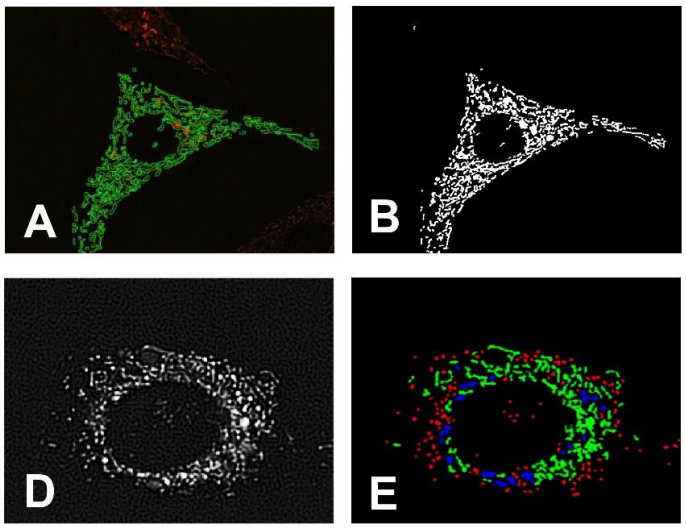

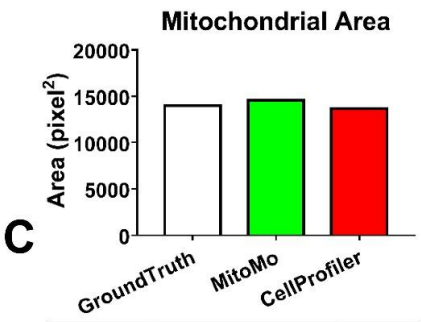

F

	Classification Rate	S.D.
KNN	78%	0.56
Naïve Bayes	88%	0.14

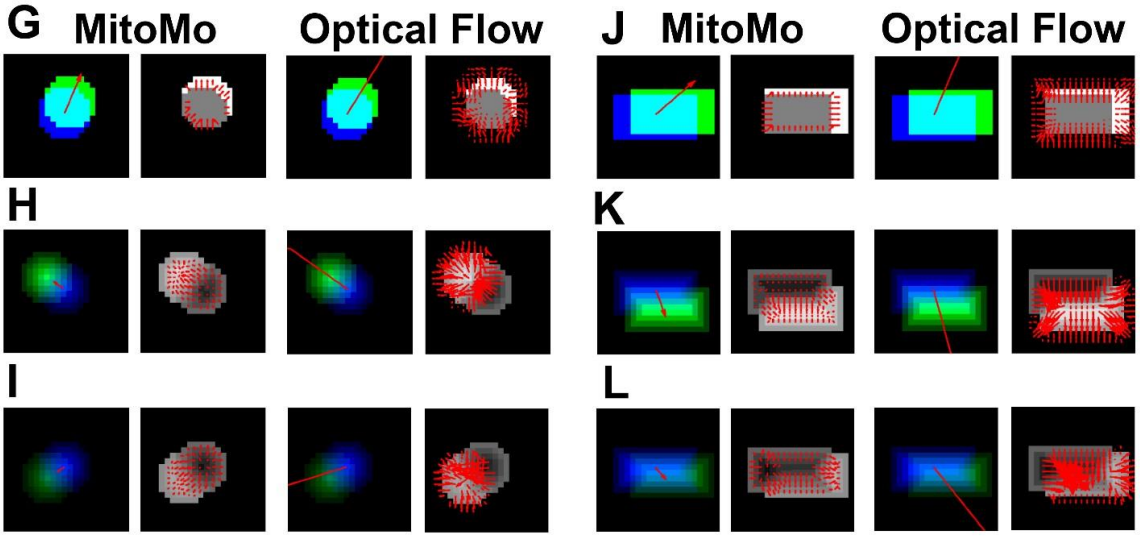

M Shape and Intensity Conditions	MitoMo's Angle Accuracy	Optical Flow's Angle Accuracy	MitoMo's Magnitude Accuracy	Optical Flow's Magnitude Accuracy
G: Solid Dot	100.00	100.00	83.33	74.37
H: Dot with Uneven Intensity	100.00	100.00	83.6	87.13
I: Dot with Uneven and Fading Intensity	100.00	100.00	82.76	42.56
J: Solid Rectangle	83.01	75.47	83.48	79.62
K: Rectangle with Uneven Intensity	82.83	100.00	82.86	91.21
L: Rectangle with Uneven and Fading Intensity	100.00	82.84	83.37	28.64

Figure 3.2. MitoMo validation and comparison of our motion analysis to optical flow. Segmentation validation: (A) Manually drawn segmentation (green) using ImageJ was compared to (B) segmentation performed by MitoMo. (C) The segmentation accuracy (area of overlaps) of the manually labeled versus automatically segmented mitochondria (MitoMo and CellProfiler) were not significantly different using one-way ANOVA with Dunnett's post hoc test. (D-E) The morphological classification was validated by comparing manually labeled mitochondria (D) against automatic classification (E). (F) There was up to 88% accuracy with Naïve Bayes and 80% accuracy with KNN in the automatic classification of mitochondrial morphology in 1761 trials using the training data. There was up to 89% accuracy with Naïve Bayes and 91% with KNN in the automatic classification of the test set. (G-L) Images showing motion analysis validation for both magnitude (blue, green cyan images) and direction (images with red arrows). Each magnitude image is a synthetic image of unique shape and change in intensity overlaid with a motion vector. Blue is object from frame 1, green is object from frame 2, and cyan is overlap of the two frames. Column 1 in Figures G-L shows summed MitoMo vector (indicated by arrow) overlaid onto color coded image. Column 2 is the normalized difference image with MitoMo motion vectors. Column 3 shows the summed Lucas-Kanade vector (indicated by arrow) overlaid onto the color-coded images. Column 4 is the normalized difference image with Lucas-Kanade motion vectors. (G) Solid dot with no change in intensity. (H) Dot with uneven intensity. (I) Disc with uneven intensity that fades to half the brightness by the second frame. (J) Solid rectangle with no change in intensity. (K) Rectangle with uneven intensity. (L) Rectangle with uneven intensity that fades to half the brightness by the second frame. (M) Table summarizes the accuracy of angle and magnitude for MitoMo versus optical flow. The angle and magnitude accuracies were statistically compared using t-test and Chi-squared tests, and the more accurate software was highlighted in yellow.

requires the appearance or brightness pattern of an object to be constant over a delta change in time [36]. MitoMo does not have this constraint because it estimates the change of intensity between frames and not the motion of specific pixels. To validate our motion analysis, synthetic motion data of various shapes were generated (Figs. 3.2G-L). For both methods, all generated vectors are summed to produce a single vector estimating the motion of the object. In the table in Fig 3.2M, MitoMo had angle accuracies ranging from 83 to 100% and magnitude accuracies ranging from 82 to 83%. MitoMo's angle and magnitude estimation performed as well or better than the Lucas-Kanade optical flow method in all cases except the uneven intensities, which better satisfy the brightness assumptions of optical flow. Two-tailed t-tests and Chi-squared tests (in cases with no variance) were performed for each comparison, revealing statistically significant improvements in accuracy with MitoMo's motion analysis in most cases (Fig 3.2M). Further details are provided in the Supplementary Data #2.

Establishing baseline phenotypes of mitochondria in healthy cells

We define phenotype to incorporate mitochondrial morphology, motion, texture, and morphogenesis. The phenotype and number of mitochondria in a cell depends on the metabolic requirements of the cell, and number may vary from one to thousands across different cell types [7]. MitoMo was first used to establish the mitochondrial phenotypes in three healthy cell types from two species: mouse neural stem cells (NSC), human lung cancer cells (A549), and human primary lung fibroblasts (hPFs) (Figs. 3.3A-C). The cells were transfected with the MitoTimer reporter and imaged live 24 hours later. While all cell types had punctate, networked, and swollen mitochondria, the percentages of each class of mitochondrion were significantly different in each cell type (Figs. 3.3D and 3.3E). Figure 3.3E summarizes the p-values for each of the morphological

groups compared across the different cell types using a 1-way ANOVA followed by Tukey's post hoc test.

The magnitude of motion of all the mitochondria in the three cell types was calculated (Fig. 3.3F) and compared statistically across cell types using a 2-way ANOVA with Tukey's multiple comparisons test. Motion in the A549 cells and hPFs, which had mainly networked mitochondria, was similar, while the punctate mitochondria in the NSCs had significantly elevated motion. The increase in motion in these healthy NSCs is directly correlated with mitochondrial morphology.

To further assess the organization of mitochondria in different cell types, texture features were analyzed. The mean fractal dimension was computed to measure the level of mitochondrial complexity at the whole-cell level (Fig. 3.3G), using a 1-way ANOVA with Bonferroni's post hoc test. In NSCs, the small punctate mitochondria are slightly variable in shape and not evenly spaced, which increased complexity and resulted in a higher fractal dimension. Similar to NSCs, the fractal dimension was also high in hPFs, since the highly meshed networks create a higher level of complexity. In contrast, the mesh-work of mitochondria in A549 was more uniformly spaced, resulting in the lowest mean fractal dimension value.

Another texture feature, lacunarity, was compared across the three cell types using a 1-way ANOVA with Bonferroni's post hoc test (Fig. 3.3H). Patterns having more or larger gaps or more heterogeneity generally have high lacunarity. This analysis showed significantly higher lacunarity in mNSC than in the other two cell types. Fractal dimension mean versus lacunarity values were plotted for all cell types, revealing distinct, well-separated clusters between the three cell types (Fig. 3.3I). This shows that texture features are another excellent means of phenotyping mitochondria in different cell types and by extension in different experimental conditions.

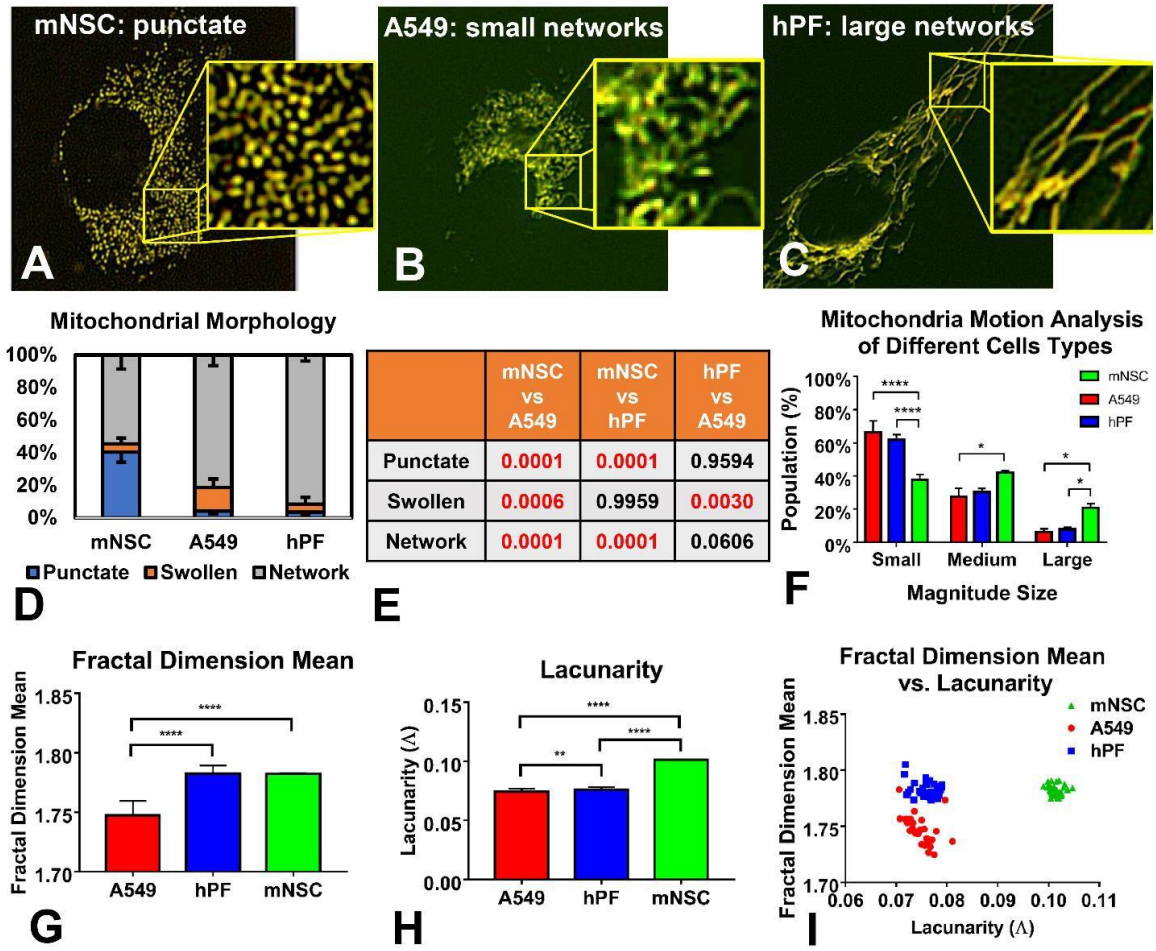

Figure 3.3. Analysis of mitochondrial phenotype (morphology and texture) in three cell types. (A-C) Mitochondrial morphology in NSC, human A549 lung epithelial cells, and hPFs during normal culture conditions. (D) A549 and hPF cells had significantly more networked mitochondria than the NSCs. (E) The table summarizes the p-values for each of the morphological groups compared across the different cell types in Fig D (1-way ANOVA with Tukey's multiple comparisons test). (F) Total motion analysis showed a significant increase in mitochondrial motion in the NSC compared to the other two cell types, which had similar motion profiles (2-way ANOVA with Tukey's multiple comparisons test). (G) Mean fractal dimension analysis showed a lower complexity level in the A549 mitochondria. (H) Lacunarity analysis showed a denser mitochondrial organization in the NSCs, which contain a high number of punctate mitochondria. Texture data were analyzed using a 1-way ANOVA with Bonferroni's multiple comparisons test. (I) Fractal dimension mean plotted versus lacunarity for the three cell types showed three distinct clusters.

MitoMo detects both directional motion and changes in direction

MitoMo has the ability to compute directional motility, in which a reference point, such as the nucleus is chosen, and changes in direction are obtained. To demonstrate the ability of MitoMo to detect motion features, NSC were treated with nocodazole and cytochalasin D to disrupt the microtubules and actin cytoskeleton, respectively, and 10 second live videos were collected (Figs. 3.4A-B). Motion analysis of the entire mitochondrial population was conducted before treatment and 4 and 5 min after treatment. The directional component of the motion away or towards the nucleus was plotted over time (video frames) revealing fluctuating localized motion in the control videos (before treatment) and arrested movement 4 and 5 min after treatment (Fig. 3.4C). The net sum of motion over all frames when quantified showed a decrease in motion after 4 and 5 min of treatment (Fig. 3.4D).

Morphology and motion analysis following stress-induced mitochondrial hyperfusion (SIMH)

Environmental toxicants can have a negative impact on mitochondria and alter their morphology [37]. To test the ability of MitoMo to detect changes in mitochondrial morphology and motion, NSC were treated with aerosol from an electronic cigarette that caused SIMH (Figs. 3.5A-B). The shift from a punctate to networked morphology was first confirmed using the morphology classifier in MitoMo (Fig. 3.5C). A statistically significant increase in networked mitochondria was detected in the hyperfused group using an unpaired two-tailed t-test. When examined microscopically, the hyperfused mitochondria did not have much motion. However, MitoMo motion analysis of the entire mitochondrial population showed a significant increase in motion in the electronic cigarette-treated, hyperfused mitochondria ($p = 0.0014$ for Chi-squared analysis with a 95% confidence interval) (Fig. 3.5D). This pixel-based analysis method is particularly powerful since it is otherwise

not possible to quantify motion in the hyperfused mitochondria, which are no longer individual trackable objects. When motion was analyzed using unpaired two-tailed t-test at the level of individual mitochondria and then averaged, a significant increase in motion was observed in the hyperfused group (Fig. 3.5E).

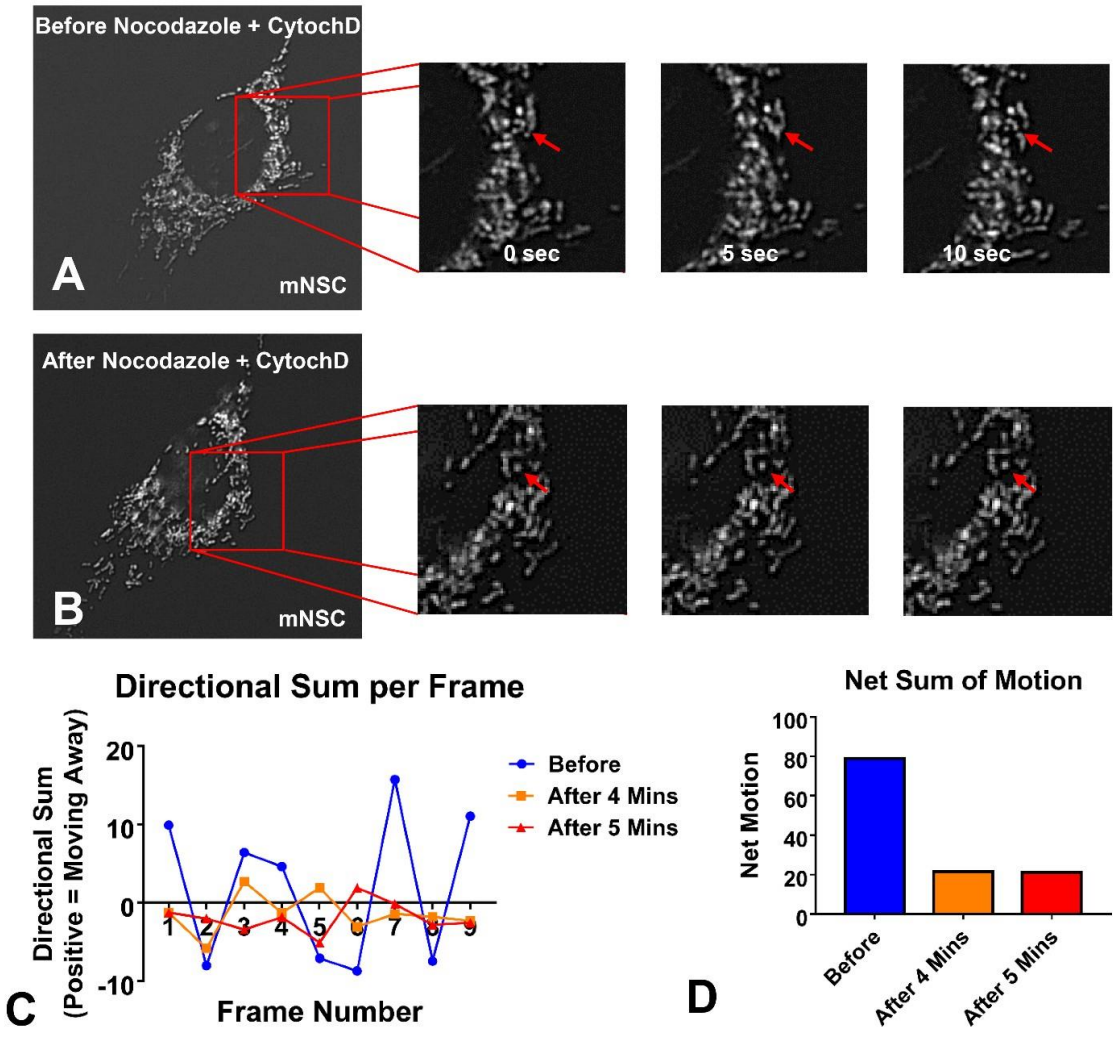

Figure 3.4. Directional motion analysis in living cells. (A-B) Images collected before and 4-5 minutes after the addition of nocodazole and cytochalasin D to destabilize the cytoskeleton. (C) MitoMo computed random localized motion in the control videos before treatment and showed that movement was arrested after treatment. (D) The net sum of motion was quantified over the entire video, showing a decrease in motion after 4 and 5 minutes.

To further isolate the increased motion to the hyperfused class, MitoMo was used to compare motion heterogeneity in morphological classes of mitochondria. The punctate population exhibited the least motion, followed by the swollen, and the networked class (Fig. 3.5F). When analyzed using a 2-way ANOVA with Sidak's multiple comparison test, the magnitude of motion was greater in the networked mitochondria of the hyperfused group than in the untreated control (Fig. 3.5F). This increased movement could be due to the intermixing of mitochondrial membrane proteins, which is consistent with occurrence of SIMH to rescue damaged mitochondria [38].

When the magnitude of motion of the networked subgroups was assessed over time, the hyperfused mitochondria had a consistently higher level of motion than mitochondria in control cells (Fig. 3.5G). To determine how intensity differed across the three morphological classes in the hyperfused condition, the mean standard deviation (S.D.) of the intensity was computed, revealing a statistically significant elevation in fluctuations of the intensity of the swollen mitochondria (Fig. 3.5H). This shows greater variation in sub-organelle intensity within the swollen mitochondria, which may be due to increased structural disorganization allowing greater movement of proteins.

Characterization of the mechanism of selenium-induced mitochondrial swelling

In another toxicological application of MitoMo, we analyzed the effects of selenium, a contaminant in some tobacco products [39, 40], on mitochondrial health. Lung A549 cells were transfected with the MitoTimer reporter (Fig. 3.6A) and treated for 24 hours with 0.01mM or Bonferroni's multiple comparisons test).

0.1mM selenium tetrachloride (SeCl4) (Fig. 3.6B). MitoMo analysis of mitochondrial morphology showed a significant increase in the swollen phenotype (Fig. 3.6C) at the 0.1 mM concentration, and a significant dose-dependent increase in the oxidation of mitochondrial proteins (Fig. 3.6D) (both statistical analyses were done using a 1-way ANOVA with Dunnett's post hoc

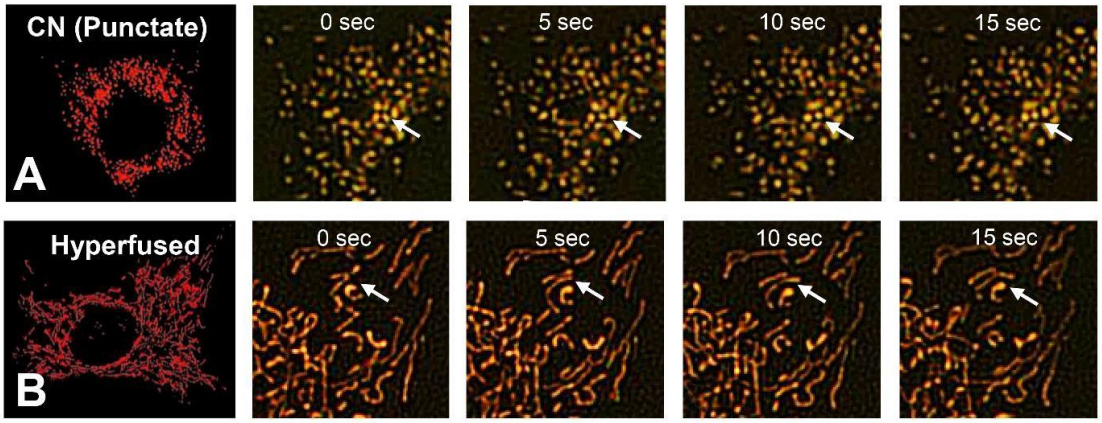
CN (Punctate)
0 sec
5 sec
10 sec
15 sec
A
Hyperfused
0 sec
5 sec
10 sec
15 sec
B

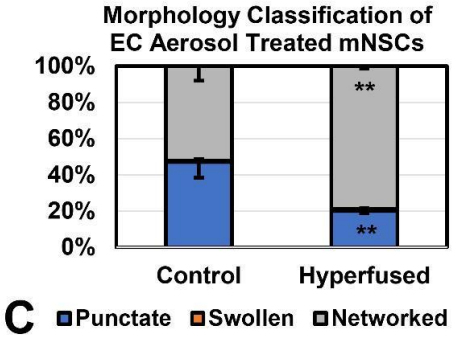
Morphology Classification of
EC Aerosol Treated mNSCs
100%
80%
60%
40%
20%
0%
**
**
Control
Hyperfused
C
Punctate
Swollen
Networked

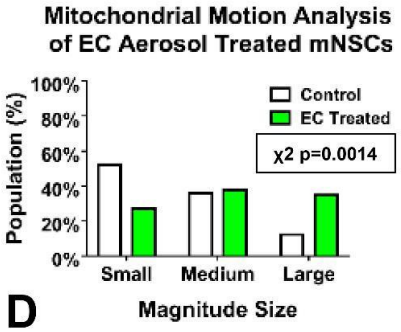
Mitochondrial Motion Analysis
of EC Aerosol Treated mNSCs
Population (%)
100%
80%
60%
40%
20%
0%
Control
EC Treated
χ2 p=0.0014
Small
Medium
Large
Magnitude Size
D

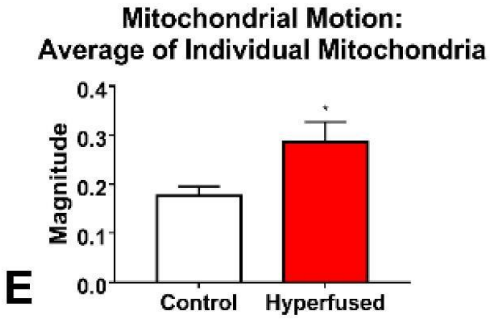
Mitochondrial Motion:
Average of Individual Mitochondria
Magnitude
0.4
0.3
0.2
0.1
0.0
*
Control
Hyperfused
E

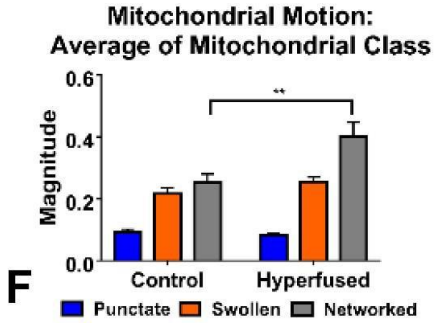
Mitochondrial Motion:
Average of Mitochondrial Class
Magnitude
0.6
0.4
0.2
0.0
**
Control
Hyperfused
F
Punctate
Swollen
Networked

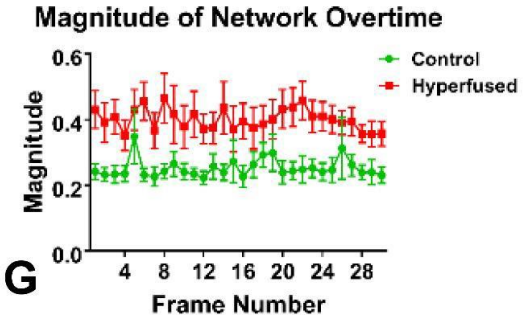
Magnitude of Network Overtime
Control
Hyperfused
Magnitude
0.6
0.4
0.2
0.0
4
8
12
16
20
24
28
Frame Number
G

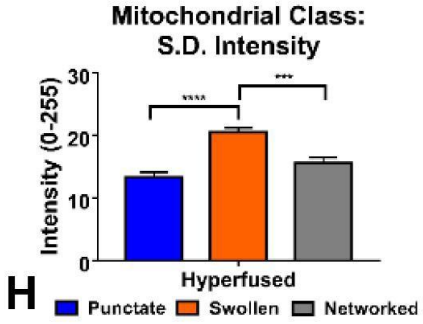
Mitochondrial Class:
S.D. Intensity
Intensity (0-255)
30
20
10
0
****
***
Hyperfused
H
Punctate
Swollen
Networked

Figure 3.5. Analysis of stress-induced mitochondrial hyperfusion (SIMH) in NSCs. (A-B) Control NSC had primarily punctate mitochondria, whereas NSC treated with a tobacco product aerosol exhibited SIMH. Consecutive frames taken over 15 seconds show an enlarged section of live cells over time; arrows show examples of localized motion in the control and the translocation of hyperfused mitochondria. (C) Morphological analysis confirmed a significant shift towards the networked (hyperfused) morphology in the treated group. An unpaired two-tailed t-test was used when each morphological group was compared between the control and the hyperfused mitochondria (D) Motion analysis at the whole cell level showed an increase in motion in the hyperfused, treated mitochondria ($p = 0.0014$ using Chi-squared statistical analysis with a 95% confidence interval). (E) Motion analysis of individual networks of hyperfused mitochondria revealed a similar increase in motion (unpaired two-tailed t-test). (F) Motion analysis at the morphological class level showed that this increase in motion was due to the networked subgroup (2-way ANOVA with Sidak's multiple comparisons test). (G) Magnitude of motion of the networked subgroup was greater than the control group over time. (H) Mean standard deviation of intensity analysis was performed for the three morphological classes in the hyperfused condition, showing that the swollen subgroup had the highest fluctuations in intensity (1-way ANOVA with

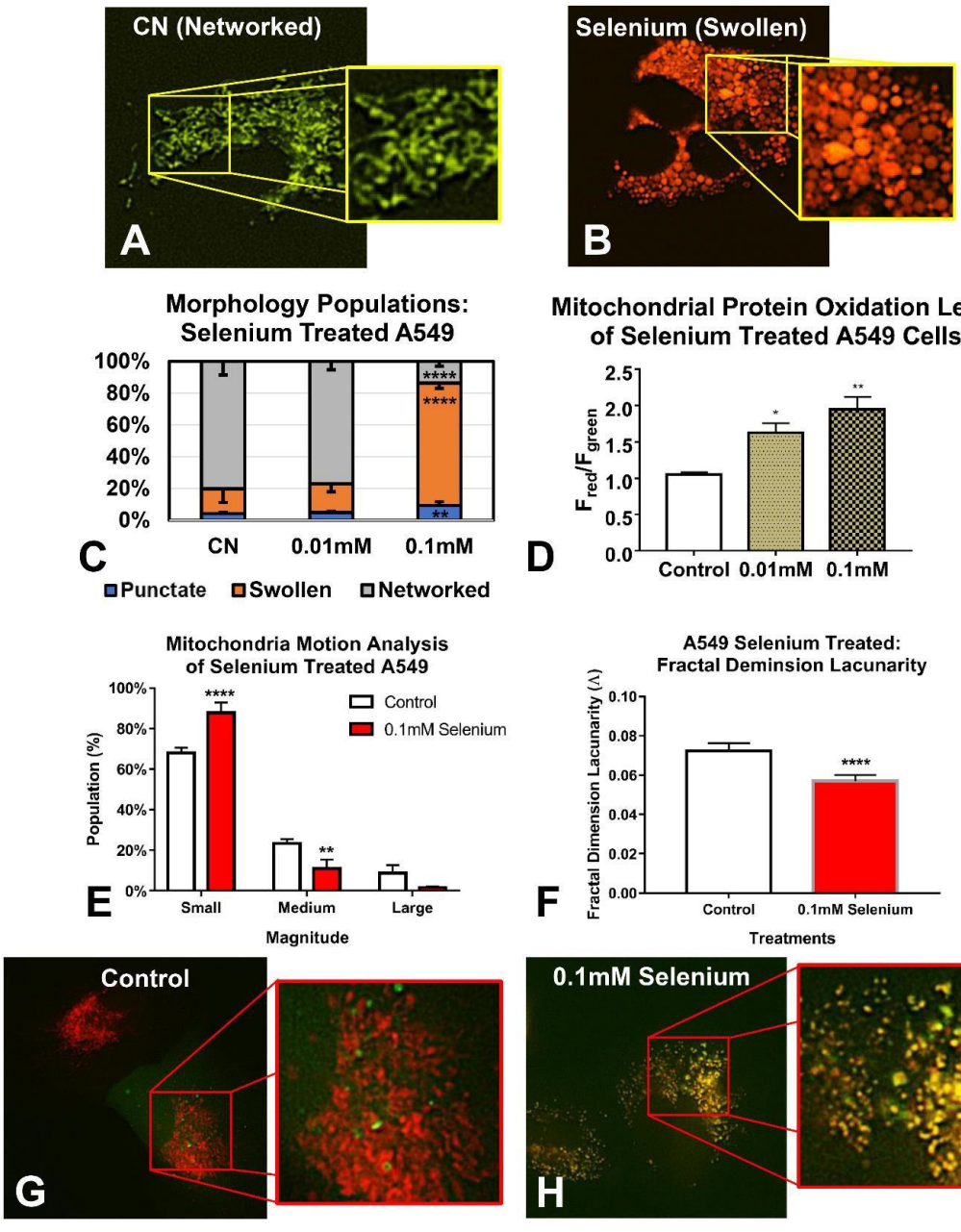
CN (Networked)
A
Selenium (Swollen)
B
Morphology Populations:
Selenium Treated A549
100%
80%
60%
40%
20%
0%
****
****
**
CN
0.01mM
0.1mM
C
Punctate
Swollen
Networked
Mitochondrial Protein Oxidation Level
of Selenium Treated A549 Cells
2.5
2.0
1.5
1.0
0.5
0.0
F_{red}/F_{green}
*
**
Control
0.01mM
0.1mM
D
Mitochondria Motion Analysis
of Selenium Treated A549
100%
80%
60%
40%
20%
0%
Population (%)
****
**
Control
0.1mM Selenium
Small
Medium
Large
Magnitude
E
A549 Selenium Treated:
Fractal Deminsion Lacunarity
Fractal Dimension Lacunarity (Λ)
0.10
0.08
0.06
0.04
0.02
0.00
****
Control
0.1mM Selenium
Treatments
F
Control
G
0.1mM Selenium
H

Figure 3.6. Analysis of swollen mitochondria in selenium treated A549 cells. (A-B) Treatment of MitoTimer-transfected A549 cells with 0.1mM SeCl4 changed mitochondrial shape from networked to swollen and increased mitochondrial protein oxidation (increase in orange/red fluorescence). (C) Selenium treatment cells produced a dose dependent increase in the swollen mitochondria (1-way ANOVA with Dunnett's multiple comparisons test). (D) The MitoTimer red/green fluorescence ratio showed a dose-response increase in mitochondrial protein oxidation in the selenium treated A549 cells (1-way ANOVA with Dunnett's multiple comparisons test). (E) Motion decreased in the swollen mitochondria in the selenium treated group (2-way ANOVA with Bonferroni's multiple comparisons test). (F) Lacunarity decreased in the treated, swollen mitochondria (unpaired two-tailed t-test). (G-H) Double labeling with GFP-LC3 showed that the mitochondria in selenium treated cells, but not in control cells, were co-localized with autophagosomes, indicating their targeted degradation.

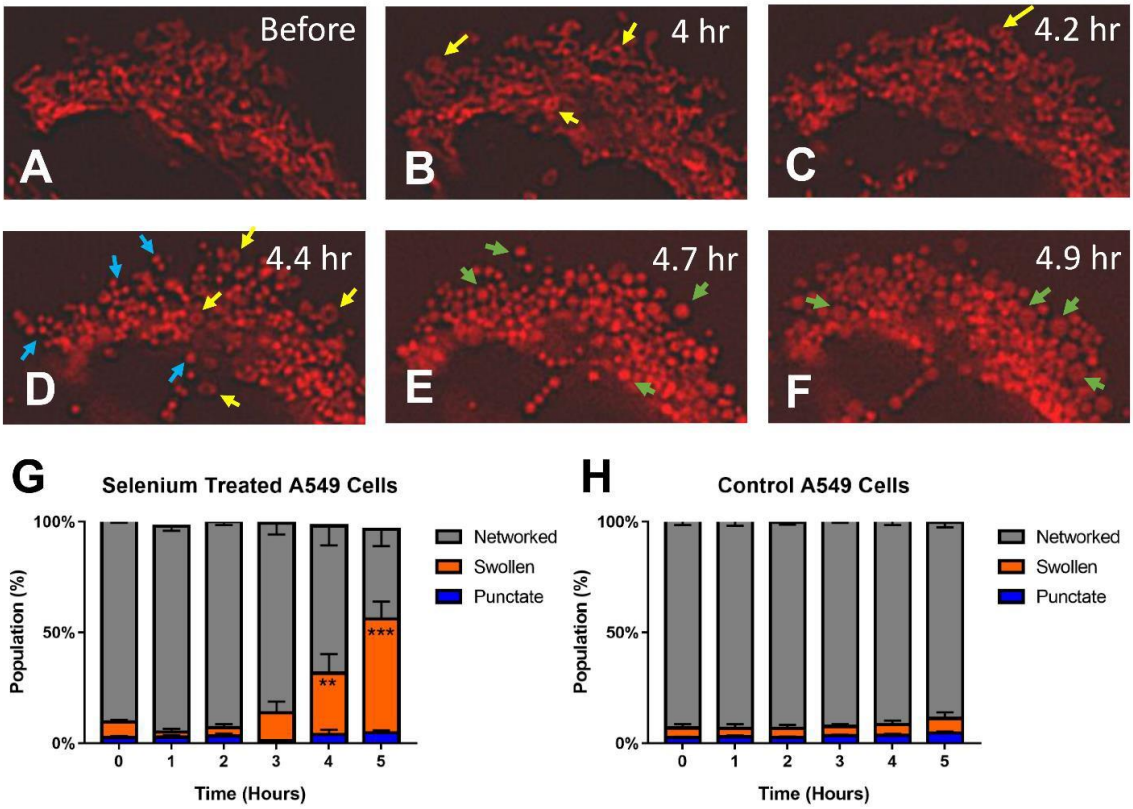

Figure 3.7. Mitochondrial morphogenesis in A549 cells during selenium treatment (A-F) Time-lapse videos of 0.1mM selenium-treated MitoTimer-transfected A549 cells were collected over several hours. The networked mitochondria first formed small tubes and donuts (yellow arrows in Figs. 3.7B-D), followed by fragmentation into the punctate morphology (blue arrows in Fig. 3.7D), before eventually expanding to form the swollen phenotype (green arrows in Figs. 3.7E- F) after approximately 5 hours of time. (G) The selenium-treated cells had an increase in the swollen mitochondria after 4 hours. (H) Control videos were also collected over several hours, and mitochondrial morphology did not change over time. Statistical analysis for 7G and 7H were done using a 2-way ANOVA with Dunnett's multiple comparisons test

test). Motion analysis demonstrated a significant decrease in mitochondrial motility in selenium treated cells when compared to controls (2-way ANOVA with Bonferroni's multiple comparisons test) (Fig. 3.6E). Texture analysis using an unpaired two-tailed t-test showed that lacunarity decreased, consistent with the denser organization caused by mitochondrial swelling (Fig. 3.6F). Double labeling with a GFP-LC3 (microtubule-associated protein light chain 3a) autophagy reporter and MitoTracker dye demonstrated that the swollen mitochondria co-labeled with autophagosomes, indicating their targeted degradation via mitophagy (Figs. 3.6G-H).

Mitochondrial morphogenesis during swelling in selenium treated A549 cells

MitoMo was used to analyze mitochondrial morphogenesis during treatment of A549 cells with 0.1 mM selenium in time-lapse videos collected every hour. By approximately 4 hours of treatment, mitochondrial morphology had changed from a primarily networked phenotype (Fig 3.7A) to small rings (yellow arrows in Fig. 3.7B-D). Mitochondrial morphology progressed to the punctate phenotype (blue arrows in Fig 3.7D), and approximately 1 hour later the punctate mitochondria expanded to form the swollen morphology (green arrows in Fig. 3.7E-F). Progression to the swollen morphology is shown quantitatively in the graphs for selenium-treated cells (Fig. 3.7J). Control cells (Figs. 3.7G-I) were also imaged every hour, and their morphologies remained primarily networked over time (Fig. 3.7K). Statistical analysis of both the treated and control groups was done using a 2-way ANOVA with Dunnett's post hoc test.

Health classification in cells using supervised learning

A549s cells treated with 0.01mM of selenium were segmented after 24 hours of incubation using their MitoTimer intensity (Fig. 3.8B). When looking at morphology alone, it was extremely difficult to distinguish the controls from the low-dose treated cells, since both exhibited highly networked mitochondria. Therefore, all 21 morphology, intensity, texture, and motion features were tested either singly or in combination to distinguish the control and treated groups using three classifier algorithms: discriminant analysis [41], K-Nearest Neighbor (KNN) [33], and error correcting [42] (Fig. 3.8C). KNN outperformed the other two classifiers in most cases, although the error correcting method had the potential to do well when there were multiple features. One feature alone resulted in maximum accuracy of 68% for morphology, 61% for motion, and 65% for texture. By combining four features, we were able to increase accuracy to 86%. This demonstrates

that MitoMo allows accurate classification of cellular stress that was not distinguishable by visual inspection of mitochondrial morphology.

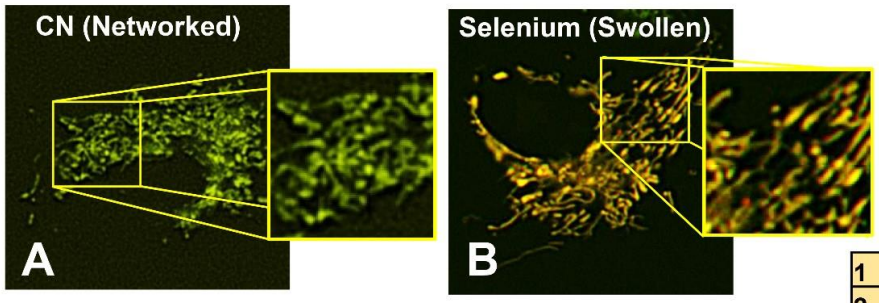

C

Features Used			Discriminant Analysis	K-Nearest Neighbor	Error Correcting
5,11	13	15	83.64 ± 4.39	**85.91 ± 1.44**	68.64 ± 4.52
3,10	14,15		75 ± 2.40	**85.91 ± 1.44**	81.82 ± 1.50
2,8,21	13		83.18 ± 4.31	84.55 ± 3.18	**85.45 ± 4.18**
1,4,7	19		71.36 ± 4.31	84. 55 ± 5.75	**85.00 ± 2.20**
2,4, 9, 10			67.73 ± 5.00	**81.82 ± 1.50**	80.00 ± 2.35
Best Feature: Morphology			56.36 ± 5.75	**68.18 ± 1.50**	66.82 ± 4.31
Best Feature: Motion			55.45 ± 4.18	**60.91 ± 3.18**	29.55 ± 9.40
Best Feature: Texture			64.55 ± 5.16	**65.45 ± 3.18**	33.63 ± 9.87

Morphology
1-11, 21
Motion
14,15, 16, 17
Texture
12, 13, 18,19,20

1	Area
2	MajorAxisLength
3	MinorAxisLength
4	Eccentricity
5	Orientation
6	Solidity
7	Extent
8	Perimeter
9	MaxRadius
10	MeanRadius
11	MedianRadius
12	IntegratedInt
13	medianSTD
14	dx
15	dy
16	Magnitude
17	Angle
18	FractalDimMean
19	FractalDimSTD
20	Lacunarity
21	Mito Class

Figure 3.8. Health classification of A549 cells in "Undetectable stress" conditions. (A-B) Treatment of MitoTimer-transfected A549 cells with 0.01mM SeCl4 did not visibly change their networked morphology (Fig 3.8C), however, health classification could distinguish treated from control cells by combining different feature types. (C) Using a single morphology, motion, or texture feature at best resulted in a 68% accuracy in distinguishing the control and treated groups. Combining feature types resulted in up to 86% accuracy for KNN, 85.5% for error correcting method, 83.5% for discriminant analysis.

DISCUSSION

Machine learning and automated analysis of still and video data are important components of modern light microscopy [43]. Software is needed that has the capability of extracting biologically relevant data from images in a reliable, unbiased, and rapid manner. MitoMo has a user-friendly interface, is open source (see Methods), and could be used to analyze any type of mitochondrial morphology given user-input trained libraries. Our segmentation is versatile (allows import of pre- segmented images) and has tunable image processing parameters allowing for high accuracy. While other mitochondrial programs often analyze a limited number of features [16, 20-23, 25, 26, 30], MitoMo enables a deep level of analysis that integrates morphology, texture, motion, morphogenesis, and cell health classification into a single program. This is important, since features that appear uninformative by themselves can be highly relevant if combined with other features. MitoMo is the only machine-learning software that provides both mitochondrial morphological classification and cell health classification based on mitochondrial features. MitoMo incorporates both still and video image analysis making morphogenesis and dynamic analyses possible with a single software program. While our data were analyzed using deconvoluted fluorescent images, confocal, super resolution and holotomographic images could also be used with MitoMo and may be easier to segment given their higher resolution.

Mitochondria have been used to study a variety of biological problems such as stress response [25,26], drug response [18, 24, 25, 44, 45], classifying cell types [10] and disease states [21, 23]. MitoMo has all of these analytical capabilities, but with a greater number of feature types allowing deeper analysis. For instance, when morphology alone was not adequate to distinguish different cell types, clear segregation of cells types was possible with texture analysis (Fig 3.3I). This was shown in the case of hPFs and A549s, where both exhibited networked mitochondria but could be distinguished using texture features. Previously, stress responses were studied using

morphology (e.g. hyperfusion or mitophagy-induced morphological changes). For example, we and others have shown that stressors such UV, antibiotics, and environmental toxicants can cause mitochondrial hyperfusion [6, 8]. Here, we show that stress-induced mitochondrial hyperfusion is also accompanied by an increase in motion.

Changes in mitochondria morphology and dynamics can correlate with mitochondrial function, as well as with various types of stimuli. For instance, mitochondria are transported to sites of energy demand [46] and changes in mitochondrial morphology correlate with permeability and respiratory functions [27]. Here, we showed that stress induced mitochondrial hyperfusion occurred in NSCs treated with electronic cigarette aerosol. We know from previous observations that this survival response correlates with increased production of ATP [6, 8], a hallmark function of mitochondria, as well as an increase in ROS, which could be damaging to the cell. Since NSC are critical for post-natal brain development [47], stress to their mitochondria would be a concern for normal functioning of these cells and corresponding tissue. Moreover, we show that response to EC aerosol-induced stress results in an increase in mitochondrial protein oxidation using intensity feature analysis of MitoTimer reporter. MitoMo goes beyond traditional intensity analysis to include features to measure how intensity values fluctuate (higher in swollen mitochondria, shown in Fig 3.5H), which expand intensity analysis to the study of dynamics. Any mitochondrial-targeted dye or reporter could be used with MitoMo to quantify functional readouts.

MitoMo's novel intensity flow method for motion analysis bypasses the limitations of traditional object tracking and optical flow motion analysis. Because MitoMo uses a pixel-based method, it is particularly powerful at quantifying mitochondrial motion when mitochondria are not trackable (e.g., when they exist in networks). Also, when movement of entire mitochondria is arrested (as in the case of selenium-induced toxicity), motion within the mitochondria can still be assessed using MitoMo. Also, MitoMo circumvents the brightness over time constraint of optical

flow, resulting in significantly higher angle and magnitude accuracies in 4 out of 6 synthetic motion conditions. Also, our software can evaluate direction of both intact mitochondria with respect to any cellular structure and directional motion within the mitochondria. Directional motion of mitochondria can be useful when mitochondria are reorganized, such as during perinuclear clustering, which could be an early biomarker of cell stress [48, 49]. In addition, directional analysis can be used to detect motion heterogeneity in mitochondrial distribution and translocation inside a cell. MitoMo was used to show direction of movement to/away from the nucleus and alteration of that movement following drug treatment. Although not shown in this paper, the ability of MitoMo to analyze intra-organelle motion can be applied to show flow of mtDNA or specific mitochondrial proteins.

MitoMo was able to evaluate morphogenesis of mitochondrial swelling and eventual mitophagy, which occurred during selenium-induced stress [50, 52]. Selenium has been implicated in mitochondrial toxicity [53, 54] and is found in some tobacco products, including electronic cigarette fluids and aerosols [39, 40]. A549 cells treated with selenium transitioned from the networked to punctate morphology consistent with fission, a process that is needed to segregate dysfunctional mitochondria for culling by mitophagy [55]. The punctate mitochondria then became swollen, likely due to increases in mtROS [56] (shown in Fig 3.6B, 3.6D). This is consistent with inhibition of the respiratory chain and the loss of mitochondrial membrane potential (MMP) following metal or selenium treatment [57]. Our data provide clear evidence that treatment of a cancer cell line with 0.1mM selenium adversely affects mitochondria and may be a mechanism contributing to treatment of cancer with selenium [58]. It will be important in future work to determine if selenium has similar adverse effects on normal cells, as such effects would impair health.

Phenotyping with MitoMo also provides the information needed to classify healthy and unhealthy cells. As shown previously, mitochondrial phenotyping based on texture can distinguish different types of cancer cells and their response to drugs [21, 23, 24]. As shown in Fig 3.8, health classification with MitoMo can identify subtle changes in mitochondria and was useful in discovering stress that was not detectable by examining mitochondrial morphology, texture, or motion alone. Subtle sub-organelle changes have traditionally been observed using ultra-high resolution techniques, such as transmission electron microscopy (TEM) [59, 60]; however, mitochondrial analysis at this scale does not allow for whole-cell phenotyping, is extremely time-consuming, and is limited to fixed cells. Early detection of mitochondrial stress has many applications including high-throughput drug testing, toxicology, and any biological research involving mitochondria.

Mitochondrial health plays an important role in many diseases, including neurodegenerative diseases such as Parkinson's, Huntington's, and Alzheimer's [11, 61], metabolic disorders [7], cancer [58, 62, 63], and mitochondria myopathies [11, 61]. Although not shown in this paper, MitoMo could be used to identify early biomarkers of specific disease by deep analysis of mitochondria from easy to obtain human biopsies, such as blood, urine, saliva, and skin. Moreover, there are numerous applications of MitoMo to disease-in-a-dish models in which changes in mitochondrial morphology, motion, and texture could be studied against control cells during disease progression. MitoMo could also be used to study the morphology and dynamics of other organelles, such as peroxisomes and autophagosomes/lysosomes, which have important links to disease. MitoMo can be used with any cell type and expanded to study the dynamics of any organelle.

In summary, MitoMo has immediate and broad utility in cell biology, drug discovery, toxicology, and medicine in that it permits deep quantitative evaluation of mitochondrial

morphology, motion, texture, morphogenesis, and cell health classification in an accessible integrated software package.

MATERIALS AND METHODS

Cell culturing and reagents.

NSC (line C17.2, provided by Dr. Evan Snyder's lab) were grown as previously described [6]. A549 lung epithelial cells (human type II pulmonary alveolar adenocarcinoma cells) were obtained from ATCC. Cells were cultured in F-12K medium (Kaighn's Modification of Ham's F-12, ATCC #30- 2004) and 10% fetal bovine serum (ATCC #30-2020). Cells were incubated at 37oC in 5% CO2 until 80% confluency, at which point they were detached using 0.25% trypsin. Cells were passaged every 2-3 days and medium was replenished every other day. Human pulmonary fibroblasts (hPF) (obtained from ScienCell) were cultured in complete fibroblast medium (ScienCell) containing 2% fetal bovine serum, 1% fibroblast growth serum, and 1% penicillin/streptomycin. hPF were grown on poly-L-lysine (2µl/1ml) coated T-25 flasks, which were prepared a day in advance of use in experiments. hPF were cultured in 5% CO2 at 37°C and 95% relative humidity until 70%-80% confluent. For sub-culturing and experimental set up, cells were washed with DPBS and detached with 0.05% trypsin diluted in DPBS for 1 minute at 37°C.

Live cell imaging.

For live imaging, cells were plated on µ-Slide Ibidi 8-well chambers (Ibidi) at approximately 6,000 cells/well. Time-lapse fluorescent images were collected using a TI inverted Nikon Eclipse microscope equipped with a LiveCell temperature and CO2-regulating, heated stage (Pathology Devices Inc). The images were collected using a Nikon 60x 0.85 NA objective with a 0.11um/pixel resolution, and a Nikon 40x 0.75 NA and 60x 1.4 NA objectives with 0.16 and 0.11

μm/pixel resolutions respectively. A high-resolution Andor Zyla VSC-04941 camera (Andor, Belfast, UK) was used. Excitation illumination was from the Nikon INTENSILIGHT C-HGFIE lamp. Videos were collected at millisecond resolution and deconvoluted using the "live de-blur" feature of the NIS Elements software (Nikon).

Transiently transfected and reporter cells and labeling of mitochondria.

NSC were cultured, detached enzymatically, and centrifuged for 3 minutes at 3,000 rpm. The pellet containing 6 x 106 cells was re-suspended in Nucleofection medium (Lonza Kit # VAPG- 1004) and nucleofected in the Amaxa Nucleofector IIb device (Lonza) using program A-033. The cells were quickly transferred to a new dish containing pre-equilibrated fresh medium, and selected with hygromycin at an optimal kill dose of 150 μg/ml. The medium and hygromycin treatment was replenished every other day for 30 days. The Mito-Timer-transfected NSC were further enriched with FAC Sorting (FACS Aria) using GFP (488nm Argon laser, 530/30 filter) and DsRed (488nm Argon laser, 610/20 filter) signals. A549 and hPF cells were transiently transfected using DNA-In reagents (MTI-GlobalStem # 73770 and 73750). The Addgene plasmids (pMitoTimer # 52659 and pEGFP-LC3 # 21073) were used to transfect the cells. A549 cells were co-labeled with MitoTracker-Red dye (ThermoFisher Scientific #M7512) to visualize mitophagy. Quantification of mitochondrial texture and motion using MitoMo.

By computing the change in intensity of fluorescently-labeled mitochondria between adjacent frames, the flow of mitochondrial proteins can be estimated at the individual pixel level. To do this, a difference image $D_{t,t+1}$ was computed as,

$$D_{t,t+1} = I_{t+1} - I_t$$

where I_t is the image at time t. Negative values in $D_{t,t+1}$ represent a decrease in intensity at that pixel location, while positive values represent an increase. $D_{t,t+1}$ shows a change in the density of fluorescent tags over time. To visualize these changes, $D_{t,t+1}$ is rescaled with the equation,

$$D'_{t,t+1} = \frac{D_{t,t+1} + 255}{510}$$

so that the pixel values are between 0 and 1. To filter out background motion and motion in other structures, a region of interest is estimated for each difference image. MitoMo used an adaptive Otsu's segmentation [64] on each frame to segment the structures of interest. The region of interest for each difference frame is defined as,

$$ROI_{t,t+1} = S_t \cup S_{t+1}$$

where S_{t+1} is Otsu's segmentation output at time t. Using $D'_{t,t+1}$ and $ROI_{t,t+1}$, motion vectors in the image sequence are computed with the following gradient equation:

$$\nabla D'_{t,t+1} = \frac{\delta D'_{t,t+1}}{\delta x}\,\hat{x} + \frac{\delta D'_{t,t+1}}{\delta y}\,\hat{y} = u\,\hat{x} + v\,\hat{y}$$

$\hat{x}$ and $\hat{y}$ are the unit vectors corresponding to the x and y axes. The equation above does not rely on the brightness assumption of optical flow and instead examines the gradient of intensity. The magnitude and angle of the motion vectors are calculated as follows,

$$M = \sqrt{u^2 + v^2} \quad ; \quad \theta = \tan^{-1}\frac{v}{u} \;;$$

While vectors can be analyzed individually, they may be combined over a region of interest. For every mitochondrion, vector addition is performed on the vectors that lay within the segmented mitochondrion. For the whole-cell level, vector addition is performed on all the vectors

within the cell. This produces a single vector representing the motion of that mitochondria or cell. In addition to the generated motion vectors, other features are extracted for each level of analysis. While basic morphological and intensity features are examined, texture features are of interest as they can analyze density of visual patterns. A differential box counting method was used to compute the fractal dimension [65] of a region around a pixel. Fractals are self-repeating patterns whose complexity can be represented by their dimension and density by their lacunarity [66].

Segmentation and classification of mitochondrial morphology using MitoMo.

MitoMo was used to segment the red fluorescent channel from MitoTimer-transfected cells. Pre-segmented images were also imported from CellProfiler software. Histogram matching 67 was performed on each video using a reference video to control intensity levels. Thresholding was performed using a global Otsu's method [64], and morphological, intensity, texture, and motion features were extracted for each segmented mitochondrion. Because segmented regions may be clustered together after thresholding, a watershed algorithm [68] was used to de-clump the segmented regions. This is done by finding the regional maximal intensities of each segmented region and computing a boundary that best separates the maxima. The extracted features were fed to supervised learning algorithms KNN and Naïve Bayes written on the MATLAB platform. The software was trained with image libraries of each morphological type (punctate, networked, swollen). An exhaustive search was carried out to identify key features and combinations that allowed accurate morphology-based classification. The experimental datasets were analyzed by the classifiers to determine the total area of each morphological subpopulation, which was normalized by the total mitochondrial area in each cell and averaged across all cells within each group.

Health classification of "stressed" cells.

MitoMo was used to segment the red fluorescence channel from MitoTimer-transfected cells. Histogram matching was done for every frame of the video with reference to the "before" (Time=0) video of the dataset, and segmentation was performed. Since classification of stressed cell conditions is done at the video scale, video features are found by computing the mean (average) of the feature value over the entire length of video. These features were previously extracted for mitochondrial analysis. Morphology, intensity, texture, and motion features were tested either singly or in combination to distinguish the two treatment conditions using three classifier algorithms: discriminant analysis, K-Nearest Neighbor (KNN), and error correcting output codes classifier.

Statistical analysis

For each set of data, three independent experiments were performed. Data were graphed and analyzed statistically using Prism software (GraphPad) as described in the figure legends. Data were considered to be significantly different for $p < 0.05$.

Source Code and Executable Files:

MitoMo was written and developed with MATLAB 2018a. The source code and an executable GUI are available online at http://vislab.ucr.edu/SOFTWARE/software.php. MitoMo.m is the main file of the code and requires the following MATLAB toolboxes: System Identification, Image Processing, Statistics and Machine Learning, and Bioinformatics. The executable requires the installation of the 64-bit version of MATLAB Runtime R2018a (9.4) available at http://www.mathworks.com/products/compiler/mcr/.

DATA AVAILABILITY

All relevant data are available within the manuscript. The source code for MitoMo and an executable GUI are available at http://vislab.ucr.edu/SOFTWARE/software.php. MitoMo.m is the main file of the code and requires the following MATLAB toolboxes: System Identification, Image Processing, Statistics and Machine Learning, and Bioinformatics. The executable requires the installation of the 64-bit version of MATLAB Runtime R2018a (9.4) available at http://www.mathworks.com/products/compiler/mcr/.

REFERENCES

[1] J. Nunnari, A. Suomalainen, Mitochondria: In sickness and in health, Cell. 148 (2012) 1145–1159.

[2] J.C. St. John, The mitochondrion, its genome and their contribution to well-being and disease, Mol. Hum. Reprod. 21 (2014) 1–2.

[3] D.H. Margineantu, D.M. Hockenbery, Mitochondrial functions in stem cells, Curr. Opin. Genet. Dev. 38 (2016) 110–117.

[4] S.L. Archer, Mitochondrial Dynamics - mitochondrial fission and fusion in human diseases, N. Engl. J. Med. 369 (2013) 2236–2251.

[5] A.M. van der Bliek, Q. Shen, S. Kawajiri, Mechanisms of Mitochondrial Fission and Fusion, Cold Spring Harb. Perspect. Biol. 5 (2013) a011072–a011072.

[6] V. Bahl, K. Johnson, R. Phandthong, A. Zahedi, S.F. Schick, P. Talbot, Thirdhand cigarette smoke causes stress-induced mitochondrial hyperfusion and alters the transcriptional profile of stem cells, Toxicol. Sci. 153 (2016) 55–69.

[7] T. Wai, T. Langer, Mitochondrial Dynamics and Metabolic Regulation, Trends Endocrinol. Metab. 27 (2016) 105–117.

[8] D. Tondera, S. Grandemange, A. Jourdain, M. Karbowski, Y. Mattenberger, S. Herzig, S. Da Cruz, P. Clerc, I. Raschke, C. Merkwirth, S. Ehses, F. Krause, D.C. Chan, C. Alexander, C. Bauer, R. Youle, T. Langer, J.-C. Martinou, SLP-2 is required for stress-induced mitochondrial hyperfusion, EMBO J. 28 (2009) 1589–1600.

[9] C. Blackstone, C.-R. Chang, Mitochondria unite to survive, Nat. Cell Biol. 13 (2011) 521–522.

[10] J.R. Friedman, J. Nunnari, Mitochondrial form and function, Nature. 505 (2014) 335–343.

[11] J. Gao, L. Wang, J. Liu, F. Xie, B. Su, X. Wang, Abnormalities of Mitochondrial Dynamics in Neurodegenerative Diseases, Antioxidants. 6 (2017) 25.

[12] J.G. McCarron, C. Wilson, M.E. Sandison, M.L. Olson, J.M. Girkin, C. Saunter, S. Chalmers, From structure to function: Mitochondrial morphology, motion and shaping in vascular smooth muscle, J. Vasc. Res. 50 (2013) 357–371.

[13] M.R. Duchen, Roles of Mitochondria in Health and Disease, Diabetes. 53 (2004).

[14] D.C. Chan, Mitochondria: Dynamic Organelles in Disease, Aging, and Development, Cell. 125 (2006) 1241–1252.

[15] R.J. Giedt, P. Fumene Feruglio, D. Pathania, K.S. Yang, A. Kilcoyne, C. Vinegoni, T.J. Mitchison, R. Weissleder, Computational imaging reveals mitochondrial morphology as a biomarker of cancer phenotype and drug response, Sci. Rep. 6 (2016) 32985.

[16] F.E. Lennon, G.C. Cianci, R. Kanteti, J.J. Riehm, Q. Arif, V.A. Poroyko, E. Lupovitch, W. Vigneswaran, A. Husain, P. Chen, J.K. Liao, M. Sattler, H.L. Kindler, R. Salgia, Unique fractal evaluation and therapeutic implications of mitochondrial morphology in malignant mesothelioma, Sci. Rep. 6 (2016) 24578.

[17] T. Yu, R.J. Fox, L.S. Burwell, Y. Yoon, Regulation of mitochondrial fission and apoptosis by the mitochondrial outer membrane protein hFis1., J. Cell Sci. 118 (2005) 4141–51.

[18] A.P. Leonard, R.B. Cameron, J.L. Speiser, B.J. Wolf, Y.K. Peterson, R.G. Schnellmann, C.C. Beeson, B. Rohrer, Quantitative analysis of mitochondrial morphology and membrane potential in living cells using high-content imaging, machine learning, and morphological binning, Biochim. Biophys. Acta - Mol. Cell Res. 1853 (2015) 348–360.

[19] L. Blanchet, J. a M. Smeitink, S.E. van Emst-de Vries, C. Vogels, M. Pellegrini, A.I. Jonckheere, R.J.T. Rodenburg, L.M.C. Buydens, J. Beyrath, P.H.G.M. Willems, W.J.H. Koopman, Quantifying small molecule phenotypic effects using mitochondrial morpho-functional fingerprinting and machine learning., Sci. Rep. 5 (2015) 8035.

[20] E. Lihavainen, J. Mäkelä, J.N. Spelbrink, A.S. Ribeiro, Mytoe: Automatic analysis of mitochondrial dynamics, Bioinformatics. 28 (2012) 1050–1051.

[21] R.J. Giedt, P. Fumene Feruglio, D. Pathania, K.S. Yang, A. Kilcoyne, C. Vinegoni, T.J. Mitchison, R. Weissleder, Computational imaging reveals mitochondrial morphology as a biomarker of cancer phenotype and drug response, Sci. Rep. 6 (2016) 32985.

[22] L. Blanchet, J.A.M. Smeitink, S.E. van Emst - de Vries, C. Vogels, M. Pellegrini, A.I. Jonckheere, R.J.T. Rodenburg, L.M.C. Buydens, J. Beyrath, P.H.G.M. Willems, W.J.H. Koopman, Quantifying small molecule phenotypic effects using mitochondrial morpho-functional fingerprinting and machine learning, Sci. Rep. 5 (2015) 8035.

[23] F.E. Lennon, G.C. Cianci, N.A. Cipriani, T.A. Hensing, H.J. Zhang, C.-T. Chen, S.D. Murgu, E.E. Vokes, M.W. Vannier, R. Salgia, Lung cancer—a fractal viewpoint, Nat. Rev. Clin. Oncol. 12 (2015) 664–675.

[24] F.E. Lennon, G.C. Cianci, R. Kanteti, J.J. Riehm, Q. Arif, V.A. Poroyko, E. Lupovitch, W. Vigneswaran, A. Husain, P. Chen, J.K. Liao, M. Sattler, H.L. Kindler, R. Salgia, Unique fractal evaluation and therapeutic implications of mitochondrial morphology in malignant mesothelioma., Sci. Rep. 6 (2016) e24578.

[25] M. Chen, Y. Li, M. Yang, X. Chen, Y. Chen, F. Yang, S. Lu, S. Yao, T. Zhou, J. Liu, L. Zhu, S. Du, J.Y. Wu, A new method for quantifying mitochondrial axonal transport, Protein Cell. 7 (2016) 804–819.

[26] Y. Reis, M. Bernardo-Faura, D. Richter, T. Wolf, B. Brors, A. Hamacher-Brady, R. Eils, N.R. Brady, Multi-parametric analysis and modeling of relationships between mitochondrial morphology and apoptosis, PLoS One. 7 (2012) e28694.

[27] M. Picard, O.S. Shirihai, B.J. Gentil, Y. Burelle, Mitochondrial morphology transitions and functions: implications for retrograde signaling?, Am. J. Physiol. Regul. Integr. Comp. Physiol. 304 (2013) R393–R406.

[28] T.E. Shutt, H.M. McBride, Staying cool in difficult times: Mitochondrial dynamics, quality control and the stress response, Biochim. Biophys. Acta - Mol. Cell Res. 1833 (2013) 417–424.

[29] J. Nunnari, A. Suomalainen, Mitochondria: In sickness and in health, Cell. 148 (2012) 1145–1159.

[30] Z.-H. Sheng, Q. Cai, Mitochondrial transport in neurons: impact on synaptic homeostasis and neurodegeneration., Nat. Rev. Neurosci. 13 (2012) 77–93.

[31] V. On, A. Zahedi, I.M. Ethell, B. Bhanu, Automated spatio-temporal analysis of dendritic spines and related protein dynamics, PLoS One. 12 (2017) 1–23.

[32] A.E. Carpenter, T.R. Jones, M.R. Lamprecht, C. Clarke, I.H. Kang, O. Friman, D. a Guertin, J.H. Chang, R. a Lindquist, J. Moffat, P. Golland, D.M. Sabatini, CellProfiler: image analysis software for identifying and quantifying cell phenotypes., Genome Biol. 7 (2006) R100.

[33] R.O. Duda, P.E. Hart, D.G. Stork, Pattern Classification, New York John Wiley, Sect. (2001) 680.

[34] P. Domingos, M. Pazzani, On the Optimality of the Simple Bayesian Classifier under Zero-One Loss, Mach. Learn. 29 (1997) 103–130.

[35] T. Brox, J. Malik, Large displacement optical flow descriptor matching in variational motion estimation, IEEE Trans. Pattern Anal. Mach. Intell. 33 (2011) 500–513.

[36] H.W. Haussecker, D.J. Fleet, Computing optical flow with physical models of brightness variation, IEEE Trans. Pattern Anal. Mach. Intell. 23 (2001) 661–673.

[37] J.N. Meyer, M.C.K. Leung, J.P. Rooney, A. Sendoel, M.O. Hengartner, G.E. Kisby, A.S. Bess, Mitochondria as a target of environmental toxicants, Toxicol. Sci. 134 (2013) 1–17.

[38] H.M. Ni, J.A. Williams, W.X. Ding, Mitochondrial dynamics and mitochondrial quality control, Redox Biol. 4 (2015) 6–13.

[39] M. Williams, K. Bozhilov, S. Ghai, P. Talbot, Elements including metals in the atomizer and aerosol of disposable electronic cigarettes and electronic hookahs, PLoS One. 12 (2017) 1–24.

[40] D. Bernhard, A. Rossmann, G. Wick, Metals in cigarette smoke, IUBMB Life. 57 (2005) 805–809.

[41] Y. Guo, T. Hastie, R. Tibshirani, Regularized linear discriminant analysis and its application in microarrays, Biostatistics. 8 (2007) 86–100.

[42] E.L. Allwein, R. Schapire, Y. Singer, Reducing multiclass to binary: A unifying approach for margin classifiers, J. Mach. Learn. Res. 1. 1 (2000) 113–141.
.
[43] B. Bhanu, P. Talbot, Video Bioinformatics, 2015.

[44] J.Y. Peng, C.C. Lin, Y.J. Chen, L. Sen Kao, Y.C. Liu, C.C. Chou, Y.H. Huang, F.R. Chang, Y.C. Wu, Y.S. Tsai, C.N. Hsu, Automatic morphological subtyping reveals new roles of caspases in mitochondrial dynamics, PLoS Comput. Biol. 7 (2011).

[45] R.J. Giedt, P.D. Koch, R. Weissleder, Single Cell Analysis of Drug Distribution by Intravital Imaging, PLoS One. 8 (2013).

[46] V. Anesti, L. Scorrano, The relationship between mitochondrial shape and function and the cytoskeleton, Biochim. Biophys. Acta - Bioenerg. 1757 (2006) 692–699.

[47] T. Bergström, K. Forsberg-Nilsson, Neural stem cells: Brain building blocks and beyond, Ups. J. Med. Sci. 117 (2012) 132–142.

[48] A.B. Al-Mehdi, V.M. Pastukh, B.M. Swiger, D.J. Reed, M.R. Patel, G.C. Bardwell, V. V. Pastukh, M.F. Alexeyev, M.N. Gillespie, Perinuclear mitochondrial clustering creates an oxidant-rich nuclear domain required for hypoxia-induced transcription, Sci. Signal. 5 (2012) 1–10.

[49] A. Hallmann, R. Milczarek, M. Lipiński, E. Kossowska, J.H. Spodnik, M. Woźniak, T. Wakabayashi, J. Klimek, Fast perinuclear clustering of mitochondria in oxidatively stressed human choriocarcinoma cells, Folia Morphol. (Warsz). 63 (2004) 407–412.

[50] G.A. Blondin, D.E. Green, The Mechanism of Mitochondrial Swelling, Arch. Biochem. Biophys. 132 (1969) 509–23.

[51] D.R. Green, G. Kroemer, The pathology of mitochondrial cell death, Science (80-.). 305 (2004) 626–629.

[52] A.E. Vercesi, A.J. Kowaltowski, M.T. Grijalba, A.R. Meinicke, R.F. Castilho, The role of reactive oxygen species in mitochondrial permeability transition, Biosci. Rep. 17 (1997) 43–52.

[53] V. Selvaraj, J. Tomblin, M. Yeager Armistead, E. Murray, Selenium (sodium selenite) causes cytotoxicity and apoptotic mediated cell death in PLHC-1 fish cell line through DNA and mitochondrial membrane potential damage, Ecotoxicol. Environ. Saf. 87 (2013) 80–88.

[54] H.J. Sun, B. Rathinasabapathi, B. Wu, J. Luo, L.P. Pu, L.Q. Ma, Arsenic and selenium toxicity and their interactive effects in humans, Environ. Int. 69 (2014) 148–158.

[55] H. Abeliovich, M. Zarei, K.T.G. Rigbolt, R.J. Youle, J. Dengjel, Involvement of mitochondrial dynamics in the segregation of mitochondrial matrix proteins during stationary phase mitophagy, Nat. Commun. 4 (2013) 1–11.

[56] T. Ahmad, K. Aggarwal, B. Pattnaik, S. Mukherjee, T. Sethi, B.K. Tiwari, M. Kumar, A. Micheal, U. Mabalirajan, B. Ghosh, S. Sinha Roy, A. Agrawal, Computational classification of mitochondrial shapes reflects stress and redox state, Cell Death Dis. 4 (2013) e461-10.

[57] E.A. Belyaeva, D. Dymkowska, M.R. Wieckowski, L. Wojtczak, Mitochondria as an important target in heavy metal toxicity in rat hepatoma AS-30D cells, Toxicol. Appl. Pharmacol. 231 (2008) 34–42.

[58] M.P. Rayman, Selenium in cancer prevention: a review of the evidence and mechanism of action, Proc. Nutr. Soc. 64 (2005) 527–542.

[59] G. Arismendi-Morillo, Electron microscopy morphology of the mitochondrial network in gliomas and their vascular microenvironment, Biochim. Biophys. Acta - Bioenerg. 1807 (2011) 602–608.

[60] W.X. Ding, M. Li, J.M. Biazik, D.G. Morgan, F. Guo, H.M. Ni, M. Goheen, E.L. Eskelinen, X.M. Yin, Electron microscopic analysis of a spherical mitochondrial structure, J. Biol. Chem. 287 (2012) 42373–42378.

[61] S.C. Correia, R.X. Santos, G. Perry, X. Zhu, P.I. Moreira, M.A. Smith, CHAPTER 16 Mitochondrial importance in Alzheimer's , huntington's and parkinson's diseases, in: Neurodegener. Dis., 2012: pp. 205–221.

[62] H. Fritz, D. Kennedy, D. Fergusson, R. Fernandes, K. Cooley, A. Seely, S. Sagar, R. Wong, D. Seely, Selenium and Lung Cancer: A Systematic Review and Meta Analysis, PLoS One. 6 (2011) 1–10.

[63] J. Li, J.C. Tharappel, S.G. Han, A.H. Cantor, E.Y. Lee, C.G. Gairola, H.P. Glauert, Effect of dietary selenium and cigarette smoke on pulmonary cell proliferation in mice, Toxicol. Sci. 111 (2009) 247–253.

[64] N. Otsu, A Threshold Selection Method from Gray-Level Histograms, 20 (1979) 62–66.

[65] D. Sankar, T. Thomas, Fractal features based on differential box counting method for the categorization of digital mammograms, Int. J. Comput. Inf. Syst. Ind. Manag. Appl. 2 (2010) 011–019.

[66] A. Karperien, H.F. Jelinek, N. Milosevic, Lacunarity Analysis and Classification of Microglia in Neuroscience, Esmtb. (2011).

[67] R. Gonzalez, R. Woods, Digital image processing, 4th ed., Pearson, 2017.

[68] J. Roerdink, A Meijster, The Watershed Transform: Definitions, Algorithms and Parallelization Strategies, Fundam. Informaticae. 41 (2000) 187–228.

Section II: Evaluation of Electronic Cigarettes on Lung Cell

Chapter 4

A Two-Tiered Screen to Identify Modes of Actions and Biomarkers of Potential Harm and Disease in Electronic Cigarettes ABSTRACT

ABSTRACT

The Surgeon General and FDA have issued warnings about the rapid rise in the use of electronic cigarettes (ECs). These devices have gained a popularity among adolescents and young adults, and there is a growing concern regarding their health effects. In this study, we developed a two-tiered screening method for identifying cytotoxic EC fluids and aerosols, and then applied it to major brands of cartomizer-style ECs. In tier 1, the MTT cytotoxicity assay and morphological assessments were used to identify two EC products of interest (GreenSmoke and Vuse) that were further studied in the tier two MOA assays. Exposure to GreenSmoke resulted in cytoskeletal depolymerization, adhesion-to-substrate defects, and eventual apoptosis. Exposure to Vuse resulted in upregulation of alpha smooth muscle actin (α-SMA) and morphological changes associated with fibroblast-to-myofibroblast differentiation in hPFs and epithelial-to-mesenchymal transition (EMT) in A549 cancer cells. The high nicotine content of Vuse resulted in a rapid upregulation of nicotinic receptors (α7 nAChR) in lung epithelial cells and desensitization of nicotine-mediated calcium influx. Treatment of neural stem cells (NSCs) resulted in mitochondrial damage and increased oxidation of mitochondrial proteins (oxidative stress). This study concludes that EC exposure from even low-voltage cartomizer-style EC products could lead to adverse health effects and potentially promote diseases such as fibrosis, cancer, and neuro-developmental defects.

Electronic cigarettes (ECs) are popular devices that enable users to inhale flavored aerosols containing nicotine, without burning tobacco [1–6]. ECs are available in a variety of styles

including disposable cartomizer models that can be discarded after each cartomizer/pod is used [7]. Recent reports from the Surgeon General and the National Academies of Sciences, Engineering and Medicine (NASEM) express serious concerns about the rising popularity of ECs among adolescents and their potential for harming health [2, 6]. Adverse health effects have been reported online by EC users [4, 8], in case reports linked to EC use [8, 9], and systematic reviews [4,10–14]. Despite their rapid increase in popularity, little is known about their potential to cause smoking-associated diseases or alternatively improve health in smokers.

Several in vitro studies suggest that EC products are not harmless [15–19]. For example, some refill fluids have cytotoxicity in the MTT assay, which measures mitochondrial reductase activity [15, 17, 20]. In the study by Bahl et al., cytotoxicity was correlated with the concentration of flavor chemicals in each product [15]. It was subsequently shown that flavor chemicals can be highly cytotoxic at the concentrations used in refill fluids [19, 21, 22]. Cinnamaldehyde is of particular concern since this highly cytotoxic/genotoxic flavoring is often used at high concentrations in refill fluids, and it is present in many EC products that do not have "cinnamon: in their flavor name [17]. Therefore, consumers may unwittingly use products that contain cinnamaldehyde or other flavor chemicals at cytotoxic doses. Upon aerosolization, the solvents and flavor chemicals in e-liquids can form reactive byproducts, such as acrolein or formaldehyde [23,24]. The high concentration of nicotine in some products is also a concern and has been associated with mislabeled and counterfeit products [25,26]. The FDA recently called the use of high nicotine content products, such as JUUL, by teens a burgeoning epidemic with risks for addiction, developmental effects, and other health hazards.

Since their introduction, the effects of ECs on cells have been investigated, with most studies focused on oxidative stress and inflammatory responses [11,16,19,27–29]. A number of chemicals found in EC e-liquids and aerosols raise concern about their potential for harming health.

Oxidants and ROS have been detected in unvaporized e-liquids, as well as in aerosols generated during heating [19]. Furthermore, heavy metals and nanoparticles, are present in ECs aerosols, and these have been linked to mitochondrial damage [7, 30–32]. EC chemicals can either directly or indirectly (co-carcinogenic) induce DNA damage [2, 16, 22, 29, 33, 34]. Some EC byproducts such as formaldehyde are "known carcinogens" (EPA) that can cause cancer in animals via inhalation [24]. Although nicotine itself is not a carcinogen, nicotine as well as the solvents PG and glycerol, can form secondary products that produce genotoxicity [6]. Canistro et al. (2017) used the micronucleus assay and 8-OHdG levels to show increased mutagenicity in reticulocytes following in vivo exposure of rats to e-liquids [35]. Some studies report that the concentrations of carcinogens in EC aerosols are lower than in tobacco smoke [18]; however, exposure levels vary significantly based on device type, nicotine/flavoring content, and user topography [24]. Hence, the safety of ECs and their application as harm-reduction devices remain incompletely understood.

Our purpose was to develop a comprehensive two-tiered toxicological screen to identify MOAs associated with EC products, or any toxicant, using in vitro models and video bioinformatics analysis. We then used this screen to first identify those EC products that were effective in the MTT assay or altered cell morphology. Products of interest were then analyzed in tier 2 to determine the MOA of each product using assays that spanned a broad range of cell processes. Evaluations were made on both the fluids and aerosols from four leading brands of cartomizer style EC, and two flavor groups, menthol and tobacco, were compared. Several cell types were used to allow identification of specific MOAs and to compare cell sensitivity to various treatments.

RESULTS

Overall Strategy for Screening EC Toxicity:

A schematic overview of our two-tiered screening method used to identify cytotoxic EC products and their MOAs is presented in Fig 4.1. After choosing the type of EC products to be tested and the relevant cell type (s), a Tier 1 screen was performed using the MTT cytotoxicity assay and morphological assessment. In Tier 2, additional assays were performed to identify MOAs that occur in cells at various concentrations, including ones that produce no cytotoxic effect in the MTT assay. The MOA assays included: (1) DNA damage, (2) cell proliferation, attachment and death using live cell imaging, (3) fibrosis, (4) epithelial-to-mesenchymal transition (EMT), (5) nicotinic receptors and their responses, (6) mitochondrial damage and oxidative stress and, (7) autophagy. These endpoints can be interpreted as biomarkers of potential harm that have been linked in prior studies to various tobacco-related diseases as shown in Fig 4.1.

Product library and cell types of interest

We applied the screening method to a library of five cartomizer-style EC brands that included menthol and tobacco flavored products. Both e-liquids and aerosols were tested from each product. Screening was done using four cell types: (1) primary human pulmonary fibroblasts (hPFs), (2) A549 cells from a human alveolar basal epithelial cell adenocarcinoma; (3) mouse neural stem cells (mNSCs) isolated from neonate cerebellum, and (4) H9 human embryonic stem cells (hESCs). Fibroblasts and epithelial cells from the lung were chosen for tier 1 analysis, as they are direct targets of exposure via inhalation. Although A549 cancer cells are generally less sensitive for MTT screening, they are excellent models for detecting morphological changes such as in EMT (a key step in cancer metastasis). Stem cells were used as in vitro models for pre- and post-natal

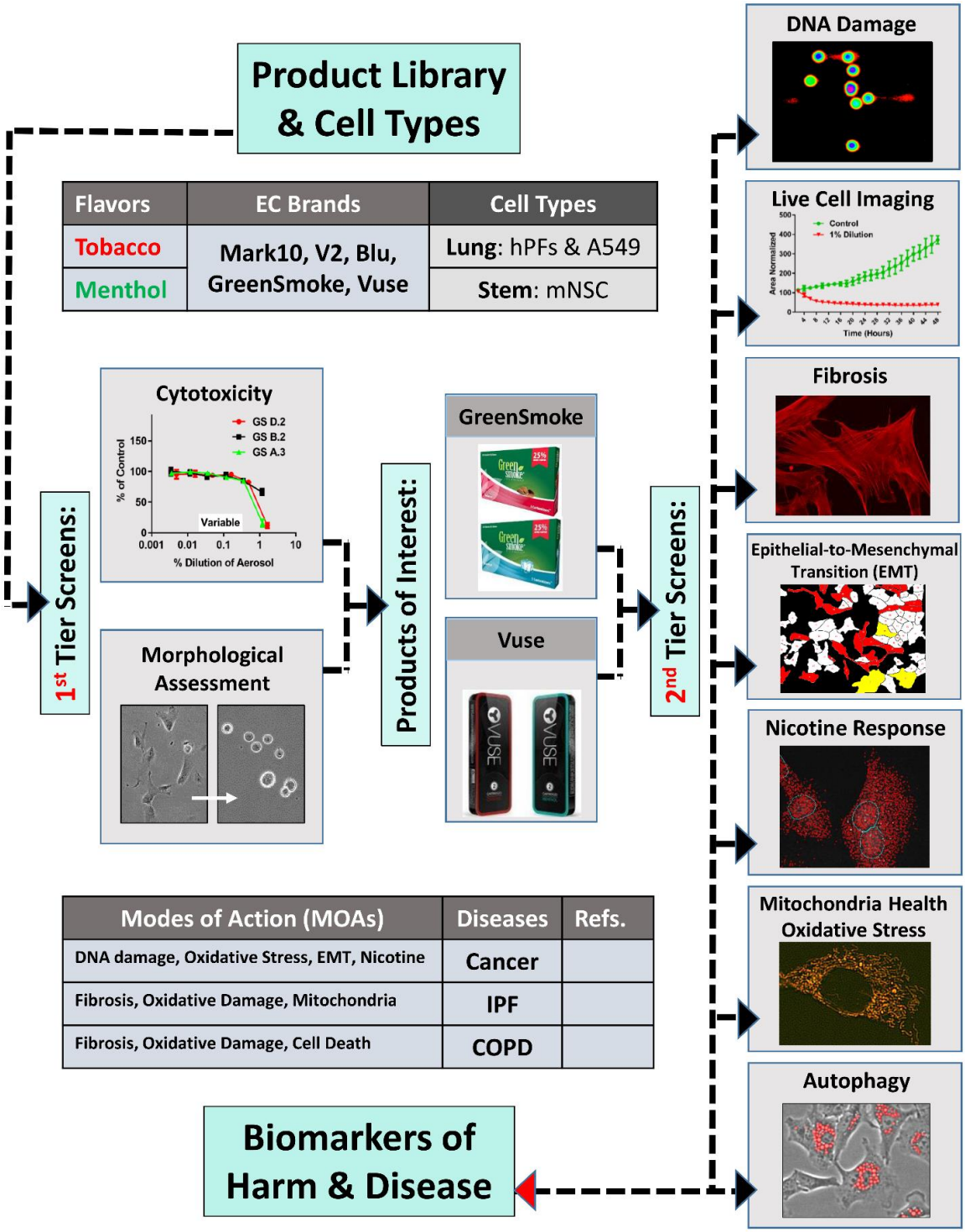
Product Library & Cell Types
Flavors
Tobacco
Menthol
EC Brands
Mark10, V2, Blu, GreenSmoke, Vuse
Cell Types
Lung: hPFs & A549
Stem: mNSC
1st Tier Screens:
Cytotoxicity
GS D.2
GS B.2
GS A.3
% of Control
Variable
% Dilution of Aerosol
Morphological Assessment
Products of Interest:
GreenSmoke
Vuse
2nd Tier Screens:
DNA Damage
Live Cell Imaging
Control
1% Dilution
Area Normalized
Time (Hours)
Fibrosis
Epithelial-to-Mesenchymal Transition (EMT)
Nicotine Response
Mitochondria Health Oxidative Stress
Autophagy
Modes of Action (MOAs)
Diseases
Refs.
DNA damage, Oxidative Stress, EMT, Nicotine
Cancer
Fibrosis, Oxidative Damage, Mitochondria
IPF
Fibrosis, Oxidative Damage, Cell Death
COPD
Biomarkers of Harm & Disease

Figure 4.1. Overview of the Two-tiered Screen Developed to Evaluate EC toxicity. User inputs include EC products and cell type(s) of interest. Initial Tier-1 screening accesses cytotoxicity using the MTT assay and visual inspection of cell morphology. Products that produce a response in either Tier-1 assay are studied further in Tier-2 to determine the modes of action (MOAs). Tier-2 assays include: (1) DNA damage, (2) growth rate (cell proliferation), (3) attachment and spreading, (4) cytoskeletal remodeling, (5) cell death, (6) fibroblast-to-myofibroblast differentiation, 7) epithelial-to-mesenchymal transition (EMT), 8) nicotine receptors and responses, 9) mitochondrial damage and oxidative stress, and (10) autophagy.

exposure, and NSC also served as targets of EC aerosols via the olfactory route. Stem cells were also used to detect mitochondrial stress.

TIER 1 SCREEN:

Cytotoxic screening using the MTT assay

In the tier 1 screen, the MTT assay was used assess the cytotoxicity of menthol and tobacco-flavored e-liquids and aerosols with hPFs and A549 cells (Fig 4.2 and Table S4.1). MTT measures mitochondrial reductase activity. Because mitochondria are often targets of toxicants, the MTT assay provides an excellent initial screening step. This step could also be performed using other assays, such as the neutral red uptake assay [36].

E-liquids and aerosols were tested on hPFs and A549 cells using three-fold dilutions with 1% and 6 TPE being the highest concentrations tested (Supplementary Figs. 4.2 and 4.3). Each product was classified into one of four categories based on its cytotoxicity: (1) neither the liquid nor the aerosol was toxic (Figs. 4.2A and B); (2) the e-liquid, but not the aerosol, was cytotoxic (Figs. 4.2C and D); (3) both the fluid and aerosol were toxic (Figs. 4.2 E and F); or (4) the aerosol was toxic for some cartomizers within a brand (Fig. 4.2G and H). Table 4.1 summarizes the cytotoxicity data and shows the percent inhibition for cells exposed to 1% e-liquid or 6TPE aerosol in comparison to untreated controls. Parentages < 70% (IC70) of the untreated control were considered cytotoxic by International Organization for Standardization (ISO 10993-5). The percent inhibition values were averaged for three replicates for e-liquids (indicated in the second column), and aerosols generated from three different cartomizer samples (indicated in fourth column). The aerosols (in TPE) were converted to average percentages for direct comparison to fluid data (Table S4.1).

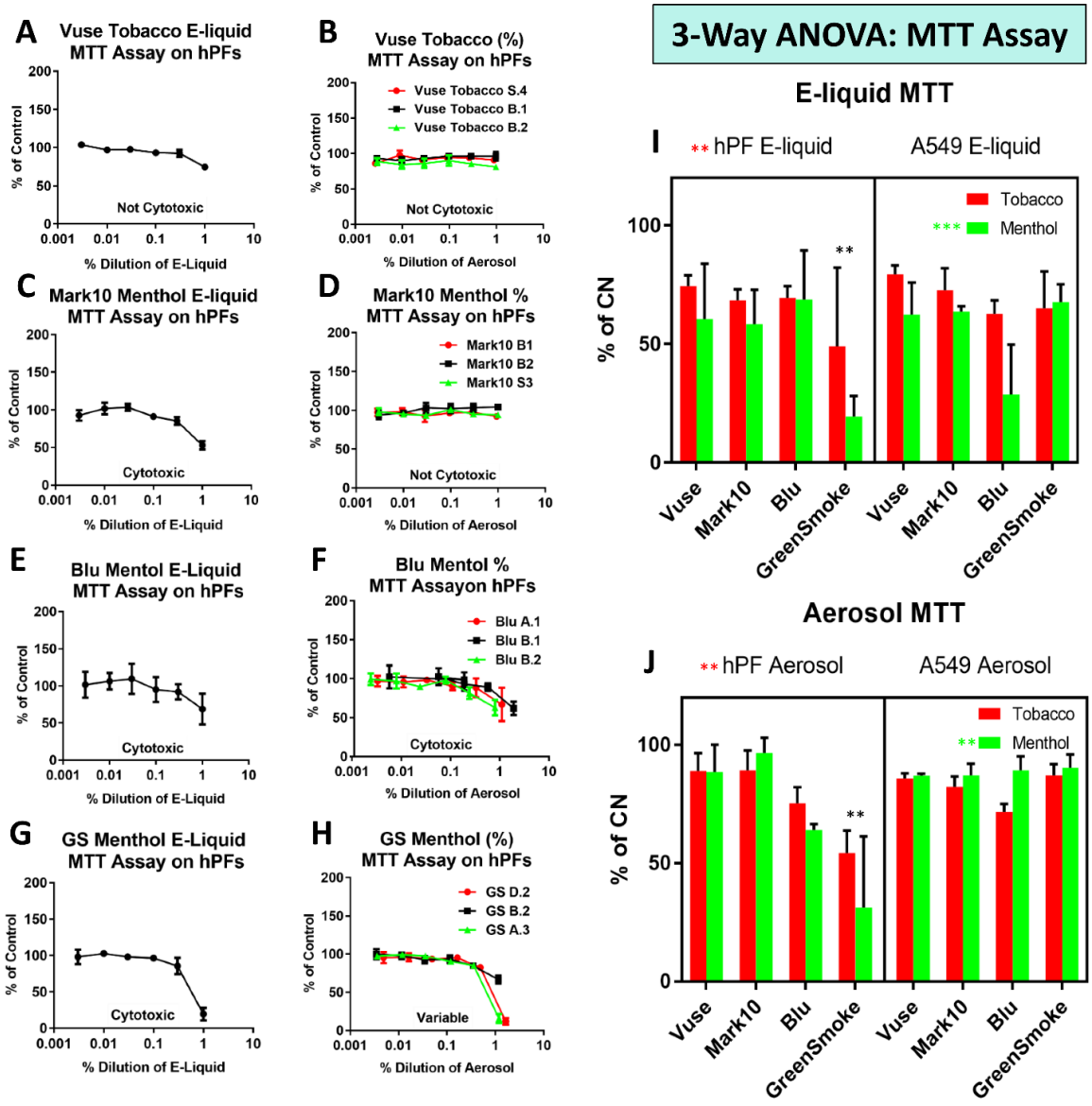

Figure 4.2: Tier-1 Screen for Cytotoxicity. E-liquids and aerosols from five brands of EC were screened in the MTT assay using hPFs and A549 cells. Both menthol and tobacco flavored EC were used for each brand. Liquids (A, C, E, and G) and the corresponding aerosols (B, D, F, and H) from four brands were tested with hPFs. E-liquid data are plotted as means ± SEM of three independent experiments. The three experiments are plotted individually for aerosols to show the variation in toxicity between cartomizers. (I-J) Bar graphs showing average effects of e-liquids (I) and aerosols (J) on hPFs and A549 cells. The asterisks (*) represent factors that were significantly affected by treatments.

Table 4.1. MTT Cytotoxicity Summary. The percent inhibition (in comparison to untreated controls) of hPFs and A549 cells exposed to 1% e-liquids or 6TPE aerosol doses).

Brands (hPF)	*E-liquid (% Inhibition)	**Cytotoxic (<70%)	***Aerosol (% Inhibition)	Cytotoxic (<70%)
Vuse Tobacco	74.3 ± 4.6	No	89.2 ± 8.8	No
Vuse Menthol	58.5 ± 20.5	Yes	88.7 ± 16.5	No
V2 Tobacco	69.6 ± 1.2	Yes	81.5 ± 12.3	No
Mark10 Tobacco	68.3 ± 4.7	Yes	89.5 ± 10.3	No
Mark10 Menthol	53.0 ± 9.5	Yes	96.9 ± 7.2	No
Blu Tobacco	69.4 ± 5.1	Yes	75.4 ± 13.4	No
Blu Menthol	68.8 ± 20.9	Yes	63.8 ± 12.7	Yes
GreenSmoke Tobacco	49.0 ± 33.3	Yes	56.6 ± 11.0	Yes
GreenSmoke Menthol	19.4 ± 8.6	Yes	31.4 ± 27.6	Yes

Brands (A549)	*E-liquid (% Inhibition)	**Cytotoxic (<70%)	***Aerosol (% Inhibition)	Cytotoxic (<70%)
Vuse Tobacco	79.3 ± 3.8	No	86.2 ± 7.1	No
Vuse Menthol	62.3 ± 13.7	Yes	87.0 ± 6.2	No
V2 Tobacco	84.7 ± 8.0	No	82.1 ± 6.9	No
Mark10 Tobacco	74.4 ± 7.0	No	82.2 ± 9.8	No
Mark10 Menthol	64.5 ± 2.9	Yes	92.5 ± 3.5	No
Blu Tobacco	62.7 ± 5.7	Yes	78.3 ± 12.6	No
Blu Menthol	28.7 ± 21.1	Yes	80.8 ± 8.4	No
GreenSmoke Tobacco	65.0 ± 15.5	Yes	87.1 ± 8.0	No
GreenSmoke Menthol	71.0 ± 6.1	No	92.9 ± 5.6	No

* Values are Avg ± s.d. of 3 replicates for 1% e-liquids

** IC70 values from MTT curves (Cytotoxic = 70% inhibition)

***Values are Avg. ± s.d. of 3 different cartomizers for 6TPE aerosols

A three-way ANOVA was used to compare brands, flavors (tobacco vs. menthol), and cells (hPFs vs. A549 cells) (Figs. 4.2I and J). Bonferroni correction was conducted in Minitab on the MTT percent of control values for 1% e-liquids. Post-hoc analysis (on Cell Type x Brand) showed that GreenSmoke e-liquids were statistically significant in comparison to Blu (p=0.001) and Mark10 (p=0.003) e-liquids on hPFs (shown as black ** on Fig 4.2I). hPFs were more affected than A549 cells (p=0.001) by GreenSmoke e-liquids (shown as red ** on Fig 4.2I). And post-hoc analysis (on Flavor) showed that menthol e-liquids were more cytotoxic (p=0.001, shown as green ** on Fig 4.2I). Post-hoc analysis (on Cell Type x Brand) showed that Greensmoke aerosols were also statistically significant in comparison to Blu (p=0.000), Mark10 (p=0.000), and Vuse

(p=0.000) aerosols on hPFs (shown as black ** on Fig 4.2J). hPFs were more affected than A549 cells (p=0.000) by GreenSmoke aerosols (shown as red ** on Fig 4.2J). And post-hoc analysis (on Cell Type x Flavor) showed that menthol aerosols were more cytotoxic on hPFs (p=0.000, shown as green ** on Fig 4.2J). For some EC brands, there was significant variability in the cytotoxicity. For example, different cartomizers of GreenSmoke menthol produced aerosols with varying levels of cytotoxicity, in agreement with other reports of significant variability in performance within EC brands [30,37]. Specifically, the B.2 menthol cartomizer was significantly less cytotoxic than the D.2 or A.3 cartomizer (Fig 4.2H).

Morphological assessment

A second endpoint, cell morphology, was used in the Tier 1 screen to maximize the chances of detecting EC products of interest. This endpoint can be acquired either before adding the MTT reagent to cells or it can be obtained in separate imaging trials. Phase-contrast images from hPFs treated with aerosols from different GreenSmoke menthol cartomizers were compared. D.2 aerosols resulted in a rapid (as early as a few hours) rounding of cells (Figs. 4.3A -C), whereas B.2 aerosols had fewer rounded cells (Figs. 4.3D).

EC products that were not highly cytotoxic were further investigated using live cell imaging in a BioStation CT to assess changes over time. This revealed that Vuse-treated A549 cells gained an EMT-like phenotype over a period of a few days. They transitioned from the normally cobble-stone morphology (Fig. 4.3E) to an enlarged morphology in e-liquid (Fig. 4.3F) and a spindle-shape in aerosol-treatment (Figs. 4.3G and H). There was also a loss of cell-to-cell contacts and an increase in cell motility.

TIER 2 SCREEN:

Based on the results of Tier 1, we proceeded to Tier 2 screening with: (1) GreenSmoke on the more sensitive hPFs/mNSCs using key doses from the MTT curves, and (2) Vuse for further analysis on A549 cancer cells. Some of the experiments in Tier 2 were performed using a concentration of liquid or aerosol that produced no effect in the MTT assay, referred to as the MTT NOAEL (no observed adverse effect level).

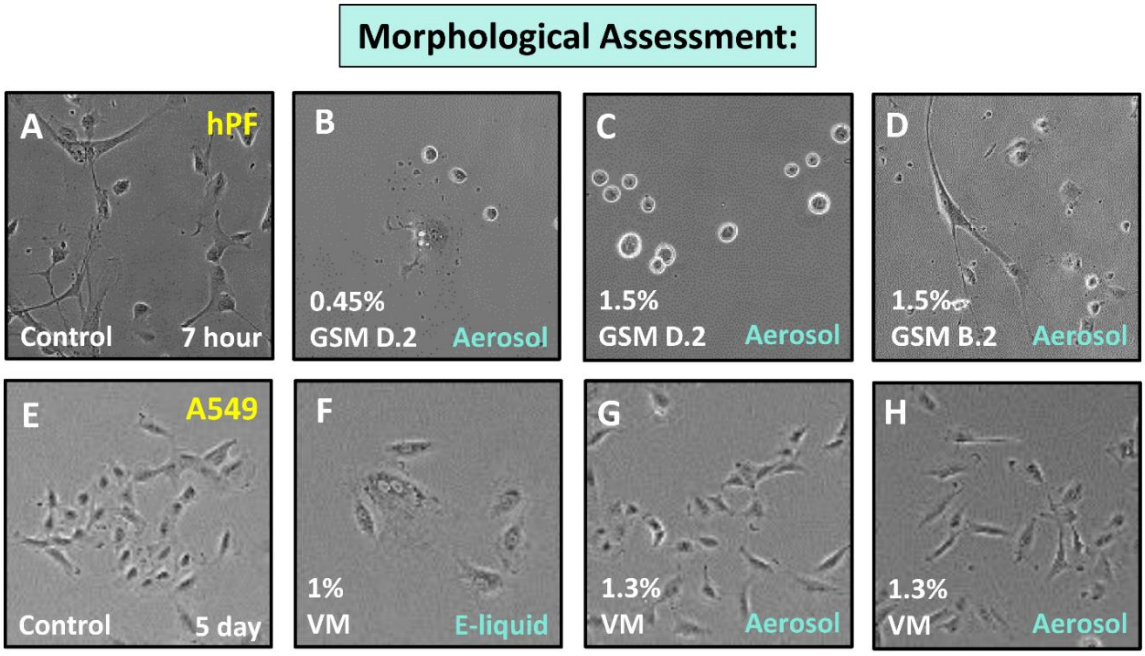

Figure 4.3: Tier-1 Screen for Morphological Effects. E-liquids and aerosols from EC were screened using morphological assessment in hPFs and A549 cells. (A-D) Phase-contrast micrographs of hPFs treated with aerosols from the GreenSmoke menthol D.2 cartomizer (B, C) and B.2 cartomizer (D), showing variability in morphological effects. D.2 aerosols were more toxic resulting in cell rounding; whereas, B.2 aerosols caused cell fragmentation. (E-F) Phase-contrast micrographs of A549 cells after 5 days of treatment with Vuse, revealing morphological changes resembling EMT. Normally cobble-stone control cells (E) transitioned to an enlarged phenotype in the e-liquid treatment (F) and spindle-like mesenchymal phenotype in the aerosol treatments (G-H).

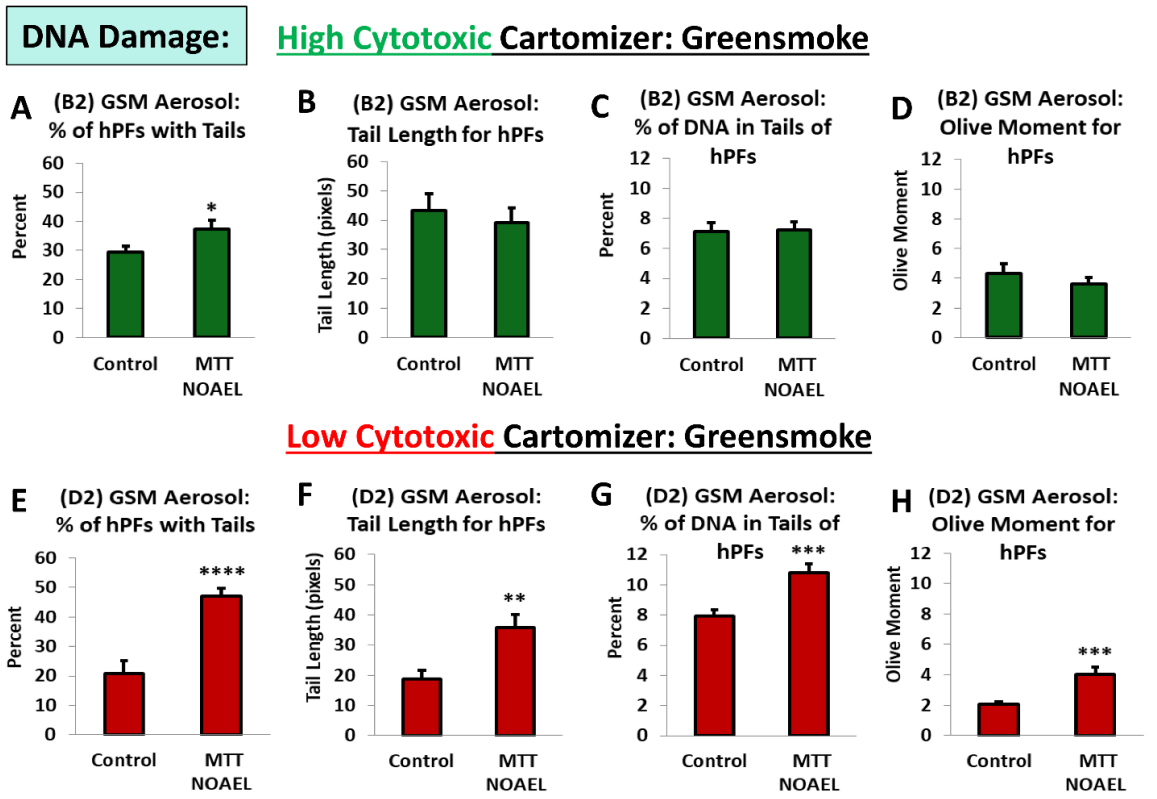

Figure 4.4. COMET Assay for DNA Damage. (A-B) hPFs were treated for 3 hours with aerosols from GreenSmoke menthol cartomizer B.2 (A) or D.2 (B), and the COMET assay was performed. Graphs show percent of cells with comet tails, average tail length, percent of DNA in the tail, and Olive moment. Each bar is the mean ± SEM of three independent experiments. $p<0.05$ = *, $p<0.01$ = **, $p<0.001$ = ***, and $p<0.0001$ = ****.

DNA Damage

To assess the effects of EC liquids and aerosols on DNA strand breaks, the Comet assay (single cell gel electrophoresis) was performed on hPFs following 3 hours of treatment at the MTT NOAEL concentration. The percentage of hPFs with tails, tail length, % of DNA in the tail, and Olive moment (tail length × fraction of DNA in tail) were quantified using the CometScore software. Aerosols from the D.2 and B.2 GreenSmoke cartomizers, which performed differently in the MTT assay, were compared in the Comet assay (Fig 4.4). While the B.2 cartomizer reached

significance only for percent of hPFs with tails (Fig 4.4A), the D.2 cartomizer produced significant effects for each of the Comet endpoints (Figs. 4.4E-H). Table S4.2 summarizes the Comet assay results for aerosols from other cartomizer products. Some products, such as Vuse produced little or no effect, while most of the Mark10 products (e.g. Mark10-C1, B1 and S2) produced significant effects in the Comet assay.

LIVE CELL IMAGING ASSAYS:

Proliferation assay

hPFs and A549 cells treated with e-liquids and aerosols were imaged live in a BioStation CT; videos were then segmented using CL-Quant image analysis software, and the total area/field

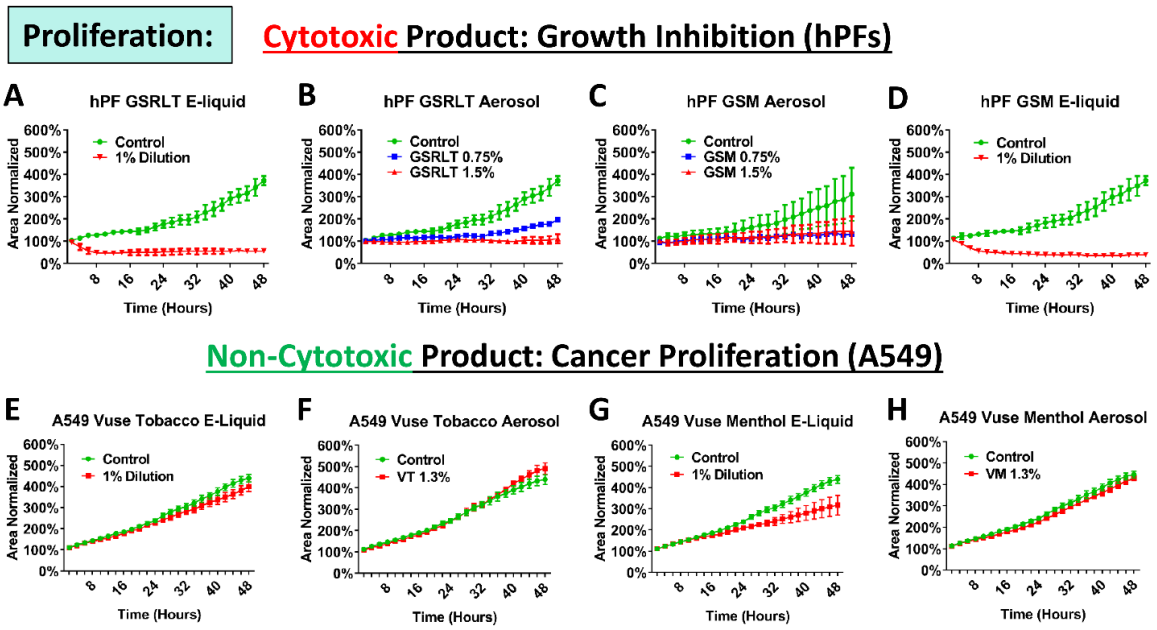

Figure 4.5. Cell Proliferation using Live Cell Imaging. Effects of EC e-liquids and aerosols on cell proliferation were assessed using live cell imaging. (A-D) Proliferation (area normalized to the initial time point) curves for hPFs treated with GreenSmoke e-liquids (A, C) and aerosols (B, D) for 48 hours. (E-H) Proliferation curves for A549 cells treated with Vuse e-liquids (E, G) and aerosols (F, H) over 48 hours.

(normalized to the initial time point) was plotted over 48 hours to determine if treatment inhibited or enhanced cell growth (Fig. 4.5). Treatment with 1% solutions of menthol or tobacco flavors of GreenSmoke completely inhibited hPF growth (Figs. 4.5A and C), in agreement with the MTT assay. The aerosols likewise inhibited growth in a concentration-dependent manner (Figs. 4.5B and D).

To determine if ECs could increase cell proliferation, Vuse cartomizer that produced no effect in the MTT assay were tested using A549 cancer cells. A549 cells were chosen as proliferation of cancer cells would be concern (Figs. 4.5E-F and H) No significant stimulation of cell growth was observed with liquid or aerosol from the Vuse products (Figs. 4.5E - H).

Cell attachment and spreading assays

To determine if the cell shrinkage observed in the morphology assay in Tier 1 was due to attachment defects, hPFs were plated and treated with GreenSmoke menthol 0.75% and 1.5% aerosols either simultaneously with plating or alternatively after pre-attachment for 2 hours (Fig 4.6). The pre-attached cells, which had spread by the time treatment started (Fig 4.6D), underwent cytoskeletal retraction that often caused cell fragments to tear off of the main body of the cells (shown in yellow arrows in Fig 4.6E). Some of the pre-attached cells were able to recover and spread (green arrows in Figs. 4.6F, L). In contrast, plating and treating cells simultaneously produced more round cells that were unable to recover after treatment removal (red arrows indicate cells that appear apoptotic in Figs. 4.6I and O). Quantification showed that most cells rounded, but attaching cells had significantly more rounding, especially at the earliest timepoints (Figs. 4.6P and Q). After 6 hours, the treatment was removed in order to evaluate the ability of hPFs to recover from cell rounding (Figs. 4.6R and S). At the higher concentrations, there was minimal recovery and no statistically significant difference between pre-attached or attaching cells (Fig 4.6R).

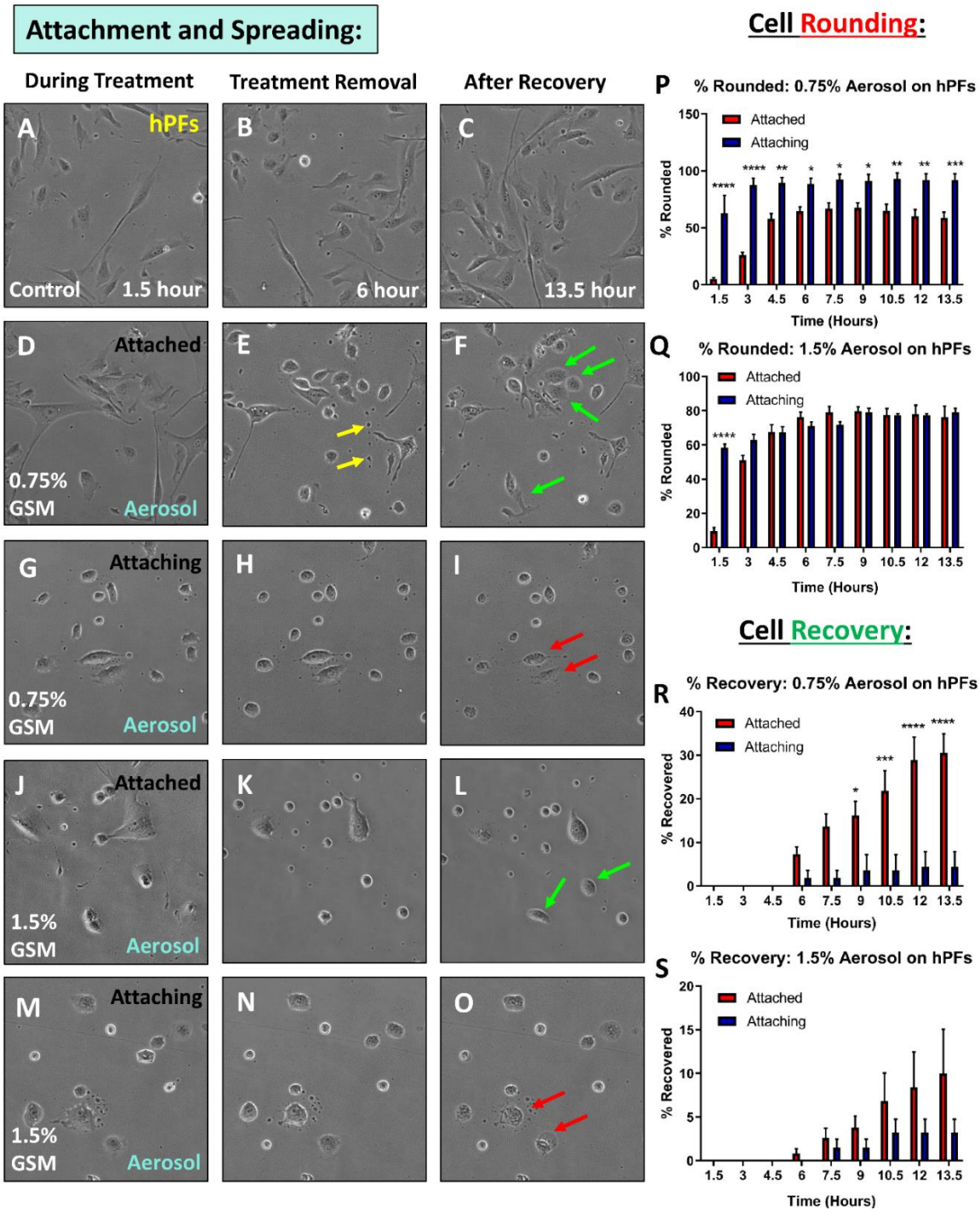
Attachment and Spreading:
During Treatment
Treatment Removal
After Recovery
A
hPFs
Control
1.5 hour
B
6 hour
C
13.5 hour
D
Attached
0.75%
GSM
Aerosol
E
F
G
Attaching
0.75%
GSM
Aerosol
H
I
J
Attached
1.5%
GSM
Aerosol
K
L
M
Attaching
1.5%
GSM
Aerosol
N
O
Cell Rounding:
P
% Rounded: 0.75% Aerosol on hPFs
Attached
Attaching
% Rounded
Time (Hours)
Q
% Rounded: 1.5% Aerosol on hPFs
Attached
Attaching
% Rounded
Time (Hours)
Cell Recovery:
R
% Recovery: 0.75% Aerosol on hPFs
Attached
Attaching
% Recovered
Time (Hours)
S
% Recovery: 1.5% Aerosol on hPFs
Attached
Attaching
% Recovered
Time (Hours)

Figure 4.6. Attachment and Spreading and Reversal of Effects. hPFs were either pre-attached for 2 hours and then treated or treated during attachment with GreenSmoke menthol aerosols from a toxic cartomizer. Recovery was assessed after 6 hours, where the treatment medium was replaced with fresh control medium. (A-C) Control cells at 1.5 hours (A), 6 hours (B), and 13.5 hours (C). (D-F) hPFs pre-attached then treated with 0.75% GreenSmoke menthol aerosol, shown during attachment (D) and after treatment removal (E-F). (G-I) hPFs treated while attaching with 0.75% GreenSmoke menthol aerosol, shown during attachment (G) and after treatment removal (H-I). (J-L) hPFs pre-attached then treated with 1.5% GreenSmoke menthol aerosol, shown during attachment (J) and after treatment removal (K-L). (M-O) hPFs treated with 1.5% GreenSmoke menthol aerosol while attaching, shown during attachment (M) and after treatment removal (N-O). (P-Q) Graphs showing percent of rounded cells in 0.75% (P) and 1.5% (Q) aerosol treatments over time. (R-S) Graphs showing recovery of cell rounding after removal of 0.75% (R) and 1.5% (S) aerosol treatments over time. In all graphs, two-way ANOVAs with Bonferroni's post hoc test were used to compare the attached and attaching conditions over time. Each bar is the mean ± SEM of three independent experiments. $p<0.05$ = *, $p<0.01$ = **, $p<0.001$ = ***, and $p<0.0001$ = ****.

However, at the lower concentration, there was a marked increase in recovery for the pre-attached cells (Fig 4.6S).

Cytoskeletal Remodeling:

Various cytoskeletal proteins such as actin and tubulin contribute to the structural integrity of the cell and can influence cell shape (rounding/collapse versus spreading). To determine the cause underlying GreenSmoke-induced cell rounding, hPFs were transfected with a tdTomato-

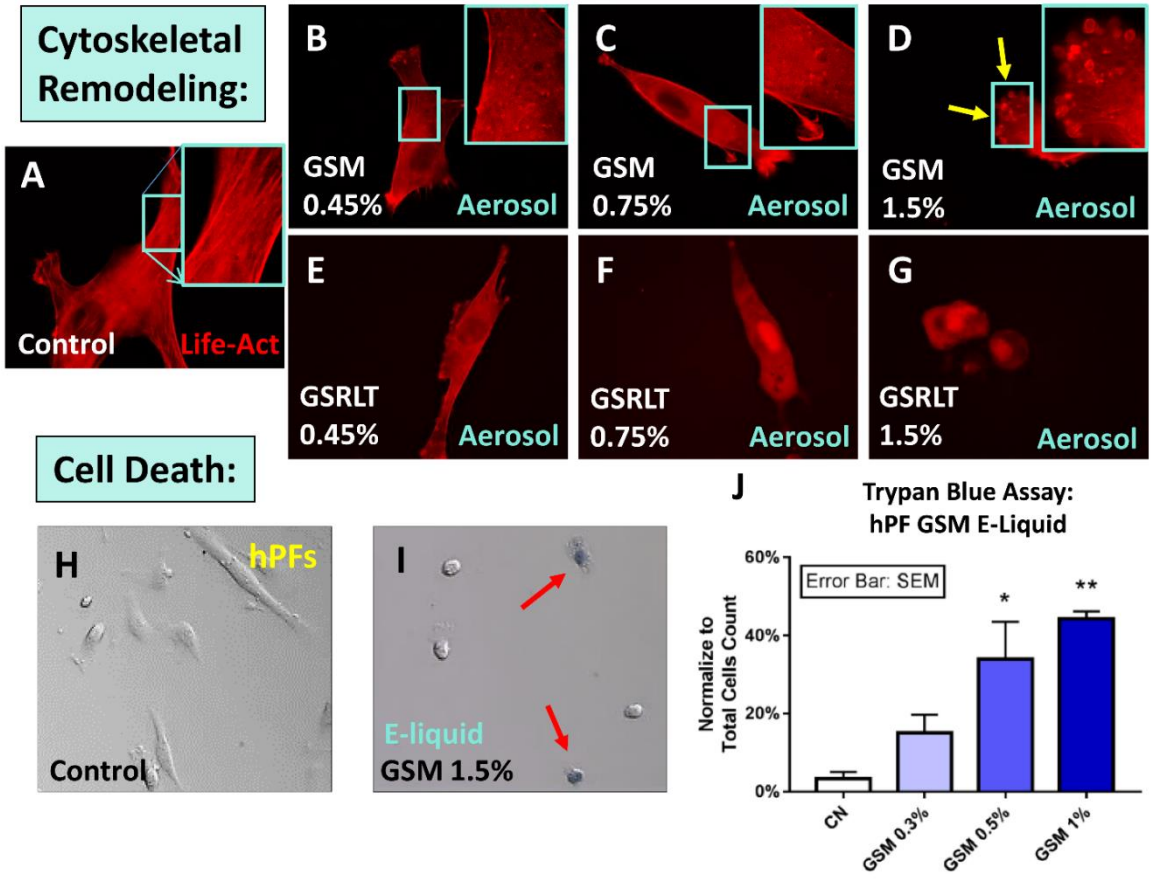

Figure 4.7. Cell Rounding, Actin Depolymerization, and Cell Death. (A-G) hPFs expressing the actin LifeAct reporter treated 24 hours with GreenSmoke menthol (B-D) and tobacco aerosols (E-G), showing actin depolymerization and cell rounding. Control (H) and 1% GreenSmoke e-liquid treated hPFs (I) were stained for Trypan blue. (J) The number of Trypan blue positive cells increased as the e-liquid concentration increased.

Lifeact plasmid to label actin microfilaments, then exposed live to either GreenSmoke menthol (Figs. 4.7B-D) or tobacco (Figs. 4.7E-G) aerosols. Control cells exhibited long polymerized actin filaments (F-actin) (Fig 4.7A). However, treatment with lower aerosol concentrations resulted in actin depolymerization (loss of actin filaments) and emergence of G-actin puncta (shown in the inserts in Figs. 4.7B and C). There was a concentration-dependent shrinking of the cytoskeleton to the point that the cell collapsed in the highest concentrations (Figs. 4.7D and G). Time-lapse videos also allowed for visualization of cell blebbing (indicted by yellow arrows in Fig 4.7D).

Cell Death

To assess the effect of GreenSmoke treatment on cell death in hPFs, a trypan blue assay was performed (Figs. 4.7H-J). The percent of trypan blue-positive cells (indicated by the red arrows in Fig 4.7I) increased with higher concentrations of GreenSmoke menthol e-liquid (Fig 4.7J. However, even at the highest and most toxic GreenSmoke menthol e-liquid concentration ((.5%), only 40% of the rounded cells were in fact dead. This suggests that cell rounding is a protective mechanism, which over time may eventually collapse leading to cell death or alternatively may reverse when the stimulus is removed.

Differentiation of Fibroblasts to Myofibroblasts

In the Tier 1 screen, Vuse did not cause cytotoxicity; however, it did alter cell morphology. To assess the MOA of Vuse on cell morphology, hPFs were exposed to Vuse aerosols and e-liquids for 24 hours followed by immunolabeling with alpha smooth muscle actin (α-SMA) (Figs. 4.8A-C). α-SMA is a marker of activated fibrogenic cells, called myofibroblasts, which are thought to contribute to fibrosis [38]. Upregulation of α-SMA can generate actin stress fibers that promote increased contractility of myofibroblasts and facilitate tissue remodeling in the lung. Exposure to

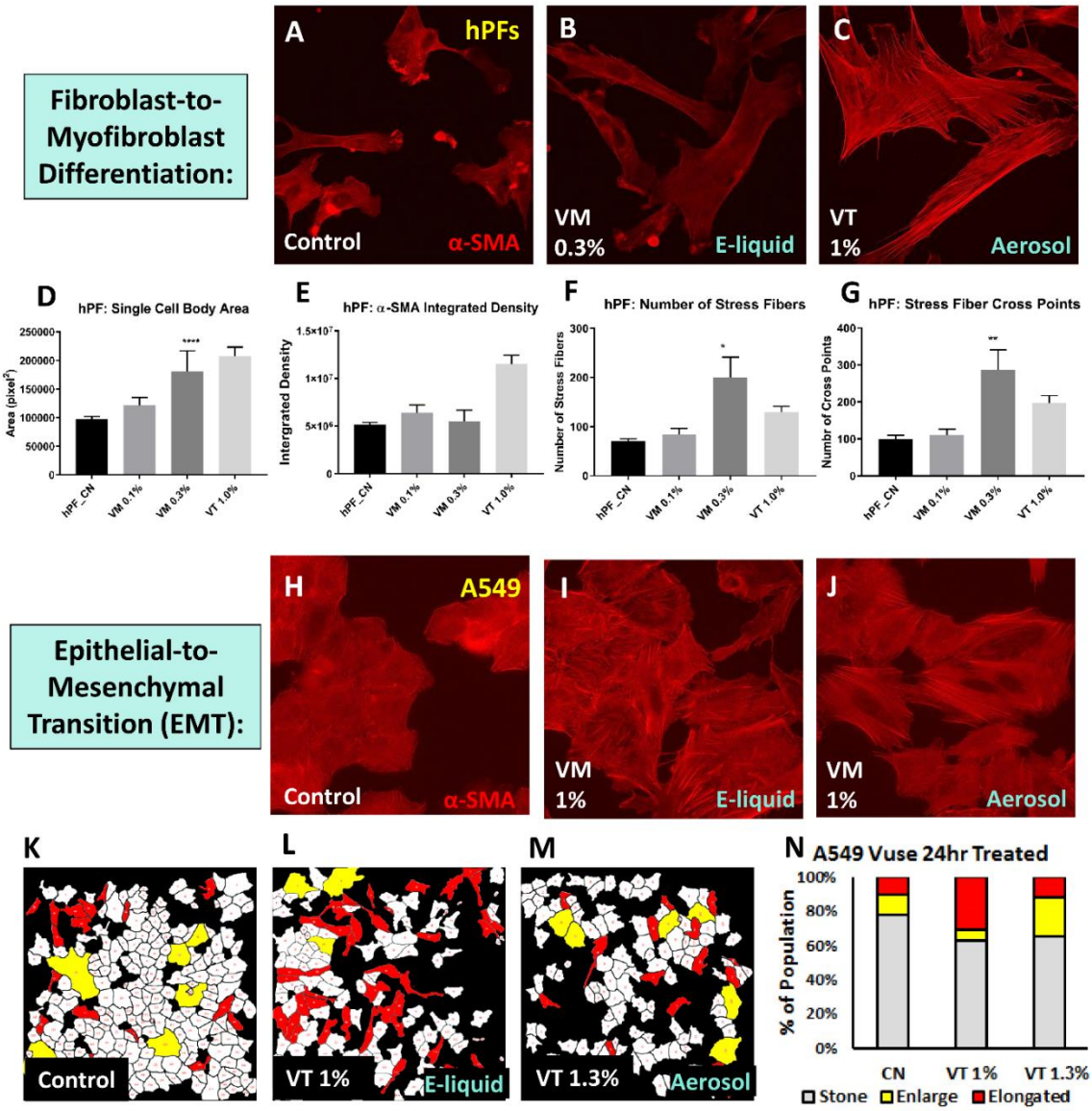

Figure 4.8. Biomarkers of Fibroblast-to-Myofibroblast Differentiation and Epithelial-to-Mesenchymal Transition (EMT). hPFs or A549 cells were treated for 24 hours with Vuse e-liquids or aerosols then labeled with an antibody to α-SMA, a marker for fibrosis and EMT. (A) Control hPFs. (B-C) hPFs treated with 0.3% Vuse menthol e-liquid (B) and 1% Vuse tobacco aerosol (C). (D) The average area of cell bodies (pixel2) were compared. (E) The integrated density of α-SMA expression (mean intensity value x area) was quantified. (F-G) The number (F) and cross points (G) of actin stress fibers were quantified. In all graphs, two-way ANOVAs with Bonferroni's post hoc test were used to compare the attached and attaching conditions over time. Each bar is the mean ± SEM of three independent experiments. $p<0.05$ = *, $p<0.01$ = **, $p<0.001$ = ***, and $p<0.0001$ = ****. (L-N) Morphology of control (L) and 24-hour Vuse e-liquid (M) and aerosol (N) treated A549 cells. White cells = cobblestone; red cells = elongated cells; yellow cells = enlarged morphology. (O) Graph showing a decrease in cobblestone and an increase in enlarged and elongated subpopulations during 24 hours of Vuse treatment.

Vuse aerosols increased the expression of α-SMA (Fig 4.8C), as assessed by an increase in total α-SMA integrated density (Fig 4.8D). This increase in smooth muscle actin was concurrent with an increase in cell size, likely due to an increase in cell spreading (Fig 4.8C). Image analysis of the stress fibers revealed an increase in their number and cross points (Figs. 4.8E-G). In the case of the 0.3% e-liquids, although there was not an increase in total α-SMA integrated density, there was an increase in the cell body area (Fig 4.8F). Also, there was an increase stress fiber number (Fig 4.8E) and cross points (Fig 4.8G), suggesting that the fibers are smaller and less polymerized.

Epithelial-to-Mesenchymal Transition in Lung Cells

We recently reported that 3-10-day exposure of A549 epithelial lung cancer cells to Vuse e-liquids and aerosols leads to an EMT, which facilitates metastasis [39]. An EMT (conversion of epithelial cells to a mesenchymal phenotype) is critical in the development of fibrosis. α-SMA is also another important biomarker that is upregulated in metastatic cancer. Here, we show that indeed A549 cells exposed to Vuse aerosols/e-liquids have increased expression of α-SMA and stress fibers (shown in bright lines in Figs. 4.8H-J). This increase in polymerized actin fibers likely contributes to changes in their cell shape from a cobblestone morphology to a more mesenchymal (spindle-shaped) phenotype.

A549 cells treated for 24 hours exhibited changes from the normal cobblestone morphology (Fig 4.8K) to the elongated and enlarged cellular phenotypes (Figs. 4.8L and M). The percent of each morphological population was quantified for control and 24 hour-treated Vuse tobacco aerosol and e-liquid cells (Fig 4.4K). As treatment time progresses, this transition becomes more pronounced in the Vuse-treated cells as seen in Tier 1 morphological assessment, shown in the 5 day A549 phase-contrast images in Figs. 4.3E-H.

Alterations in nicotine receptors and cellular responses to nicotine

Exposure to nicotine can cause changes in the number/distribution of nicotinic receptors and alter their sensitivity to nicotine [40–43]. To determine if EC treatment altered the number of nAChRs, 4-day Vuse e-liquid, aerosol, and 1% nicotine-treated A549 cells were immune-labeled with the α7 subunit of nicotinic acetylcholine receptors (nAChRs) (Figs. 4.9A-D). There was an increase in the number of receptors (red puncta in Figs. 4.9E-H) in the treated cells, indicating their upregulation during exposure to nicotine in Vuse or pure nicotine.

To determine how this increase in nAChRs affected cellular response to nicotine, we used a Gcamp5 Ca2+ reporter to measure the intracellular calcium influx upon nicotine exposure, after pre-treating cells for 4 days with EC aerosols. This reporter is comprised of a green fluorescent protein (cpGFP), calmodulin (CaM), and the Ca2+/CaM-binding "M13" peptide [44]. First, the response of normal, untreated A549 cells upon addition of a low dose of 1.1 μg/ml nicotine was tested. Before nicotine addition, the cells had low fluorescence, with variability among the cells (Fig 4.9I). After 1min of nicotine addition, there was a strong elevation of green fluorescence in most cells (Fig 4.9J). The process was repeated for cells pre-treated for 4 days with menthol (Fig 4.9K and L) and tobacco aerosol (Figs 4.9M and N). The change in intensity was quantified, revealing that the initial calcium spike at 1 min in aerosol-treated responses were damped relative to control cells (Fig 4.9O). Furthermore, the signal did not decay back down over time, which suggests that Ca2+ turnover and/or efflux mechanisms may be affected.

Assays for mitochondrial stress and oxidation of mitochondrial proteins

mNSCs were exposed to e-liquids and aerosols from tobacco and menthol-flavored GreenSmoke EC (Fig 4.10). Modules available in our open-source MitoMo software [45] were used to quantify mitochondrial number, morphology and protein oxidation. Exposure to

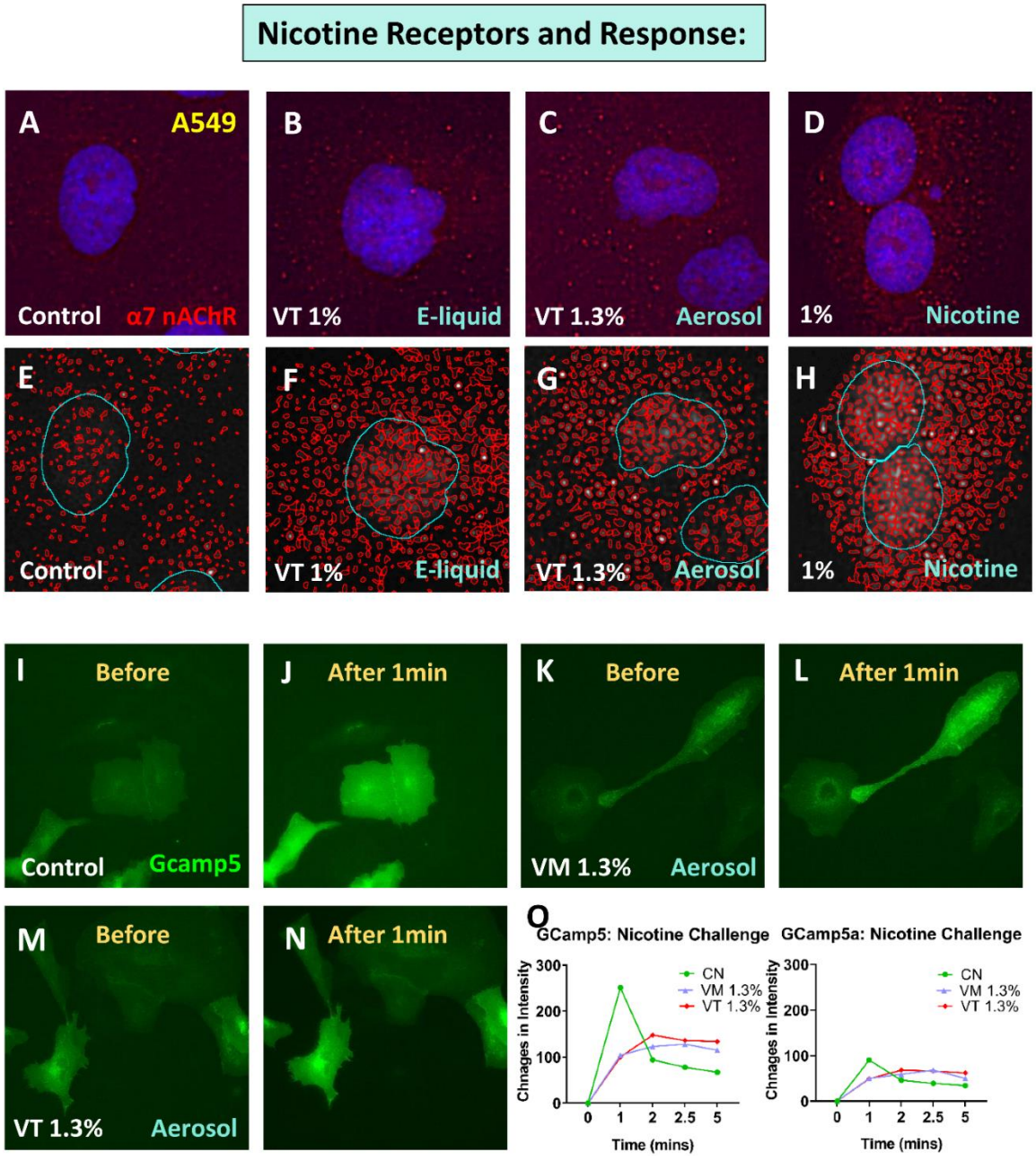

Figure 4.9. Upregulation of Nicotinic Receptors and Altered Responses to Nicotine. A549 cells were labeled with an antibody to α7 nAChR after and their calcium influx responses were tested after 4 days of Vuse and nicotine treatment. (A-D) Control cells expressed a moderate number of α7 nAChR. This number increased following treatment with 1% Vuse tobacco e-liquid (B), 1.3 % Vuse aerosol (C), or 1% of pure nicotine (D). (E-H) CL-Quant software was used to segment and count the number of α7 nACh receptors. (I-N) A549 cells transfected with a Gcamp5 calcium reporter were imaged live before (I, K, M) and 1 minute after addition of a nicotine challenge (J, L, N). (O) The change in concentration of intracellular calcium was quantified over time, where intensity values were normalized to the intensity values in the "before" timeframe (time = 0).

GreenSmoke e-liquids and aerosols resulted in stress-induced mitochondrial hyperfusion (SIMH), in which punctate mitochondria fused to form interconnected networks (Figs. 4.10A-C). The number of mitochondria significantly decreased after 24 hours of exposure, which is consistent with hyperfusion (Figs. 4.10D and E). The mitochondria were classified as punctate, networked or swollen using MitoMo software [45]. Morphological classification revealed a concentration-dependent increase in networked mitochondria and a corresponding decrease in punctate forms, confirming hyperfusion (Figs. 4.10F and G). In addition, the red/ green fluorescence ratio of the MitoTimer reporter (green-to-red shift is indictive of oxidative stress) showed a concentration-dependent increase in mitochondrial protein oxidation (Figs. 4.10H and I).

Assay for autophagy

We next applied live phase-contrast imaging and video bioinformatics to the detection and quantification of autophagy in EC treated A549 cells. A549 cells treated with Vuse e-liquids had a rapid increase in the number of intracellular vacuoles (pseudo-colored as red puncta in Figs. 4.11B and C). These vacuoles were confirmed to be autophagosomes by transfecting the e-liquid-treated cells with an LC3 (microtubule-associated protein 1 light chain 3 beta) reporter (Fig 4.11D). A fluorescent shift from red-to-yellow-to-green indicates a loss of acidification within the autophagosomes, which can result in the loss of their ability to digest damaged cargo.

DISCUSSION

We used a two-tiered screening strategy to first identify EC liquids and aerosols that were cytotoxic to lung cells in the MTT and morphological assays, and then in tier 2 to determine the MOAs of those products that were most effected in tier 1. By including morphological analysis in tier 1, we were able to identify Vuse (which was not cytotoxic in the MTT assay) as a candidate

for further evaluation. The assays in tier 1 are rapid and adaptable to most labs. Three-way ANOVA analysis of the MTT data showed significant effects on: (1) flavor (menthol was more potent than tobacco), (2) cell type (hPFs were more sensitive than A549 cells), and (3) EC brand (GreenSmoke was the most cytotoxic of the four brands studied). There were variations in toxicity across cartomizer-style EC brands, as well as within brands (different GreenSmoke cartomizers). Tier 2 identified the MOA for those products (highly cytotoxic GreenSmoke and Vuse which induced morphological changes) that moved through the pipeline from tier 1.

The Comet and mitochondrial assays were the most sensitive assays. Mitochondrial morphology was the most sensitive assay, detecting SIMH in mNSCs at concentrations of Greensmoke aerosol as low as 1.8 TPE (0.3%). Comet analysis detected DNA damage in hPFs treated with the MTT NOAEL concentration of GreenSmoke menthol aerosols (1.8 TPE corresponding to 0.45% e-liquid by weight). For GreenSmoke aerosols, the hierarchy of sensitivity for the MOAs from most to least sensitive was: (1) mitochondrial morphology in mNSC (2) DNA damage, (3) actin cytoskeletal remodeling, (4) mitochondrial protein oxidation, (5) cell death, and (6) cell proliferation and attachment. Future investigations can incorporate this information when selecting the best assays to use.

The MOA data provided insight into diseases that could develop during long-term use of EC products. There are several possible routes for development of myofibroblasts: direct differentiation of fibroblasts, as well as EMT of epithelial cells [38,46,47]. Treatment with Vuse aerosol caused fibroblast-to-myofibroblast differentiation and an EMT in A549 cancer cells. Vuse treatment increased a-SMA stress fibers, which can increase the contractile force that participates in tissue remodeling during fibrosis, and generate fibrotic lesions and scarring in the lung [48]. Contractile activity of myofibroblasts can also lead to activation of transforming growth factor beta 1 (TGF-β1), a key EMT inducer [49]. Myofibroblasts, epithelial cell barrier disruption, and

oxidative damage can all contribute to obstructive pulmonary disease (COPD) and idiopathic pulmonary fibrosis (IPF), two chronic lung diseases.

An EMT allows cells to acquire mesenchymal features, which are implicated in the pathogenesis of lung fibrosis as well as cancer metastasis [50–52]. EMT of cancer cells could have important implications for metastasis [51,52] of a pre-existing tumor in former or heavy cigarette smokers who may be at risk for cancer. Previous research has shown EMT in lung cancer cells exposed to conventional cigarette smoke [50,53–57]. Although not shown directly in our work, we speculate that the high nicotine concentration in Vuse was driving the EMT phenotype. Nicotine has been shown to promote an EMT in other cancer cell types [54,58].

Another important MOA identified in Vuse was upregulation of nicotinic receptors and alterations in their sensitivity to nicotine, which can have implications for nicotine tolerance [40,43]. The Surgeon General recently warned that nicotine dependence via EC use, particularly addiction of adolescents, is a growing concern of "epidemic" proportions [2]. Nicotine can have harmful side effects on the developing adolescent's brain leading to increased susceptibility to addiction and psychological conditions. Potential exposure to nicotine is alarming due to: (1) high-nicotine content products such as Vuse and JUUL, (2) compensatory vaping profiles leading to greater exposure, (3) unlabeled or mislabeled ECs and/or do-it-yourself e-liquids that may contain more nicotine than the users realizes [25,26]. For example, one flavored JUUL pod equates to 20 cigarettes worth of nicotine [59], and most youth who experiment with tobacco begin with a flavored product [60]. Nicotine can also. The National Academies of Science, Engineering, and Medicine (NASEM) reported substantial evidence that EC use by youth increased their risk of switching to conventional cigarettes [6]. The amount of nicotine, its protonated state, and delivery (emission) profile varies within EC brands [61,62]. Another study revealed that using glycerol (versus PG) in e-liquids provides a higher release of nicotine from the aerosol [63]. All of these

factors can affect the amount of nicotine uptake via different EC products (e.g. as evidenced in high urinary cotinine levels among pod users [64]), and hence their abuse potential. In our studies, A549 cells showed evidence of nicotine tolerance after sub-chronic exposure to Vuse aerosols. Therefore, an in vitro screening method to assess development of nicotine tolerance is a valuable tool and should be included as part of toxicological screening for ECs. The fact that Vuse-treated cells did not exhibit the same calcium decay profiles as controls suggests that Ca2+ turnover and/or efflux may be affected in cells following prolonged exposure to nicotine. More research is needed to investigate the underlying mechanisms associated with these observations.

Exposure to high levels of nicotine during pregnancy can also be a major risk factor for a developing fetus, leading to increased morbidity and developmental defects [65]. Since functional nAChRs are present at very early stages of neuronal development, exposure to any nicotine-containing device during this critical time should be avoided. ECs are often recommended to pregnant mothers as harm-reduction alternatives; however, our data suggest that they should be advised to abstain from EC use [66].

In our studies, NSCs were used as an in vitro model since they may be targets of inhaled EC aerosols that pass directly to the brain through the olfactory tracts [67]. The mitochondria of NSCs proved to be particularly sensitive to EC aerosols, which would make the excellent assays for detecting stress. The MOA of aerosols on mitochondria was characterized as stress-induced mitochondrial hyperfusion (SIMH), a transient survival response accompanied by increased oxidative stress. Bahl et. al. (2016) previously characterized this response in thirdhand smoke (THS) treated mNSCs [68]. In another recent paper, we showed that these mitochondrial stress responses were attributed to the high nicotine in ECs [69], further demonstrating that ECs with high nicotine content are unsafe. Damage to stem cells can cause harm to: (1) a developing embryo during gestation, (2) infants and adolescents whose brains are still developing, and (3) adults, which

need stem cells for normal tissue repair/homeostasis throughout their entire life. The mitochondrial findings are critical considering that nicotine is now widely available in EC refill fluids and as a pure chemical for use in do-it-yourself EC products. In a broader sense, any nicotine containing product may likewise stress stem cells with long-term repercussions for users and passively exposed individuals.

Exposure to Vuse e-liquids also induced the formation of autophagosomes. A previous paper has reported that EC aerosols cause autophagy [70]. Autophagy is an important process in normal cell homeostasis, as well as cancer therapeutics [71–74]. Autophagy can also lead to cell death [75]. Defects in autophagy clearance, as indicated by the loss of the GFP signal from the autophagosome reporter in Vuse e-liquid treated A549 cells, indicates the inability of the cells to digest damaged cargo. Moon et. al. (2014) have shown that endoplasmic reticulum (ER) stress causes autophagy activation through c-Src, which can lead to induction of an EMT in epithelial cells [76]. This may serve as a potential explanation for the EMT observation and necessitates follow-up investigation.

The MOAs for hPFs treated with cytotoxic GreenSmoke were DNA damage, mitochondrial and oxidative damage, inhibition of proliferation, cytoskeletal depolymerization, and cell death. DNA damage and oxidative stress can both contribute to the development of cancer [77–80]. However, considering that hPFs rounded up (attachment defects) within a few hours, the impact of GreenSmoke might be much more immediate in the form of cell damage/death in the lung tissue. Detachment from the matrix can also activate a specialized form of apoptosis, called anoikis [81]. Oxidative stress caused by EC can induce mucus secretion in the lung, which can make the airways susceptible to infection and lead to bronchitis [65]. Oxidants can also cause ER stress and an unfolded protein response (UPR) [82], two MOAs that could be added to the screening pipeline in future studies.

Cell rounding and subsequent cell death in GreenSmoke-treated hPFs may have occurred because the actin cytoskeleton acted as a detector of environmental stressors. The actin cytoskeleton can sense oxidative stress and can regulate apoptotic signaling [81]. In A549 cells, knockdown of α5- and α3-nAChR suppressed cell adhesion and lead to apoptotic responses [83]. Furthermore, the TRPM8 receptor (which gets activated by menthol) is linked to regulation of cell adhesion (cell rounding and loss of matrix adhesion), which is coupled to Ca2+ influx through these channels [84]. The fact that cell rounding was reversible in some cells is consistent with the idea that rounding is a dynamic protective response contingent upon the presence of toxicants.

Menthol-flavored ECs generally had higher toxicity in both tier 1 and tier 2 assays. This is consistent with previous reports that menthol is cytotoxic [85]. It can inhibit fatty acid-induced cell respiration and can increase osmotic swelling in mitochondria [86]. Menthol can be found at high concentrations in some EC products [11,21]. Menthol also enhances abuse liability for ECs [6,87], decreases nicotine's clearance by two-fold, increases AUC (area under the plasma drug concentration-time curve) which reflects exposure to drug, and increases the intensity of withdrawal signs [88]. Alsharari et al. (2015) showed that chronic exposure to menthol increases the levels and distribution of α4 and β2 nAChRs in the hippocampus, prefrontal cortex and striatum of mice brains [88]. One study reported that consumers using menthol ECs took at least three times as many puffs as those using non-mentholated products [89]. Menthol may improve the appeal of ECs by its coolness/minty flavor and analgesic effect (reducing the harshness of high nicotine-containing ECs) [90]. Menthol may also act by stimulating the trigeminal nerve to elicit a "liking" response for a tobacco product [91].

In conclusion, our two-tiered toxicity screen identified EC products that were cytotoxic or exhibited a potentially pathogenic response and characterized their MOAs. Our screening strategy could be applied to any toxicants including other new EC products as they are introduced. The

video bioinformatics analysis tools used in tier 2 are freely-available on the Internet and would facilitate quantification of the MOA assays [39,45,92]. While eight MOA assays were included in our study, this number and the specific assays could be changed depending on the goals of a particular project.

MATERIALS & METHODS

Electronic Cigarettes: Cartomizer-style ECs, EC starter kits, and refill cartridges were purchased through the internet or local retailers. Ten popular EC brands manufactured by US Tobacco companies were selected: (1) GreenSmoke Menthol (GSM) and Red Label Tobacco (GSRLT) from Altria; (2) BluCig Menthol and Tobacco from Lorillard (now Imperial Tobacco Group), (3) V2 Tobacco from Swedish Match, (4) Vuse Menthol (VM) and Tobacco (VT) from RJ Reynolds, and (5) Mark10 Menthol and Classic Tobacco from Nu Mark (formerly Altria). These products were selected as low-voltage EC brands that have high distribution rates and sales.

Aerosol generation and cartridge fluid collection: The aerosols were generated with a custom smoking machine taking 4.3 sec puffs (typical EC user topography) as previously described [93]. 6 total-puff-equivalent (TPE) (6 puffs of aerosol dissolved per 1 mL of medium) were collected in a 250 mL round-bottom flask suspended in an ethanol/dry ice bath. The aerosols were then thawed, filtered using 0.2µm Supor filter membranes (# 4612, PALL Corporation) and flash frozen in a dry ice/ethanol bath for long-term storage in -80oC. The refill cartridges were dissected using forceps, inner and outer fibers were removed and centrifuged in a MiniElute Spin column (Qiagen, Valencia, CA) at 14000 rpm for 8 minutes in an Eppendorff Centrifuge to separate the fluid from the fibers [7]. 1% dilution by volume of e-liquid samples were prepared from the EC fluids. Each EC brand was smoked at the lowest airflow rate that produced a consistent puff.

Mitochondrial Damage:

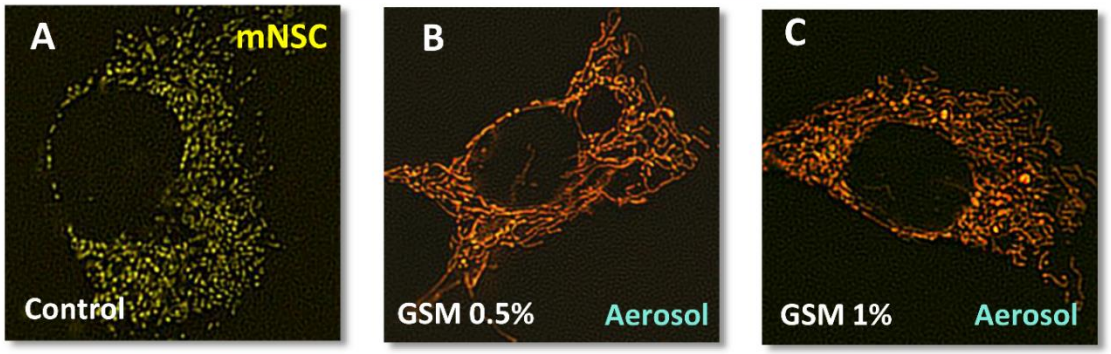

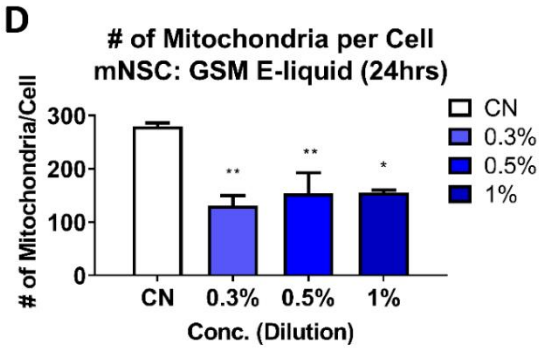

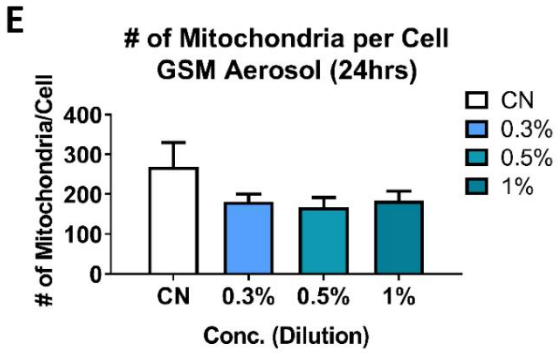

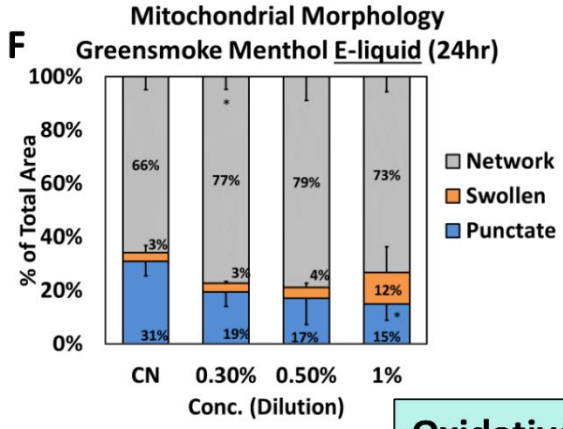

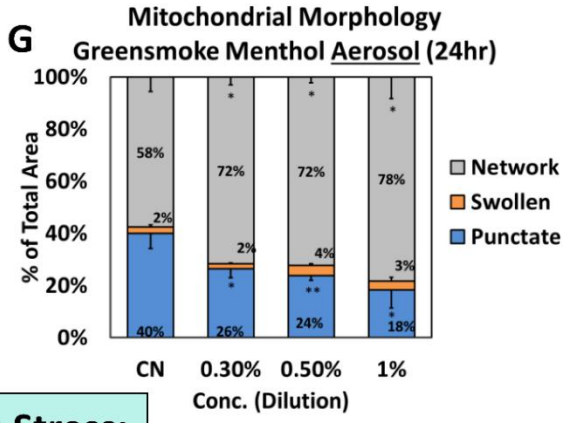

Oxidative Stress:

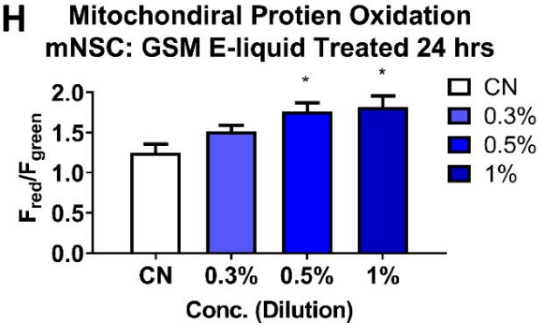

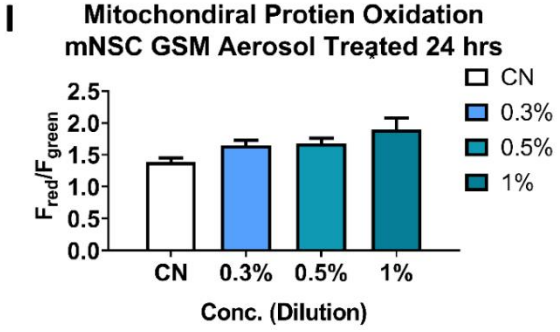

Figure 4.10. Mitochondrial Numbers, Morphology, and Protein Oxidation. mNSCs expressing a MitoTimer reporter were treated with GreenSmoke e-liquids and aerosols for 24 hours and their number, morphology, and protein oxidation were assessed. (A-C) Fluorescent images of control (A), 0.5% (B) and 1% (C) GreenSmoke menthol aerosol-treated mNSC-MitoTimer cells. The number of mitochondria per cell for menthol-flavored GreenSmoke e-liquid (D) and aerosol (E) treated cells. (D-E) Classification of mitochondrial morphology as punctate, networked or swollen for the e-liquid (H) and aerosol (I) treatments. Mitochondrial protein oxidation following treatment with E-liquid (H) or aerosol (I). Each point in the graphs is the mean ± SEM of three independent experiments. $p<0.05$ = *, $p<0.01$ = **.

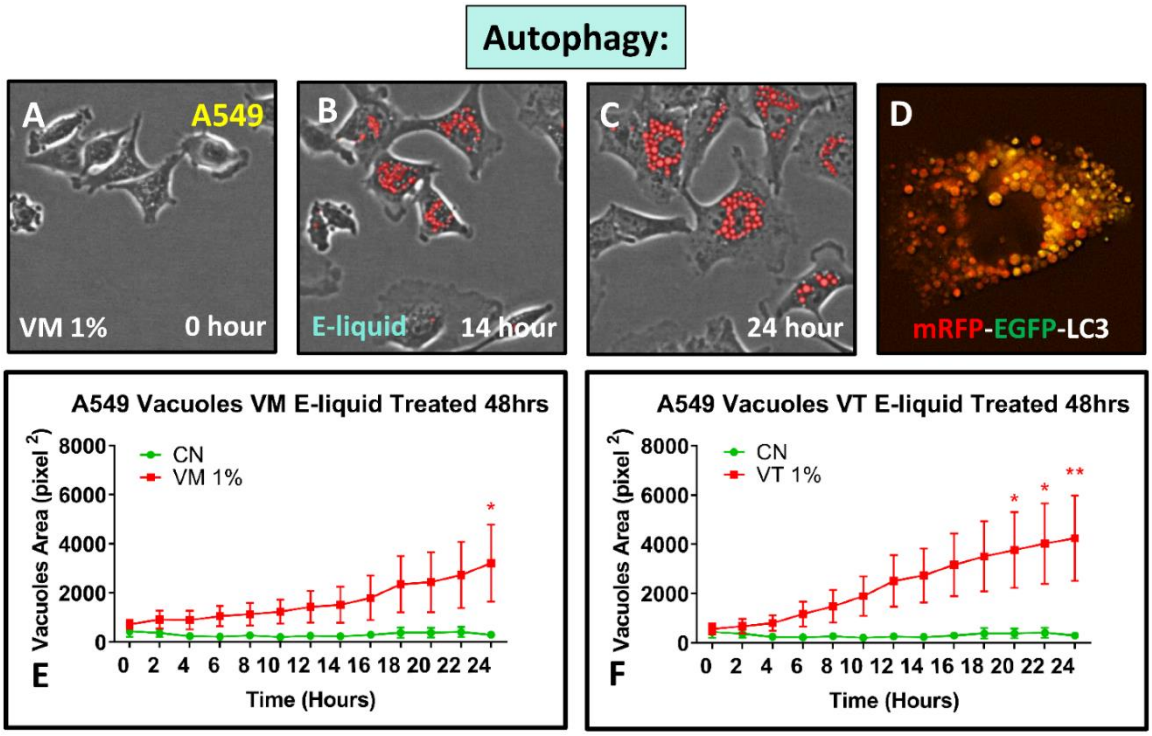

Figure 4.11. Detection and Quantification of Autophagy. A549 cells treated Vuse e-liquids had an increase in intracellular vacuoles that were identified as autophagosomes. (A-C) Phase-contrast images of A549 cells treated over 28 hours develop vacuoles which are segmented and highlighted as red vesicles. D) Vuse e-liquid treated A549 cells transfected to express an mRFP-GFP-LC3 reporter that labels autophagosomes. E-F) The total area of segmented vacuoles from the phase-contrast images are plotted over 24 hours. The Vuse menthol (E) and tobacco (F) e-liquids conditions were compared to untreated controls. Each bar is the mean ± SEM of three independent experiments. $p<0.05$ = *, $p<0.01$ = **.

The average aerosols concentrations in TPE were converted to percentages for direct comparison to fluid data. The weight/puff for each brand and the density of the e-liquids were measured, and then converted to mL/puff. The percentage of e-liquid in each condition was defined as:

% = number of puffs x volume of 1 puff / volume of medium used to dissolve the aerosol

Cell Culturing: Human pulmonary fibroblasts (hPFs) (ScienCell, Carlsbad, CA) were cultured in complete fibroblast medium (ScienCell) containing 2% fetal bovine serum, 1% fibroblast growth serum, and 1% penicillin/streptomycin. hPFs were grown on poly-L-lysine (2μl dissolved per 1mL of water) coated T-25 flasks, which were prepared a day in advance. For passaging and experiments, cells were washed with DPBS and detached with 0.05% trypsin diluted in DPBS for 1 minute at 37°C. A549 CCL-185 lung epithelial cells (human type II pulmonary alveolar adenocarcinoma cells) were obtained from ATCC (Rockville, MD). A549 cells were cultured in Ham's F-12 and 10% fetal bovine serum obtained from ATCC (#30-2004) and detached using 0.25% Trypsin-EDTA. Mouse neural stem cells (mNSCs) (a generous gift from Dr. Evan Snyder's lab) were cultured in Dulbecco's modified Eagle's medium (DMEM) (Lonza, Walkersville, MD) containing 10% fetal bovine serum (FBS), 5% horse serum, 1% penicillin-streptomycin (GIBCO, Invitrogen, Carlsbad, CA). mNSCs were detached using 0.05% trypsin for 1 minute.

Viability Screening using the MTT Assay: To set up MTT experiments, hPFs and A549 cells were plated in 96-well Falcon plates (#353072, Corning, Corning, NY, USA). The 96-well plates layouts contained negative controls in rows A and H, and serial dilutions of aerosols or e-liquids in rows B-G. The control placed next to the highest concentration was used to determine if there was a vapor effect [94]. Plating densities were chosen to give about 80% confluency in control wells after 48 hours. Cell concentrations were determined using a BioMate 3S Spectrophotometer (Thermo Fisher Scientific, Chino, CA). The MTT reagent (3-(4,5-Dimethylthiazol-2-yl)-2,5-diphenyltetrazolium bromide, Sigma-Aldrich, St. Louis, MO) measures mitochondrial reductase conversion of yellow tetrazole (MTT) to purple formazan, which occurs only in healthy cells with active mitochondria. After 48 hours of treatment, 20 μL of MTT reagent was added to each well.

After 2 hours, MTT was removed, and cells were solubilized with 100 µL of DMSO. Absorbance was read at 570 nM in an Epoch microplate spectrophotometer (Biotek, Winooski, VT).

Detecting DNA Damage using the COMET Assay: hPFs were treated with aerosols or control medium for 3 h at 37 °C. Some hPFs were treated with 100 µM hydrogen peroxide for 10 min at 4 °C as a positive control. The Comet Assay Kit (Trevigen, Gaithersburg, MD) was used to evaluate Comet tail formation. Cells were mixed with low melting agarose at a ratio of 1:10 for encapsulation and were subjected to electrophoresis at 21 V for 30 min. Slides were stained with SYBR green dye (Trevigen, Gaithersburg, MD) and dried overnight at room temperature. Fluorescent images of the cells were captured using CometScore software on a Nikon Ti Eclipse microscope. The tail length, % tail of total single cells, % DNA in tail, and Olive moment (tail length × fraction of DNA in tail) scores were computed using the CometScore software.

Proliferation (Cell Growth) Assay: hPFs and A549 were cultured in 24 well plates and treated with various aerosols or e-liquids. The plates were simultaneously incubated and imaged live in a Nikon BioStation CT (Nikon, Melville, NY), and phase-contrast time-lapse videos were captured in 10x magnification. CL-Quant software (DR Vision, Seattle, WA) was used to segment the cells from the background and discard small objects (cell debris) by size exclusion. Total area occupied by the cells was extracted from the segmented cells for each individual timeframe. Growth rate (area normalized to the initial time point) was quantified using CL Quant software and growth curves were examined over time.

Attachment Assay and Effect on Recovery: hPFs were allowed to attach to the culture dish for 2 hours before (attached) or plated simultaneously with GreenSmoke aerosols (attaching). After 6 hours, EC treatments were removed and replaced by fresh medium in all groups, allowing cells to recover for another 7.5 hours. Time-lapse images were collected at 10x magnification every 20 minutes. The number of rounding and recovered (rounded cells that spread back down after

treatment removal) cells were counted. For each time frame, the percent of rounding or recovered cells were normalized to total cell count. The attaching versus pre-attached conditions were compared for all treatment conditions.

Cytoskeletal (Actin) Remodeling: hPFs cells were transfected with a tdTomato-LifeAct-7 plasmid (Addgene #54528) using DNA-In Transfection reagent (MTI-GlobalStem, Gaithersburg, MD USA). The cells were incubated overnight to allow for actin expression, then split and re-plated onto μ-Slide Ibidi 8-well chambers (Ibidi, Munich, Germany) with the GreenSmoke aerosol/e-liquid treatments. After 24 hours, the cells were fixed with 4% paraformaldehyde (PFA) for 15 min and mounted in Vectashield antifade medium containing DAPI (Vector Laboratories, Burlingame, CA, USA). Fluorescent images were collected using a Nikon TI inverted Eclipse microscope (Nikon Instruments, Tokyo, Japan) equipped with a high-resolution Andor Zyla VSC-04941 camera (Andor, Belfast, UK). The images were deconvoluted using the "live de-blur" feature of the NIS Elements software (Nikon). Time-lapse images allowed for visualization of actin depolymerization, as well as cytoskeletal remodeling events including retraction, blebbing, and eventual collapse.

Trypan Blue (Cell Death) Assay: After 24 hours of GreenSmoke treatment, cells were stained with trypan blue dye (xxx), which penetrates dead cells. Images were captured using a 4x Hoffman objective made by Nikon Eclipse. Number of trypan blue stained cells were counted and normalized to total cell counts, revealing the percentage of death cells for each treatment condition.

Fibrosis and Epithelial-to-Mesenchymal Transition: hPFs and A549 cells were treated for 48 hours in Ibidi chamber slides and fixed using 4% paraformaldehyde. Cells were blocked with 10% donkey normal serum (Sigma-Aldrich, St. Louis, MO, USA) in 0.1% Triton-X (Bio-Rad, Hercules, CA, USA) in DPBS. Cells were incubated overnight at 4oC with an alpha smooth muscle actin antibody (α-SMA) (#ab124964, Abcam, Cambridge, MA, USA) diluted in 0.2% Tween

(Sigma-Aldrich, St. Louis, MO, USA) in DPBS. The chambers were incubated in Alexa Fluor 594 secondary antibody (Life Technologies, Eugene, OR, USA) at room temperature for 1 hour. Lastly, the cells were mounted in Vectashield medium and imaged using the Nikon TI inverted Eclipse microscope. For the morphological assessment of EMT in A549 cells, individual cells within each treatment were classified as cobblestone, enlarged, and elongated phenotypes, as previously described [39]. The percent of each sub-group was presented as population plots.

Nicotinic Receptors and Calcium Reporter Analysis: Briefly, A549 cells were treated for 4 days with Vuse e-liquid/aerosols and nicotine, and labeled with α7 nAChR antibody (#ab216485, Abcam, Cambridge, MA, USA) using the same immunocytochemistry procedure described in the above paragraph. Also, 4-day Vuse aerosol treated cells were transfected with the Gcamp5 reporter (Addgene #31788, Cambridge, MA USA) using the DNA-In A549 Transfection reagent (MTI-Globalstem, Gaithersburg, MD USA). The cells were incubated for another 24 hours, totaling 4 days of treatments with menthol and tobacco 6TPE aerosol. On day 4, the cells were imaged live before, and after addition of a 1.1µg/mL challenge dose of nicotine. The average Gcamp5 fluorescence intensity of individual cells at each timepoint (time = 0, 1, 2, 2.5 and 5 minutes) were extracted using CL-Quant software. Intensity levels inside the cell were corrected by subtracting the background noise. Change in intensity were plotted as a function of time after normalization to "time = 0" (Fig 4.8I).

Mitochondrial Numbers, Morphology, and Protein Oxidation: Mitochondria are sensitive to stress, and mNSC have well-defined mitochondria amenable for bioinformatic analysis. mNSCs generated to stably express a MitoTimer reporter [95] were used as previously described [45]. MitoTimer-mNSCs were plated on µ-Slide Ibidi 8-well chamber slides (Ibidi, Munich, Germany) at approximately 6,000 cells/well. Two untreated control wells were used for comparison to the e-liquid and aerosol treated wells. CellProfiler software was used for segment the

mitochondria using MitoTimer signal (red channel) and thresholding was performed using Otsu's adaptive method. An intensity-based de-clumping method was used to separate clusters of mitochondria. Total mitochondrial counts and morphological features of individual mitochondria were extracted. These features were fed to an algorithmic decision tree operating on a Matlab platform (MathWorks, Natick, MA, USA) to automatically classify the mitochondria into 3 distinct morphological categories: fragmented, networked, and swollen. For the analysis of mitochondrial protein oxidation, video bioinformatics software was developed using CL-Quant (DR Vision, Seattle, WA USA) to quantify the ratio of red to green MitoTimer fluorescence. Multi-channel images were imported into CL-Quant, and soft-matching based segmentation was applied to both the red and green channels. Intensity data were collected and used to calculate the red/green ratio, which is a measure of oxidized proteins in the mitochondria.

Live Imaging of Vacuoles and Detection Autophagosomes: Time-lapse phase-contrast videos of A549 cells were captured in the Nikon Biostation CT Incubator, and imported into CL-Quant software. To augment the distinguishable feature of vacuoles, which is the whiteness of the vacuoles (high pixel intensity), two segmentation procedures were created. One was to segment the vacuoles, and the other procedure was to segment the "halo" rings around the cells which also have high pixel intensity. Next, the vacuole segmentations were subtracted by the halo segmentations, yielding the area of interest that only contain vacuoles. The total area of vacuoles in each condition was extracted for each frame and plotted over time.

To confirm the identity of the vacuoles, A549 cells were transfected with a reporter for LC3 (microtubule-associated protein 1 light chain 3 beta), which is expressed on autophagosomes. This ptfLC3 reporter (Addgene #21074, Cambridge, MA USA) is tandem-tagged with a photo-stable mRFP, as well as EGFP, which quenches in the acidic environment of autophagosomes [96].

Transfection was performed using the DNA-In reagent, as described in the above paragraphs. The red and green channels were overlain and depicted as a merged image.

Statistical analysis: All statistical analysis was conducted using Minitab (State College, PA USA) or Prism software (GraphPad, San Diego, CA). In Fig 4.2, MTT assay results obtained from cells treated with e-liquid and aerosol were statistically analyzed by three-way ANOVA using Minitab software (State College, PA, USA). Important interactions with significant were selected to show in the figure. In Fig 4.4, statistical analysis for Comet scores were computed using the CometScore software. In Fig 4.6, time-lapse percent data of rounded cells and recovered cells from e-liquid and aerosol treatments were analyzed using two-way ANOVA with Bonferroni's multiple comparisons test. The rounding/recovery results from attaching versus attachment conditions were compared against each other for all time points. In Fig 4.7, one-way ANOVA with Dunnett's post hoc test was used to compare the percent of trypan blue positive cells in the treated groups to the control group. In Fig 4.8, for the α-SMA and all fiber data, one-way ANOVAs with Dunnett's post hoc tests were performed to compare the treated group to the control group. In Fig 4.9, for mitochondria count data, one-way ANOVA with Dunnett's post hoc test was used to compare the treated group to the control group. For mitochondrial morphology analysis, one-way ANOVA with Dunnett's post hoc test was used to compare the treated group to the control for each morphological class. In the colorimetric ratio analysis, one-way ANOVA with Dunnett's post hoc test was used to compare the red-to-green MitoTimer ratio of treated groups to control. In Fig 4.11, the total area of autophagosomes were compared over time using a two-way ANOVA. ($p<0.05$ = *, $p<0.01$ = **, $p<0.001$ = ***, and $p<0.0001$ = ****).

Table S4.1. COMET Genotoxicity Summary. hPFs were treated for 4 hours with the NOAEL doses (calculated from MTT curves), and COMET assay was performed. The percent of cells with COMET tails, tail length, percent of DNA in tail, and olive moment were calculated relative to controls.

Comet Assay Aerosol HPF 3hrs Treated					
Name	Conc * TPE	Result			
		Cell with Tails (% of Control) **	Tail Length(pixel) (% of Control) **	%DNA in Tail (% of Control) **	Olive Moment (% of Control) **
GS	1.8	167 ± 16.0**	113 ± 10.2	91 ± 9.4	98 ± 10.5
GS	1.8	125 ± 16.2	117 ± 8.6	135 ± 13.3*	130 ± 12.4*
GSM-D2	1.8	224 ± 12.7****	188 ± 23.3**	135 ± 7.6***	201 ± 23.9***
GSM-A3	1.8	194 ± 38.0	155 ± 32.0	178 ± 12.6****	165 ± 24.0*
GSM-D5	1.8	131 ± 32.0	94 ± 20.8	100 ± 9.8	103 ± 14.1
GSM-D5	3	220 ± 47.4*	232 ± 47.4*	132 ± 8.3*	164 ± 20.4*
GSM-B2	1.8	128 ± 11.0*	91 ± 11.5	103 ± 7.9	90 ± 11.5
Blue M-B1	1.8	148 ± 14.0**	118 ± 13.5	115 ± 8.0	114 ± 14.2
Blue M-A1	1.8	165 ± 15.5**	138 ± 14.7	101 ± 7.7	116 ± 14.7
Blue M-B2	1.8	146 ± 12.0**	139 ± 14.2*	98 ± 8.6	123 ± 14.1
V2 Red18M.3	1.8	344 ± 33.1***	179 ± 23.2**	111 ± 8.5	152 ± 20.9*
V.2-P.2	6	87 ± 16.0	77 ± 12.8	104 ± 11.6	97 ± 18.6
Vuse-T-S.4	6	135 ± 20.4	116 ± 16.6	133 ± 13.2	126 ± 19.3
Vuse-T-B.2	6	82 ± 16.8	103 ± 16.4	126 ± 14.9	134 ± 23.3
Vuse-M-Q.2	6	182 ± 28.3*	149 ± 17.0	145 ± 11.9*	132 ± 19.2
Vuse-M-B.1	6	103 ± 15.7	105 ± 15.6	119 ± 12.1	122 ± 19.7
Vuse-M-S.1	6	126 ± 17.4	94 ± 14.1	107 ± 11.3	90 ± 16.4
Mark10C-D2	6	181 ± 27.0	128 ± 22.2	135 ± 14.1	123 ± 19.9
Mark10M-B2	6	203 ± 41.5	150 ± 25.7	138 ± 13.8	136 ± 20.7
Mark10C-C1	6	303 ± 43.2***	338 ± 52.2***	184 ± 20.1***	301 ± 51.5***
Mark10M-B1	6	219 ± 30.7**	484 ± 71.3***	180 ± 20.6*	511 ± 86.9***
Mark10C-S2	6	202 ± 29.7*	433 ± 67.6***	195 ± 22.5**	520 ±100.6***
Mark10 Menthol- S3	6	170 ± 35.8	351 ± 62.5**	159 ± 21.6	391 ± 77.2*
Mark10M-B1(Old)	6	145 ± 11.6	131 ± 16.4	124 ± 10.1	128 ± 19.6
Mark10C-S2(Old)	6	102 ± 19.0	79 ± 12.2	82 ± 10.3	75 ± 13.7
Mark10C-S2(New)	6	189 ± 24.1**	138 ± 15.9	117 ± 11.0	111 ± 15.8
Mark10M-B2	6	179 ± 44.1	57 ± 8.0	132 ± 14.9	98 ± 12.0
Mark10M-B2(New)	6	301 ± 43.8**	215 ± 27.8***	210.± 19.2***	233 ± 25.8***
Mark10M-B2(New)	6	174 ± 11.3*	178 ± 18.1***	151 ± 13.2**	172 ± 22.6*
Mark10C-S2(New)	6	150 ± 12.7	150 ± 14.9	159 ± 12.5**	141 ± 16.3

* NOAEL doses calculated from MTT dose-response curves

** Values are Avg ± s.d percent of COMET scores relative to controls

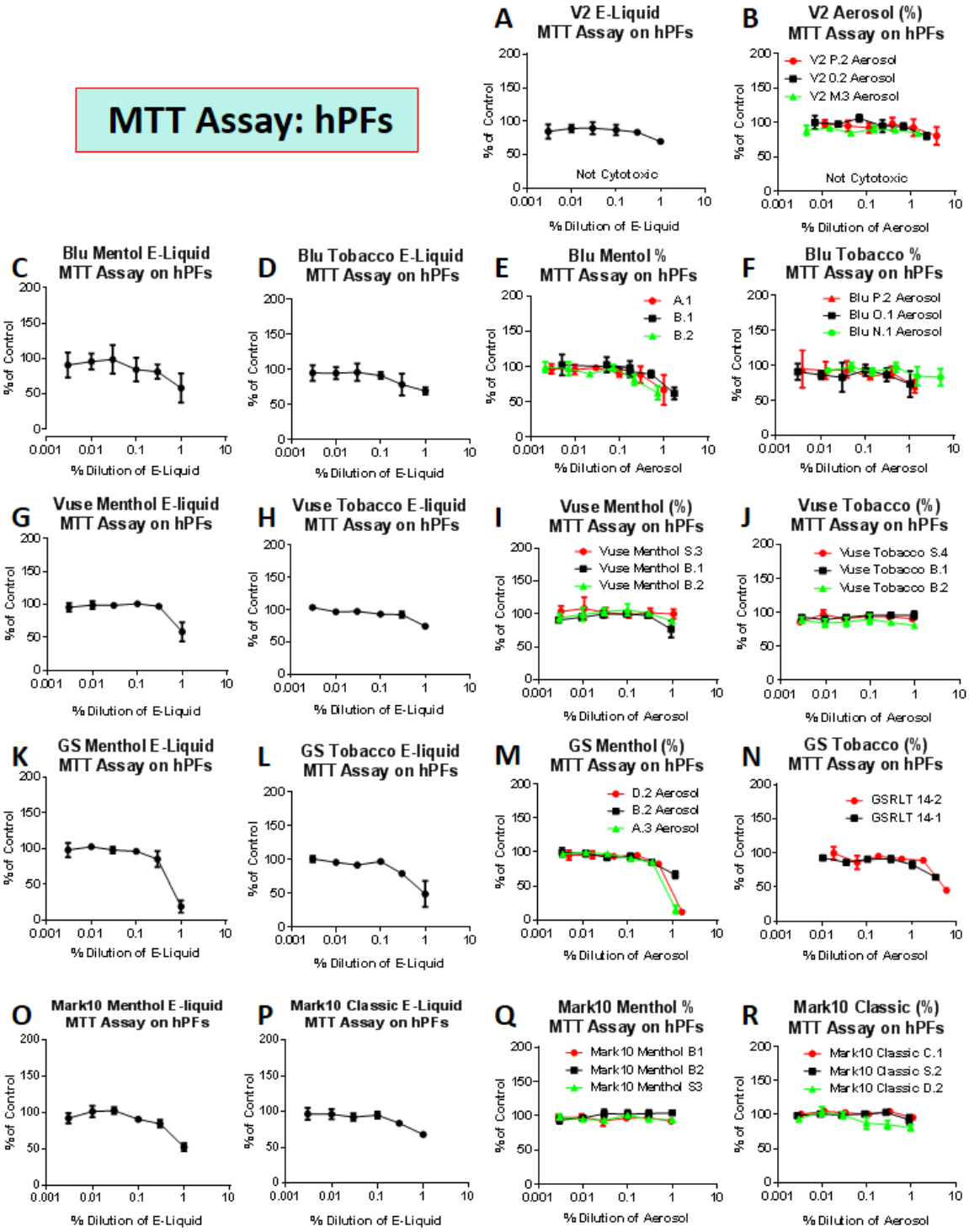

Figure S4.1. MTT Concentration Response Curves for hPFs Treated with E-liquids and Aerosols from Four Brands of EC.

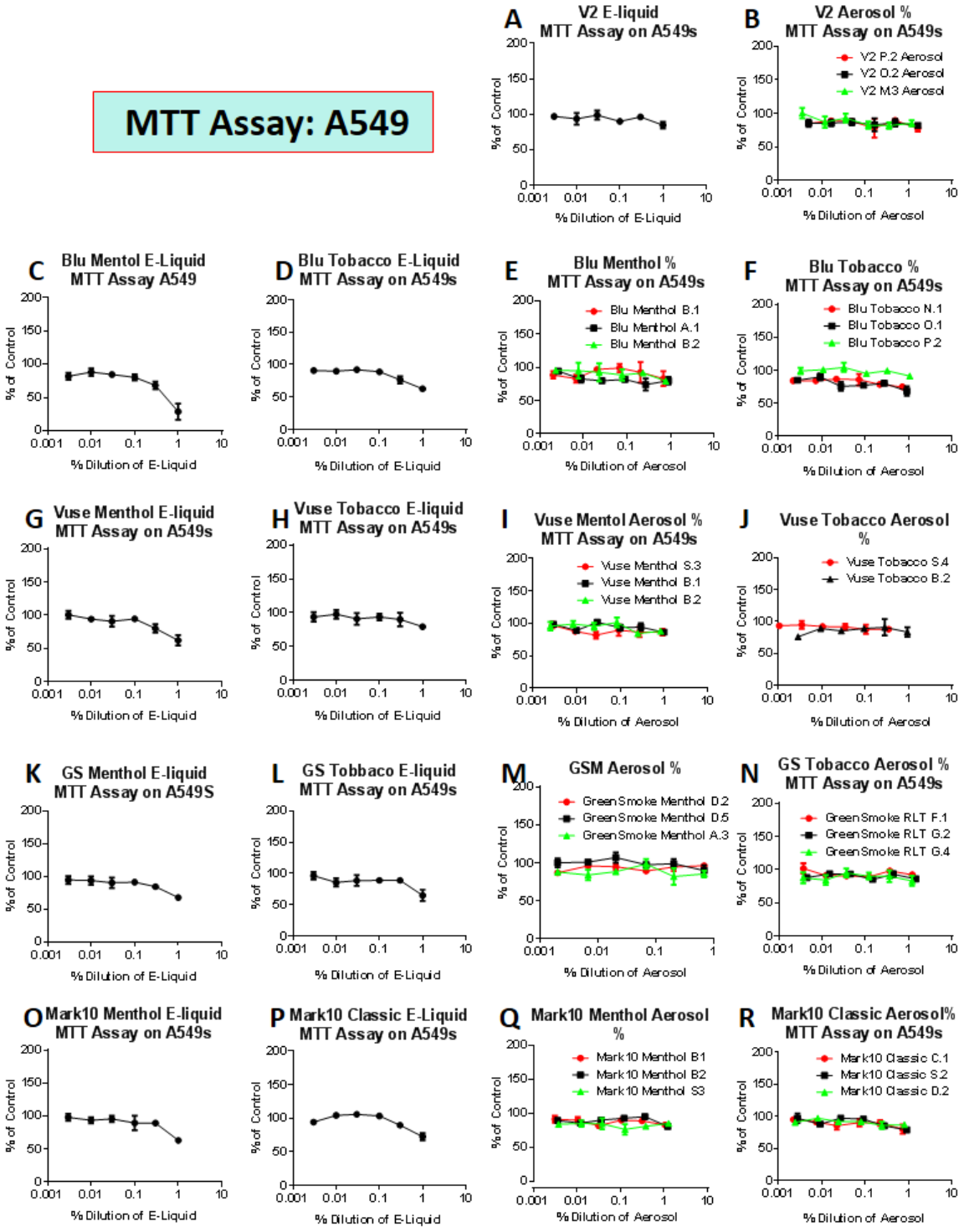

Figure S4.2. MTT Curves for A549 Cells Treated with E-liquids and Aerosols from Four Brands of EC.

REFERENCES

[1] A. Trtchounian, P. Talbot, Electronic nicotine delivery systems: is there a need for regulation?, Tob. Control. 20 (2010) 47–52.

[2] United States Department of Health and Human Services, E-Cigarette use among youth and young adults: a report of the surgeon general, 2016.

[3] R. Polosa, B. Rodu, P. Caponnetto, M. Maglia, C. Raciti, A fresh look at tobacco harm reduction: The case for the electronic cigarette, Harm Reduct. J. 10 (2013) 1–11.

[4] C. Pisinger, M. Døssing, A systematic review of health effects of electronic cigarettes, Prev. Med. (Baltim). 69 (2014) 248–260.

[5] Z. Cahn, M. Siegel, Electronic cigarettes as a harm reduction strategy for tobacco control: A step forward or a repeat of past mistakes?, J. Public Health Policy. 32 (2011) 16–31.

[6] and M. National Academies of Sciences, Engineering, Public Health Consequences of E-Cigarettes, The National Academies Press, Washington, DC, 2018.

[7] M. Williams, A. Villarreal, K. Bozhilov, S. Lin, P. Talbot, Metal and silicate particles including nanoparticles are present in electronic cigarette cartomizer fluid and aerosol, PLoS One. 8 (2013) e57987.

[8] M. Hua, P. Talbot, Potential health effects of electronic cigarettes: A systematic review of case reports, Prev. Med. Reports. 4 (2016) 169–178.

[9] M.S. Khan, F. Khateeb, J. Akhtar, Z. Khan, A. Lal, V. Kholodovych, J. Hammersley, Organizing pneumonia related to electronic cigarette use: A case report and review of literature, Clin. Respir. J. 12 (2018) 1295–1299.

[10] A.M. Glasser, L. Katz, J.L. Pearson, R.S. Niaura, D.B. Abrams, C. Andrea, Overview of Electronic Nicotine Delivery Systems: A Systematic Review, Am. J. Prev. Med. 52 (2017) 1–65.

[11] P.G. Shields, M. Berman, T.M. Brasky, J.L. Freudenheim, E. Mathe, J.P. McElroy, M.-A. Song, M.D. Wewers, A Review of Pulmonary Toxicity of Electronic Cigarettes In The Context of Smoking: A Focus On Inflammation, Cancer Epidemiol. Biomarkers Prev. 36 (2016) 1011–1014.

[12] J.R. Whittington, P.M. Simmons, A.M. Phillips, S.K. Gammill, R. Cen, E.F. Magann, V.M. Cardenas, The Use of Electronic Cigarettes in Pregnancy: A Review of the Literature, Obstet. Gynecol. Surv. 73 (2018) 544–549.

[13] T.R. Rowell, R. Tarran, Will chronic e-cigarette use cause lung disease?, Am. J. Physiol. - Lung Cell. Mol. Physiol. 309 (2015) L1398–L1409.

[14] P. Callahan-Lyon, Electronic cigarettes: Human health effects, Tob. Control. 23 (2014).

[15] V. Bahl, S. Lin, N. Xu, B. Davis, Y.H. Wang, P. Talbot, Comparison of electronic cigarette refill fluid cytotoxicity using embryonic and adult models, Reprod. Toxicol. 34 (2012) 529–537.

[16] C. Anderson, A. Majeste, J. Hanus, S. Wang, E-Cigarette Aerosol Exposure Induces Reactive Oxygen Species, DNA Damage, and Cell Death in Vascular Endothelial Cells., Toxicol. Sci. 154 (2016) 1–9.

[17] R.Z. Behar, B. Davis, Y. Wang, V. Bahl, S. Lin, P. Talbot, Identification of toxicants in cinnamon-flavored electronic cigarette refill fluids, Toxicol. Vitr. 28 (2014) 198–208.

[18] M.L. Goniewicz, J. Knysak, M. Gawron, L. Kosmider, A. Sobczak, J. Kurek, A. Prokopowicz, M. Jablonska-Czapla, C. Rosik-Dulewska, C. Havel, P. Jacob, N. Benowitz, Levels of selected carcinogens and toxicants in vapour from electronic cigarettes, Tob. Control. 23 (2014) 133–139.

[19] C.A. Lerner, I.K. Sundar, H. Yao, J. Gerloff, D.J. Ossip, S. McIntosh, R. Robinson, I. Rahman, Vapors produced by electronic cigarettes and E-juices with flavorings induce toxicity, oxidative stress, and inflammatory response in lung epithelial cells and in mouse lung, PLoS One. 10 (2015) 1–26.

[20] R.Z. Behar, Y. Wang, P. Talbot, Comparing the cytotoxicity of electronic cigarette fluids, aerosols and solvents, Tob. Control. (2017) 1–9.

[21] R.Z. Behar, W. Luo, K.J. Mcwhirter, J.F. Pankow, P. Talbot, Analytical and toxicological evaluation of flavor chemicals in electronic cigarette refill fluids, Sci. Rep. 8 (2018) 1–11.

[22] R.Z. Behar, W. Luo, S.C. Lin, Y. Wang, J. Valle, J.F. Pankow, P. Talbot, Distribution, quantification and toxicity of cinnamaldehyde in electronic cigarette refill fluids and aerosols, Tob. Control. 25 (2016) ii94-ii102.

[23] M.A. Ogunwale, M. Li, M. V. Ramakrishnam Raju, Y. Chen, M.H. Nantz, D.J. Conklin, X.A. Fu, Aldehyde Detection in Electronic Cigarette Aerosols, ACS Omega. 2 (2017) 1207–1214.

[24] P.R. Jensen, W. Luo, J.F. Pankow, R.M. Strongin, D.H. Peyton, Hidden Formaldehyde in E-Cigarette Aerosols, N. Engl. J. Med. 372 (2015) 392–394.

[25] E.E. Omaiye, I. Cordova, B. Davis, P. Talbot, Counterfeit Electronic Cigarette Products with Mislabeled Nicotine Concentrations, Tob. Regul. Sci. 3 (2017) 347–357.

[26] B. Davis, M. Dang, J. Kim, P. Talbot, Nicotine concentrations in electronic cigarette refill and do-it-yourself fluids, Nicotine Tob. Res. 17 (2015) 134–141.

[27] A. Scott, S.T. Lugg, K. Aldridge, K.E. Lewis, A. Bowden, R.Y. Mahida, F.S. Grudzinska, D. Dosanjh, D. Parekh, R. Foronjy, E. Sapey, B. Naidu, D.R. Thickett, Pro-inflammatory effects of e-cigarette vapour condensate on human alveolar macrophages, Thorax. (2018) 1–9.

[28] Q. Wu, D. Jiang, M. Minor, H.W. Chu, Electronic cigarette liquid increases inflammation and virus infection in primary human airway epithelial cells, PLoS One. 9 (2014).

[29] C.A. Lerner, P. Rutagarama, T. Ahmad, I.K. Sundar, A. Elder, I. Rahman, Electronic cigarette aerosols and copper nanoparticles induce mitochondrial stress and promote DNA fragmentation in lung fibroblasts, Biochem. Biophys. Res. Commun. 477 (2016) 620–625.

[30] M. Williams, K. Bozhilov, S. Ghai, P. Talbot, Elements including metals in the atomizer and aerosol of disposable electronic cigarettes and electronic hookahs, PLoS One. 12 (2017) 1–24.

[31] V.B. Mikheev, M.C. Brinkman, C.A. Granville, S.M. Gordon, P.I. Clark, Real-time measurement of electronic cigarette aerosol size distribution and metals content analysis, Nicotine Tob. Res. 18 (2016) 1895–1902.

[32] P. Olmedo, W. Goessler, S. Tanda, M. Grau-Perez, S. Jarmul, A. Aherrera, R. Chen, M. Hilpert, J.E. Cohen, A. Navas-Acien, A.M. Rule, Metal Concentrations in e-Cigarette Liquid and Aerosol Samples: The Contribution of Metallic Coils, Environ. Health Perspect. 126 (2018).

[33] D. Thorne, I. Crooks, M. Hollings, A. Seymour, C. Meredith, M. Gaca, The mutagenic assessment of an electronic-cigarette and reference cigarette smoke using the Ames assay in strains TA98 and TA100, Mutat. Res. Toxicol. Environ. Mutagen. 812 (2016) 29–38.

[34] H.-W. Lee, S.-H. Park, M. Weng, H.-T. Wang, W.C. Huang, H. Lepor, X.-R. Wu, L.-C. Chen, M. Tang, E-cigarette smoke damages DNA and reduces repair activity in mouse lung, heart, and bladder as well as in human lung and bladder cells, Proc. Natl. Acad. Sci. 115 (2018) E1560–E1569.

[35] D. Canistro, F. Vivarelli, S. Cirillo, C. Babot Marquillas, A. Buschini, M. Lazzaretti, L. Marchi, V. Cardenia, M.T. Rodriguez-Estrada, M. Lodovici, C. Cipriani, A. Lorenzini, E. Croco, S. Marchionni, P. Franchi, M. Lucarini, V. Longo, C.M. Della Croce, A. Vornoli, A. Colacci, M. Vaccari, A. Sapone, M. Paolini, E-cigarettes induce toxicological effects that can raise the cancer risk, Sci. Rep. 7 (2017) 2028.

[36] T.L. Riss, R.A. Moravec, A.L. Niles, S. Duellman, H.A. Benink, T.J. Worzella, L. Minor, Cell Viability Assays, 2004.

[37] C.J. Brown, J.M. Cheng, Electronic cigarettes: Product characterization and design considerations, Tob. Control. 23 (2014).

[38] A.C. Midgley, M. Rogers, M.B. Hallett, A. Clayton, T. Bowen, A.O. Phillips, R. Steadman, Transforming growth factor-β1 (TGF-β1)-stimulated fibroblast to myofibroblast differentiation is mediated by hyaluronan (HA)-facilitated epidermal growth factor receptor (EGFR) and CD44 co-localization in lipid rafts, J. Biol. Chem. 288 (2013) 14824–14838.

[39] A. Zahedi, R. Phandthong, A. Chaili, G. Lemark, P. Talbot, Epithelial-to-Mesenchymal Transition of A549 Lung Cancer Cells Exposed to Electronic Cigarettes, Lung Cancer. 122 (2018) 224–233.

[40] N. Benowitz, Nicotine Addiction, N. Engl. J. Med. 362 (2010) 2295–2303.

[41] X. Peng, V. Gerzanich, R. Anand, P.J. Whiting, J. Lindstrom, Nicotine-induced increase in neuronal nicotinic receptors results from a decrease in the rate of receptor turnover, Mol. Pharmacol. 46 (1994) 523–530.

[42] M.I. Damaj, Calcium-Acting Drugs Modulate Expression and Development of Chronic Tolerance to Nicotine-Induced Antinociception in Mice, J. Pharmacol. Exp. Ther. 315 (2005) 959–964.

[43] A.P. Govind, P. Vezina, W.N. Green, Nicotine-induced upregulation of nicotinic receptors: Underlying mechanisms and relevance to nicotine addiction, Biochem. Pharmacol. 78 (2009) 756–765.

[44] J. Akerboom, T.-W. Chen, T.J. Wardill, L. Tian, J.S. Marvin, S. Mutlu, N.C. Calderon, F. Esposti, B.G. Borghuis, X.R. Sun, A. Gordus, M.B. Orger, R. Portugues, F. Engert, J.J. Macklin, A. Filosa, A. Aggarwal, R.A. Kerr, R. Takagi, S. Kracun, E. Shigetomi, B.S. Khakh, H. Baier, L. Lagnado, S.S.-H. Wang, C.I. Bargmann, B.E. Kimmel, V. Jayaraman, K. Svoboda, D.S. Kim, E.R. Schreiter, L.L. Looger, Optimization of a GCaMP Calcium Indicator for Neural Activity Imaging, J. Neurosci. 32 (2012) 13819–13840.

[45] A. Zahedi, V. On, R. Phandthong, A. Chaili, G. Remark, B. Bhanu, P. Talbot, Deep Analysis of Mitochondria and Cell Health Using Machine Learning, Sci. Rep. (2018) 1–15.

[46] R. Kalluri, E.G. Neilson, Epithelial-mesenchymal transition and its implications for fibrosis, J. Clin. Invest. 112 (2003) 1776–1784.

[47] R.C. Stone, I. Pastar, N. Ojeh, V. Chen, S. Liu, K.I. Garzon, M. Tomic-canic, Epithelial-Mesenchymal Transition in Tissue Repair and Fibrosis, Cell Tissue Res. 365 (2016) 495–506.

[48] M. Selman, A. Pardo, Idiopathic pulmonary fibrosis: An epithelial/fibroblastic cross-talk disorder, Respir. Res. 3 (2001) 1–8.

[49] P.J. Wipff, D.B. Rifkin, J.J. Meister, B. Hinz, Myofibroblast contraction activates latent TGF-β1 from the extracellular matrix, J. Cell Biol. 179 (2007) 1311–1323.

[50] H. Zhang, H. Liu, Z. Borok, K.J.A. Davies, F. Ursini, H.J. Forman, Cigarette smoke extract stimulates epithelial-mesenchymal transition through Src activation, Free Radic. Biol. Med. 52 (2012) 1437–1442.

[51] S. Heerboth, G. Housman, M. Leary, M. Longacre, S. Byler, K. Lapinska, A. Willbanks, S. Sarkar, EMT and tumor metastasis, Clin. Transl. Med. 4 (2015) 6.

[52] A.W. Lambert, D.R. Pattabiraman, R.A. Weinberg, Emerging Biological Principles of Metastasis, Cell. 168 (2017) 670–691.

[53] S. Singh, S. Pillai, S. Chellappan, Nicotinic Acetylcholine Receptor Signaling in Tumor Growth and Metastasis, J. Oncol. 2011 (2011) 1–11.

[54] P. Dasgupta, W. Rizwani, S. Pillai, R. Kinkade, M. Kovacs, S. Banerjee, M. Carless, E. Kim, D. Coppola, Nicotine induces cell proliferation, invasion and epithelial- mesenchymal transition in a variety of human cancer cell lines, Int. J. Cancer. 124 (2009) 36–45.

[55] W. Zou, Y. Zou, Z. Zhao, B. Li, P. Ran, Nicotine-induced epithelial-mesenchymal transition via Wnt/β-catenin signaling in human airway epithelial cells, Am. J. Physiol. Cell. Mol. Physiol. 304 (2013) L199–L209.

[56] E. Veljkovic, J. Jiricny, M. Menigatti, H. Rehrauer, W. Han, Chronic exposure to cigarette smoke condensate in vitro induces epithelial to mesenchymal transition-like changes in human bronchial epithelial cells, BEAS-2B, Toxicol. Vitr. 25 (2011) 446–453.

[57] D. Li, L. Zhang, J. Zhou, H. Chen, Cigarette smoke extract exposure induces EGFR-TKI resistance in EGFR-mutated NSCLC via mediating Src activation and EMT, Lung Cancer. 93 (2016) 35–42.

[58] M.A. Yu, A. Kiang, J. Wang-Rodriguez, E. Rahimy, M. Haas, V. Yu, L.G. Ellies, J. Chen, J.B. Fan, K.T. Brumund, R.A. Weisman, W.M. Ongkeko, Nicotine Promotes Acquisition of Stem Cell and Epithelial-to-Mesenchymal Properties in Head and Neck Squamous Cell Carcinoma, PLoS One. 7 (2012) 1–14.

[59] J.G. Willett, M. Bennett, E.C. Hair, H. Xiao, M.S. Greenberg, E. Harvey, J. Cantrell, D. Vallone, Recognition , use and perceptions of JUUL among youth and young adults, Tob. Control. (2018) 1–2.

[60] B.K. Ambrose, H.R. Day, B. Rostron, K.P. Conway, N. Borek, A. Hyland, A.C. Villanti, Flavored Tobacco Product Use Among US Youth Aged 12-17 Years , 2013-2014, 314 (2015) 1871–1873.

[61] A. El-Hellani, R. El-Hage, R. Baalbaki, S. Talih, A. Shihadeh, N. Saliba, Quantification of free-base and protonated nicotine in electronic cigarette liquids and aerosol emissions, Chem. Res. Toxicol. 28 (2015) 1532–1537.

[62] M.L. Goniewicz, T. Kuma, M. Gawron, J. Knysak, L. Kosmider, Nicotine levels in electronic cigarettes, Nicotine Tob. Res. 15 (2013) 158–166.

[63] S. Lundegard, Measuring volatile nicotine from electronic cigarettes, Ergonomics and Aerosol Technology, 2017.

[64] M.L. Goniewicz, R. Boykan, C.R. Messina, A. Eliscu, J. Tolentino, High exposure to nicotine among adolescents who use Juul and other vape pod systems ('pods'), Tob. Control. (2018) 1–2.

[65] R. Wickstrom, Effects of Nicotine During Pregnancy: Human and Experimental Evidence, Curr. Neuropharmacol. 5 (2007) 213–222.

[66] W. Hofhuis, J.C. De Jongste, P.J.F.M. Merkus, Adverse health effects of prenatal and postnatal tobacco smoke exposure on children, (2003) 1086–1090.

[67] L. Kozlovskaya, M. Abou-Kaoud, D. Stepensky, Quantitative analysis of drug delivery to the brain via nasal route, J. Control. Release. 189 (2014) 133–140.

[68] V. Bahl, K. Johnson, R. Phandthong, A. Zahedi, S.F. Schick, P. Talbot, Thirdhand cigarette smoke causes stress-induced mitochondrial hyperfusion and alters the transcriptional profile of stem cells, Toxicol. Sci. 153 (2016) 55–69.

[69] A. Zahedi, R. Phandthong, A. Chaili, S. Leung, E. Omaiye, P. Talbot, A Mitochondrial Stress Response in Neural Stem Cells Exposed to Electronic Cigarettes, IScience. (n.d.).

[70] P.C. Shivalingappa, R. Hole, C. Van Westphal, N. Vij, Airway exposure to e-cigarette vapors impairs autophagy and induces aggresome formation, Antioxid. Redox Signal. 24 (2015) 186–204.

[71] D. Glick, S. Barth, K.F. Macleod, Autophagy: cellular and molecular mechanisms, J. Pathol. 221 (2010) 3–12.

[72] D.C. Rubinsztein, P. Codogno, B. Levine, Autophagy modulation as a potential therapeutic target for diverse diseases, Nat. Rev. Drug Discov. 11 (2012) 709–730.

[73] S. Piao, R.K. Amaravadi, Targeting the lysosome in cancer, Ann. N. Y. Acad. Sci. 1371 (2016) 45–54.

[74] S. Pavlides, I. Vera, R. Gandara, S. Sneddon, R.G. Pestell, I. Mercier, U.E. Martinez-Outschoorn, D. Whitaker-Menezes, A. Howell, F. Sotgia, M.P. Lisanti, Warburg Meets Autophagy: Cancer-Associated Fibroblasts Accelerate Tumor Growth and Metastasis via Oxidative Stress, Mitophagy, and Aerobic Glycolysis, Antioxid. Redox Signal. 16 (2012) 1264–1284.

[75] L.E. Bröker, F.A.E. Kruyt, G. Giaccone, Cell death Independent of Caspases:A Review, Clin. Cancer Res. 11 (2005) 3155–62.

[76] S.Y. Moon, H.S. Kim, K.W. Nho, Y.J. Jang, S.K. Lee, Endoplasmic reticulum stress induces epithelial-mesenchymal transition through autophagy via activation of c-src kinase, Nephron - Exp. Nephrol. 126 (2014) 127–140.

[77] S.P. Jackson, J. Bartek, The DNA-damage response in human biology and disease, Nature. 461 (2010) 1071–1078.

[78] J.E. Klaunig, Z. Wang, X. Pu, S. Zhou, Oxidative stress and oxidative damage in chemical carcinogenesis, Toxicol. Appl. Pharmacol. 254 (2011) 86–99.

[79] D. Hanahan, R.A. Weinberg, Hallmarks of Cancer: The Next Generation, Cell. 144 (2011) 646–674.

[80] S.S. Hecht, Lung carcinogenesis by tobacco smoke, Int. J. Cancer. 131 (2012) 2724–2732.

[81] M. Desouza, P.W. Gunning, J.R. Stehn, The Actin Cytoskeleton as a Sensor and Mediator of Apoptosis, Bioarchitecture. 2 (2012) 75–87.

[82] A.M. Cantin, Cellular Response to Cigarette Smoke and Oxidants: Adapting to Survive, Proc. Am. Thorac. Soc. 7 (2010) 368–375.

[83] Y. Zhao, The Oncogenic Functions of Nicotinic Acetylcholine Receptors, J. Oncol. 2016 (2016).

[84] L.-T. Su, M.A. Agapito, M. Li, W. Simpson, A. Huttenlocker, R. Habas, L. Yue, L.W. Runnels, TRPM7 Regulates Cell Adhesion by Controlling the Calcium Dependent Protease Calpain, J. Biol. Chem. 281 (2006) 11260–11270.

[85] A.C. Hoffman, The health effects of menthol cigarettes as compared to non-menthol cigarettes, Tob. Induc. Dis. 9 (2011) S7.

[86] V.S. Bernson, B. Pettersson, The toxicity of menthol in short-term bioassays, (1983) 233–246.

[87] A.C. Villanti, L.K. Collins, R.S. Niaura, S.Y. Gagosian, D.B. Abrams, Menthol cigarettes and the public health standard: A systematic review, BMC Public Health. 17 (2017) 1–13.

[88] S.D. Alsharari, J.R. King, J.C. Nordman, P.P. Muldoon, A. Jackson, A.Z.X. Zhu, R.F. Tyndale, N. Kabbani, M.I. Damaj, Effects of menthol on nicotine pharmacokinetic, pharmacology and dependence in mice, PLoS One. 10 (2015) 1–16.

[89] J. Audrain-McGovern, A.A. Strasser, P.E. Wileyto, The impact of flavoring on the rewarding and reinforcing value of e-cigarettes with nicotine among young adult smokers, Cell Rep. 166 (2016) 263–267.

[90] K. Rosbrook, B.G. Green, Sensory effects of Menthol and Nicotine in an E-cigarette, Nicotine Tob. Res. 18 (2016) 1588–1595.

[91] V.B. Yerger, Menthol's potential effects on nicotine dependence: a tobacco industry perspective, Tob. Control. 20 (2011) ii29-ii36.

[92] A. Zahedi, V. On, S.C. Lin, B.C. Bays, E. Omaiye, B. Bhanu, P. Talbot, Evaluating cell processes, quality, and biomarkers in pluripotent stem cells using video bioinformatics, PLoS One. 11 (2016) 1–22.

[93] R.Z. Behar, M. Hua, P. Talbot, Puffing topography and nicotine intake of electronic cigarette users, PLoS One. 10 (2015) 1–18.

[94] R.Z. Behar, V. Bahl, Y. Wang, S. Lin, N. Xu, B. Davis, P. Talbot, A method for rapid dose-response screening of environmental chemicals using human embryonic stem cells, J. Pharmacol. Toxicol. Methods. 66 (2012) 238–245.

[95] R.C. Laker, P. Xu, K.A. Ryall, A. Sujkowski, B.M. Kenwood, K.H. Chain, M. Zhang, M.A. Royal, K.L. Hoehn, M. Driscoll, P.N. Adler, R.J. Wessells, J.J. Saucerman, Z. Yan, A novel mitotimer reporter gene for mitochondrial content, structure, stress, and damage in vivo, J. Biol. Chem. 289 (2014) 12005–12015.
[96] S. Kimura, T. Noda, T. Yoshimori, Dissection of the autophagosome maturation process by a novel reporter protein, tandem fluorescent-tagged LC3, Autophagy. 3 (2007) 452–460.

Section III: Evaluation of Electronic Cigarettes on Neural Stem Cells

Chapter 5

A Mitochondrial Stress Response in Neural Stem Cells Exposed to Electronic Cigarettes

ABSTRACT

Stem cells are critical throughout human ontogeny and provide a sensitive model to study exposure to toxicants, such as cigarette smoke. Electronic cigarettes (ECs) are popular nicotine-delivery devices that are often targeted to youth and pregnant mothers. However, little is known about the relationship between neural stem cells and the toxicity of the chemicals in ECs. Stem cells have evolved survival mechanisms that include mitochondria, organelles that maintain cell functionality and health. Here, we apply advanced imaging techniques and quantitative bioinformatics tools to assess the effects of ECs on mitophagy, mitochondrial morphology and dynamics, mitochondrial membrane potential, protein oxidation, calcium levels, and mtDNA nucleoids. The mechanism underlying EC-induced stem cell toxicity was characterized as stress-induced mitochondrial hyperfusion (SIMH), a transient survival response accompanied by increased mitochondrial oxidative stress. We identify SIMH as a survival response to nicotine. These observed mitochondrial alterations combined with autophagy dysfunction to clear damaged mitochondria could lead to faulty stem cell populations, which in turn could accelerate cellular aging and lead to acquired mitochondriopathies. These findings are important given that nicotine is now widely available in EC refill fluids and as a pure chemical for use in do-it-yourself EC products. In a broader sense, any nicotine containing product may likewise stress stem cells with long-term repercussions for users and passively exposed individuals.

INTRODUCTION

Throughout life, stem cells are critical in organ development, maintenance of homeostasis, and tissue renewal/repair. The damage to stem cells that accumulates normally or following exposure to toxicants alters their ability to maintain cell functioning and can lead to disease or aging in adults [1–4]. During development, stem cells of the nervous system are particularly vulnerable to toxicants [5]. Because stem cells are present throughout life, their risk of accumulating damage is high. Stem cells are also often more sensitive to stress than differentiated cells [6, 7], making them excellent models for evaluating safe limits of exposure to potential toxicants [8–12] .

Toxicants, such as tobacco smoke, have detrimental effects on the health of stem cells [8, 13–17]. Stem cells exposed to tobacco products or nicotine have diminished regenerative potential because they are less proliferative, migratory, and able to differentiate [18–20]. Electronic cigarettes (EC) are popular new tobacco products that aerosolize nicotine and flavor chemicals through heating [21]. Although originally introduced as safer or smoking cessation replacements, recent studies have shown that ECs indeed cause various forms of toxicity [22]. Embryonic stem cells and neural stem cells were highly sensitive to some electronic cigarette refill fluids in vitro [6, 7]. However, little is known about the mechanisms underlying stem cell toxicity and the toxicants present in EC.

Mitochondria are excellent models for toxicological studies with stem cells since they are sensitive indicators of stress [23–25]. Furthermore, mitochondria control stemness [26–28], and their decline may underlie age-related changes in stem cell functioning [29–32]. Stem cells have evolved pro-survival mechanisms centered around mitochondria, such as autophagic turnover (mitophagy) [33], asymmetric segregation of mitochondria and damaged proteins during cell division [34–36], and stress-induced mitochondrial hyperfusion (SIMH) [37–39]. These studies support the idea that mitochondria are critical in regulating stem cell health. However, it is not fully

understood which stress responses stem cells activate when exposed to EC and which chemicals are responsible for inducing stress.

To date, the effects of ECs on mitochondrial dysfunction are relatively unexplored [40]. The purpose of this study was to characterize the effects of EC refill fluids and their aerosols on stem cell mitochondria and to identify the ingredient in EC products that activates SIMH. Neural stem cells (NSCs) were chosen for study as their mitochondria are well-defined and amenable to analysis using video bioinformatics tools [6,39,41]. Equally important, NSCs are potential targets of EC aerosol as inhaled chemicals travel efficiently to the brain via the olfactory tracks [42].

RESULTS

EC Liquids and Aerosols Inhibit Autophagic Flux in Stem Cells

To assess the effect of EC fluids and aerosols on autophagy, NSC were transfected with a tandem-tagged microtubule-associated protein 1 light chain 3 beta reporter (ptfLC3 plasmid), which labels autophagosomes. The reporter is tagged to both mRFP, which is photostable, and GFP, which quenches in the acidic environment of autophagosomes and autolysosomes [43]. Figures 5.1A-F show mGFP and mRFP fluorescence in control and EC treated NSC. By 24 hours of treatment, the autophagosomes in the treated group were larger than in the control and had more GFP fluorescence (resulting in a yellow colocalized image in Fig 5.1B), indicating an increase in autophagosome pH.

CellProfiler image processing software was used to segment and quantify the total area of the autophagosomes in cells treated 4 hours (Figs. 5.1A-C, 5.1G) and 24 hours (Figs. 5.1D-F, 5.1H) with e-liquid or aerosol. There was a time dependent increase in the total area of the autophagosomes with e-liquids inducing a greater increase than aerosols. There was also a slight increase in the number of autophagosomes by 4 hours, but by 24 hours the number of

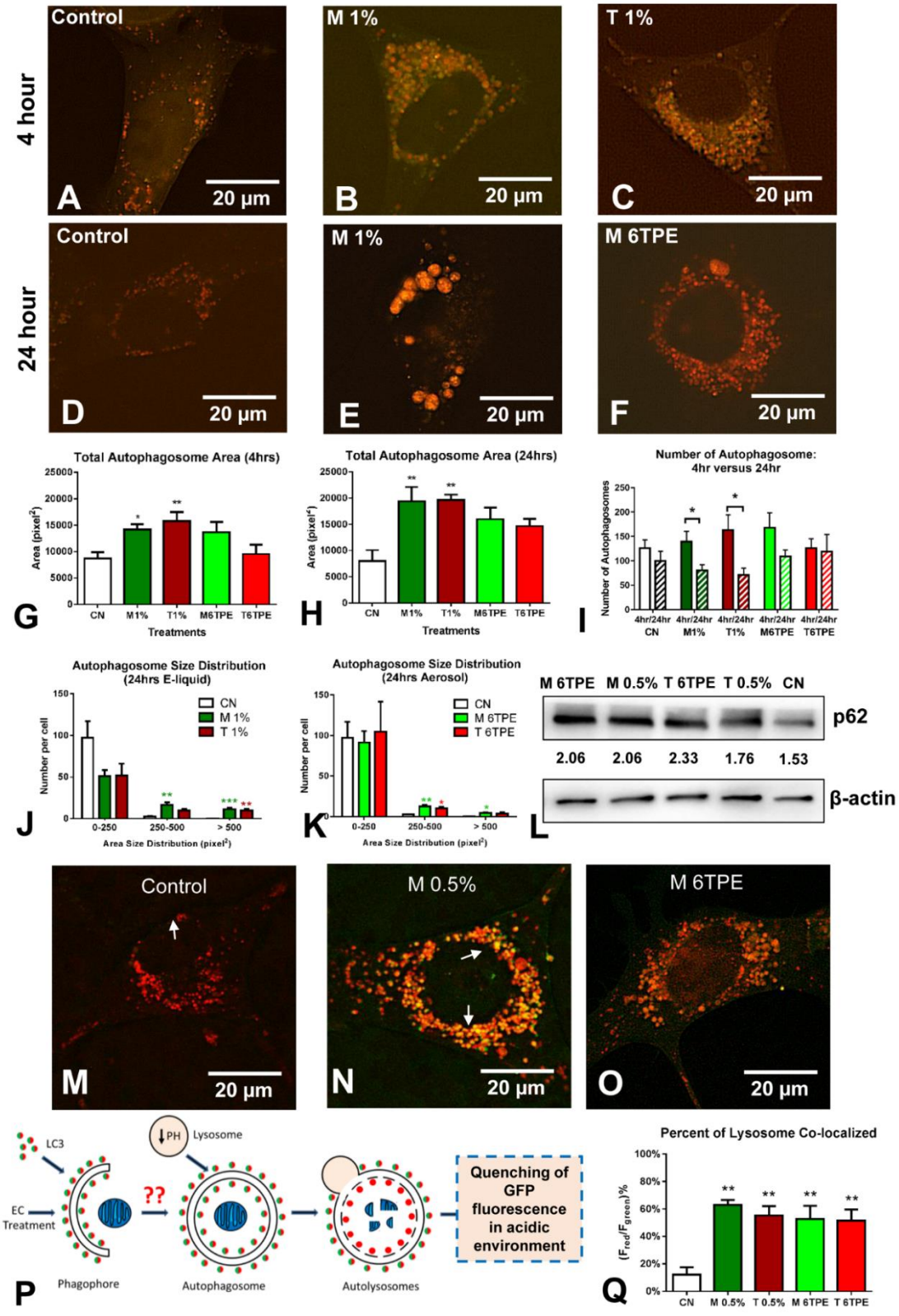
4 hour
24 hour
Control
M 1%
T 1%
M 6TPE
20 μm
A
B
C
D
E
F
Total Autophagosome Area (4hrs)
Total Autophagosome Area (24hrs)
Area (pixel²)
CN
M1%
T1%
M6TPE
T6TPE
Treatments
G
H
Number of Autophagosome: 4hr versus 24hr
Number of Autophagosomes
4hr/24hr
I
Autophagosome Size Distribution (24hrs E-liquid)
Autophagosome Size Distribution (24hrs Aerosol)
Number per cell
M 1%
T 1%
M 6TPE
T 6TPE
0-250
250-500
> 500
Area Size Distribution (pixel²)
J
K
M 6TPE
M 0.5%
T 6TPE
T 0.5%
CN
p62
2.06
2.06
2.33
1.76
1.53
β-actin
L
Control
M 0.5%
M 6TPE
M
N
O
LC3
EC Treatment
PH
Lysosome
??
Phagophore
Autophagosome
Autolysosomes
Quenching of GFP fluorescence in acidic environment
P
Percent of Lysosome Co-localized
(F_red/F_green)%
Q

Figure 5.1. EC Liquid or Aerosol Exposure Impairs Autophagy Clearance. (A-C) Autophagy mRFP-EGFP-LC3 reporter images of control, menthol 1% e-liquid, and tobacco 1% liquid NSCs after 4 hours. (D-F) Autophagy reporter images of control, menthol 1% e-liquid, menthol 6TPE aerosol-treated NSCs after 24 hours. (G-H). Quantification of total autophagosome area after 4 hours and 24 hours of treatment. (I) Comparison of number of autophagosomes between 4 hours and 24 hours of treatment. Significant of autophagosomes number was determine by comparing the two time points. (J-K) Size distribution plot revealing an increase in medium and large autophagosomes in 24-hour e-liquid and aerosol treated NSCs. (L) Western blot analysis of p62, an autophagy marker revealing increased expression in e-liquid and aerosol treatments. (M-O) Autolysosome (mApple-pHluorin-LAMP1) reporter images of control, menthol 0.5% e-liquid, and menthol aerosol-treated NSCs after 24 hours. (P) A schematic diagram showing the autophagosome to autolysosome maturation and quenching of pHluorin (green) fluorescence intensity upon lysosome acidification. (Q) Red-to-green fluorescence ratio of the autolysosome reporter showing a loss of the acidity of the autolysosome. Asterisks on top of each bar indicate the statistical significance. (* = $p < 0.05$. ** = $p < 0.01$. *** = $p < 0.001$. **** = $p < 0.0001$).

autophagosomes in e-liquid exposed cells decreased, likely due to fusion of autophagosomes into large autolysosomes (Fig. 5.1I). The enlarged autophagosomes also had higher GFP fluorescence, indicative of a pH increase. The data were plotted as size distribution graphs, separating the autophagosomes into three bin sizes (Figs. 5.1J-K). This analysis showed an increase in the medium and large-sized autophagosomes in all treatment groups. After 24 hours of treatment, p62 (sequestosome-1), which targets toxic cellular waste for autophagy, was also increased in all conditions (Fig. 5.1L).

Autophagosomes normally merge with lysosomes, forming autolysosomes in which damaged cargo is degraded. An autolysosome-targeted pHluorein-LAMP1 reporter was used to determine if an increase in the pH of autolysosomes diminished proteolysis (Figs. 5.1M-O). This reporter is tagged with both mApple, which is photostable, and pHluorin (a pH-sensitive GFP), which quenches in the acidic environment of autolysosomes (Fig. 5.1P). In contrast to controls, which showed predominantly red fluorescence (Fig. 5.1M), merged images of liquid and aerosol treated cells showed an increase in yellow/orange signal indicating the pH in autolysosomes was not acidic (Fig. 5.1N-O). The percent of co-localization of the mApple and pHluorin channels increased in all treatment groups, indicating a higher than normal pH in autolysosomes (Fig. 5.1Q), which could decrease degradation and contribute to increased autophagic load and backup of flux.

Mitochondria Exposed to E-liquids and Aerosols are Mostly Protected Against Mitophagy

Mitophagy (mitochondrial autophagy) protects cells by eliminating damaged or dysfunctional mitochondria thereby preventing propagation of pro-apoptotic signaling [44]. To quantity mitophagy, NSC were co-transfected with the ptfLC3 plasmid, which targets autophagosomes (only mRFP channel shown) and an mCerulean-tagged mitochondria-targeted plasmid (Fig 5.2A). Cells were treated for 4 and 24 hours, and images were taken using Nikon Ti

Eclipse microscope and a Zeiss Airyscan super-resolution microscope. Similar to untreated controls (Fig. 5.2B), cells treated with e-liquid (Fig. 5.2C) or aerosol (Fig. 5.2D) and their corresponding 3D Zeiss Airyscan super-resolution videos (Videos S5.1-S5.6) showed little overlap of the mitochondria and autophagosomes. CellProfiler software was used to quantify the percentage of overlap (co-localization) between the mCerulean and mRFP channels. After 4 and 24 hours of treatment, mitophagy had not increased significantly, except in the high dose 1% menthol group (Figs. 5.2E-H). These data show that mitochondria, for the most part, are protected from mitophagy in cells treated with e-liquids and aerosols.

EC Liquids and Aerosols Altered Mitochondrial Dynamics

Mitochondrial motion analysis was done on time-lapse images of living cells using MitoMo (http://vislab.ucr.edu/SOFTWARE/software.php), a motion-magnification algorithm that quantifies and sums the magnitude of mitochondrial motion over all pixels. Motion analysis at the pixel level allows quantification in cases where tracking individual organelles is not possible. Examples of the motion vectors obtained with MitoMo are depicted in Figs 5.2I-K. The total motion (net sum of all motion vectors) was classified as small, medium, or large. Treatment with e-liquids decreased motion relative to controls (Fig 5.2L). In contrast, menthol aerosol treated NSCs exhibited a decrease in small motion and an increase in large motion (Fig 5.2M). The tobacco aerosol treated group showed a similar increase in large motion, but was not statistically significant, (Fig 5.2M). The hyperfused mitochondria (aerosol) had greater motion than the control, whereas the swollen mitochondria (high e-liquid concentrations) had less motion than the control.

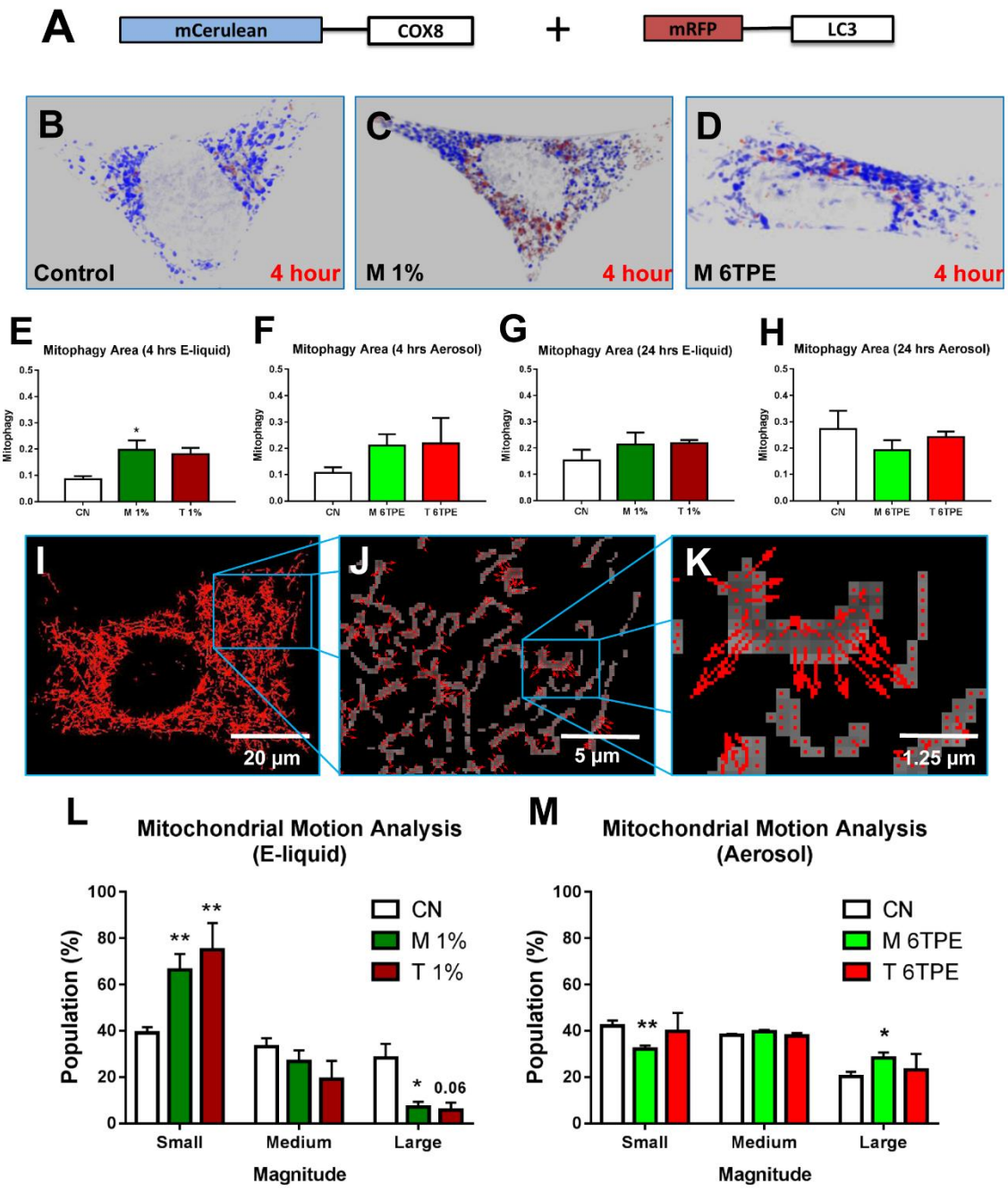
A
mCerulean
COX8
+
mRFP
LC3
B
Control
4 hour
C
M 1%
4 hour
D
M 6TPE
4 hour
E
Mitophagy Area (4 hrs E-liquid)
F
Mitophagy Area (4 hrs Aerosol)
G
Mitophagy Area (24 hrs E-liquid)
H
Mitophagy Area (24 hrs Aerosol)
Mitophagy
CN
M 1%
T 1%
M 6TPE
T 6TPE
I
20 µm
J
5 µm
K
1.25 µm
L
Mitochondrial Motion Analysis
(E-liquid)
M
Mitochondrial Motion Analysis
(Aerosol)
Population (%)
Small
Medium
Large
Magnitude
0.06

Figure 5.2. Mitochondria are Protected Against Mitophagy and Display Altered Motion. (A) Dual transfection with an mCerulean mitochondrial-targeted (blue) and mRFP-tagged autophagosome (red) reporters. (B-D) Control and 4-hour e-liquid and aerosol treated NSC super-resolution images were 3D reconstructed to visualize mitophagy (blue mitochondria engulfed by red autophagosomes). (E-H) Ratio of co-localized area divided by total mitochondrial area after 4 and 24 hour treatments showed primarily no significant change in mitophagy except in the 4-hour menthol e-liquid treatment. (I-K) Motion images at increasing magnifications of a NSC treated with a low dose of e-liquids. Arrows indicate direction and magnitude of motion for each pixel. (L) Motion analysis of 24-hour e-liquid treatments showed a significant increase in small magnitude vectors, and a decrease in large magnitude vectors, indicating an overall decrease in motion. (M) Motion analysis of 24-hour aerosol treatments showed a significant decrease in small magnitude vectors, and an increase in large magnitude vectors for the menthol group, indicting an overall increase in motion. Asterisks on top of each bar indicate the statistical significance. (* = $p < 0.05$. ** = $p < 0.01$. *** = $p < 0.001$. **** = $p < 0.0001$).

EC Caused Mitochondrial Swelling and Stress-Induced Mitochondrial Hyperfusion (SIMH)

The effect of e-liquid and aerosol on mitochondrial number and morphology was investigated using a stably-transfected MitoTimer-NSC line, which provided a strong fluorescent signal suitable for segmenting and classifying mitochondrial morphology. Cells were incubated for 24 hours with menthol or tobacco-flavored e-liquids or aerosols and compared against untreated controls by segmenting and quantifying mitochondrial number and area using CellProfiler software. The number of mitochondria in e-liquid and aerosol-treated cells decreased dose-dependently (Figs. 5.3A-B), while the total mitochondrial area increased in some treatments (Figs. 5.3C-D). These data support the hypothesis that mitochondria are undergoing hyperfusion, which results in a decrease in the number of mitochondria. The increase in total mitochondrial area in some concentrations supports mitochondrial biogenesis.

To further investigate EC-induced hyperfusion, mitochondria in treated cells were classified morphologically as punctate, swollen, or networked using MitoMo software. Transition from the punctate to networked morphology occurs during hyperfusion [38, 39]. The percentage of each morphological type was calculated relative to total mitochondrial area (Figs. 5.3E-H). In the e-liquid treated cells, mitochondrial hyperfusion increased at the 0.3% concentration and swelling increased in the 0.5% and 1% treatment groups (Figs. 5.3E-F). Menthol and tobacco aerosols caused a decrease in the number of punctate mitochondria and a corresponding increase in the networked morphology (Figs. 5.3G-H). These changes further support the idea that EC aerosol caused stress-induced mitochondrial hyperfusion (SIMH), which is a pro-survival protective response [38, 39]. Time-lapse imaging of living cells showed examples of punctate mitochondria fusing to form larger networked mitochondria (Fig 5.3I).

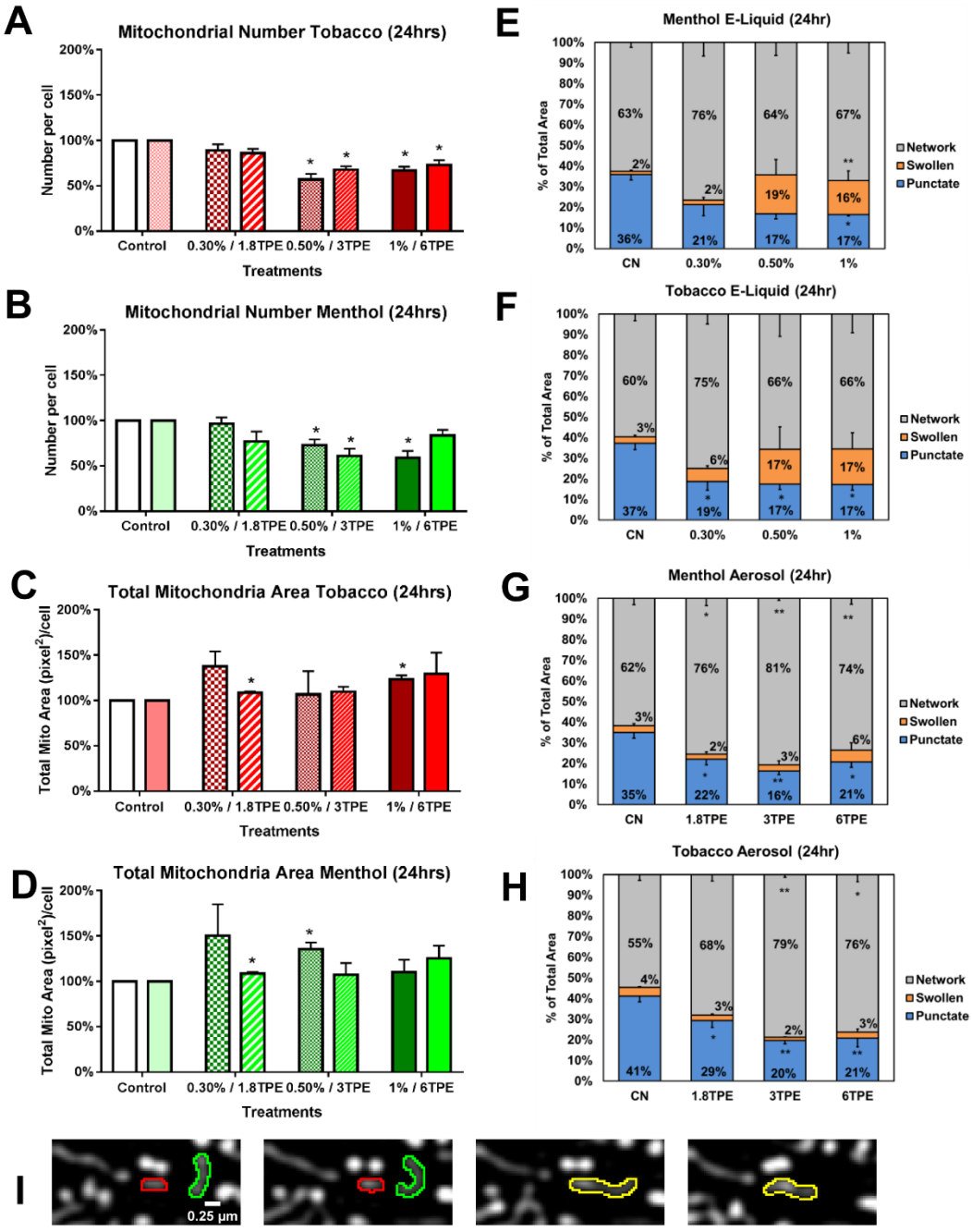
A
Mitochondrial Number Tobacco (24hrs)
Number per cell
200%
150%
100%
50%
0%
Control
0.30% / 1.8TPE
0.50% / 3TPE
1% / 6TPE
Treatments
B
Mitochondrial Number Menthol (24hrs)
Number per cell
Treatments
C
Total Mitochondria Area Tobacco (24hrs)
Total Mito Area (pixel²)/cell
Treatments
D
Total Mitochondria Area Menthol (24hrs)
Total Mito Area (pixel²)/cell
Treatments
E
Menthol E-Liquid (24hr)
% of Total Area
63%
2%
36%
76%
2%
21%
64%
19%
17%
67%
16%
17%
CN
0.30%
0.50%
1%
Network
Swollen
Punctate
F
Tobacco E-Liquid (24hr)
60%
3%
37%
75%
6%
19%
66%
17%
17%
66%
17%
17%
G
Menthol Aerosol (24hr)
62%
3%
35%
76%
2%
22%
81%
3%
16%
74%
6%
21%
CN
1.8TPE
3TPE
6TPE
H
Tobacco Aerosol (24hr)
55%
4%
41%
68%
3%
29%
79%
2%
20%
76%
3%
21%
I
0.25 µm

Figure 5.3. EC Liquid or Aerosol Exposure Results in Swollen and Hyperfused Mitochondria. (A-B) Mitochondrial number was quantified and normalized to the control group for 24-hour tobacco and menthol e-liquid and aerosol treatments, showing a general decrease in mitochondria number. (C-D) Total mitochondrial area was quantified and normalized to the control group for 24-hour tobacco and menthol e-liquid and aerosol treatments, revealing an increase in some concentrations. (E-F) Morphological classification of dotted, networked, and swollen mitochondria treated for 24 hours with menthol or tobacco e-liquid, showing mitochondrial hyperfusion in the low concentrations and swelling in the higher concentrations. (G-H) Morphological classification of dotted, networked, and swollen mitochondria after 24 hours of treatment with menthol or tobacco aerosol, showing mitochondrial hyperfusion in all concentrations. (I) A representative image of two mitochondria fusing to form the networked phenotype. Asterisks on top of each bar indicate the statistical significance. (* = $p < 0.05$. ** = $p < 0.01$. *** = $p < 0.001$. **** = $p < 0.0001$)

EC Liquids and Aerosols Increased Mitochondrial Superoxide Levels

Because hyperfusion can increase superoxide production [39], we next loaded cells with MitoSOX Red, a mitochondrial-targeted dye that produces red fluorescence in the presence of

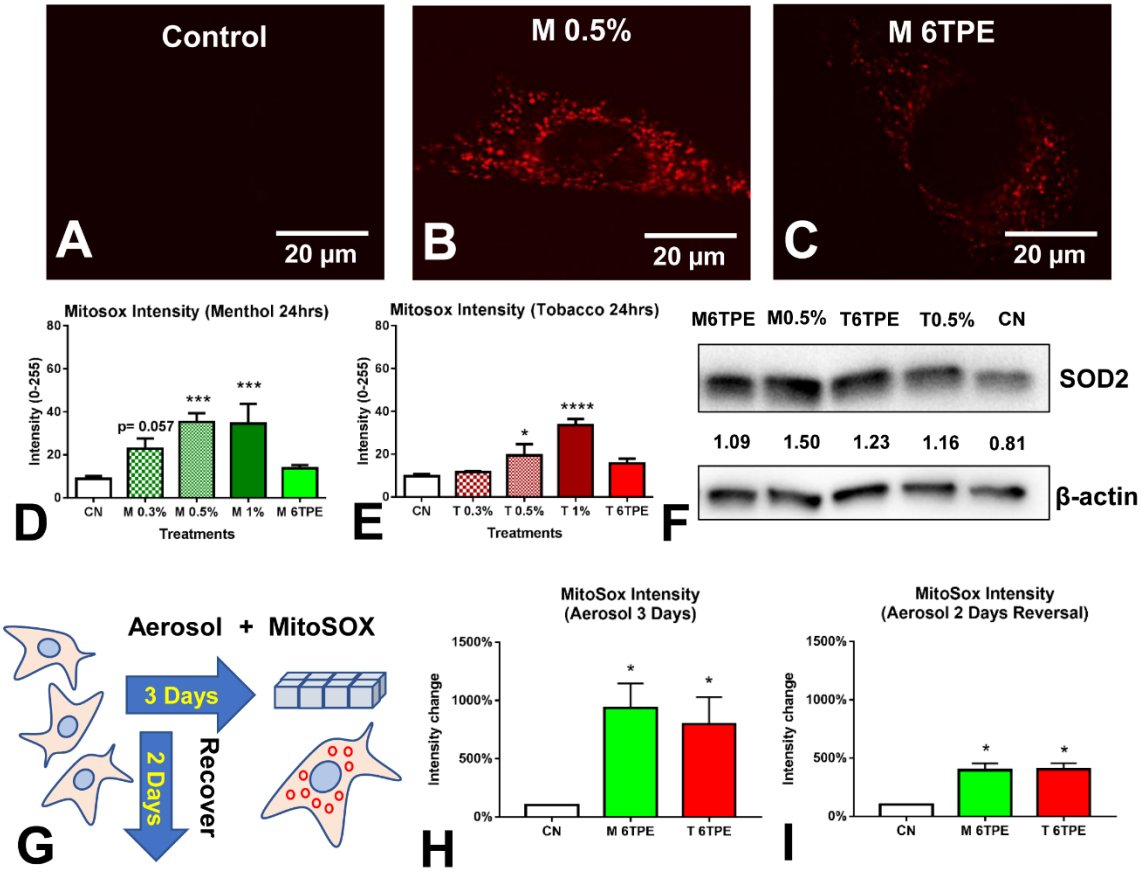

Figure 5.4. Exposure to EC liquid or Aerosol Causes Super-Oxide Production and an Antioxidant Response. (A-C) Control and 24-hour e-liquid and aerosol treated NSCs labeled with MitoSOX Red showing increased levels of superoxide in the mitochondria. (D-E) MitoSOX intensity levels were quantified for all menthol and tobacco treatments and showed a concentration response increase in all groups with the e-liquid groups being significant. (F) Western blot of superoxide dismutase 2 (SOD2), a superoxide scavenger, showing increase expression in most treatment groups. (G) A schematic diagram representing prolonged (3 days treated) aerosol treatments and reversal (2 days treated, 2 days reversal) experiments, followed by MitoSOX quantification. (H) 3-day aerosol treatment caused an increase in MitoSOX intensity relative to control cells. (I) 2-day aerosol treatment followed by 2 days of recovery decreased intensity relative to figure H but did not produce a full recovery. Asterisks on top of each bar indicate the statistical significance. (* = p <0.05. ** = p <0.01. *** = p <0.001. **** = p <0.0001)

superoxide anion. Loaded cells were incubated for 24 hours with menthol and tobacco e-liquids or aerosols, and MitoSOX fluorescence was analyzed using CL-Quant software. There was a dose-dependent increase in MitoSOX intensity in the e-liquid-treated cells, and a modest increase in the aerosol treatments after 24 hours (Fig 5.4A-E). To determine if the increase in mitochondrial ROS induced an antioxidant response, superoxide dismutase 2 (SOD2), a mitochondrial enzyme that converts superoxide into hydrogen peroxide and diatomic oxygen, was quantified using Western blots. Cells treated for 24-hours with either e-liquid or aerosol had significantly elevated SOD2 levels when compared to controls (Fig 5.4F).

To determine if longer aerosol treatment would elevate mitochondrial ROS levels, NSC were treated for 3 days then loaded with MitoSOX dye (Fig 5.4G). There was a statistically significant increase in MitoSOX fluorescence in the menthol and tobacco 6TPE aerosol treated cells (Fig 5.4H). Furthermore, treatment for 2 days followed by 2 days of recovery did not completely reverse the MitoSOX fluorescence (Fig 5.4I), suggesting that the increase in mitochondrial ROS was not readily reversible.

EC Exposure Induces Mitochondrial Protein Oxidation

The MitoTimer reporter cell line was used to assess the effects of EC liquid and aerosol on mitochondrial protein oxidation. MitoTimer is composed of the colorimeter Timer protein tagged to the cytochrome c oxidase subunit VIII gene, which targets it to the mitochondria [45]. This reporter detects an increase in mitochondrial protein oxidation or aging by an increase in the red/green fluorescence ratio (Fig 5.5A). MitoTimer-NSCs were treated for 24 hours with EC liquids or aerosols. Menthol aerosol-treated cells showed an increase in red fluorescence, as demonstrated in the merged images of the red and green channels (Fig 5.5C-D). The red/green fluorescence ratio was quantified using CL-Quant image processing software and showed a concentration-dependent

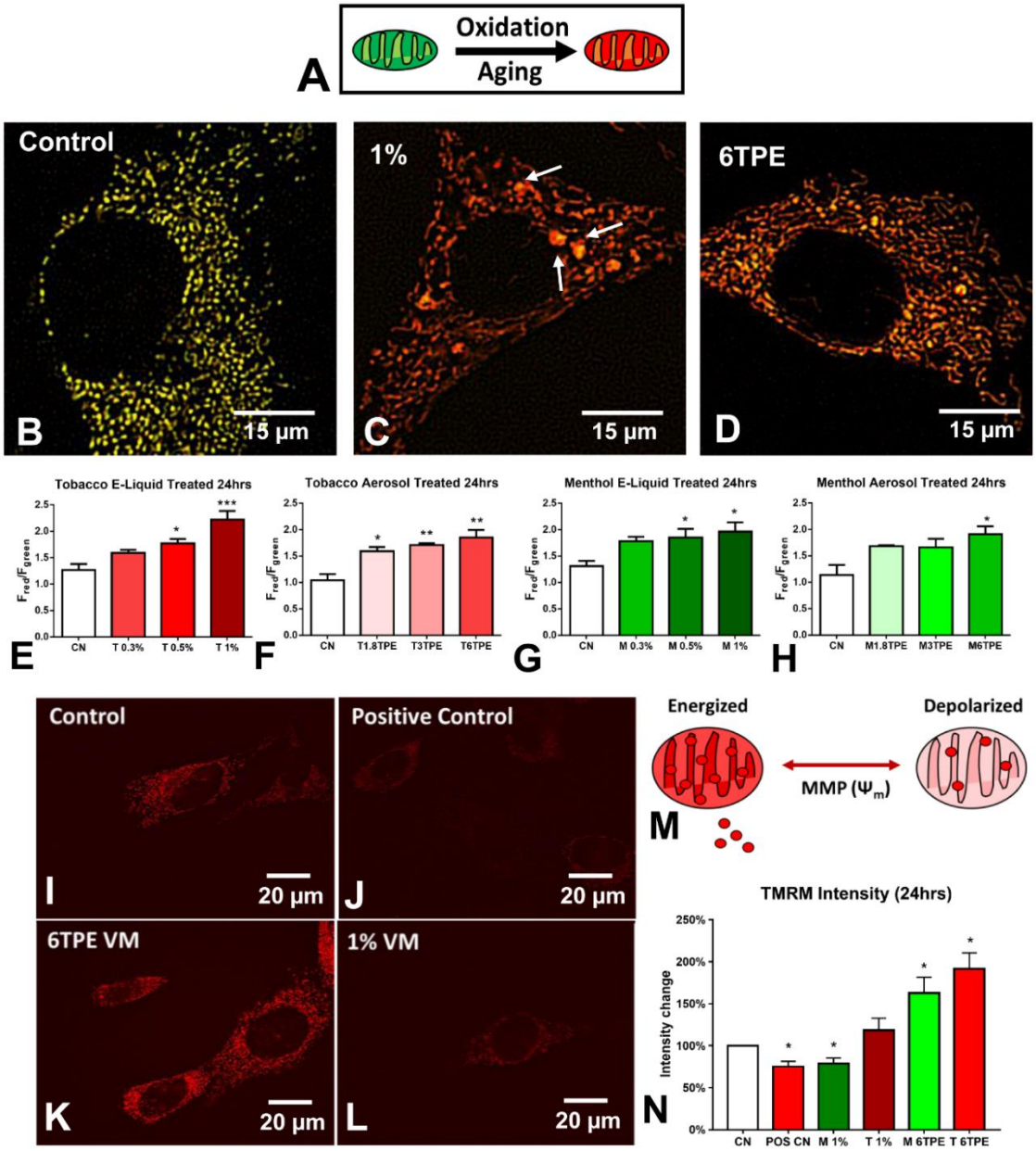

Figure 5.5. EC Liquids and Aerosols Increase Mitochondrial Protein Oxidation and Membrane Potential. (A) A schematic of the mitochondrial-targeted reporter MitoTimer, which shifts from green to red fluorescence upon protein oxidation and/or aging. (B-D) Control and 24-hour e-liquid and aerosol treated MitoTimer-NSCs. (E-H) MitoTimer red to green ratio indicative of mitochondrial protein oxidation levels were quantified revealing a dose-response increase in all treatments. (I-L) Control and 24-hour menthol e-liquid, menthol aerosol, and KCN/oligomycin treated NSCs labeled with the mitochondrial membrane potential dye TMRM. (M) A schematic of TMRM dye sequestering by normal mitochondria, versus depolarized mitochondria which are leaky and have weaker TMRM fluorescence. (N) TMRM fluorescence intensity was quantified and normalized to the control group, showing a loss of membrane potential in the menthol 1% high concentration and increased membrane potential in both aerosol treatments.

increase in all e-liquid and aerosol treatments (Figs 5.5E-H). The swollen mitochondria also had a high red-to-green MitoTimer ratio, indicative of high levels of ROS (white arrows in Fig. 5.5C). These increases in the red/green ratio correspond to a significant elevation in oxidation of mitochondrial proteins in e-liquid and aerosol treated cells compared to untreated controls.

EC Liquids and Aerosols Alter the Mitochondrial Membrane Potential

To examine mitochondrial membrane potential (MMP), cells were labeled with tetramethylrhodamine, methyl ester (TMRM) dye, then treated with e-liquid or aerosol for 24 hours (Figs 5.5I-L). This cell-permeant, cationic, red dye is sequestered by active mitochondria in live cells but leaks out of depolarized mitochondria (Fig 5.5M). As a positive control, cells were de-energized with 2.5 mM potassium cyanide (KCN), a respiratory inhibitor and 1 µg/mL of oligomycin, a mitochondrial ATPase inhibitor (Fig 5.5J). Treatment with menthol aerosols increased TMRM accumulation in the mitochondria (Fig 5.5K), which is consistent with the observed mitochondrial hyperfusion and subsequent metabolic shift; however, the TMRM signal was decreased in the 1% menthol e-liquid group (Fig 5.5L), suggesting this concentration damages the mitochondria and causes membrane leakage. The TMRM fluorescence intensity was quantified using CL-Quant software and normalized to the control (Fig 5.5N). In agreement with the fluorescent images, the positive control and 1% menthol e-liquid decreased the MMP, while the aerosols significantly increased the potential. TMRM measurements were then done after 30 minutes, 1 hour, 2 hours, 4 hours, and 24 hours for the menthol e-liquid group. Initially the membrane potential rises (likely due to an increase in ROS), but by 24 hours, it dropped due to membrane damage (Fig S5.1).

EC Treatment Induced Aggregation of Mitochondrial Nucleoids and mtDNA Damage

Elevation of ROS in mitochondria could affect their DNA (mtDNA). To investigate this possibility, cells were treated with e-liquids (0.5%) and aerosols (6TPE) for 24 hours then incubated with Quant-iT PicoGreen dye, which labels dsDNA including mitochondrial nucleoids. Control cells exhibited multiple small fluorescent green nucleoids (Fig 5.6A), whereas the treated cells had larger brighter nucleoids (Figs 5.6B-C), indicative of mtDNA nucleoid aggregation. Quantification using CL Quant demonstrated an increase in both the average mtDNA nucleoid area/cell and nucleoid intensity in all treated groups relative to controls (Fig 5.6D, E). There was also an increase in the nuclear PicoGreen signal, especially in the e-liquid treated group (Fig 5.6B), perhaps due to damage of the nuclear envelope. PicoGreen signal was also co-labeled with Mitotracker dye (Figs 5.6F-G), revealing aggregated PicoGreen signals within the swollen mitochondria treated with 1% menthol e-liquid.

Nicotine Caused Increased Protein Oxidation and Mitochondrial Hyperfusion

Nicotine concentrations in 1% EC liquids and 6TPE aerosols from tobacco and menthol-flavored disposable cartomizers were analyzed using high-performance liquid chromatography (HPLC), as described previously [6]. E-liquids had an average of 44 mg of nicotine/mL, while aerosols had lower concentrations of 110 µg/mL (Fig 5.7A). To determine if nicotine was contributing to oxidative stress in mitochondria, cells were treated for 3 days with 110 or 220 µg of nicotine/mL (corresponding to concentrations found in aerosol), and labeled with MitoSOX Red. Fluorescent images were captured, and average intensity/cell was quantified using CL-Quant software. There was a statistically significant increase in the average MitoSOX fluorescent intensity, relative to untreated controls, in the nicotine-treated groups (Fig 5.7B). Superoxide production was lower in cells that were allowed to recover for 2 days following 2 days of nicotine

treatment, nevertheless superoxide remained significantly elevated compared to the untreated control (Fig 5.7C).

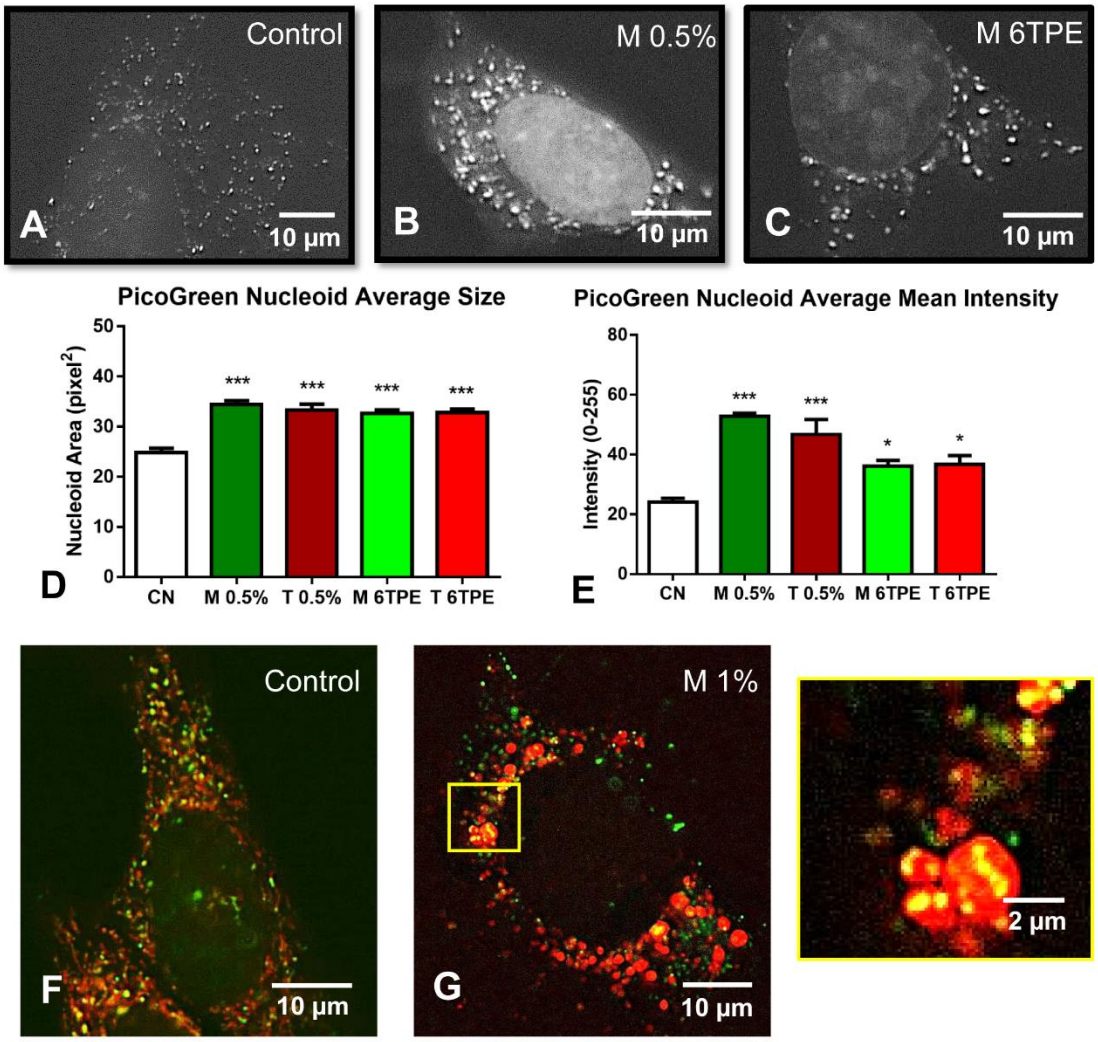

Figure 5.6. EC Liquids and Aerosols Cause Aggregation of mtDNA Nucleoids. (A-C) Control and 24-hour menthol e-liquid and aerosol treated NSC imaged lived with PicoGreen dye, which labels mtDNA. (D-E) PicoGreen fluorescence puncta were quantified to show an increase in average mtDNA nucleoid size and average mean intensity. (F-G) Control and 24-hour menthol e-liquid treated NSCs labeled with PicoGreen (mtDNA) and MitoTracker-Red (mitochondria), showing aggregated mtDNA in the menthol 1% e-liquid treated condition.

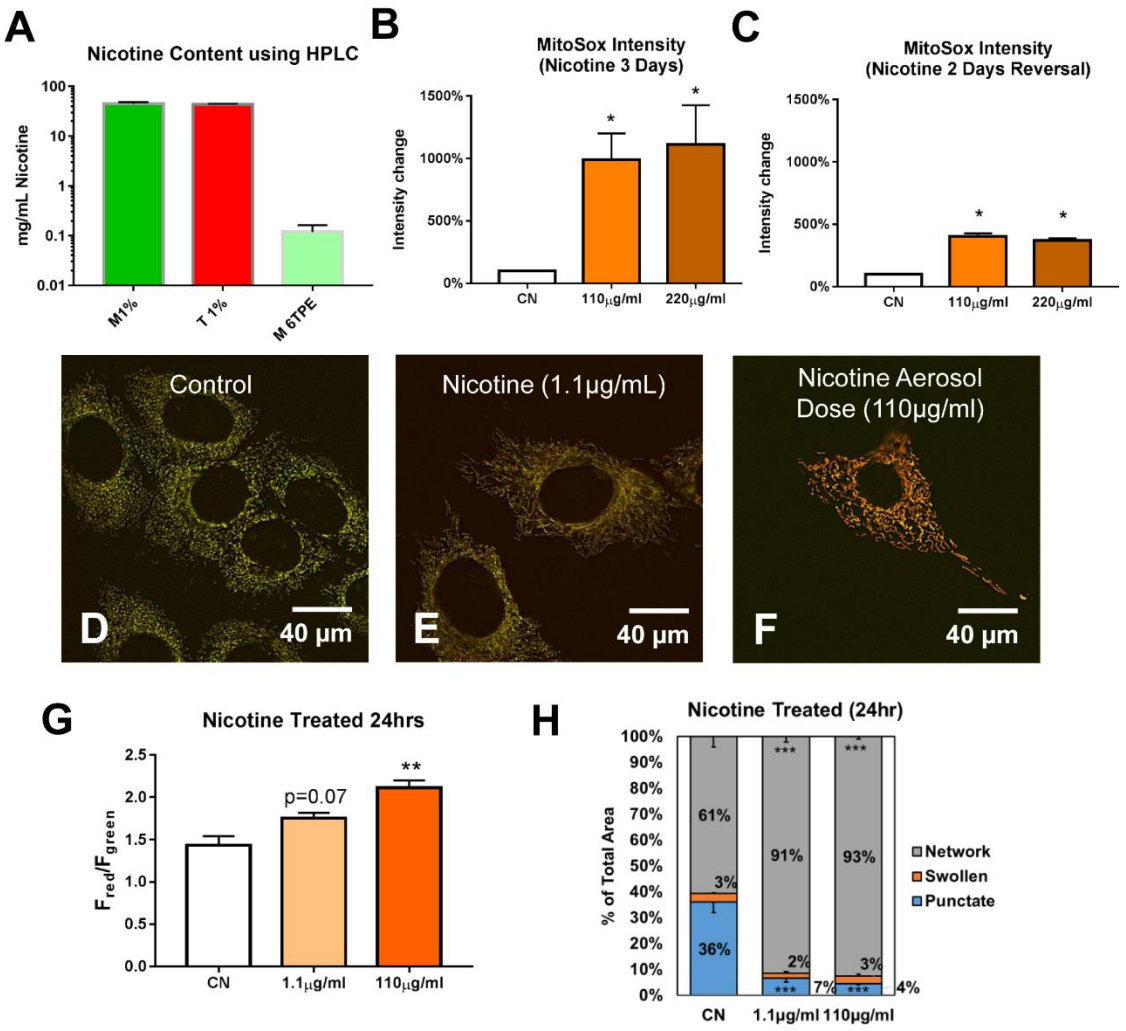

Figure 5.7. Nicotine-Induced Mitochondrial Protein Oxidation and Hyperfusion. (A) Nicotine concentrations in the 1% e-liquid and 6TPE aerosols were quantified using HPLC. (B) 3-day nicotine treatments (110 µg/mL and 220 µg/mL, corresponding to amount of nicotine found in aerosols) increased MitoSOX intensity relative to control cells. (C) 2-day nicotine treatment followed by 2 days of recovery, decreased ROS production, but did not produce a full recovery. (D-F) Control and 24-hour nicotine treatment (110 µg/mL, and 1.1 µg/mL corresponding to a 100-fold lower concentration). (G) Both concentrations of nicotine increased the MitoTimer red/green fluorescent ratio indicative of mitochondrial protein oxidation. (H) Both concentrations of nicotine caused a significant increase in mitochondrial hyperfusion (increase of networked mitochondria relative to punctate and swollen morphologies). Asterisks on top of each bar indicate the statistical significance. (* = p <0.05. ** = p <0.01. *** = p <0.001. **** = p <0.0001)

To determine if nicotine was contributing to mitochondrial protein oxidation and SIMH, the MitoTimer-NSCs were treated with nicotine at 110 µg/mL (corresponding to 6TPE of aerosol) and 1.1 µg/mL (100-fold lower concentration than found in aerosol) (Figs 5.7E-F). Live images were collected after 24 hours and the fluorescent ratios of the red to green channels were quantified using CL-Quant software. There was a concentration-dependent effect on mitochondrial protein oxidation in both nicotine treated groups, with a statistically significant increase in the 110 µg/mL dose (Fig 5.7G). The mitochondrial morphologies showed both a statistically significant increase in the networked mitochondria and a decrease in the punctate mitochondria in both treatment groups (Fig 5.7H). The induction by nicotine of mitochondrial hyperfusion and an increase in superoxide production is consistent with the changes observed in the aerosol treated cells (Figs 5.3G-H, 5.4H-I, 5.5F, 5.5H).

EC and Nicotine Exposure Induces Ca2+ Influx Leading to Plasma Membrane Retraction and Intracellular Calcium Overload

Nicotine can activate nicotinic acetylcholine receptors (nAChRs) on cell membranes in the central nervous system (CNS) and other non-neuronal cells, resulting in an influx of cations, including Ca2+ [46]. To evaluate the effect of nicotine and EC exposure on nAChR-calcium signaling, NSCs were transfected with a calcium reporter (GCaMP5) consisting of a circularly permuted green fluorescent protein (cpGFP), calmodulin (CaM), and the Ca2+/CaM-binding "M13" peptide [47]. Transfected cells were imaged live before and after the addition of e-liquids, aerosols, and various concentrations of nicotine. A rapid increase in fluorescence was visible within 1 minute of adding of 6TPE aerosol (Fig 5.8A) and 1.1 µg/mL of nicotine (Fig 5.8B). The fluorescence signal accumulated in the perinuclear region, presumably due to sequestering of calcium by the endoplasmic reticulum (ER). In addition, the plasma membrane began to retract,

particularly at cell-to-cell contacts (white arrow in Fig 5.8B, higher magnification shown in Fig 5.8C). After approximately 170 minutes, some of these retractions pinched off forming small extracellular fragments with elevated fluorescence indicative of high levels of calcium (red arrows in Fig 5.8B and higher magnification shown in Fig 5.8D). The GCaMP5 fluorescence intensity was quantified for all concentrations over time (Figs 5.8E-F), and statistical analysis was done by comparing each time to time = 0 min (Table S5.1). These data show that Ca2+ levels did not return to control levels in the higher doses, resulting in Ca2+ overload.

EC-Induced Mitochondrial Calcium Influx can be Blocked to Prevent Mitochondria Damage

Intracellular calcium can accumulate in mitochondria, where it regulates various cellular functions [48]. Unlike the ER, mitochondria are a passive Ca2+ buffer, and calcium accumulation in the mitochondria triggers ROS production [49]. To examine the effect of nicotine and EC exposure on mitochondrial calcium levels, NSC were transfected with a genetically encoded Ca2+ indicator, calcium-measuring organelle-entrapped protein indicator (CEPIA) [50]. Transfected cells were imaged live before and after the addition of e-liquids, aerosols, and various concentrations of nicotine. All treatments resulted in an increase in fluorescence signal within 1 minute of treatment followed by a decrease in fluorescence by 44 minutes (Figs 5.8G). The fluorescence intensity was quantified using CL-Quant software and the normalized change in intensity relative to the “before” (0 min) timepoint was plotted (green lines on Figs 5.8J-O). Most treatments were significantly different than the 0-minute control, and fluorescent intensity returned to basal levels in some groups by 20 minutes (Figs 5.8K, 8M-O). However, in the case of 0.5% menthol and the 220 μg/mL of nicotine, the calcium levels did not return to resting states (Figs 5.8J, 5.8L), indicating a persistent elevation in mitochondrial calcium.

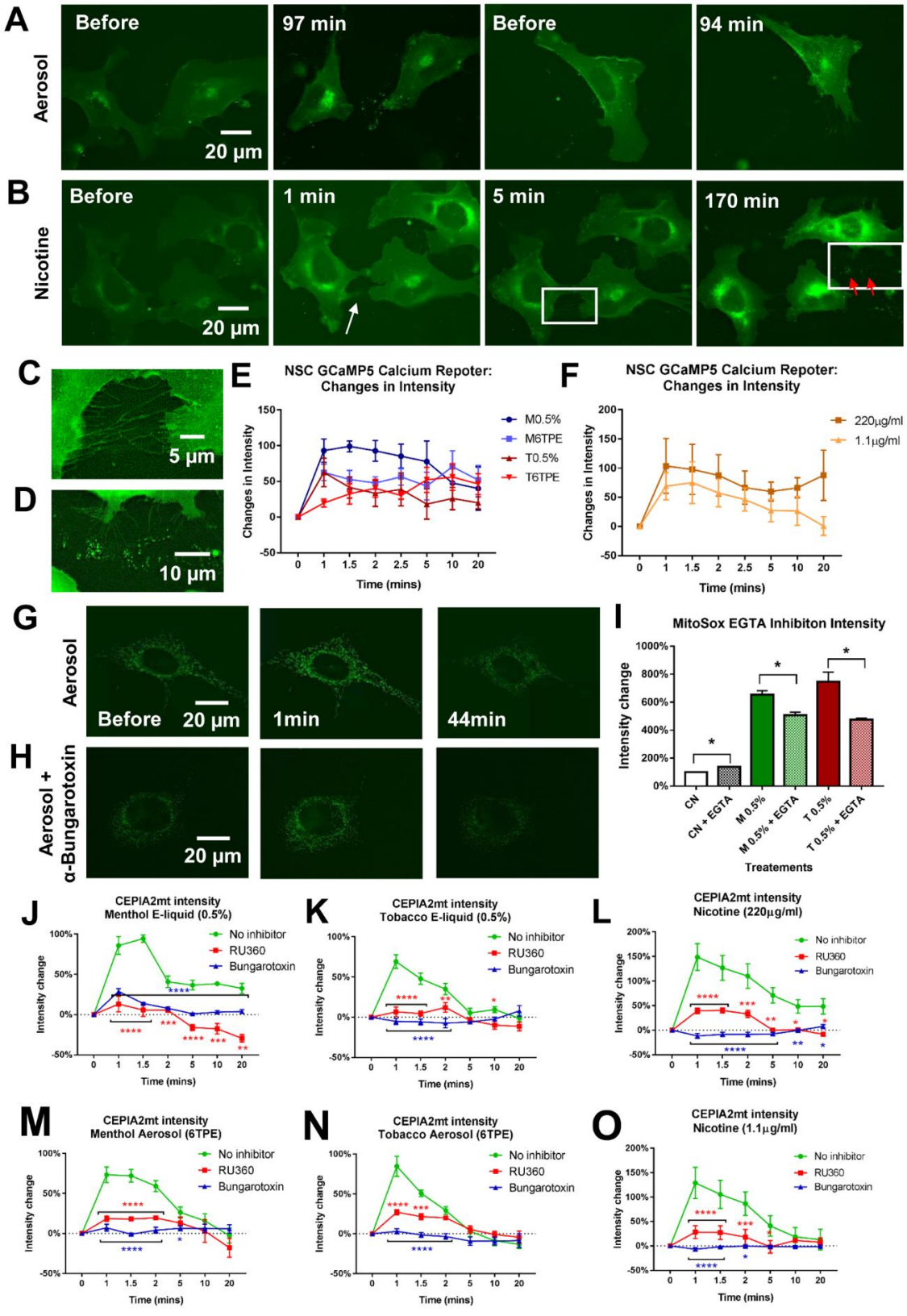
A
Aerosol
Before
97 min
Before
94 min
20 μm
B
Nicotine
Before
1 min
5 min
170 min
20 μm
C
5 μm
D
10 μm
E
NSC GCaMP5 Calcium Repoter: Changes in Intensity
Changes in Intensity
Time (mins)
M0.5%
M6TPE
T0.5%
T6TPE
F
NSC GCaMP5 Calcium Repoter: Changes in Intensity
Changes in Intensity
Time (mins)
220μg/ml
1.1μg/ml
G
Aerosol
Before
20 μm
1min
44min
H
Aerosol + α-Bungarotoxin
20 μm
I
MitoSox EGTA Inhibiton Intensity
Intensity change
CN
CN + EGTA
M 0.5%
M 0.5% + EGTA
T 0.5%
T 0.5% + EGTA
Treatements
J
CEPIA2mt intensity Menthol E-liquid (0.5%)
K
CEPIA2mt intensity Tobacco E-liquid (0.5%)
L
CEPIA2mt intensity Nicotine (220μg/ml)
M
CEPIA2mt intensity Menthol Aerosol (6TPE)
N
CEPIA2mt intensity Tobacco Aerosol (6TPE)
O
CEPIA2mt intensity Nicotine (1.1μg/ml)
No inhibitor
RU360
Bungarotoxin
Intensity change
Time (mins)

Figure 5.8. EC Liquids and Aerosols Elevate Mitochondrial Calcium. Treatment of GCaMP5-transfected NSC with (A) Aerosol T 6TPE and (B) 110 µµg/mL of nicotine caused a rapid influx of calcium which remained elevated in perinuclear regions. (C) Nicotine treatment resulted in a rapid retraction of cell membranes and dissociation of cell-to-cell adhesion. (D) Nicotine treatment resulted in pinching off of small extracellular fragments with elevated fluorescence indicative of high levels of calcium. (E-F) GCaMP5 fluorescence intensity prior to and after addition of e-liquids, aerosols, and nicotine. (G) Treatment of CEPIA2mt (mitochondrial-targeted calcium reporter)-transfected NSCs with aerosol caused a rapid increase in fluorescence intensity indicative of mitochondrial calcium influx. (H)The increase in CEPIA2mt fluorescence was attenuated in the presence of α-bungarotoxin, an α7 nAChR blocker. (I) Increased MitoSOX Red fluorescence intensity was partially inhibited by the calcium chelator EGTA. (J-O) Mitochondrial calcium levels were assessed using CEPIA2mt fluorescence intensity prior and after addition of e-liquids, aerosols, and nicotine doses (green lines). Red lines represent calcium levels in the presence of RU360 and blue lines in the presence of α-bungarotoxin. Statistical analysis was conducted comparing inhibitor curves against the control curves. Asterisks on top of each bar and points indicate the statistical significance. (* = $p < 0.05$. ** = $p < 0.01$. *** = $p < 0.001$. **** = $p < 0.0001$)

Mitochondria have Ca2+ transporters, such as the mitochondrial Ca2+ uniporter (MCU) [48], that allow import of a high Ca2+ load against a concentration gradient. To block Ca2+ uptake through MCU, NSC were pre-incubated with Ru360, a cell-permeable dinuclear ruthenium amine complex that binds to MCU with high affinity. Similar to previous CEPIA2mt experiments, cells were treated with e-liquids, aerosols, and various concentrations of nicotine, this time following 10 minutes of pre-treatment with 10uM Ru360 (red lines on Figs 5.8I-N). The changes in normalized fluorescent intensity were plotted over 20 minutes, revealing a significant dampening of the intracellular calcium level.

Functional α7 nAChRs are found in the cell plasma membrane, and recently they have been found in the mitochondrial membrane [51, 52]. To block the α7 nAChRs receptors on the cell membrane and the mitochondria, CEPIA2mt-transfected NSCs were pretreated for 10 min with 100 nM of the antagonist α-bungarotoxin, then treated with various concentrations of e-liquids, aerosols and nicotine (Fig 5.8G, blue lines on Fig 5.8I-N). The changes in normalized fluorescent intensity over 20 min revealed a significant inhibition of the mitochondrial calcium influx, likely due to dual blockage of the nicotinic receptors at the cell and mitochondrial membranes.

Lastly, to test whether calcium blockage could inhibit mitochondrial effects, NSCs were incubated with 1uM of calcium chelator EGTA and treated with 0.5% e-liquid doses for 4 hours. The MitoSOX fluorescence intensity was quantified revealing a statistically significant decrease in mitochondrial superoxide production compared to the treatments without EGTA (Fig 5.8H). These data indicate that calcium overload is a contributing factor to the EC-induced mitochondrial defects.

Limitations of the Study

Although the focus of our study was on neural stem cells (NSCs), it would be appropriate in the future to expand work on EC to other cells, such as human respiratory epithelium, and also

to look at effects of sub-chronic and chronic exposure. Our study was done using one of the leading brands of cig-alike type EC, but other brands and tank styles EC should be examined in future work to determine how widespread EC induced stem cell toxicity is.

DISCUSION

This is the first demonstration that e-liquids and aerosols from a leading brand of EC induce a stress response in stem cells that includes interruption of autophagic flux without mitophagy, mitochondrial hyperfusion accompanied by oxidative stress, and mtDNA aggregation. Moreover, this is the first demonstration that these cellular responses can be attributed to nicotine, which by itself mimicked the EC products. Nicotine concentrations that caused cellular stress responses were lower than or similar to the concentrations found in the aerosols that we tested. The hyperfusion stress response appears to be a protective mechanism to guard against mitophagy. We further showed that nicotine caused increased mitochondrial superoxide production, which could be reduced by inhibiting calcium influx. Calcium influx, due to EC or nicotine exposure, could be reversed using an α7 nAChR blocker, chelating extracellular calcium, and/or blocking the mitochondrial calcium uniporter channel. Taken together, these data support the conclusion that tobacco products containing nicotine can stress stem cells and induce a transient survival response.

Autophagy promotes quality control and cell health by sequestering and degrading damaged cellular proteins and organelles, including mitochondria [33, 53]. Degradation within autolysosomes depends on acidity and the functioning of acid hydrolases and vacuolar-type proton ATPase [43]. Factors that elevate the pH in autolysosomes prevent degradation and turnover of cellular components. Treatment of NSC with EC products resulted in an increase in autophagosomes and autolysosomes, in agreement with a recent study showing an increase in LC3, an autophagy marker, in airway epithelial cells exposed to EC aerosols [54]. Our study shows that

backup of autophagic flux is due to loss of the acidic environment within autolysosomes. The increase in lysosomal pH is likely caused by nicotine, a weak base, that can diffuse across the cell membrane and accumulate in lysosomes by proton trapping [55, 56].

Mitophagy normally occurs when damaged mitochondria fragment into small punctate mitochondria that can readily be engulfed by autophagosomes [57, 58]. Treatment with EC liquids and aerosols triggered autophagy, but paradoxically, not mitophagy. Treated mitochondria formed interconnected tubular networks (hyperfusion), which likely protected them from mitophagy (Fig 5.2E-H). The small but significant increase in mitophagy seen in the 1% menthol e-liquid is likely due to clearance of the swollen mitochondria, which were elevated in this group (Fig 5.2E). In agreement with this idea, swelling was accompanied by loss of the mitochondrial membrane potential, thereby putting the leaky mitochondria at risk for targeted degradation (Fig 5.5L). Thus, while SIMH has several consequences for the mitochondria, one of them appears to be to protect mitochondria from mitophagy.

High concentrations of e-liquids caused mitochondrial swelling, likely due to an excess of mitochondrial calcium, which did not protect against mitophagy. Calcium overload can trigger mitochondrial impairment, especially in cases where calcium uptake is accompanied by oxidative stress [47]. It is now known that nAChRs are also present on the mitochondrial membrane [51, 52], and that nicotine can enter cells. As shown in our study, nicotine treatment (binding to nAChRs) leads to a large influx of calcium, both into the cytoplasm as well as into the mitochondria. The e-liquids had much higher concentrations of nicotine than the aerosol, which likely accounts for the production of swollen mitochondria due to calcium overload. An excess of mitochondrial calcium may cause opening of the mitochondrial permeability transition pore (MTP), which in turn can lead to swelling of the mitochondrial matrix as water, small molecules, and protons enter, resulting in outer membrane rupture [59]. The nicotine concentration difference between the e-liquid and

aerosol probably comes about because of the relatively poor transfer of nicotine to the aerosol upon heating in the cig-a-like product used in this study.

SIMH, which was first described by Tondera et. al. in response to treatment with stress stimuli (e.g., UV irradiation, actinomycin D, cycloheximide), is now recognized as a transient survival response in cells exposed to toxic substances [38,60]. Our data show that cells responded to low doses of EC liquids and aerosol and nicotine by undergoing SIMH accompanied by increased ROS production, which in turn increased oxidation of mitochondrial proteins. Increased protein oxidation can irreversibly damage mitochondria and thereby cause changes in the integrity of mitochondrial membranes and their membrane potential [61, 62]. Changes in the permeability of the mitochondrial membrane to proteins, such as cytochrome C, is a critical initiation factor for apoptosis and other signaling cascades [52, 63], suggesting that high doses or prolonged exposure to EC aerosols eventually result in cell death.

Changes similar to those observed in our study have also been reported in NSC treated with thirdhand smoke (THS) extracts [39]. THS is a rich source of nicotine, which likely caused SIMH and the accompanying changes. During chronic treatment of NSC with THS for 15 days, mitochondria maintained an elevated membrane potential (MMP) and proliferated at a faster rate than untreated controls. However, by 30 days of exposure, both the MMP and proliferation rate had decreased, demonstrating that by this time the SIMH survival response was collapsing. This is likely due to the accumulated oxidative stress and suggests that cell death would follow. These data support the idea that SIMH is a transient survival response that enables mitochondria and cells to combat stress, but that chronic exposure may eventually overwhelm the protection provided by SIMH. It is probable that respiratory cells in the users of these products would respond to aerosolized nicotine with SIMH rather than mitochondrial swelling.

We further showed for the first time that SIMH is accompanied by aggregation of mitochondrial nucleoids. mtDNA aggregation has also been observed in cells in which Drp1, a protein required for mitochondrial fission, has been knocked out [64,65]. Other studies show that anti-cancer drugs such as doxorubicin intercalate into mtDNA, causing their aggregation accompanied by mitochondrial hyperfusion [38, 66]. This study suggests that remodeled nucleoids were able to exclude doxorubicin and maintain mtDNA synthesis. These studies show that mitochondrial nucleoids are dynamic structures that aggregate when cells are stressed, or genes are knocked out in a manner leading to mitochondrial fusion. Nucleoid aggregation may occur as part of the SIMH scenario to protect mtDNA from the high levels of DNA damage-inducing superoxide that form during hyperfusion [63, 67]. Alternatively, EC chemical(s) capable of intercalating into DNA may cause nucleoid aggregation.

In addition to initiating a cascade of responses in mitochondria, calcium influx led to retraction of cell-to-cell contacts and calcium accumulation inside the cell and mitochondria. The massive calcium influx that occurred during treatment with e-liquids, aerosols, and nicotine could be inhibited by ruthenium RU360 and α -bungarotoxin, a blocker of α7 nicotinic receptors. Calcium overload can pose serious cellular effects [68–70]. Fragments encapsulating Ca2+ (shown in Fig 5.8D) may provide a protective mechanism for sequestering and expelling excessive amounts of intracellular calcium. This cellular retraction may have significant implications in epithelial cells that depend on tight cell junctions to maintain selectively permeable barriers [71]. Intracellular calcium levels can return to resting levels by efflux through the plasma membrane Ca2+ transport ATPase (PMCA) and the Na+/Ca2+ exchanger (NCX), as well as uptake into the ER/SR via the sarco/endoplasmic reticulum Ca2+-ATPase (SERCA) [69]. Although it appears that in the short-term (by 20 minutes, Figs 5.8E-F) calcium is lowered, prolonged incubation (170 minutes, Fig 5.8B) resulted in an accumulation of intracellular calcium. This increase in perinuclear calcium

after 3 hours of treatment, which is likely accumulation in the ER, could potentially lead to ER stress. Eventually, calcium overload can cause cell death via several mechanisms including Ca2+-mediated mitochondrial permeabilization [69].

Mitochondrial dysfunction and oxidative damage are hallmarks of aging and disease [72]. Tobacco smoke and nicotine cause premature aging [73] and other disorders such as cancer [74–76], neurodegenerative disorders [37, 77], and cardiovascular disease [78] due to their effects on the mitochondria. Our studies suggest that chronic exposure to EC aerosols could contribute to aging via several pathways including: (1) impaired autophagy and the inability to clear damaged cellular components, (2) increased oxidative stress and protein oxidation, and (3) mtDNA aggregation leading to impaired segregation of nucleoids. The elevation of mitochondrial ROS can induce mtDNA damage, which in turn can accelerate aging by interfering with the antioxidant response and the mitochondrial life cycle [1, 41]. Aggregated mitochondrial nucleoids, which were observed in the hyperfused mitochondria, may further impair a cell's ability to segregate mutated nucleoids, which would contribute to mitochondrial dysfunction and aging [50].

EC are often considered harm reduction products [21, 79]. However, our data show that nicotine, which is found in most ECs, elicits cellular responses similar to those observed in EC aerosol-treated NSCs and those reported previously in thirdhand smoke treated cells [39]. The concentrations of nicotine that we tested are likely relevant to what an EC user would receive. In our study, the EC aerosol had nicotine concentrations of 110 μg/ml on average. Nicotine concentrations of 1.1 μg/ml (100-fold less than what was found in our EC aerosols) induced the SIMH and increased mitochondrial superoxide. One study reported that when participants used an EC containing 36 mg/ml nicotine, their plasma nicotine levels received a "boost" of 12.5 ng/ml [80]. This is comparable to what conventional cigarette users achieve (nicotine boost of ~ 16 ng/ml). When delivered through the lung, the concentration in brain nicotine "boost" after smoking

one conventional cigarette is 0.7 μg/ml (434 nM) on average [81]. The 1.1 μg/ml nicotine concentration tested in this study is in the range that NSCs can be exposed to in vivo.

SIMH occurred in response to EC and nicotine induced stress and represents a transient survival response that may enable stem cells to live until the stress is removed. However, removal of aerosol or nicotine treatment did not fully restore superoxide and MMP to basal levels. During the exposure period, oxidative damage accumulates in mitochondrial proteins and probably also in mtDNA [67], so that even if cells recover, they may be genetically and physiologically abnormal due to increased oxidative damage. These observations are critical as they suggest that EC aerosols are not without harm and that long-term exposures could elevate the possibility of premature aging and disease. By extension, any nicotine-delivery device could have the same effects and may not be safe for long-term use. This situation is confounded by several observations. First, nicotine has been reported in counterfeit EC and in some refill fluids labeled to contain no nicotine [82, 83], making it difficult for EC users to avoid nicotine even if they wish to do so. Secondly, when ECs deliver nicotine poorly, EC users show compensatory puffing to achieve adequate nicotine [84, 85], making it likely that EC users will adjust their topography to receive sufficient nicotine to stress stem cells.

Recent studies suggest that teens who use ECs are up to seven times more likely to start smoking conventional cigarettes [22], and tobacco is ranked extremely high on the addiction scale [86]. Past studies have shown that adolescents are not likely to refrain from smoking tobacco cigarettes when told that smoking may shorten their life expectancy because death is so remote from their young age. However, endpoints that are proximal to their age, such as smoking induces facial wrinkles by age 25, have had greater impact on smoking initiation and cessation in adolescents [87, 88]. Our data, which show oxidative damage to stem cells, when expanded in

future studies may likewise be helpful in providing information that could prevent the use of nicotine-containing products that may diminish the quality of life and life expectancy.

Damage to stem cells could have significant impact on a developing embryo or infant [16]. Cigarette smoking during pregnancy can induce physical impairments and cognitive defects in the progeny [89, 90]. Prenatal exposure to nicotine also alters pathways in the brain that are critical for motor and cognitive functions and behavioral responses [91, 92]. This is a concern given the fact that nicotine is still present in devices, such as nicotine patches and EC, that are often recommended as cigarette substitutes for pregnant women who smoke. Our data support re-evaluation of recommending any nicotine products to women during pregnancy.

In conclusion, our data show that exposure of stem cells to e-liquids, aerosols, or nicotine produces a stress response that leads to SIMH, which itself increases oxidative stress in cells. Of particular importance is the finding that nicotine alone can induce the changes observed with EC aerosols. This supports the idea that EC are not as harmless as often claimed and that even short-term exposure can stress cells in a manner that may lead, with chronic use, to morbidity or disease. These observations are likely to pertain to any product containing nicotine.

METHODS:

Culturing NSCs. NSCs are excellent models for quick screening and assessment of pre- and post-natal exposure to EC toxicants [39]. This cell type was chosen due to its fast replication rate in vitro and ease of use for screening purposes, as well as their well-defined spherical mitochondria that can be analyzed quantitatively using video bioinformatics techniques. Moreover, these cells were isolated from brains which may be readily exposed to EC aerosol that is inhaled and passes from the nasal sinuses through the olfactory tract to the brain (refs). Mouse neural stem cells (mNSC line C17.2 generously provided by Dr. Evan Snyder) were grown in Dulbecco's

modified Eagle's medium (DMEM) (Lonza, Walkersville, MD) supplemented with 10% fetal bovine serum (Sigma-Aldrich, St. Louis, MO), 5% horse serum (Invitrogen, Grand Island, NY), 1% sodium pyruvate (Lonza, Walkersville, MD) and 1% Penicillin-streptomycin (GIBCO, Invitrogen, Carlsbad, CA). The cells were cultured in Nunc T-25 tissue culture flasks (Fisher Scientific, Tustin CA) and passaged at approximately 80% confluency using 0.05% trypsin EDTA/DPBS (GIBCO, Invitrogen, Carlsbad, CA). Medium was replenished every other day.

Generation of MitoTimer Stable Cell Line. NSC were cultured, detached enzymatically using 0.05% trypsin, and centrifuged for 3 minutes at 3,000 rpm. The pellet containing 6 x 106 cells was re-suspended in Nucleofection medium (Lonza Kit # VAPG-1004) and nucleofected with a pMitoTimer plasmid (Addgene #52659, Cambridge, MA USA) in the Amaxa Nucleofection IIb device (Lonza, Basel, Switzerland) using program A-033. The cells were quickly transferred to a new dish containing pre-equilibrated fresh medium, and selected with hygromycin at the previously determined optimal kill dose of 150 µg/ml. The medium and hygromycin treatment was replenished every other day for 30 days. The MitoTimer-transfected NSCs were further enriched with FAC Sorting (FACS Aria) using GFP (488nm Argon laser, 530/30 filter) and DsRed (488nm Argon laser, 610/20 filter) signals.

Plasmids and Transient Transfection. The following plasmids were purchased from Addgene (Cambridge, MA USA) and used for transient transfections: (1) mRFP-GFP-tagged LC3 (Addgene #21704), (2) mApple-LAMP1-pHluorin-N-8 (Addgene #54918), (3) mCerulean3-Mito-7 (Addgene #55433), (4) pCMV-CEPIA2mt (Addgene #58218), (5) GCaMP5. (Addgene #31788). Transfections were carried out using DNA-In STEM reagents (MTI-GlobalStem, Gaithersburg, MD USA). Briefly, cells were plated so they will be 70% confluent at the time of transfection. The DNA and lipid complexes were prepared according to manufacturer recommendation and incubated for 5 min before addition to cells.

Source of EC E-liquids and Aerosol, and Nicotine. Menthol and tobacco flavored cartomizer style EC manufactured by a major US tobacco company were evaluated. These products were selected since they are popular brands with high sales volume in the United States. This EC is a basic cig-a-like design with a rechargeable battery and replaceable cartomizers that are offered as tobacco and menthol flavors. Liquid (-)-nicotine (catalog # N3876) was obtained from Sigma-Aldrich (St. Louis, MO).

Preparing E-liquids and EC Aerosols. Aerosol was produced using a smoking machine described in detail previously [93, 94]. Puffs of aerosol were made using the lowest airflow rate that gave a robust puff and were collected in culture medium at a concentration of 6 total-puff-equivalents (TPE) where 1 TPE represents one puff in 1 ml of culture medium. EC puffs lasted 4.3 seconds based on [85] and were taken every minute. The aerosol was captured in the cell medium, flash frozen using dry ice/ethanol bath, and stored in -80oC for later use. E-liquids were collected from three different cartomizers for each brand. E-liquids contain various flavor chemicals (Behar et al 2018), nicotine, and a solvent(s), such as propylene glycol (PG) and/or vegetable glycerin (VG). Cartomizers were purchased from third party vendors on the Internet, local gas stations, and grocery stores. Fresh unused cartomizers were dissected to separate the fibers from the atomizing unit, as described previously [95]. The inner and outer fibers were centrifuged in MinElute Spin columns (Qiagen, Valencia, CA) at 14,000 revolutions/minute for 4–6 minutes to separate the fluid from the fibers.

Concentration-Dependent Exposure of Cells. NSCs were plated in ibidi 8-well chambers at approximately 6,000 cells/well and allowed to attach overnight or treated right away. NSCs were incubated for 4 or 24 hours with menthol or tobacco-flavored e-liquids (0.3%, 0.5%, and 1% dilutions) or aerosols (1.8 TPE, 3 TPE, and 6 TPE). Three independent experiments were using from different passage numbers, and results were averaged across the three data sets.

Live Cell Time-lapse and Super-Resolution Fluorescence Microscopy. Time-lapse fluorescent images were collected using an inverted Eclipse Ti microscope (Nikon Instruments, Melville, NY) using a 40X and 60X objectives equipped with numerical apertures of 0.75 and 0.85 with 0.16 µm/pixel and 0.11 µm/pixel resolutions, respectively, on a high-resolution Andor Zyla VSC-04941 camera (Andor, Belfast, UK). The live cells were kept in a 37oC temperature, 5% CO2, and 90% relative humidity-regulated incubation chamber (Pathology Devices Inc., San Diego, CA USA). The videos were collected at millisecond exposures and de-convoluted using the Live De-blur feature with the same settings in the NIS Elements software (DR Vision). Zeiss 880 Airyscan super-resolution microscope (Zeiss, Oberkochen, Germany) was used with a 63x/1.4 Oil immersion objective with 160nm resolution on Airy Fast mode.

Quantifying Autophagosome Size and Morphology. NSCs were plated on a 12-well plate at approximately 24,000 cells/ well and allowed to attach overnight. The cells were transfected with a ptfLC3 reporter (Addgene #21074, Cambridge, MA USA) consisting of (LC3-II) fused to mRFP and EGFP fluorophores. Transfection was done using DNA-In Stem reagent (MTI-GlobalStem # GST-2130) and cells were then incubated overnight before re-plating on an ibidi 8-well chamber and treatment with e-liquids and aerosols. After 4 hours and 24hrs of incubation, the cells were imaged live and analyzed using CellProfiler software. A three-class adaptive Otsu segmentation strategy was used to segment the autophagosomes using the mRFP channel (which is photostable). The total area and the number of autophagosomes were extracted and plotted. Individual autophagosome size data were also sorted into three bins: objects with area $\leq$ 200 pixels, objects with area between 200-500 pixels, and objects with area $\geq$ 500 pixels.

Identifying Defects in Autolysosome Acidification Using PHluorin. NSCs were transfected with an autolysosome-targeted LAMP1 reporter (Addgene #54918, Cambridge, MA USA). This reporter is dual tagged with both mApple, which is photostable, and pHluorin (a pH-

sensitive GFP), which quenches in the acidic environment of the lysosome. CellProfiler imaging software was used to segment both mApple (red) and pHluorin (green) channels. The ratio of the red to green channels was used to assess autolysosome acidity.

MitoTimer Analysis: Number of Mitochondria and Classification of Morphology. CellProfiler software was used for segmenting the red channel and thresholding using Otsu's adaptive method. Morphological features were extracted for each mitochondrion. These features were fed to an algorithmic decision tree operating on a Matlab (MathWorks, Natick, MA, USA) platform to automatically classify the mitochondria into four distinct categories: fragmented, networked, swollen, and donut-shaped.

MitoTimer Analysis: Ratiometric Analysis of Mitochondrial Protein Oxidation. MitoTimer-transfected NSCs were plated on µ-Slide Ibidi 8-well chamber slides (Ibidi, Munich, Germany) at approximately 6,000 cells/well. Two untreated control wells were used for comparison to the e-liquid and aerosol treated wells. AA video bioinformatics software was developed using CL-Quant (DR Vision, Seattle, WA USA) to quantify the protein oxidation levels based on relative amount of red to green fluorescence. Multi-channel images were imported into CL-Quant, and soft-matching based segmentation was applied to both the red and green channels. Intensity data were collected and used to calculate the red/green ratio, which is a measure of oxidized proteins in the mitochondria.

Mitochondrial Motion Magnification Algorithm. The density of fluorescently-tagged structures (e.g. MitoTimer signal in the mitochondria) is proportional to the pixel intensity. By computing the change in intensity between adjacent frames, the dynamics of mitochondria were analyzed at the individual pixel level. To do this, a difference image $D_{t,t+1}$ was computed as,

$$D_{t,t+1} = I_{t+1} - I_t$$

where I_t is the image frame at time t. The equation is revised to rescale pixel values between 0 and 1:

$$D'_{t,t+1} = \frac{D_{t,t+1} + 255}{510}$$

Otsu's segmentation method in CellProfiler software was used to segment the region of interest (ROI) defined as:

$$ROI_{t,t+1} = S_t \cup S_{t+1}$$

where S_t was Otsu's segmentation output at time t. For an image sequence, motion vectors were calculated with the following gradient equation:

$$\nabla D'_{t,t+1} = \frac{\delta D'_{t,t+1}}{\delta x}\,\hat{x} + \frac{\delta D'_{t,t+1}}{\delta y}\,\hat{y} = u\,\hat{x} + v\,\hat{y}$$

$\hat{x}$ and $\hat{y}$ are the unit vectors for the x- and y-axes respectively. The magnitude and angle of the motion vectors were calculated using the following definitions,

$$M = \sqrt{u^2 + v^2} \quad ; \quad \theta = \tan^{-1}\frac{v}{u} \;;$$

The magnitude values were reported and compared between treatment groups.

Measuring Mitochondrial Membrane Potential using TMRM. NSCs were treated for 24 hours, and then incubated for 30 min with 1uM of TMRM probe (ThermoFisher Scientific #T668), a cationic red-orange fluorescent probes that can be used to detect changes in mitochondrial membrane potential. Next, the cells were rinsed with PBS+ three times, and fresh medium was added to the wells. One well was treated as the positive control, where mitochondria were de-energized with 2.5 mM KCN (a respiratory inhibitor) and 1ug/mL oligomycin (a mitochondrial ATPase inhibitor). The cells were imaged live and the fluorescence intensity was quantified using CL-Quant software. Intensity values from non-segmented regions were extracted and used to subtract intensity value from the segmented regions. The intensity values from the treated group were normalized to the corresponding control group in each experiment.

Measuring Mitochondrial Superoxide Levels using MitoSOX. NSCs were plated onto ibidi 8-well chambers at approximately 6,000 cells/per well and allowed to attach overnight. The cells were then treated for 24 hours with e-liquid or aerosol and incubated for 10 min with 5μM of MitoSOX™ Red (ThermoFisher Scientific #M36008). Oxidation of MitoSOX™ Red reagent by superoxide produces red fluorescence in the mitochondria. The cells were rinsed with PBS+ three times, and fresh medium was added to the wells. The cells were imaged live. CL-Quant imaging software was used to segment the superoxide signal in mitochondria. The intensity values from non-segmented regions were extracted and used to subtract intensity values from the segmented regions. The intensity values from the treated group were normalized to the corresponding control group in each experiment.

Measuring mtDNA Response Using PicoGreen Dye. NSCs were treated for 24 hours with e-liquid or aerosol, then incubated for 1 hour with 3uL/mL of Quant-iTTM PicoGreen dsDNA dye (ThermoFisher Scientific #P7581). The cells were rinsed with PBS+ three times, and fresh medium was added to the wells. The cells were imaged live, and the mtDNA nucleoid puncta were segmented using CL-Quant software. The number of puncta, total area, and average intensity were extracted. DAPI stained nuclei were segmented and used to subtract background signals from the nucleus.

HPLC Quantification of Nicotine. Nicotine concentrations in EC fluid were evaluated using a method previously described [83]. The nicotine limit of quantification for this method was 10 μg/ml with a limit of detection of 50 ng/ml. The values reported are the means and standard deviations of the three runs.

Whole-cell and Mitochondria Calcium Imaging. NSCs were transfected using DNA-In Stem reagent (MTI-GlobalStem # GST-2130) with a GCaMP5 (Addgene #31788, Cambridge, MA USA) or CEPIA2mt (Addgene #58218, Cambridge, MA USA) fluorescent reporters. The cells were

imaged live in the on-stage incubation chamber before and after the addition of EC or nicotine treatments. The images were analyzed for the average fluorescence intensity using CL-Quant software. For whole-cell intensity extraction, segmentation was done manually by tracing around the cell of interest in all time frames. Intensity in the background was extracted and used to subtract the cell body intensity. For mitochondrial intensity extraction, tophat image processing was used to remove background noise. Bright region image processing was applied to enhance the mitochondria signal. Threshold base segmentation was used to extract the enhanced signal. "Logical not" operation was used to segment the background. Both cell and background segmented regions were transposed on the original image to extract the original intensity values. Small errors were edited manually. Both whole-cell and mitochondrial intensity data were used to determine changes in in intensity.

Blocking Calcium at the Cell- and Mitochondrial-Levels. Cells were pre-incubated with the mitochondrial calcium uniporter blocker RU360 (Millipore, Burlington, MA, USA), α7 nAChR-blocker α-Bungarotoxin (Abcam, Cambridge, UK), and calcium chelator ethylene glycol-bis(β-aminoethyl ether)-N,N,N',N'-tetraacetic acid) (EGTA) (Sigma-Aldrich, St. Louis, MO) to block calcium entry into the cell and mitochondria. To measure changes in calcium fluorescence intensity (GCaMP5 or CEPIA), the intensity at each time point was normalized back to the "before" timepoint (t=0). The significance was analyzed for each time point after treatment (after t=0).

Western Blot Analysis. Cells were treated for 24 hours in 6-well plates after which the plates were placed on ice and washed with PBS. After aspirating the PBS, 100 µl of RIPA buffer and protease inhibitor cocktails (ChemCruz, Dallas, TX, USA) were added to each well. The cells were scraped using a plastic cell scraper, and maintained in constant agitation for 30 min at 4°C. The cells were spun at 16,000 x g for 15 min in a 4°C pre-cooled centrifuge, and the supernatant was transferred to a fresh tube kept on ice. A small volume of lysate was used to perform the Pierce

BCA assay (ThermoFisher Scientific, Waltham, MA) to determine protein concentrations. Laemmli buffer (Bio-Rad, Hercules, CA) was added to 5 µg of each sample and boiled at 95°C for 5 min. Samples were loaded on a Mini-PROTEAN TGX Precast SDS-PAGE gel (Bio-Rad, Hercules, CA USA) with molecular weight markers. The gel was run at 100 volts on the Bio-Rad Powerpac Basic power supply (Bio-Rad, Hercules, CA), and the membrane was transferred overnight at 150 mAmps. The membrane was removed and blocked in 5% milk in Tween in tris-buffered saline (TBST) for 30 min at room temperature, followed by addition of primary antibodies to β-actin, p62, and SOD2 (Cell Signaling, Danvers, MA) in 3% albumin in TBST and incubation at 4oC overnight. The membranes were washed and incubated with HRP-conjugated anti-rabbit secondary antibodies diluted in 5% milk in TBST for 3 hours at room temperature. The protein bands were imaged using Clarity Western ECL substrate (Bio-Rad, Hercules, CA).

Mitophagy Imaging and Quantification. The ptfLC3 and mCerulean7-Mito3 dual-transfected NSCs were imaged using RFP (red) and mCerulean (blue) signals. CellProfiler software was used to segment multichannel images. RFP-autophagosomes and mCerulean-mitochondria were segmented by a three- and two- class adaptive Otsu segmentation methods respectively. After segmentation, autophagosomes and mitochondria were overlaid to identify co-localized areas. The ratio of mitophagy was calculated by dividing the co-localized area by the total mitochondrial area. Mitophagy quantification (ratio between 0 to 1) was done for 4 and 24 hour treated data.

Statistical Analysis. All statistical analysis was conducted using Minitab (State College, PA USA) or Prism software (GraphPad, San Diego, CA). In Fig 5.1, the total autophagosome area of treated groups were compared back to control using one-way ANOVA with Dunnett's post hoc test (n=4 experiments). For autophagosome number analysis, two tailed T-tests were used to compare 4hr and 24hr data against each other in each treatment groups. For the autophagosome size distribution graphs, one-way ANOVA with Dunnett's post hoc test were performed on three

size groups (0-250, 250-500 and >500 pixel2). Treated groups were compared back to the control. One-way ANOVA with Dunnett's post hoc test were performed on percent of lysosome co-localization data. In Fig 5.2, for the mitophagy area, one-way ANOVA with Dunnett's post hoc test were performed to compare the treated group to the control at 4hrs and 24hr. For mitochondrial motion, one-way ANOVA with Bonferroni post hoc test were performed to compare between treatment groups in the three sub-classes (small, medium and large). In Fig 5.3, two tail T-test with hypothetical value (100%) were used to analyze mitochondrial number and area data. One-way ANOVA was not used because the data was normalized to the control group, resulting in no variance. For mitochondrial morphology analysis, one-way ANOVA with Dunnett's post hoc test was used to compare the treated group back to the control for each morphological class. In Fig 5.4, One-way ANOVA with Dunnett's post hoc test was used to analyze MitoSOX intensity. Two tail T-test with hypothetical value (100%) were used to analyze the 3 days aerosol exposure and 2 days reversal. In Fig 5.5, one-way ANOVA with Dunnett's post hoc test was used to compare the red-to-green MitoTimer colorimetric ratio of treated groups back to control. For TMRM intensity, two tails T-test with hypothetical value (100%) was used. In Fig 5.6, mtDNA (PicoGreen) nucleoid average size and mean intensity was analyzed by one-way ANOVA with Dunnett's post hoc test. In Fig 5.7, for nicotine 3 days exposure and 2 days reversal, two tail T-test with hypothetical value (100%) was used. One-way ANOVA with Dunnett's post hoc test was used to analyze the red-to-green MitoTimer colorimetric ratio for nicotine data. For nicotine morphology data, One-way ANOVA with Dunnett's post hoc test was used to analyze between groups for each morphological class (dot, swollen and network). In Fig 5.8, GCaMP5 changes in intensity data from e-liquid, aerosol and nicotine treatments were analyzed using two-ways ANOVA with Dunnett's post hoc test. All time points in each treatment were compared backed to T=0. MitoSox EGTA inhibition intensity data were analyzed by two-tail T-test. Each condition was compared against their EGTA

counterpart. CEPIA2mt intensity data were analyzed by two-ways ANOVA with Dunnett's post hoc test. In each time points, samples with RU360 and α-bungarotoxin inhibitor were compared to samples with no inhibitor. All error bars on the plots are the mean +/- standard error of the mean (SEM) of 3-4 independent experiments.

SUMMARY

Exposure to toxicants, including ones found in tobacco products, are detrimental to stem cell, which are critical in development, normal cell homeostasis, and tissue repair. Mitochondria are important targets of toxicants and sensitive detectors of cell harm. Here, we investigated the effects of a popular EC product on autophagy dysfunction and mitochondrial toxicity in neural stem cells. EC exposure resulted in changes in mitochondrial morphology and dynamics, increased mitochondrial superoxide production and protein oxidation, altered membrane potential, aggregated mtDNA nucleoids, and elevated intracellular calcium. Nicotine, a bioactive chemical that was dominant in EC fluids and aerosols, was responsible for the stress induced mitochondrial hyperfusion (SIMH) (low doses), and mitochondrial swelling (high doses). This study demonstrates clear adverse effects on stem cells by a popular EC product and further shows that the survival response initiated by EC fluids or aerosols can be attributed to nicotine.

SUPPLEMENTAL INFORMATION

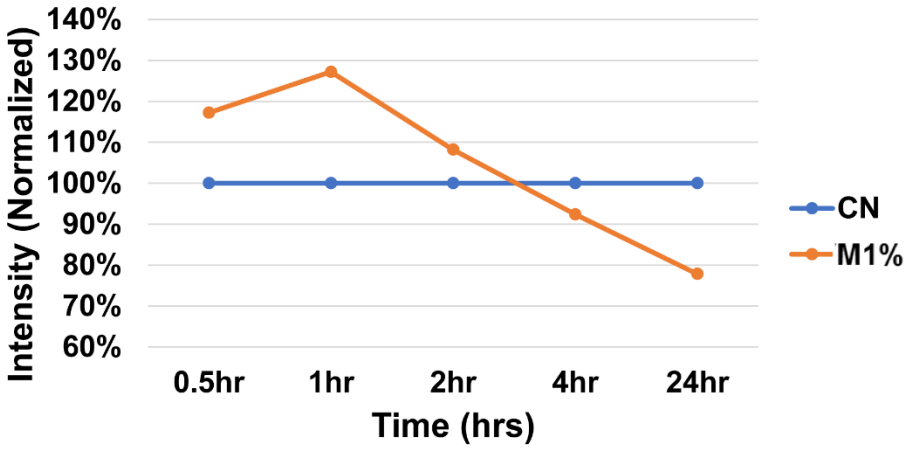

Figure S5.1. TMRM Time Course for Menthol 1% E-liquid. Menthol 1% e-liquid treated NSCs labeled with the mitochondrial membrane potential dye TMRM at different time points over 24 hours. TMRM fluorescence intensity was quantified and normalized to the control group, showing an initial increase before the loss of membrane potential in the menthol 1% high concentration.

Table S5.1. Analysis of Intracellular Calcium Intensity Decay Over Time. GCaMP5 fluorescence intensity after addition of e-liquids, aerosols, and nicotine were statistically compared back to time = 0min using two-way ANOVA with Dunnett's post hoc test (* = p <0.05. ** = p <0.01. *** = p <0.001. **** = p <0.0001).

	T 6TPE	M 6TPE	T 0.5%	M 0.5%	1.1 µg/ml	220 µg/ml
0 vs. 1 min	ns	****	**	****	*	***
0 vs. 1.5 min	ns	**	ns	****	**	***
0 vs. 2 min	*	**	ns	****	ns	**
0 vs. 2.5 min	ns	***	ns	***	ns	**
0 vs. 5 min	***	*	ns	***	ns	*
0 vs. 10 min	***	****	ns	ns	ns	*
0 vs. 20 min	**	**	ns	ns	ns	**

Videos S5.1. Mitophagy video control 24hr
http://www.editorialmanager.com/iscience/download.aspx?id=1085696&guid=01cfbccc-99b9-46d4-a2d0-cd9c844dc0d0&scheme=1

Videos S5.2. Mitophagy video Vuse Menthol E-liquid 24hr
http://www.editorialmanager.com/iscience/download.aspx?id=1085697&guid=7949124f-46f4-47b5-967c-5a1e2b2180f0&scheme=1

Videos S5.3. Mitophagy video Vuse Menthol Aerosol 24hr
http://www.editorialmanager.com/iscience/download.aspx?id=1085698&guid=56f2b606-62d5-4310-a26a-d3a896a7d2e3&scheme=1

Videos S5.4. Mitophagy video control 4hr
http://www.editorialmanager.com/iscience/download.aspx?id=1085699&guid=ab7c1e6c-b7f7-4d83-9bd5-db850d8309f9&scheme=1

Videos S5.5. Mitophagy video Vuse Menthol E-liquid 4hr
http://www.editorialmanager.com/iscience/download.aspx?id=1085700&guid=f7a86ade-e6da-4cc5-abe5-87e717e298a5&scheme=1

Videos S5.6. Mitophagy video Vuse Menthol Aerosol 4hr
http://www.editorialmanager.com/iscience/download.aspx?id=1085701&guid=7548e4cc-6c06-483f-8e66-184febf00100&scheme=1

REFERENCES

[1] J. Oh, Y.D. Lee, A.J. Wagers, Stem cell aging: mechanisms, regulators and therapeutic opportunities, Nat. Med. 20 (2014) 870–880.

[2] A. Behrens, Impact of genomic damage and ageing on stem cell function, Nat. Cell Biol. 16 (2014) 201–207.

[3] M.B. Schultz, D.A. Sinclair, When stem cells grow old: phenotypes and mechanisms of stem cell aging, Development. 143 (2016) 3–14.

[4] S.K. Pazhanisamy, Stem cells, DNA damage, ageing and cancer, Hematol. Oncol. Stem Cell Ther. 2 (2009) 375–384.

[5] P.M. Rodier, Developing brain as a target of toxicity, Environ. Health Perspect. 103 (1995) 73–76.

[6] V. Bahl, S. Lin, N. Xu, B. Davis, Y.H. Wang, P. Talbot, Comparison of electronic cigarette refill fluid cytotoxicity using embryonic and adult models, Reprod. Toxicol. 34 (2012) 529–537.

[7] R.Z. Behar, B. Davis, Y. Wang, V. Bahl, S. Lin, P. Talbot, Identification of toxicants in cinnamon-flavored electronic cigarette refill fluids, Toxicol. Vitr. 28 (2014) 198–208.

[8] P. Talbot, S. Lin, Mouse and human embryonic stem cells: can they improve human health by preventing disease?, Curr. Top. Med. Chem. 11 (2011) 1638–1652.

[9] P. Talbot, N.I. Nieden, S. Lin, I. Martinez, B. Guan, B. Bhanu, Use of Video Bioinformatics Tools in Stem Cell Toxicology, in: Handb. Nanotoxicology, Nanomedicine Stem Cell Use Toxicol., 2014: pp. 379–402.

[10] S. Liu, N. Yin, F. Faiola, Prospects and Frontiers of Stem Cell Toxicology, Stem Cells Dev. 26 (2017) scd.2017.0150.

[11] N. Yin, X. Yao, Z. Qin, Y.L. Wang, F. Faiola, Assessment of Bisphenol A (BPA) neurotoxicity in vitro with mouse embryonic stem cells, J. Environ. Sci. (China). 36 (2015) 181–187.

[12] K.S. Betts, Growing Knowledge: Using Stem Cells to Study Developmental Neurotoxicity, Environ. Health Perspect. 118 (2010) a432–a437.

[13] S. Lin, S. Fonteno, J.-H. Weng, P. Talbot, Comparison of the toxicity of smoke from conventional and harm reduction cigarettes using human embryonic stem cells., Toxicol. Sci. 118 (2010) 202–12.

[14] S. Lin, V. Tran, P. Talbot, Comparison of toxicity of smoke from traditional and harm-reduction cigarettes using mouse embryonic stem cells as a novel model for preimplantation development., Hum. Reprod. 24 (2009) 386–97.

[15] S.C. Lin, H. Yip, R. Phandthong, B. Davis, P. Talbot, Evaluation of Dynamic Cell Processes and Behavior Using Video Bioinformatics Tools, in: Video Bioinforma., Springer, 2015: pp. 167–186.

[16] K. Kee, M. Flores, M.I. Cedars, R.A.R. Pera, Human Primordial Germ Cell Formation Is Diminished by Exposure to Environmental Toxicants Acting through the AHR Signaling Pathway, Toxicol. Sci. 117 (2010) 218–224.

[17] P. Talbot, In vitro assessment of reproductive toxicity of tobacco smoke and its constituents, Birth Defects Res. Part C - Embryo Today Rev. 84 (2008) 61–72.

[18] J.M. Greenberg, C.M. Carballosa, H.S. Cheung, Concise Review: The Deleterious Effects of Cigarette Smoking and Nicotine Usage and Mesenchymal Stem Cell Function and Implications for Cell-Based Therapies, Stem Cells Transl. Med. 6 (2017) 1815–1821.

[19] A. Shaito, J. Saliba, A. Husari, M. El-Harakeh, H. Chhouri, Y. Hashem, A. Shihadeh, M. El-Sabban, Electronic Cigarette Smoke Impairs Normal Mesenchymal Stem Cell Differentiation, Sci. Rep. 7 (2017) 1–11.

[20] T.K. Ng, L. Huang, D. Cao, Y.W.-Y. Yip, W.M. Tsang, G.H.-F. Yam, C.P. Pang, H.S. Cheung, Cigarette smoking hinders human periodontal ligament-derived stem cell proliferation, migration and differentiation potentials, Sci. Rep. 5 (2015) 7828.

[21] K.-H. Kim, E. Kabir, S.A. Jahan, Review of electronic cigarettes as tobacco cigarette substitutes: Their potential human health impact, J. Environ. Sci. Heal. Part C. 34 (2016) 262–275.

[22] and M. National Academies of Sciences, Engineering, Public Health Consequences of E-Cigarettes, The National Academies Press, Washington, DC, 2018.

[23] M.S. Attene-Ramos, R. Huang, S. Sakamuru, K.L. Witt, G.C. Beeson, L. Shou, R.G. Schnellmann, C.C. Beeson, R.R. Tice, C.P. Austin, M. Xia, Systematic Study of Mitochondrial Toxicity of Environmental Chemicals Using Quantitative High Throughput Screening, Chem. Res. Toxicol. 26 (2013) 1323–1332.

[24] J.N. Meyer, M.C.K. Leung, J.P. Rooney, A. Sendoel, M.O. Hengartner, G.E. Kisby, A.S. Bess, Mitochondria as a target of environmental toxicants, Toxicol. Sci. 134 (2013) 1–17.

[25] E.A. Belyaeva, D. Dymkowska, M.R. Wieckowski, L. Wojtczak, Mitochondria as an important target in heavy metal toxicity in rat hepatoma AS-30D cells, Toxicol. Appl. Pharmacol. 231 (2008) 34–42.

[26] E. Berger, E. Rath, D. Yuan, N. Waldschmitt, S. Khaloian, M. Allgauer, O. Staszewski, E.M. Lobner, T. Schottl, P. Giesbertz, O.I. Coleman, M. Prinz, A. Weber, M. Gerhard, M. Klingenspor, K.P. Janssen, M. Heikenwalder, D. Haller, Mitochondrial function controls intestinal epithelial stemness and proliferation, Nat. Commun. 7 (2016).

[27] A. Wanet, T. Arnould, M. Najimi, P. Renard, Connecting Mitochondria, Metabolism, and Stem Cell Fate, Stem Cells Dev. 24 (2015) 1957–1971.

[28] D.H. Margineantu, D.M. Hockenbery, Mitochondrial functions in stem cells, Curr. Opin. Genet. Dev. 38 (2016) 110–117.

[29] J.L. Tilly, D.A. Sinclair, Germline energetics, aging, and female infertility, Cell Metab. 17 (2013) 838–850.

[30] G.L. Norddahl, C.J. Pronk, M. Wahlestedt, G. Sten, J.M. Nygren, A. Ugale, M. Sigvardsson, D. Bryder, Accumulating mitochondrial DNA mutations drive premature hematopoietic aging phenotypes distinct from physiological stem cell aging, Cell Stem Cell. 8 (2011) 499–510.

[31] J.M. Ross, J.B. Stewart, E. Hagström, S. Brené, A. Mourier, G. Coppotelli, C. Freyer, M. Lagouge, B.J. Hoffer, L. Olson, N.G. Larsson, Germline mitochondrial DNA mutations aggravate ageing and can impair brain development, Nature. 501 (2013) 412–415.

[32] H. Zhang, K.J. Menzies, J. Auwerx, The role of mitochondria in stem cell fate and aging, Development. 145 (2018) dev143420.

[33] D.R. Green, L. Galluzzi, G. Kroemer, Mitochondria and the autophagy-inflammation-cell death axis in organismal aging, Science (80-.). 333 (2011) 1109–1112.

[34] P. Katajisto, J. Dohla, C.L. Chaffer, N. Pentinmikko, N. Marjanovic, S. Iqbal, R. Zoncu, W. Chen, R.A. Weinberg, D.M. Sabatini, Asymmetric apportioning of aged mitochondria between daughter cells is required for stemness, Science (80-.). 348 (2015) 340–343.

[35] M.R. Bufalino, B. DeVeale, D. van der Kooy, The asymmetric segregation of damaged proteins is stem cell-type dependent, J. Cell Biol. 201 (2013) 523–530.

[36] M.A. Rujano, F. Bosveld, F.A. Salomons, F. Dijk, M.A.W.H. Van Waarde, J.J.L. Van Der Want, R.A.I. De Vos, E.R. Brunt, O.C.M. Sibon, H.H. Kampinga, Polarised asymmetric inheritance of accumulated protein damage in higher eukaryotes, PLoS Biol. 4 (2006) 2325–2335.

[37] J. Nunnari, A. Suomalainen, Mitochondria: In sickness and in health, Cell. 148 (2012) 1145–1159. doi:10.1016/j.cell.2012.02.035.

[38] D. Tondera, S. Grandemange, A. Jourdain, M. Karbowski, Y. Mattenberger, S. Herzig, S. Da Cruz, P. Clerc, I. Raschke, C. Merkwirth, S. Ehses, F. Krause, D.C. Chan, C. Alexander, C. Bauer, R. Youle, T. Langer, J.-C. Martinou, SLP-2 is required for stress-induced mitochondrial hyperfusion, EMBO J. 28 (2009) 1589–1600.

[39] V. Bahl, K. Johnson, R. Phandthong, A. Zahedi, S.F. Schick, P. Talbot, Thirdhand cigarette smoke causes stress-induced mitochondrial hyperfusion and alters the transcriptional profile of stem cells, Toxicol. Sci. 153 (2016) 55–69.

[40] C.A. Lerner, P. Rutagarama, T. Ahmad, I.K. Sundar, A. Elder, I. Rahman, Electronic cigarette aerosols and copper nanoparticles induce mitochondrial stress and promote DNA fragmentation in lung fibroblasts, Biochem. Biophys. Res. Commun. 477 (2016) 620–625.

[41] B. Bhanu, P. Talbot, Video Bioinformatics, 2015.

[42] L. Kozlovskaya, M. Abou-Kaoud, D. Stepensky, Quantitative analysis of drug delivery to the brain via nasal route, J. Control. Release. 189 (2014) 133–140.

[43] S. Kimura, T. Noda, T. Yoshimori, Dissection of the autophagosome maturation process by a novel reporter protein, tandem fluorescent-tagged LC3, Autophagy. 3 (2007) 452–460.

[44] United States Department of Health and Human Services, E-Cigarette use among youth and young adults: a report of the surgeon general, 2016.

[45] R.C. Laker, P. Xu, K.A. Ryall, A. Sujkowski, B.M. Kenwood, K.H. Chain, M. Zhang, M.A. Royal, K.L. Hoehn, M. Driscoll, P.N. Adler, R.J. Wessells, J.J. Saucerman, Z. Yan, A novel mitotimer reporter gene for mitochondrial content, structure, stress, and damage in vivo, J. Biol. Chem. 289 (2014) 12005–12015.

[46] G. Sharma, S. Vijayaraghavan, Nicotinic receptor signaling in nonexcitable cells, J. Neurobiol. 53 (2002) 524–534.

[47] J. Akerboom, T.-W. Chen, T.J. Wardill, L. Tian, J.S. Marvin, S. Mutlu, N.C. Calderon, F. Esposti, B.G. Borghuis, X.R. Sun, A. Gordus, M.B. Orger, R. Portugues, F. Engert, J.J. Macklin, A. Filosa, A. Aggarwal, R.A. Kerr, R. Takagi, S. Kracun, E. Shigetomi, B.S. Khakh, H. Baier, L. Lagnado, S.S.-H. Wang, C.I. Bargmann, B.E. Kimmel, V. Jayaraman, K. Svoboda, D.S. Kim, E.R. Schreiter, L.L. Looger, Optimization of a GCaMP Calcium Indicator for Neural Activity Imaging, J. Neurosci. 32 (2012) 13819–13840.

[48] J. Santo-Domingo, N. Demaurex, Calcium uptake mechanisms of mitochondria, Biochim. Biophys. Acta - Bioenerg. 1797 (2010) 907–912.

[49] R. Rizzuto, D. De Stefani, A. Raffaello, C. Mammucari, Mitochondria as sensors and regulators of calcium signalling, Nat. Rev. Mol. Cell Biol. 13 (2012) 566–578.

[50] J. Suzuki, K. Kanemaru, K. Ishii, M. Ohkura, Y. Okubo, M. Iino, Imaging intraorganellar Ca2+ at subcellular resolution using CEPIA, Nat. Commun. 5 (2014) 1–13.

[51] M. Skok, G. Gergalova, O. Lykhmus, O. Kalashnyk, L. Koval, K. Uspenska, Nicotinic acetylcholine receptors in mitochondria : subunit composition , function and signaling, Neurotransmitter. 3 (2016) 1–12. doi:10.14800/nt.1290.

[52] G. Gergalova, O. Lykhmus, O. Kalashnyk, L. Koval, V. Chernyshov, E. Kryukova, V. Tsetlin, S. Komisarenko, M. Skok, Mitochondria express α7 nicotinic acetylcholine receptors to regulate Ca2+ accumulation and cytochrome c release: study on isolated mitochondria, PLoS One. 7 (2012) 1–8.

[53] D. Glick, S. Barth, K.F. Macleod, Autophagy: cellular and molecular mechanisms, J. Pathol. 221 (2010) 3–12.

[54] P.C. Shivalingappa, R. Hole, C. Van Westphal, N. Vij, Airway exposure to e-cigarette vapors impairs autophagy and induces aggresome formation, Antioxid. Redox Signal. 24 (2015) 186–204.

[55] J. Thyberg, U. Hedin, K. Stenseth, J. Nilsson, Effects of nicotine on the fine structure of cultivated mouse peritoneal macrophages., Acta Pathol. Microbiol. Immunol. Scand. A. 91 (1983) 23–30.

[56] A.P. Govind, P. Vezina, W.N. Green, Nicotine-induced upregulation of nicotinic receptors: Underlying mechanisms and relevance to nicotine addiction, Biochem. Pharmacol. 78 (2009) 756–765.

[57] G. Ashrafi, T.L. Schwarz, The pathways of mitophagy for quality control and clearance of mitochondria, Cell Death Differ. 20 (2012) 31–42.

[58] H.M. Ni, J.A. Williams, W.X. Ding, Mitochondrial dynamics and mitochondrial quality control, Redox Biol. 4 (2015) 6–13.

[59] J. Lemasters, T. Theruvath, Z. Zhong, A. Nieminen, Mitochondrial Calcium and the Permeability Transition in Cell Death, Biochim. Biophys. Acta. 1787 (2009) 1395–1401.

[60] T.E. Shutt, H.M. McBride, Staying cool in difficult times: Mitochondrial dynamics, quality control and the stress response, Biochim. Biophys. Acta - Mol. Cell Res. 1833 (2013) 417–424.

[61] M. Lagouge, N.G. Larsson, The role of mitochondrial DNA mutations and free radicals in disease and ageing, J. Intern. Med. 273 (2013) 529–543.

[62] D.E. Handy, J. Loscalzo, Redox regulation of mitochondrial function, Antioxid. Redox Signal. 16 (2012) 1323–1367.

[63] G. Lenaz, Role of mitochondria in oxidative stress and ageing, Biochim. Biophys. Acta - Bioenerg. 1366 (1998) 53–67.

[64] R. Ban-Ishihara, T. Ishihara, N. Sasaki, K. Mihara, N. Ishihara, Dynamics of nucleoid structure regulated by mitochondrial fission contributes to cristae reformation and release of cytochrome c, Proc. Natl. Acad. Sci. 110 (2013) 11863–11868.

[65] T. Ishihara, R. Ban-Ishihara, M. Maeda, Y. Matsunaga, A. Ichimura, S. Kyogoku, H. Aoki, S. Katada, K. Nakada, M. Nomura, N. Mizushima, K. Mihara, N. Ishihara, Dynamics of Mitochondrial DNA Nucleoids Regulated by Mitochondrial Fission Is Essential for Maintenance of Homogeneously Active Mitochondria during Neonatal Heart Development, Mol. Cell. Biol. 35 (2015) 211–223.

[66] N. Ashley, J. Poulton, Anti-cancer DNA Intercalators cause p53 Dependent Mitochondrial DNA Nucleoid Re-modelling, Oncogene. 28 (2009) 3880–3891.

[67] I. Shokolenko, N. Venediktova, A. Bochkareva, G.L. Wilson, M.F. Alexeyev, Oxidative stress induces degradation of mitochondrial DNA, Nucleic Acids Res. 37 (2009) 2539–2548.

[68] F. Celsi, P. Pizzo, M. Brini, S. Leo, C. Fotino, P. Pinton, R. Rizzuto, Mitochondria, calcium and cell death: A deadly triad in neurodegeneration, Biochim. Biophys. Acta - Bioenerg. 1787 (2009) 335–344.

[69] R. Bagur, G. Hajnóczky, Intracellular Ca2+ Sensing: Its Role in Calcium Homeostasis and Signaling, Mol. Cell. 66 (2017) 780–788.

[70] B. Zhivotovsky, S. Orrenius, Calcium and cell death mechanisms: A perspective from the cell death community, Cell Calcium. 50 (2011) 211–221.

[71] K. Brune, J. Frank, A. Schwingshackl, J. Finigan, V.K. Sidhaye, Pulmonary epithelial barrier function: some new players and mechanisms, Am. J. Physiol. - Lung Cell. Mol. Physiol. 308 (2015) L731–L745.

[72] D.F. Bogenhagen, Does MtDNA nucleoid organization impact aging?, Exp. Gerontol. 45 (2010) 473–477.

[73] D. Spano, C. Heck, P. De Antonellis, G. Christofori, M. Zollo, Molecular networks that regulate cancer metastasis, Semin. Cancer Biol. 22 (2012) 234–249.

[74] D. Tan, D.S. Goerlitz, R.G. Dumitrescu, D. Han, F. Seillier-Moiseiwitsch, S.M. Spernak, R.A. Orden, J. Chen, R. Goldman, P.G. Shields, Associations between cigarette smoking and mitochondrial DNA abnormalities in buccal cells, Carcinogenesis. 29 (2008) 1170–1177.

[75] S.A. Grando, Connections of nicotine to cancer, Nat. Rev. Cancer. 14 (2014) 419–429.

[76] K.F. Macleod, M.L. Boland, A.H. Chourasia, K.F. Macleod, Mitochondrial Dysfunction in Cancer, 3 (2013) 1–28.

[77] L.J. Martin, Biology of mitochondria in neurodegenerative diseases, 2012.

[78] U.S. Department of Health and Human Services, How Tobacco Smoke Causes Disease: The Biology and Behavioral Basis for Smoking-Attributable Disease, 1st ed, Centers for Disease Control and Prevention, National Center for Chronic Disease Prevention and Health Promotion, Office on Smoking and Health, Atlanta, 2010.

[79] A. Mcneill, L.S. Brose, R. Calder, S.C. Hitchman, P. Hajek, M. H, E-cigarettes : an evidence update A report commissioned by Public Health England, 2015. www.gov.uk/government/uploads/system/uploads/attachment_data/file/454516/Ecigarettes_an_evidence_update_A_report_commissioned_by_Public_Health_England.pdf.

[80] A.A. Lopez, M.M. Hiler, E.K. Soule, C.P. Ramôa, N. V. Karaoghlanian, T. Lipato, A.B. Breland, A.L. Shihadeh, T. Eissenberg, Effects of electronic cigarette liquid nicotine concentration on plasma nicotine and puff topography in tobacco cigarette smokers: A preliminary report, Nicotine Tob. Res. 18 (2016) 720–723.

[81] J.E. Rose, A.G. Mukhin, S.J. Lokitz, T.G. Turkington, J. Herskovic, F.M. Behm, S. Garg, P.K. Garg, Kinetics of brain nicotine accumulation in dependent and nondependent smokers

assessed with PET and cigarettes containing 11C-nicotine, Proc. Natl. Acad. Sci. 107 (2010) 5190–5195.

[82] E.E. Omaiye, I. Cordova, B. Davis, P. Talbot, Counterfeit Electronic Cigarette Products with Mislabeled Nicotine Concentrations, Tob. Regul. Sci. 3 (2017) 347–357.

[83] B. Davis, M. Dang, J. Kim, P. Talbot, Nicotine concentrations in electronic cigarette refill and do-it-yourself fluids, Nicotine Tob. Res. 17 (2015) 134–141.

[84] M.J. Schroeder, A.C. Hoffman, Electronic cigarettes and nicotine clinical pharmacology, Tob. Control. 23 (2014) ii30-ii35.

[85] R.Z. Behar, M. Hua, P. Talbot, Puffing topography and nicotine intake of electronic cigarette users, PLoS One. 10 (2015) 1–18.

[86] D. Nutt, L.A. King, W. Saulsbury, C. Blakemore, Development of a rational scale to assess the harm of drugs of potential misuse, Lancet. 369 (2007) 1047–1053.

[87] C.M. Seitz, R.W. Strack, D.L. Wyrick, Cigarette smoking and facial wrinkles: A review of the literature, J. Smok. Cessat. 7 (2012) 18–24.

[88] A. Morita, Tobacco smoke causes premature skin aging, J. Dermatol. Sci. 48 (2007) 169–175.

[89] A. Clifford, L. Lang, R. Chen, Effects of maternal cigarette smoking during pregnancy on cognitive parameters of children and young adults: A literature review, Neurotoxicol. Teratol. 34 (2012) 560–570.

[90] M. Mund, F. Louwen, D. Klingelhoefer, A. Gerber, Smoking and pregnancy - A review on the first major environmental risk factor of the unborn, Int. J. Environ. Res. Public Health. 10 (2013) 6485–6499.

[91] R. Wickstrom, Effects of Nicotine During Pregnancy: Human and Experimental Evidence, Curr. Neuropharmacol. 5 (2007) 213–222.

[92] J.B. Dwyer, S.C. McQuown, F.M. Leslie, The dynamic effects of nicotine on the developing brain, Pharmacol. Ther. 122 (2009) 125–139.

[93] A. Trtchounian, P. Talbot, Electronic nicotine delivery systems: is there a need for regulation?, Tob. Control. 20 (2011) 47–52.

[94] M. Knoll, P. Talbot, Cigarette smoke inhibits oocyte cumulus complex pick-up by oviduct in vitro independent ciliary beat frequency, Reprod. Toxicol. 12 (1998) 57–68.

[95] M. Williams, A. Villarreal, K. Bozhilov, S. Lin, P. Talbot, Metal and silicate particles including nanoparticles are present in electronic cigarette cartomizer fluid and aerosol, PLoS One. 8 (2013) e57987.

Section IV: Evaluation of Electronic Cigarettes on Cancer Metastasis

Chapter 6

Epithelial-to-mesenchymal transition of A549 lung cancer cells exposed to electronic cigarettes

ABSTRACT

Epithelial-to-mesenchymal transition (EMT) is the initial step enabling the metastasis of cancer cells, which often leads to death. Although smoking is a major risk factor for lung cancer, there is still widespread use of conventional cigarettes. Recently, the tobacco industry has been transformed by the introduction of electronic cigarettes (ECs), which have lower levels of carcinogens and may provide a safer alternative. Here, we investigate the ability of EC liquids and aerosols to induce an EMT in A549 lung cancer cells.

Materials and Methods: Human adenocarcinoma alveolar basal epithelial cells (A549) were exposed to EC liquids and aerosols from a popular product for 3–8 days. Live cell imaging, EMT biomarker analysis, and machine learning/image processing algorithms were used to characterize changes associated with EMT.

Results: Long-term exposure of A549 cells to menthol or tobacco-flavored EC liquids or aerosols induced an EMT that was characterized by acquisition of a fibroblast-like morphology, loss of cell-to-cell junctions, internalization of E-cadherin, increased motility, and upregulation of other EMT markers. The EMT was concurrent with plasma membrane to nuclear translocation of active β-catenin.

INTRODUCTION

Metastasis is a multi-step process in which cancer cells undergo an epithelial-to-mesenchymal transition (EMT), then detach from the primary tumor, and migrate to neighboring

or distant organs, where they can create new tumors [1]. Once cancer cells have metastasized, treatment becomes very difficult, and the chances of survival are diminished [2]. Lung cancer accounts for the highest number of cancer-related deaths, most of which are due to the metastasis of tumor cells [3, 4].

Tobacco use is the main risk factor for lung cancer and is responsible for approximately 22% of cancer-related deaths globally [5]. Cigarette smoke promotes metastasis through induction of an EMT in existing airway epithelial tumors by down-regulating epithelial cadherin (E-cadherin), which leads to loss of cell–cell adhesion and apical–basal polarity [6–8].

Electronic cigarettes (EC) are tobacco products that have rapidly gained worldwide acceptance and are often promoted as harm-reduction or smoking-cessation alternatives [9]. Their introduction into world markets has come without much prior research on their potential to cause cancer or effect cancer progression. Prior in vitro studies on EC have focused on their toxicity [10, 11], with one recent in vitro study showing that EC aerosol produced little mutagenicity [12]. These studies were all done over relatively short exposure periods, usually lasting only 24–48 hours. Other studies demonstrated that EC exposure resulted in carcinogenic transformation in Salmonella typhimurium [13] and DNA damage in a rat lung model [14] and mouse organs [15].

No study to date has examined the potential for EC to cause an EMT and contribute to the progression of a pre-existing tumor. In this study, we tested the hypothesis that longer exposures of lung cancer cells to EC liquids and aerosols, typical of those EC users receive, induces an EMT, thereby creating the potential for metastasis.

MATERIALS AND METHODS

EC liquids and aerosols

Menthol and tobacco flavors of a leading cartomizer style EC were purchased at local markets in Southern California. Product boxes were labeled to contain propylene glycol, glycerol, and nicotine (48 mg/ml). Flavor chemicals were not listed on product packaging but were presumed to be present to impart menthol and tobacco flavor. Liquids were removed from cartomizers by centrifugation, and 1% dilutions by volume were prepared in A549 culture medium. Aerosols were generated using a smoking machine by taking 4.3 s puffs (average for EC users) every 1 min with an adjusted flow rate to produce a consistent robust puff. Aerosols were collected in A549 culture medium in a 250 mL round-bottom flask, which was suspended in an ethanol and dry ice bath to allow immediate condensation and capture of aerosol puffs. After collection, medium was warmed to room temperature, aliquoted, then immediately frozen and stored at - 80 °C until used. Six puffs were dissolved per 1 mL of A549 culture medium, which is referred to as 6 total-puff-equivalents (TPE) of aerosol. Both e-liquids and aerosols were passed through a 0.2 μm filter before use in experiments.

Long-term culturing of A549 lung cancer cells

A549 CCL-185 cells (ATCC, Manassas, VA USA), which were previously derived from a human lung adenocarcinoma, were grown on non-coated T-25 flasks and cultured in ATCC F-12 K medium with 10% A549-specific fetal bovine serum in 5% CO2 at 37 °C. Cells were incubated in control medium or medium containing dilutions of aerosol or EC liquid until 80% confluent, then passaged using 0.25% trypsin, and grown in control or treatment medium for 3–8 days.

Morphological analysis

Cell morphology was classified as cobblestone (normal morphology), enlarged, or elongated using CL-Quant (DR Vision, Seattle WA), CellProfiler image processing software [16] and a custom ma- chine learning algorithm written in MATLAB software (MathWorks Natick, MA, USA). Each image was segmented using CL-Quant software and manually modified to separate individual cells. The binary image of the segmentation was exported into CellProfiler to extract 61 morphological features from which six (area, compactness, eccentricity, major axis length, minor axis length, and solidity) were used to develop a learning library. A library consisting of 126 cells was manually classified to provide ground truth for the three morphological classes. Next, 10-fold cross-validation was conducted resulting in 97% accuracy in classification. Three separate (untrained) datasets consisting of 359 cells were run through the supervised machine learning algorithm and were validated manually, resulting in 89% accuracy. Datasets presented in this paper were automatically analyzed using this classifier.

Immunocytochemistry

Immunocytochemistry was performed using antibodies to EMT markers that included E-cadherin and vimentin (Millipore, Burlington, MA, USA), N- cadherin (R&D Systems, Minneapolis, MN, USA), metalloproteinase 9 (MMP9) and P120 (Abcam, Cambridge, MA, USA), and active (non-phosphorylated) β-catenin (Cell Signaling, Danvers, MA, USA). Also, an early endosome antigen 1 (EEA1) antibody (Cell Signaling, Danvers, MA, USA) was used for the E-cadherin co-localization study. Briefly, cells were grown in Ibidi chamber slides (Ibidi, Munich, Germany) and fixed using 4% paraformaldehyde. Cells were blocked in 10% donkey serum (Sigma-Aldrich, St. Louis, MO, USA) in 0.1% Triton-X (Bio-Rad, Hercules, CA, USA) in PBS, and primary antibodies were diluted in PBST (0.2% Tween (Sigma-Aldrich, St. Louis, MO, USA)

in PBS) and incubated at 4 °C overnight. Cells were next washed in PBST then incubated in Alexa Fluor 594 and 488 secondary antibodies (Life Technologies, Eugene OR USA) at room temperature for 1 h, then mounted in Vectashield (Vector Laboratories, Burlingame, CA USA).

E-cadherin transfection and internalization

For the E-cadherin/EEA1 co-localization study, cells were first transfected with an E-cadherin-GFP plasmid (Addgene #28009, Cambridge, MA USA). Briefly, cells were plated the day before transfection, a DNA-In A549 transfection reagent was used (MTI- GlobalStem, Gaithersburg, MD USA), and cells were incubated for 18–24 hours to allow gene expression. Next, the transfected cells were trypsinized and re-plated with EC liquids or aerosol for 4 days. Lastly, cells were immunolabeled with an early endosome marker, EEA1, to demonstrate co-localization and internalization of E-cadherin into endocytic vesicles.

To confirm co-localization of E-cadherin and EEA1, a line scanning method was used. Briefly, intensity data for representative images were collected by the line intensity tool in Nikon Elements Advanced Research software (Nikon Instruments, Melville, NY). Lines with a relative length equivalent to 35 μm were drawn on representative images. Pixel intensity data were collected along the line from both green (E-cadherin) and red (EEA1) channels. To rescale intensity data to a 0 to 1 range, raw intensity data were normalized with the feature scaling equation:

$$z_i = \frac{x_i - \min(x)}{\max(x) - \min(x)}$$

where z_i represents the normalized intensity value, which was computed using min and max intensity values in the set x. x_i represents the intensity value before normalization. Normalized intensity values were plotted using GraphPad Prism.

Fluorescence and phase contrast microscopy

Time-lapse fluorescent images were collected using an inverted Eclipse Ti-E microscope (Nikon Instruments, Melville, NY) equipped with a 60X objective (numerical aperture 0.85) and captured on the high-resolution Andor Zyla VSC-04941 camera (Andor, Belfast, UK). The live cells were placed in a LiveCell incubation chamber (Pathology Devices Inc., San Diego CA USA), which were kept at 37 °C, 5% CO2, and 90% relative humidity. The images were de-convoluted using the Live De-blur setting in the Nikon NIS Elements software. Fluorescence analysis was quantified using CL-Quant software (DR Vision, Seattle, WA) and CellProfiler. Phase contrast time-lapse videos of A549 cells were captured in a BioStation CT Incubator (Nikon Instruments, Tokyo, Japan).

Motility and migration analysis

Phase contrast and Hoechst 33342 (ImmunoChemistry Technologies, Bloomington, MN USA) fluorescent time-lapse images were captured every 15 min using a BioStation CT. CL-Quant software was used to track and extract motility information. First, the tophat preprocessing method was used to remove noise and strengthen the signal in the Hoechst (blue) channel (excitation 350 nm). Small object removal and background subtraction procedures were applied to minimize background noise. The tracking procedure was applied to the final signal segmentation to create trajectory tracks for cells with fluorescent signal. Tracking data were exported to Excel and imported into MATLAB to generate migratory graphs, which displayed the total length traveled and the initial-final position displacement for each cell. Motility of control and treated cells was also compared using the wound healing assay, as described preciously [17]. Three independent experiments were done for each parameter studied, and statistical analyses were done using one-

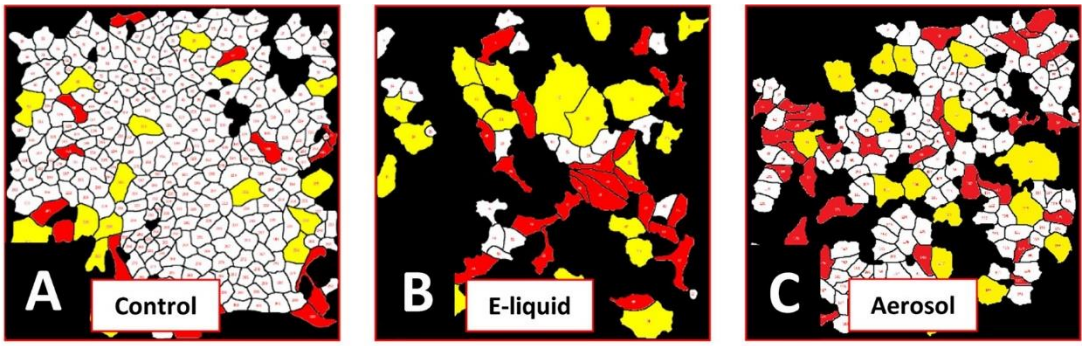
A
Control
B
E-liquid
C
Aerosol

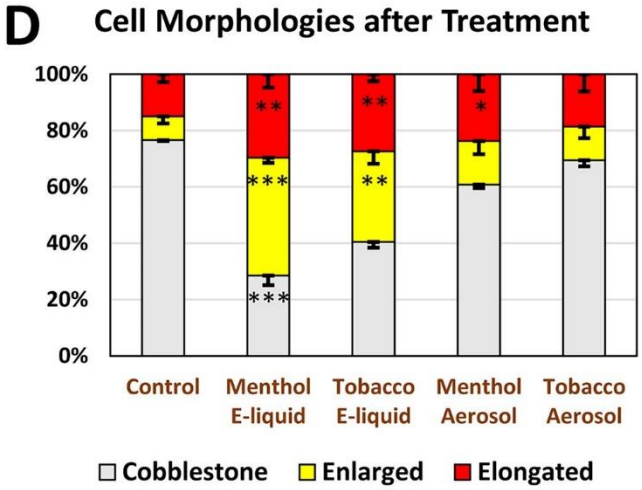
D
Cell Morphologies after Treatment
100%
80%
60%
40%
20%
0%
Control
Menthol E-liquid
Tobacco E-liquid
Menthol Aerosol
Tobacco Aerosol
Cobblestone
Enlarged
Elongated

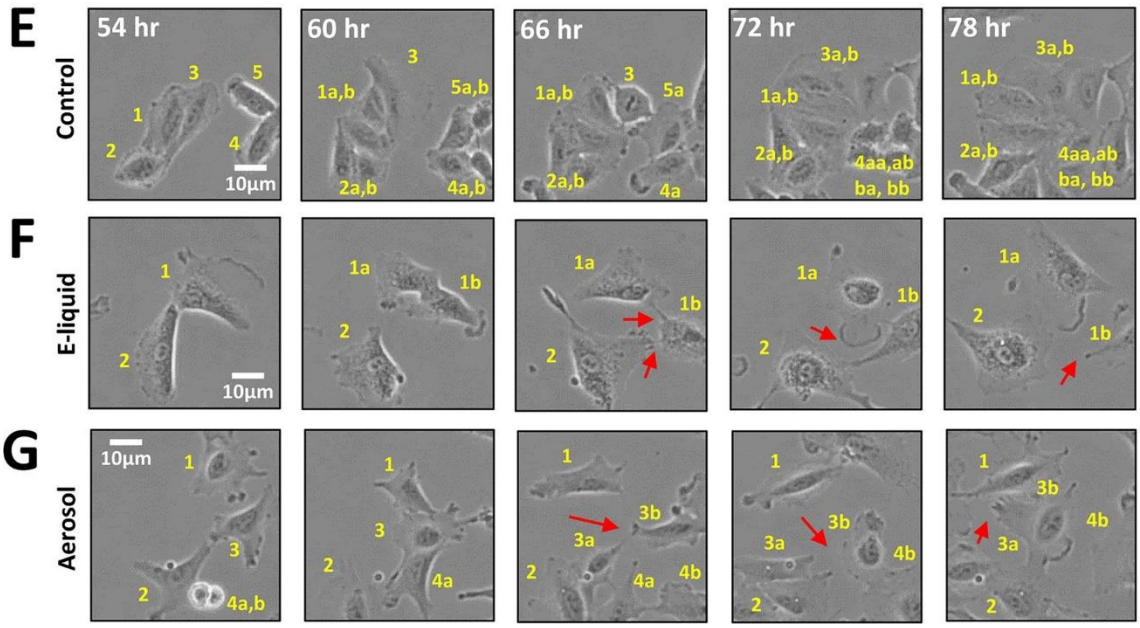
E
Control
54 hr
60 hr
66 hr
72 hr
78 hr
10μm
F
E-liquid
G
Aerosol

Figure 6.1. A549 Cell Morphology after EC Treatment. (A–C) Control A549 cells and cells treated 3–4 days with e-liquid or aerosol were image processed to quantify the percent of cobblestone (white), enlarged (yellow), and elongated (red) morphologies. (D) E-liquid and aerosol treatment decreased the cobblestone and increased the elongated (mesenchymal-like) sub-populations. Each error bar is the mean ± standard error of the mean (SEM) of three independent experiments. Statistical analysis was done on arcsine transformed data using a one-way ANOVA with Dunnett's post hoc test. (E–G) Film-strips show that control cells adhered with neighbors, while treated cells failed to adhere. Individual cells are labeled numerically and then labeled with an additional "a" and "b" to denote daughter cells produced by division. Red arrows point to areas where tight junctions failed to form between treated cells.

way ANOVAs with Prism (GraphPad, San Diego, CA USA) and Minitab software (State College, PA USA).

Quantification of active β-catenin

Active β-catenin and P120 were visualized using immunocytochemistry and nuclei were labeled with DAPI-Vectashield (Vector Laboratories, Burlingame, CA USA). For the β-catenin (red channel) signals, images were first smoothed to normalize uneven pixel distribution and rescaled to change the fluorescence signal from 0 to 1. Tophat and bottomhat methods were used to enhance the signal, and adaptive MOG (mixture of Gaussian) thresholding was applied to remove noise (Supplementary Methods). Otsu's method was used to segment and extract fluorescent β-catenin signals [18]. Active β-catenin and nuclei segmentations were co-localized. The percent of active β- catenin counts or area inside the nucleus was calculated by dividing the co-localized signal by the total β-catenin signal. For both area and count data, statistical analyses were done on arcsine transformed percent data using a one-way ANOVA with Dunnett's post hoc test, in which treated groups were compared to the control.

Quantification of P120 internalization

P120 images were imported into CL-Quant for analysis. Tophat was used to remove background noise (Supplementary Methods). P120 signals were segmented using the global threshold method. At the tight junction, P120 signals were band-like, whereas internalized P120 was punctate. Segmented small puncta were filtered out based on size. The remaining larger objects were then "skeletonized" as described in the CL-Quant instruction manual to enhance the band-like morphology and remove non- band-like objects. The skeletons were overlaid on the original segmentation and used to separate P120 signals at tight junctions from internalized signal. Counts

and area information were extracted from both signals. One-way ANOVAs with Dunnett's post hoc test were performed on the data. Treated groups were compared to the control group.

RESULTS

EC E-liquids and aerosols induce morphological changes consistent with an EMT

A549 cells normally grow as tightly adhering "cobblestone" mono- layers with a few elongated and large cells interspersed among the cobblestone cells (Fig. 6.1A). The relative abundance of each cell type was evaluated using a custom protocol developed with CL-Quant, CellProfiler, and MATLAB software. By 3–4 days of treatment with e- liquid or aerosol, there was a significant decrease in the cobblestone cells and a corresponding increase in single elongated mesenchymal- like cells, consistent with an EMT (Figs. 6.1A–D). There was also an in- crease in enlarged cells, which were more pronounced in the e-liquid treatments (Fig. 6.1B, D) and often multinucleated (Supplementary Fig. S6.1). In time-lapse videos, e-liquid and aerosol treated cells frequently contacted but did not adhere to neighboring cells, whereas control cells formed tight cell-to-cell connections with each other (Fig. 6.1E–G). In Fig. 6.1E–G, each individual cell was numbered, and the progeny were followed over time.

Molecular markers of an EMT

To confirm that the above changes were due to an EMT, molecular markers characteristic of cells transitioning from an epithelial-to-mesenchymal phenotype were used. Cancer cell-produced MMP9 is required for invasion through the extracellular matrix during metastasis [19]. MMP9 was upregulated by day 4 in A549 cells treated with either e-liquid or aerosol (Fig. 6.2A, C). By 8 days of treatment, E-cadherin was lost from the cell surface (Fig. 6.2B), consistent with the observed lack of cell-to-cell adhesion (Fig. 6.1E–G). Immunocytochemistry also revealed an

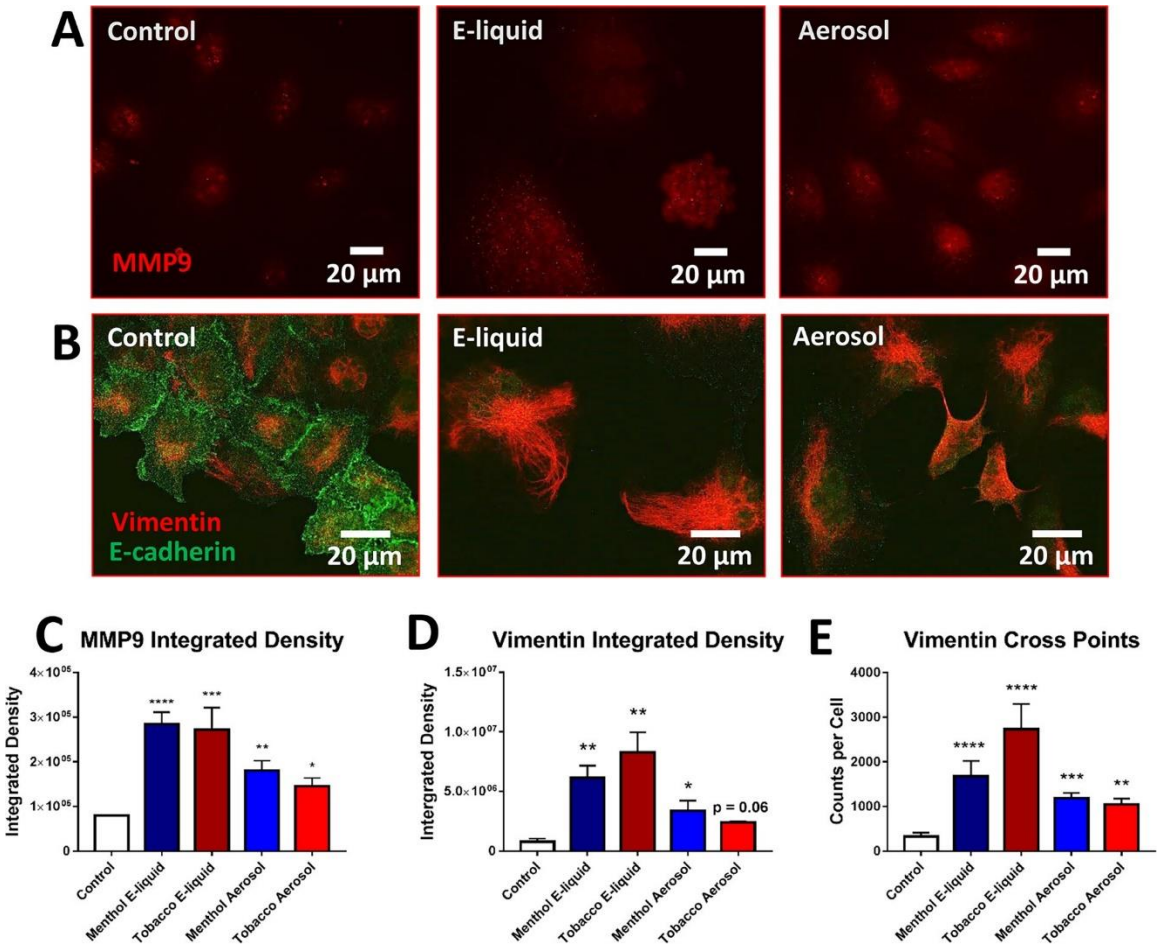

Figure 6.2. Upregulation of EMT Markers in E-liquid and Aerosol Treated Cells. (A) Immunofluorescence of 4-day treated A549 cells labeled with MMP9 antibody. (B) Immunofluorescence of 8-day treated A549 cells co-labeled with E-cadherin and vimentin antibodies. (C) Quantification of integrated density (total area x mean intensity) of MMP9 fluorescent images. Each error bar is the mean ± SEM of three independent experiments. (D–E) Integrated density and cross points of vimentin fluorescent images. Increase of integrated density and cross points are indicative of increased protein expression. Each error bar is the mean ± SEM of five independent experiments. One-way ANOVAs with Dunnett's post hoc test were performed on natural log transformed data. Asterisks on top of each bar indicate the statistical significance. (* = $p < 0.05$. ** = $p < 0.01$. *** = $p < 0.001$. **** = $p < 0.0001$).

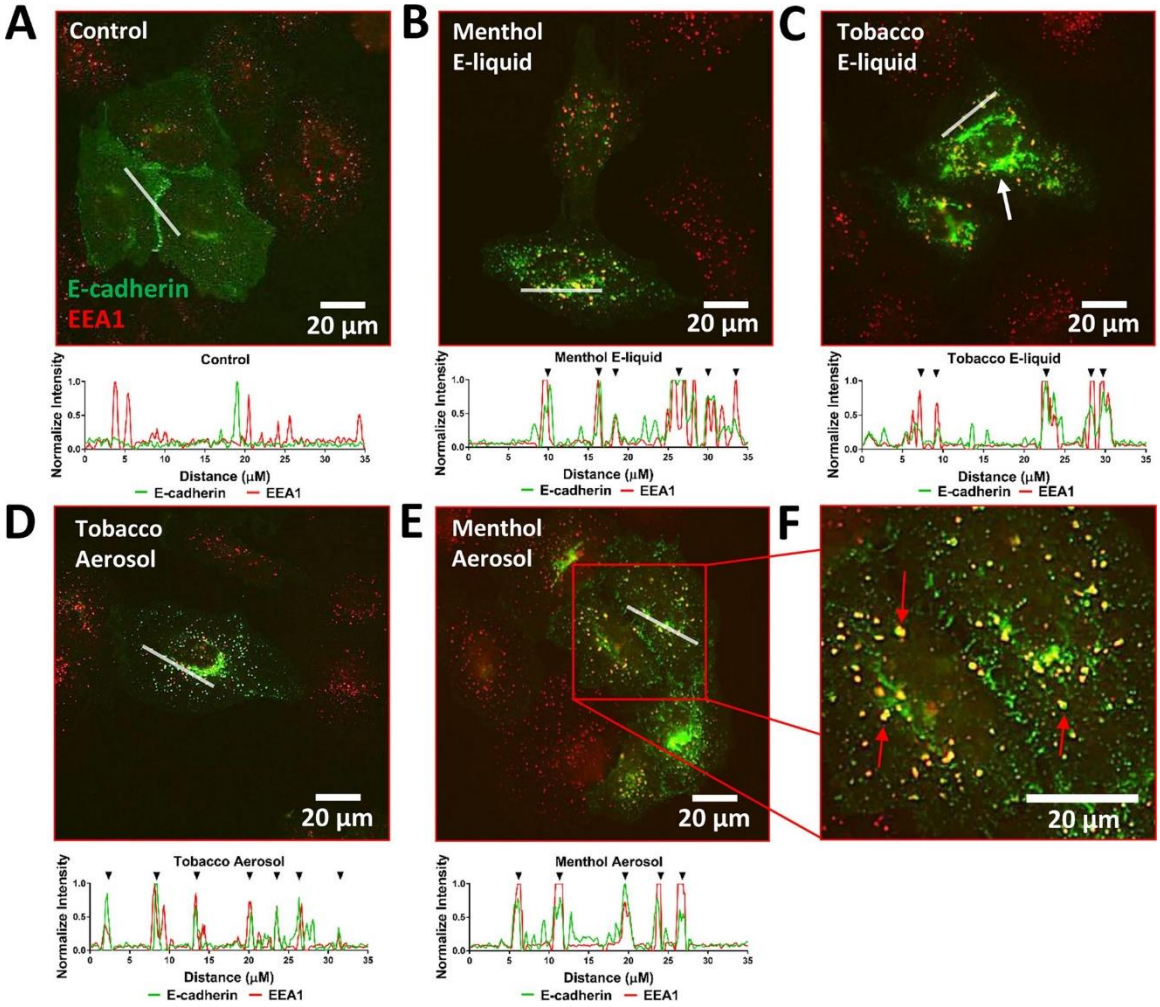

Figure 6.3. E-cadherin Internalization by Endocytosis. (A–E) 4-day treated A549 cells were transfected with an E-cadherin plasmid and co-immuno-labelled with an EEA1 antibody to demonstrate internalization of E-cadherin. A line scanning method was used to do intensity profiling to confirm the co-localization of the E-cadherin and EEA1 signals. Black arrowheads above each graph (except control) show co-localization of the two channels. (F) Enlarged image of 4-day menthol aerosol treated cells. Red arrows show co-localization of E-cadherin and EEA1.

increase in total vimentin after 4 days (Supplementary Fig. S6.2 A–C) and 8–9 days of exposure (Fig. 6.2B, D integrated density) and an increase in vimentin cross points at day 8, indicative of increased filament density (Fig. 6.2E). Vimentin is overexpressed in epithelial cancers undergoing an EMT and facilitates accelerated tumor growth and invasion [20]. These changes in vimentin likely facilitate the transition of cells to a more elongated phenotype. In addition, N-cadherin,

another marker for an EMT, was also increased in cells exposed to EC products (Supplementary Fig. S6.3). These molecular marker data collectively support the idea that EC treated cells undergo an EMT during 4-8-days of exposure.

Internalization of E-cadherin during the EMT

One of the primary modes of EMT initiation is the reduction of membrane E-cadherin via the endocytic machinery. To assess whether the decrease in E-cadherin expression at the cell membrane was due to its internalization, 4 day-treated A549 cells were transfected with an E-cadherin plasmid and then immuno-labeled with an early endosome marker (EEA1). The control cells revealed very few co-localized signals; whereas both the menthol and tobacco e-liquid and aerosol treated groups had distinct co-labeled puncta indicative of internalized E-cadherin cargo (Fig. 6.3A–F). Accumulation of E-cadherin was seen in the perinuclear region (Fig. 6.3C, white arrow)

Treatment with EC liquid and aerosol increased cell motility

An increase in cell motility is characteristic of cancer cells under- going an EMT [1]. To determine if EC-treatment enhanced cell migration, A549 cells were labeled with the Hoechst 33342 live cell nuclear dye and monitored over time in a BioStation CT. A dual fluorescence and phase contrast tracking algorithm was developed to monitor the motility of each cell. Cells treated with e-liquids and aerosols for 3–4 days showed an increase in the population of motile cells (total distance traveled > 25 μm) (Fig. 6.4A–E). Migration graphs also showed that control cells mainly exhibited a random-walk (Brownian) type motion, whereas most of the treated cells exhibited a

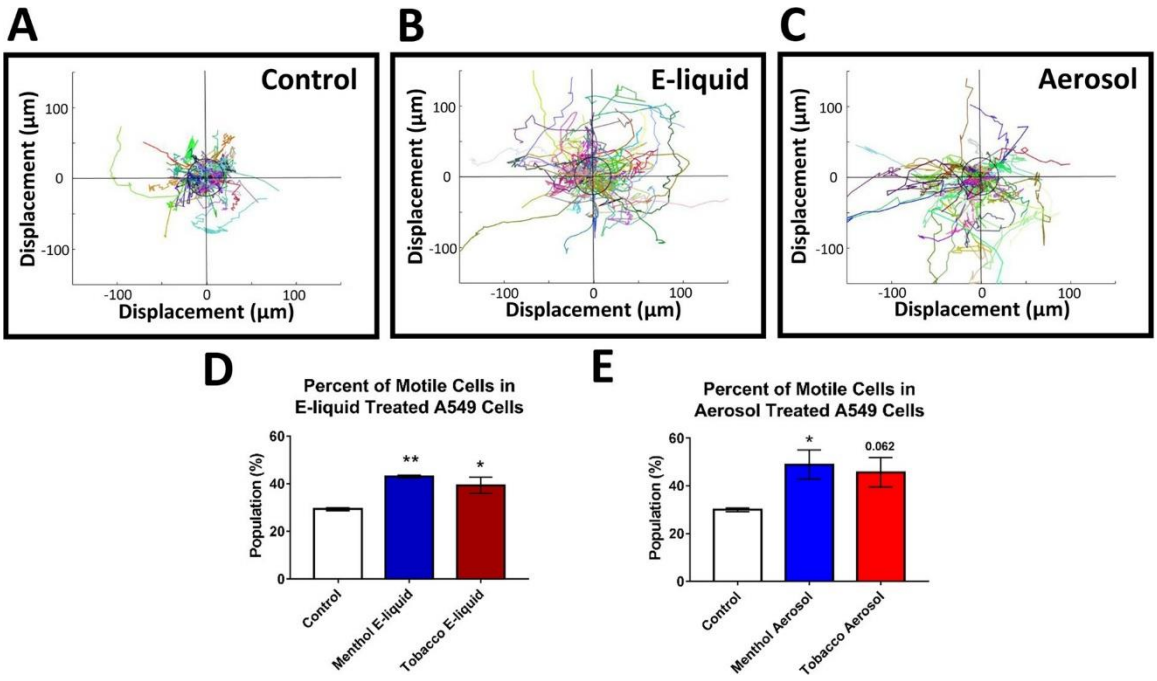

Figure 6.4. Increased Motility after EC Treatment (A–C) Motility graphs show compilation of trajectories and distance traveled by individual control and treated cells (central circles are positioned 25 µm from the starting location). Different colors correlate with different cells tracks. (D–E) The percent of "motile cells" (displacement > 25 µm) increased in treated groups. Each error bar is the mean ± SEM of four independent experiments. Motility data statistical analysis were done using a one-way ANOVA with Dunnett's post hoc test; treated groups were compared to the control. Asterisks on top of each bar indicate the statistical significance. (*= $p < 0.05$. ** = $p < 0.01$.).

"directed" movement (Fig. 6.4A–C). The increase in cell motility was confirmed using the wound healing (scratch) assay. Again, both the e-liquid and aerosol treated cells showed significantly greater motility than untreated controls (Supplementary Fig. S6.4).

Translocation of active β-catenin and P120 from the plasma membrane to the cytoplasm and nucleus

Immunocytochemistry was performed to compare the localization of β-catenin and P120, two adherens junction proteins important in cell polarity, in the control and treated groups. In treated cells, the active form of β-catenin showed a marked decrease in cell junctions and a

corresponding increase inside the cells (Fig. 6.5A). If de-phosphorylated (active), β-catenin is stabilized and protected against degradation by GSK-3β and can move into the nucleus to initiate transcription. Image processing software was used to quantify colocalization of active β- catenin with the nuclear DAPI-stain. A significant increase in the number and area (%) of β-catenin puncta in the nucleus was observed in treated cells (Fig. 6.5B–C). Treatment of A549 cells with e-liquid or aerosol caused a decrease in P120 at the cell membranes after 3–5 days of treatment (Fig. 6.5D) and an increase in cytoplasmic levels (percent of P120 internalized by area and count shown in Fig. 6.5E and F respectively). Unlike β-catenin, P120 did not show an accumulation in the nuclei of aerosol treated groups (Fig. 6.5D), and therefore was not quantified.

DISCUSSION

Previous in vitro studies with normal and cancer lung cells have generally used short-term exposures to EC fluids or aerosols [21]. These studies have shown various effects including decreased metabolic activity often accompanied by cell death [10, 11, 22–24], increased inflammation [25], oxidative stress [26], DNA damage [18], and mitochondrial stress [27]. The current study is the first to examine 4-8-day exposure of cancer cells to EC liquids and aerosols and to report that such exposure causes changes in cell morphology, cell-to-cell adhesion, molecular markers, and motility consistent with an EMT. These changes include transformation of cobblestone monolayers to mesenchymal-like cells, decreased E-cadherin, increased vimentin and MMP9, and in- creased cell motility. There was also an increase in the number of cells with an enlarged phenotype, consistent with a case report in which a lung biopsy from an EC user had multinucleated giant cells [28]. An EMT was induced in A549 cells by both the menthol and tobacco flavored EC liquids and aerosols from the leading product of EC used in this study. This shows that the factor(s) causing the EMT is present in the fluid before heating and is not a chemical

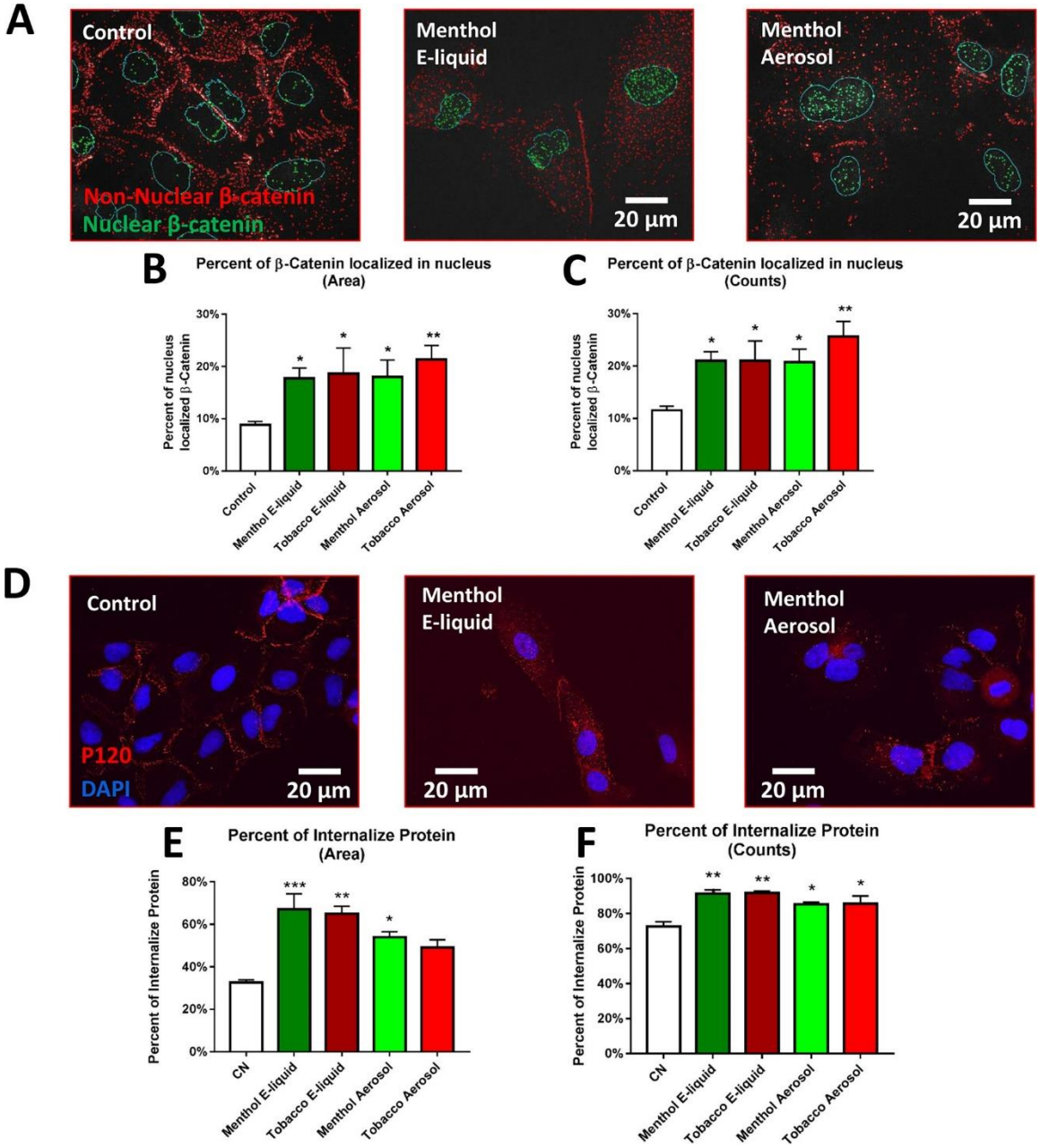

Figure 6.5. Translocation of Two Catenin-Family Transcription Factors. (A) Active β-catenin in the nucleus (green) and cytoplasm (red) in segmented images. (B–C) Quantification of percent area and counts of active β-catenin puncta inside the nucleus. Each error bar is the mean ± SEM of six independent experiments. One-way ANOVA with Dunnett's post hoc test was performed on B and C arcsine-transformed percent data; treated groups were compared to the control. (D) 8-day treated A549 cells immunolabeled with P120. (E–F) Quantification of the percent area and counts of internalized P120. Each error bar is the mean ± SEM of three independent experiments. One-way ANOVA with Dunnett's post hoc test was performed on E and F. Asterisks on top of each bar indicate the statistical significance. (*= $p < 0.05$. ** = $p < 0.01$. *** = $p < 0.001$.).

produced as a result of aerosolization. EC users do sometimes draw e-liquid into their mouths and get e-liquid on their skin. Although not a topic in this study, there is a possibility that a similar EMT would occur in tumors localized in these tissues as well.

The EC-induced EMT was characterized by the internalization of E-cadherin via endocytosis into early endosomes with subsequent accumulation in the perinuclear region, which may be the endocytic recycling compartment (ERC) [29]. Loss of E-cadherin from junctional complexes is a ubiquitous feature of an EMT and a necessary step that enables subsequent cell migration away from a tumor during metastasis [1]. We also observed enhanced migration of cells that were no longer able to adhere to other cells.

EC treatment also resulted in the translocation of active β-catenin and P120 catenin from the plasma membrane to the cytoplasm, and β- catenin was further translocated to the nucleus. β-catenin and P120 are essential components of the cadherin-based adherens junctions, and their cytoplasmic accumulation likely contributes to the destabilization of cell junctions. Other studies have shown that the transport of these catenins to the nucleus activates Wnt-signaling (β-catenin) and Rho GTPase (P120) pathways, which in turn contribute to an EMT [29, 30]. The appearance of β-catenin in the nucleus following EC liquid or aerosol treatment suggests that the EMT observed in our study was further activated by the Wnt/β-catenin pathway.

An EMT is a critical initiation step in the metastasis of lung cancer cells [1]. During an EMT, epithelial cells lose their polarity, cell-cell junctions, and cell-matrix adhesions, allowing them to migrate and invade other tissues, often remote from the primary tumor [1]. A549 adenocarcinoma cells are part of the non-small cell lung cancer (NSCLC) group. Once such cells have undergone an EMT and metastasized in patients, treatment is difficult and survival rates are very low [31].

ECs are often promoted as harm reduction products, and Public Health England has stated that they are 95% safer than conventional cigarettes [32]. These claims are often based on the observation that EC aerosols have fewer chemicals than conventional cigarettes and harmful chemicals are usually lower in concentration in ECs [33]. However, most work done on cell and animal responses to EC aerosol have not to- date looked for metastasis. One recent paper describes the formation of tumors in rat lungs exposed to EC aerosol [14]. Our data are the first to show an EMT in human lung cancer cells, a critical observation that suggests EC might lead to metastasis of existing tumors. While additional work will be required to determine if a similar EMT occurs in humans using EC, our data demonstrate an important need for additional information on this topic.

Conventional cigarette constituents induce tumor formation and contribute to cancer progression by initiating an EMT [7, 8, 19, 34–36]. The effects induced by EC liquids and aerosols are similar to those re- ported for cigarette smoke, which include morphological changes, in- creased migratory behavior, and initiation of EMT signaling pathways. This again calls into question the safety of ECs and raises concerns about their designation as harm reduction products.

The aerosol concentration used in our study corresponds to what a user would receive while inhaling 6 puffs of EC aerosol. Although puffing topography varies with each individual [37], an average user puffs roughly 175 times/day [38]. While our work was done using continuous exposure over multiple days, the concentration of aerosol during our exposures was less than the total exposure an EC user would receive in a day (6 TPE vs 175 puffs/day). It will be important in the future to mimic human inhalation of EC aerosol with in vitro models that use intermittent air liquid interface exposure.

It is not yet known if this EC produces an EMT in other types of tumor cells from the lung or other organs, and this will be an important topic for future work. Since the EMT was observed with a leading EC product, the number of users who could potentially be impacted is high. This

critical finding has significant implications for dual EC users or former cigarette users who have switched to EC and may be at risk for lung cancer or who may already have a lung tumor. For EC users with no existing cancer (e.g., young users), there are also significant implications such as the loss of cell junctions in normal epithelial cells which could lead to a leaky epithelial barrier in the lung and increased permeability. This could in turn lead to inflammation, chronic obstructive pulmonary disease, and acute lung injury [39]. Given these findings, it would be advisable for health care workers to include EC use in patient medical records, particularly those with a history of cigarette smoking or dual use of EC and tobacco cigarettes. Our data warn that caution should be exercised when using EC given their ability to induce an EMT in a cancer cell line. These data bring to focus the overall need for better understanding of the effects of ECs on health, particularly with respect to cancer progression. This study further supports the 2016 Surgeon General's conclusion that EC aerosol is not harm-free [9] and that the FDA may need to regulate ECs under its authority.

CONCLUSION

This is the first known study to show an EMT of lung cancer cells during exposure to EC products. Because an EMT is an initial step leading to metastasis, an intractable problem that often leads to patient death, this critical finding has significant implications for former or heavy cigarette smokers who are using EC and may be at risk for lung cancer or who may already have a lung tumor.

SUPPLEMENTARY METHODS USED FOR IMAGE PROCESSING

Pre-processing: For pre-processing, a gray scale image was translated into a mathematical matrix composed of individual pixel intensities using CellProfiler.

Tophat: The purpose of "tophat" was to enhance contrast of bright objects in an image and to reduce the background noise, while preserving the original image information. The "tophat" operation can be written as

$$I_{tophat} = I_{orignal} - I_{open}$$

I refers to an image. The tophat operation consisted of subtracting the open image (I_{open}) from the original image ($I_{orignal}$). Opening an image consisted of "erosion" followed by image "dilation". Erosion decreased pixel intensity surrounding the immunofluorescence signal. By applying this operation, small background noise was removed, and the signal appeared smaller. Dilation was then used to correct the size of the altered signals.

Bottomhat: The purpose of "bottomhat" was to correct detailed structural elements that were lost by "tophat" image processing. The "bottomhat" operation can be written as

$$I_{bottomhat} = I_{close} - I_{original}$$

I refers to an image. The "bottomhat" operation consisted of subtracting the original image ($I_{original}$) from the close image (I_{close}). Closing an image consisted of "dilation" followed by image "erosion". Dilation filled in holes in regions of pixel discontinuity. Erosion was then used to correct the distorted regions introduced by dilation. Bottomhat allowed extraction of small dark regions that were surrounded by bright fluorescence. The bottomhat image was inverted and converted to a binary image (black or white). The binary image was subtracted from the "tophat" image to correct the structural elements.

Adaptive Mixture of Gaussian (MOG) Thresholding: The purpose of adaptive MOG thresholding after preprocessing was to remove background noise that remained after tophat and bottomhat. An adaptive strategy was used to overcome non-uniform intensity in images. Images were partitioned into tiles, and threshold values were calculated for each tile using MOG thresholding. The MOG method used a user-determined estimate of the percent of pixels in the

foreground to calculate the actual number of pixels in the foreground and background [40]. After thresholding, the remaining pixels with intensity greater than zero were considered potential fluorescent signals, which were then subjected to adaptive Otsu's thresholding.

Adaptive Otsu's Thresholding: Otsu's thresholding method was used to segment immunofluorescence signal in CellProfiler. First, an adaptive strategy was used to partition an image into tiles, and threshold values were automatically determined by Otsu's method for each tile. Otsu's method used pixel clustering to separate total pixels into foreground and background. To optimize pixel clustering, Otsu's method reduced gray values to binary values [41]. Foreground pixel clusters in each image were identified as objects of interest.

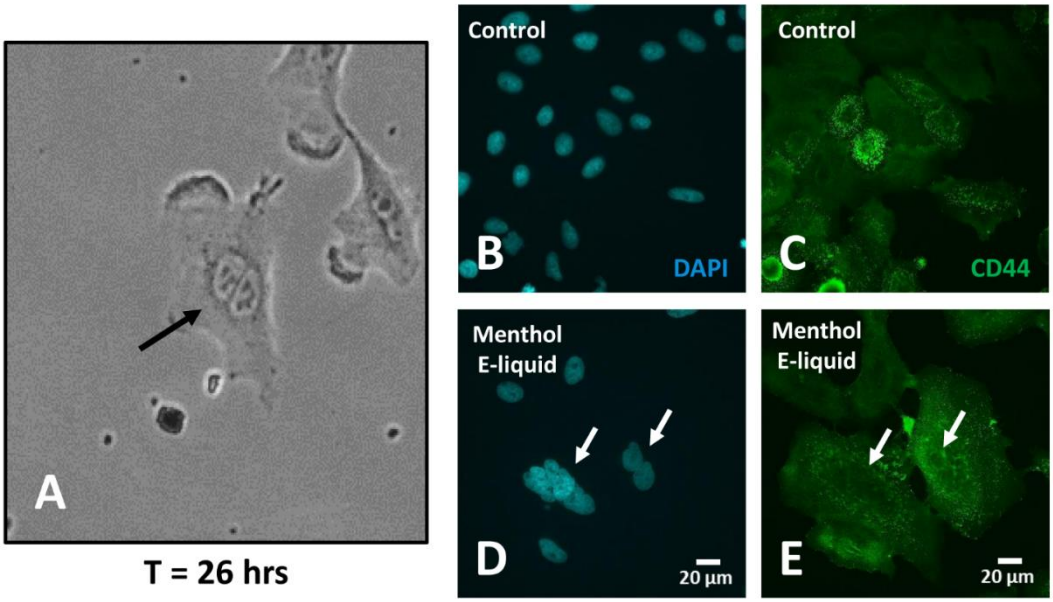

Figure S6.1. Enlarged multinucleated cells. (A) A phase contrast image of a multinucleated cell following 26 hours of treatment with menthol e-liquid. Arrow indicates two nuclei in one cell. (B-C) Control cells labeled with DAPI (B) and CD44 antibody (C) to show that most cells have a single nucleus. (D-E) Cells treated 4 days with menthol e-liquid showing multiple nuclei labeled with DAPI (D) and cell membranes labeled with CD44 antibody (E). Arrows indicate multiple nuclei in cells.

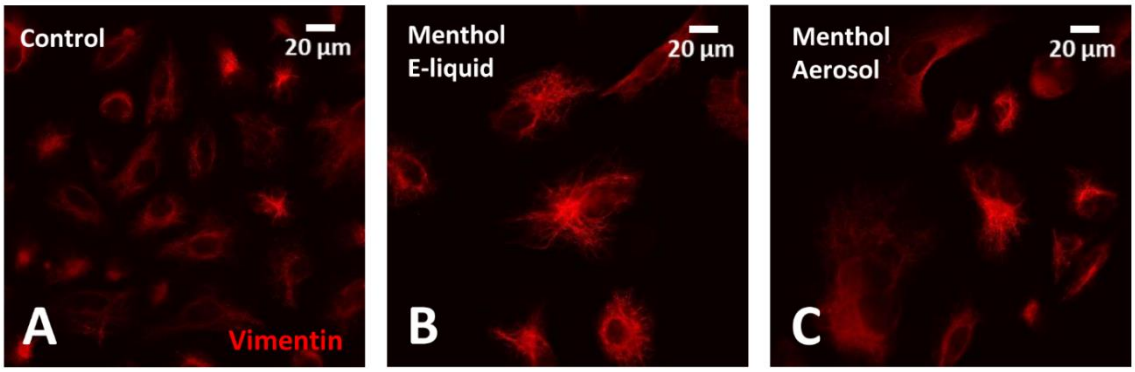

Figure S6.2. Increased vimentin at 4 days of treatment. A-C are images of control (A), menthol e-liquid treated (B), and menthol aerosol treated (C) cells labeled to show that vimentin increased by 4 days in treated cells.

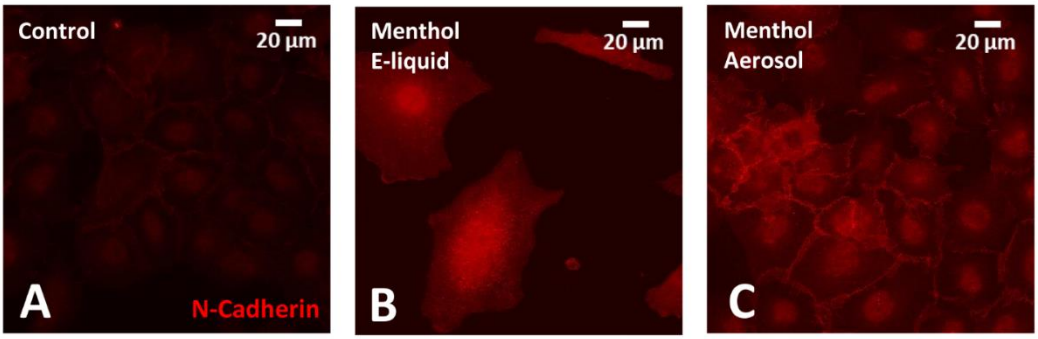

Figure S6.3. Increased expression of N-cadherin in treated cells. Control cells (A), menthol e-liquid treated cells (B), and menthol aerosol treated cells (C) showing increased expression of N-cadherin after 7 days of treatment.

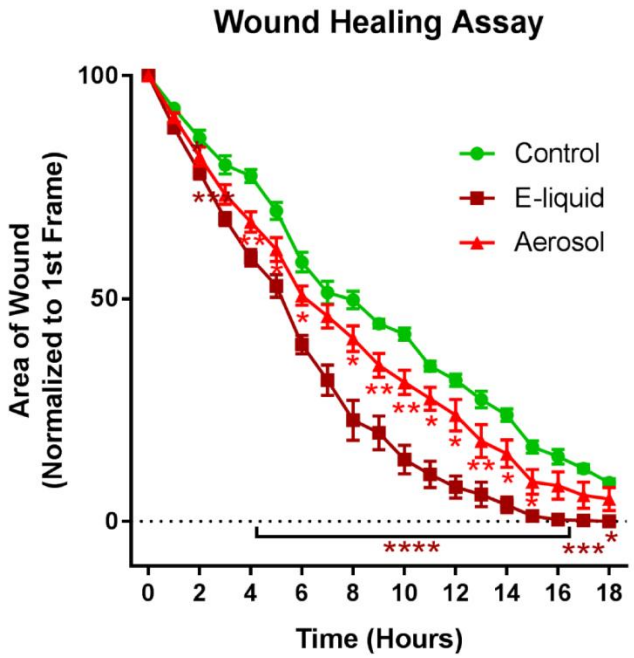

Figure S6.4. Wound healing assay. Rate of wound closure for control, e-liquid treated, and aerosol treated cells. Both e-liquid and aerosol treated cells closed (migrated) significantly faster than the control group. Data were analyzed by a 2-way ANOVA with Dunnett post-hoc test. * = $p < 0.05$; ** = $p < 0.01$; *** = $p < 0.001$; **** = $p < 0.0001$.

REFERENCES

[1] A.W. Lambert, D.R. Pattabiraman, R.A. Weinberg, Emerging biological principles of metastasis, Cell 168 (2017) 670–691.

[2] L. Chirieac, Biology of lung cancer metastases, Precis. Mol. Pathol. Lung Cancer (2018) 199–211.

[3] B.W. Stewart, C.P. Wild, World cancer report 2014, World Heal. Organ. (2014) 1–2.

[4] D. Spano, C. Heck, P. De Antonellis, G. Christofori, M. Zollo, Molecular networks that regulate cancer metastasis, Semin. Cancer Biol. 22 (2012) 234–249.

[5] M.H. Forouzanfar, A. Afshin, L.T. Alexander, S. Biryukov, M. Brauer, K. Cercy, F.J. Charlson, A.J. Cohen, et al, Global, regional, and national comparative risk assessment of 79 behavioural, environmental and occupational, and metabolic risks or clusters of risks, 1990–2015: a systematic analysis for the global burden of disease study 2015, Lancet 388 (2016) 1659–1724.

[6] CDC, What Are the Risk Factors for Lung Cancer? Www.Cdc.Gov., 2017.

[7] E. Veljkovic, J. Jiricny, M. Menigatti, H. Rehrauer, W. Han, Chronic exposure to cigarette smoke condensate in vitro induces epithelial to mesenchymal transition- like changes in human bronchial epithelial cells, BEAS-2B, Toxicol. Vitr. 25 (2011) 446–453.

[8] L. Zhang, M. Gallup, L. Zlock, C. Basbaum, W.E. Finkbeiner, N.A. McNamara, Cigarette smoke disrupts the integrity of airway adherens junctions through the aberrant interaction of p120-catenin with the cytoplasmic tail of MUC1, J. Pathol. 229 (2013) 74–86.

[9] V.H. Murthy, E-Cigarette Use Among Youth and Young Adults: A Report of the Surgeon General, (2016).

[10] R.Z. Behar, B. Davis, Y. Wang, V. Bahl, S. Lin, P. Talbot, Identification of toxicants in cinnamon-flavored electronic cigarette refill fluids, Toxicol. Vitr. 28 (2014) 198–208.

[11] V. Bahl, S. Lin, N. Xu, B. Davis, Y.H. Wang, P. Talbot, Comparison of electronic cigarette refill fluid cytotoxicity using embryonic and adult models, Reprod. Toxicol. 34 (2012) 529–537, http://dx.doi.org/10.1016/j.reprotox.2012.08.001. [12] S. Tommasi, S.E. Bates, R.Z. Behar, P. Talbot, A. Besaratinia, Limited mutagenicity of electronic cigarettes in mouse or human cells in vitro, Lung Cancer 112 (2017) 41–46.

[13] D. Thorne, I. Crooks, M. Hollings, A. Seymour, C. Meredith, M. Gaca, The mutagenic assessment of an electronic-cigarette and reference cigarette smoke using the Ames assay in strains TA98 and TA100, Mutat. Res. - Genet. Toxicol. Environ. Mutagen. 812 (2016) 29–38.

[14] D. Canistro, F. Vivarelli, S. Cirillo, C.B. Marquillas, A. Buschini, M. Lazzaretti, L. Marchi, V. Cardenia, M.T. Rodriguez-Estrada, M. Lodovici, C. Cipriani, A. Lorenzini, E. Croco, S. Marchionni, P. Franchi, M. Lucarini, V. Longo, C.M. Della Croce, A. Vornoli, A. Colacci, M.

Vaccari, A. Sapone, M. Paolini, E-cigarettes induce toxicological effects that can raise the cancer risk, Sci. Rep. 7 (2017) 1–9.

[15] H.-W. Lee, S.-H. Park, M. Weng, H.-T. Wang, W.C. Huang, H. Lepor, X.-R. Wu, L.-C. Chen, M. Tang, E-cigarette smoke damages DNA and reduces repair activity in mouse lung, heart, and bladder as well as in human lung and bladder cells, Proc. Natl. Acad. Sci. 115 (2018) E1560–E1569.

[16] A.E. Carpenter, T.R. Jones, M.R. Lamprecht, C. Clarke, I.H. Kang, O. Friman, D. a Guertin, J.H. Chang, R. a Lindquist, J. Moffat, P. Golland, D.M. Sabatini, CellProfiler: image analysis software for identifying and quantifying cell pheno- types, Genome Biol. 7 (2006) R100.

[17] S.C. Lin, H. Yip, R. Phandthong, B. Davis, P. Talbot, Evaluation of dynamic cell processes and behavior using video bioinformatics tools, Video Bioinforma, Springer, 2015, pp. 167–186.

[18] N. Otsu, A threshold selection method from gray-level histograms, IEEE Trans. Syst. Man. Cybern. 9 (1979) 62–66.

[19] S. Heerboth, G. Housman, M. Leary, M. Longacre, S. Byler, K. Lapinska, A. Willbanks, S. Sarkar, EMT and tumor metastasis, Clin. Transl. Med. 4 (2015) 6.

[20] H.H. Popper, Progression and metastasis of lung cancer, Cancer Metastasis Rev. 35 (2016) 75–91.

[21] K. Stratton, L.Y. Kwan, D.L. Eaton, P. Health, P.H. Practice, M. Division, Public Health Consequences of E-Cigarettes, (2018).

[22] R.Z. Behar, V. Bahl, Y. Wang, S. Lin, N. Xu, B. Davis, P. Talbot, A method for rapid dose-response screening of environmental chemicals using human embryonic stem cells, J. Pharmacol. Toxicol. Methods 66 (2012) 238–245.

[23] R.Z. Behar, W. Luo, S.C. Lin, Y. Wang, J. Valle, J.F. Pankow, P. Talbot, Distribution, quantification and toxicity of cinnamaldehyde in electronic cigarette refill fluids and aerosols, Tob. Control. 25 (2016) ii94–ii102.

[24] R.Z. Behar, W. Luo, K.J. Mcwhirter, J.F. Pankow, P. Talbot, Analytical and tox- icological evaluation of flavor chemicals in electronic cigarette refill fluids, Sci. Rep. 8 (2018) 1–11.

[25] Q. Wu, D. Jiang, M. Minor, H.W. Chu, Electronic cigarette liquid increases in- flammation and virus infection in primary human airway epithelial cells, PLoS One 9 (2014).

[26] C.A. Lerner, I.K. Sundar, H. Yao, J. Gerloff, D.J. Ossip, S. McIntosh, R. Robinson, I. Rahman, Vapors produced by electronic cigarettes and e-juices with flavorings induce toxicity, oxidative stress, and inflammatory response in lung epithelial cells and in mouse lung, PLoS One 10 (2015) 1–26.

[27] C.A. Lerner, P. Rutagarama, T. Ahmad, I.K. Sundar, A. Elder, I. Rahman, Electronic cigarette aerosols and copper nanoparticles induce mitochondrial stress and pro- mote DNA fragmentation in lung fibroblasts, Biochem. Biophys. Res. Commun. 477 (2016) 620–625.

[28] L.R. Madsen, N.H.V. Krarup, T.K. Bergmann, S. Brentzen, S. Neghabat, L. Duval, S.T. Knudsen, A cancer that went up in smoke pulmonary reaction to e-cigarettes imitating metastatic cancer, Chest 149 (2016) e65–e67.

[29] Y. Kam, V. Quaranta, Cadherin-bound β-catenin feeds into the Wnt pathway upon adherens junctions dissociation: evidence for an intersection between β-catenin pools, PLoS One 4 (2009).

[30] A.B. Reynolds, Epithelial organization: new perspective on α-catenin from an- cient source, Curr. Biol. 21 (2011) R430–R432.

[31] P. Goldstraw, K. Chansky, J. Crowley, R. Rami-Porta, H. Asamura, W.E.E. Eberhardt, et. al., The IASLC lung cancer staging project: proposals for revision of the TNM stage groupings in the forth- coming (eighth) edition of the TNM classification for lung cancer, J. Thorac. Oncol. 11(2016) 39–51.

[32] A. Mcneill, L.S. Brose, R. Calder, S.C. Hitchman, P. Hajek, M. H, E-Cigarettes : an Evidence Update A Report Commissioned by Public Health England, (2015).

[33] M.L. Goniewicz, J. Knysak, M. Gawron, L. Kosmider, A. Sobczak, J. Kurek, A. Prokopowicz, M. Jablonska-Czapla, C. Rosik-Dulewska, C. Havel, P. Jacob, N. Benowitz, Levels of selected carcinogens and toxicants in vapour from electronic cigarettes, Tob. Control. 23 (2014) 133–139.

[34] W. Zou, Y. Zou, Z. Zhao, B. Li, P. Ran, Nicotine-induced epithelial-mesenchymal transition via Wnt/β-catenin signaling in human airway epithelial cells, Am. J. Physiol. Cell. Mol. Physiol. 304 (2013) L199–L209.

[35] P. Dasgupta, W. Rizwani, S. Pillai, R. Kinkade, M. Kovacs, S. Banerjee, M. Carless, E. Kim, D. Coppola, Nicotine induces cell proliferation, invasion and epithelial- mesenchymal transition in a variety of human cancer cell lines, Int. J. Cancer 124 (2009) 36–45.

[36] S.A. Grando, Connections of nicotine to cancer, Nat. Rev. Cancer 14 (2014) 419–429.

[37] R.Z. Behar, M. Hua, P. Talbot, Puffing topography and nicotine intake of electronic cigarette users, PLoS One 10 (2015) 1–18.

[38] J.F. Etter, Electronic cigarettes: a survey of users, BMC Public. Health 10 (2010).

[39] K. Brune, J. Frank, A. Schwingshackl, J. Finigan, V.K. Sidhaye, Pulmonary epithelial barrier function: some new players and mechanisms, Am. J. Physiol. - Lung Cell. Mol. Physiol. 308 (2015) L731–L745.

[40] A.E. Carpenter, T.R. Jones, M.R. Lamprecht, C. Clarke, I.H. Kang, O. Friman, D. a Guertin, J.H. Chang, R. a Lindquist, J. Moffat, P. Golland, D.M. Sabatini, CellProfiler: image analysis software for identifying and quantifying cell phenotypes., Genome Biol. 7 (2006) R100.

[41] N. Otsu, A Threshold selection method from gray-level histograms, IEEE Trans. Syst. Man. Cybern. 9 (1979) 62–66.

Chapter 7

Conclusion

OVERVIEW

KEY FINDINGS

Chapter 2: StemCellQC: A video bioinformatics method for analysis of pluripotent stem cell colonies

- There is a foundational need for quality control tools in stem cell laboratories engaged in basic research, regenerative therapies, and toxicological studies. These tools require automated methods for evaluating cell processes and quality during in vitro passaging, expansion, maintenance, and differentiation.
- StemCellQC software was developed as an automated high-content profiling toolkit that non-invasively extracts information on pluripotent stem cell colony quality and cellular processes from time-lapse phase-contrast videos. The software was used to analyze the effects of conventional cigarette smoke on human embryonic stem cells (hESCs).
- Morphological and dynamic features related to growth, motility, and cell death were analyzed in healthy, unhealthy, and dying human embryonic stem cell (hESC) colonies. Biomarkers were discovered that predicted cell processes before they were detectable by manual observation. StemCellQC distinguished healthy and unhealthy/dying hESC colonies with 96% accuracy.

Chapter 3: MitoMo: A Powerful Software Toolkit for Assessing Mitochondria Morphology and Health

- MitoMo, a video bioinformatics software toolkit for analysis of mitochondria health, was developed to integrate options for analysis of morphology, motion, texture, morphogenesis, and health classification into a single software package.
- MitoMo can reveal subtle, sub-organelle changes in mitochondrial motion, which may not be visible to the eye or cannot easily be tracked when mitochondria exist in networks. In addition, it can analyze directional motion of mitochondria relative to other cellular structures, such as the nucleus.
- MitoMo can analyze mitochondrial motion at the whole cell, organelle, and sub-organelle (pixel) levels, as well as in subpopulations of morphological classes of mitochondria. MitoMo can be used to establish baseline mitochondrial phenotype for any cell type.
- MitoMo was able to classify mitochondria as healthy or unhealthy by combining morphology, texture, intensity, and motion features. Treatment of MitoTimer-transfected A549 cells with 0.01mM SeCl4 did not visibly change their networked morphology, however, automatic classification could distinguish them from healthy controls by combining feature types.
- MitoMo was used to study stress-induced mitochondrial hyperfusion (SIMH) in mouse neural stem cells (mNSCs) exposed to electronic cigarette (EC). Morphological analysis confirmed a shift towards the networked (hyperfused) mitochondria in the treated group. Motion analysis at the whole cell level showed an increase in motion in the hyperfused cells, which due to the networked mitochondria.
- MitoMo was used to track the morphogenesis of selenium-induced mitochondrial toxicity. The normally networked mitochondria in A549 lung epithelial cells first formed dynamic donuts and loops, followed by fragmenting into the punctate morphology, before swelling to form the

swollen phenotype. Texture analysis (lacunarity) revealed a denser mitochondrial organization, and motion analysis revealed decreased motion in the swollen mitochondria. MitoTimer red/green fluorescence ratio showed a dose-dependent increase in mitochondrial protein oxidation. Labeling with a GFP-LC3 reporter showed the mitochondria in selenium treated cells are co-localized with autophagosomes indicating their mitophagy (targeted degradation).

- Because MitoMo can be used with any cell type, it should find broad application in basic research, drug development, medicine, and toxicology.

Chapter 4: A Two-Tiered Screen to Identify Modes of Action (MOAs) and Biomarkers of Potential Harm and Disease

- In this study, we developed a two-tiered screening method for identifying cytotoxic EC fluids and aerosols, and then applied it to major brands of cartomizer-style ECs. In tier 1, the MTT cytotoxicity assay and morphological assessments were used to identify two EC products of interest (GreenSmoke and Vuse). In tier 2, multiple bioassays and image processing approaches were used to assess: (1) DNA damage, (2) changes in cell proliferation, attachment, and cell death, (3) fibroblast-to-myofibroblast transition, (4) epithelial-to-mesenchymal transition (EMT), (5) altered nicotinic receptor expression and function, (6) mitochondrial health, and (7) autophagy.
- Exposure to GreenSmoke resulted in cytoskeletal depolymerization, adhesion-to-substrate defects, and eventual apoptosis.
- Exposure to Vuse resulted in upregulation of alpha smooth muscle actin (α-SMA) and morphological changes associated with fibroblast-to-myofibroblast differentiation in hPFs and EMT in A549 cancer cells.

- The high nicotine content of Vuse resulted in a rapid upregulation of nicotinic receptors (α7 nAChR) in lung epithelial cells and altered their sensitivity to nicotine-mediated calcium influx. This has the potential to cause nicotine tolerance with prolonged exposure
- This study concluded that EC exposure from even low-voltage cartomizer-style EC products could lead to adverse health effects and potentially promote diseases such as fibrosis, cancer, and neuro-developmental defects.

Chapter 5: EC Exposure Cause a Stress-Induced Mitochondrial Hyperfusion (SIMH) Response Mediated by Nicotine

- EC treatment caused an increase in the number and size of autophagosomes compared to controls. However, a dual-tagged mApple-pHluorin-LAMP1 reporter indicated the loss of auto-lysosomal acidic environment, resulting in the backup of autophagic flux.
- EC e-liquids/aerosols were also investigated for their ability to induce mitophagy. However, little to no mitophagy was detected, suggesting that SIMH may be protective against mitochondria degradation.
- A stable MitoTimer-NSC reporter cell line which was treated with EC liquids or aerosols from Vuse showed significant elevation in mitochondrial protein oxidation.
- MitoMo software was used to classify the control and EC-treated mitochondrial images into punctate, networked, or swollen morphological subgroups. Treated NSCs exhibited a dose-dependent shift from the punctate (control) to networked (low dose) to swollen (high dose) phenotypes.
- Mitochondrial dynamics were quantified using the pixel-based motion magnification algorithm in MitoMo. Low dose treatment resulted in a significant increase in movement possibly

due to increase of mitochondrial fusion resulting in the networked phenotype. High dose resulted in little or no movement.

- Mitochondrial membrane potential, measured using a TMRM dye, was elevated at low doses, and lost at high doses, indicating leaky, damaged mitochondria.
- EC exposure caused aggregation of mitochondrial DNA (mtDNA) nucleoids.
- The increase in SIMH, mitochondrial protein oxidation and superoxide (MitoSOX) production were shown to be caused by the nicotine concentration in Vuse.
- EC exposure also caused elevation of cytoplasmic and mitochondrial calcium levels via α7 nAChR. EC-induced MitoSOX production was also inhibited in the presence of EGTA, a calcium chelator.
- Damage to stem cells and their mitochondria could impact important biological processes to name a few: 1) neurogenesis during development, 2) differentiation to replace lost or injured tissue/cells, 3) decline of proliferation leading to a diminished stem cell pool, and 4) metabolism.

Chapter 6: EC Exposure Causes an Epithelial-to-Mesenchymal Transition (EMT) in A549 Lung Cancer Cells

- Human adenocarcinoma alveolar basal epithelial cells (A549) were exposed in vitro to liquids and aerosols from a popular EC product, Vuse. The purpose of our study was to: (1) investigate the effects of EC on EMT of lung cancer cells, and (2) characterize the morphological, molecular and behavioral phenotypes of EC-treated cancer cells.
- Several video bioinformatic approaches were developed to quantify the morphological sub-populations (cobblestone, enlarged, and elongated mesenchymal-like) using supervised machine learning algorithms. Also, Hoechst-labeled cells were individually tracked using another software

Cl-Quant, and migration graphs were plotted using Matlab showing cell motility trajectories and increase in the percent of motile population.

- In-vitro sub-chronic exposure (5-8 days) of A549 lung cancer cells to EC aerosols and e-liquids induced an EMT that was characterized by: (1) transformation of cobble-stone colonies into enlarged and elongated mesenchymal-like morphologies, (2) loss of cell-to-cell junctions, which was congruent with downregulation of E-cadherin due to its internalization via endocytosis, (3) increase in the population of motile cells and migratory behavior, (4) upregulation of other classical EMT markers including vimentin, MMP9, N-cadherin, and Snail, and (5) nuclear translocation of β-catenin, a key transcription factor (and another stabilizer of adherens junctions).

SIGNIFICANCE

Smoking is a major risk factor for lung cancer, the number one preventable cause of death. Recently, the tobacco industry has been transformed by the introduction of ECs, which are sometimes considered harm reduction products. Some studies report that the concentrations of carcinogens in EC aerosols are lower than in tobacco smoke; however, exposure levels vary significantly based on device type, nicotine/flavoring content, and user topography. Moreover, there is no research to date on the effects of ECs on cancer progression (e.g. metastasis). This study is the first to show the fibrogenic/metastatic potential of Vuse (a high-nicotine content EC products) to: 1) upregulate key biomarkers of myofibroblast differentiation in treated pulmonary lung fibroblasts and 3) induce an EMT in epithelial lung cancer cells. Our data support the idea that EC use over time could lead to pulmonary fibrosis and cancer metastasis, which has significant implications for former or current smokers who may be at risk for lung diseases such idiopathic pulmonary fibrosis (IPF) and cancer, or who may have a pre-existing tumor.

EC-induced mitochondrial damage and autophagy dysfunction to clear damaged mitochondria/mtDNA can cause deleterious effects in stem cell populations, which in turn could accelerate aging and lead to a variety of diseases (e.g. developmental defects, cancer, neurodegenerative disorders, etc.). This study further demonstrated that the SIMH survival response initiated by EC fluids or aerosols was attributable to nicotine. These findings are important given that nicotine is now widely available in EC refill fluids and as a pure chemical for use in do-it-yourself EC products. Also, there is evidence of mislabeled or unlabeled EC products containing nicotine. In a broader sense, any nicotine containing product may likewise stress stem cells with long-term repercussions for users and passively exposed individuals. This supports the idea that EC are not as harmless as often claimed and that even short-term exposure can stress cells in a manner that may lead, with chronic use, to morbidity or disease.

The software and toxicological high-content screening method developed in this dissertation can be further applied to other potentially toxic EC products, EC constituents, or any chemical/product of interest, to gain insights into their MOAs. With over 7,000 refill fluids and countless new EC products coming onto the market, there is a great risk to consumers, particularly youth who may be more sensitive and prone to marketing strategies. We hope that our data can inform regulatory agencies regarding the dangers of EC use and affect implementation of policies. We believe that special attention should be given to nicotine, which is present in almost all EC product (some at extremely high concentrations). High nicotine content EC products (such as JUUL) is a big concern. We hope that regulatory agencies enforced assays involving nicotine MOAs before approving any EC product under the FDA deeming regulations.